Cryogenic silicon resonators as stable ultra-low-drift frequency references

Inaugural dissertation

for the attainment of the title of doctor

in the Faculty of Mathematics and Natural Sciences

at the Heinrich Heine University Düsseldorf

presented by

Eugen Wiens

from Pyatigorsk, Russia

Düsseldorf, June 2021

from the Institut für Experimentalphysik
at the Heinrich Heine University Düsseldorf

Published by permission of the
Faculty of Mathematics and Natural Sciences at
Heinrich Heine University Düsseldorf

Superviser: Prof. Dr. Stephan Schiller
Date of the oral examination: 24.06.2021

Affidavit

I declare under oath that I have produced my thesis independently and without any undue assistance by third parties under consideration of the “Principles for the Safeguarding of Good Scientic Practice at Heinrich Heine University Düsseldorf”

Düsseldorf, 24.06.2021

Eugen Wiens

ABSTRACT

This work describes all stages of the development of three silicon mono-crystal optical resonators and their operation in the deep cryogenic regime at 1.5 K in a pulse-tube cryostat with an attached Joule-Thomson stage and active stabilization of tilt. The first system, consisting of a horizontally-oriented resonator with a length of 25 cm, was mounted inside a copper frame with a ten-point support configuration and operated uninterrupted for three years at the temperature of 1.5 K, except for short maintenance intervals of the cryostat. During this time the sensitivity of the resonator to temperature, vibrations, tilt, and optical power was characterized. The resonator possesses an extremely low coefficient of thermal expansion of 1.4×10^{-13}/K at the temperature of 1.5 K. Additionally, the thermal response was investigated in the temperature range from 1.5 K to 23.8 K, and a zero-crossing of sensitivity with a temperature derivative equal to -6×10^{-10}/K^2 was found at a temperature of 16.8 K. The mean sensitivity to vibrations along all three spatial directions was measured using the eigenvibrations of the pulse-tube in the frequency range up to 200 Hz. We found it to be on the order of $1 \times 10^{-8}/g$. The frequency stability of a 1.5 µm laser locked to the TEM_{00} mode was measured against a hydrogen maser corrected for frequency drift using a GNSS atomic reference. It is comparable to the stability of a hydrogen maser for the integration times between 1 s and 10 000 s. We also monitored the long-term drift of the resonator. The most stable half-year interval displayed the lowest drift ever measured with optical resonators, $< 1.4 \times 10^{-20}$/s in fractional terms. After evaluation of all sensitivities, the system was shown to have the potential to reach instabilities of 1×10^{-16} at median integration times with a short-term instability limited by vibrations inside the cryostat together with a high vibration sensitivity of the resonator.

To minimize the influence of the pulse-tube-generated vibrations we designed a 5 cm long, vertically oriented silicon optical resonator installed inside a copper frame using three support points. Designed for low acceleration sensitivity, this system displayed a sensitivity of 133 kHz/g ($6.9 \times 10^{-10}/g$). Besides a zero crossing of temperature sensitivity at 17 K, this resonator exhibits an additional zero crossing of thermal sensitivity at 3.5 K with a temperature derivative of 8.5×10^{-12}/K^2. Locking a 1.5 µm laser, prestabilized to a room-temperature ULE resonator to the silicon resonator, the latter was found to provide an optical frequency with instability comparable to that of a hydrogen maser and reached a minimum frequency instability of 2×10^{-15} at 1000 s integration time. We estimate that in an optimized, low-vibration cryostat the resonator should reach an instability of 1×10^{-15} at 100 s. The long-term frequency drift was found to be sensitive to the intensity of the laser wave used for the interrogation and the duty cycle. By minimizing the intensity to 100 nW and keeping the duty cycle at 30% we could reduce the drift rate to 49(4) µHz/s ($< 3 \times 10^{-19}$/s). With further reduction of intensity, this feature could allow to null the frequency drift rate.

Results obtained with the 5 cm long resonator allowed to build and install a 190 cm long resonator inside a Leiden Cryogenics cryostat equipped with a home-built two-stage vibration isolation system, which reduces vibrations at the experiment by a factor of 40. This system is still an ongoing project, that has already shown hydrogen-maser-matched performance, long-term frequency drift on the order of 1×10^{-20}/s, and vibration sensitivity of $1 \times 10^{-10}/g$.

Using the frequency stability of the 25 cm long horizontal resonator we search for hypothetical violations of Lorentz Local Invariance (LLI) and Local Position Invariance (LPI) in the ratio of the frequency of a cryogenic silicon optical resonator and a hydrogen maser. The analysis of LLI was done within the Robertson-Mansouri-Sexl kinematic test theory, assuming the Cosmic Microwave Background (CMB) as the reference frame. The violation parameter is $P_{KT} = (0.9 \pm 1.1) \cdot 10^{-5}$. The analysis of LPI is done by a null redshift test, using the natural motion of the Earth in the sun's gravitational potential. We obtain the violation parameter $\beta = (1.0 \pm 1.1) \cdot 10^{-5}$. The 1 σ upper limit for $|\beta|$ is better than the best previous result obtained with an electromagnetic resonator.

ACKNOWLEDGMENTS

It is a pleasure for me to thank the many people I worked with during the past years and who helped me with the completion of my work.

First of all, I would like to express deep gratitude to my supervisor Professor Stephan Schiller for his guidance and constant encouragement with his great knowledge, expertise, and patience which I deeply appreciate. He instructed me on how to design sophisticated experiments, carefully analyze the results, and how to present them in form of skilled scientific publications.

I am grateful to Dr. Alexander Nevsky for his kind invitation to work in this exciting area of research. With his broad knowledge and experience, he provided tremendous help and expert direction. He taught me just about everything on how to do experiments and how to manage things in the lab.

I am obliged to Dmitri Iwaschko for building the electronics that strongly contributed to the success of this work and for always providing quick and efficient solutions to many problems.

I thank Chang Jian Kwong for the optical contacting of the 5 cm Si resonator and many valuable discussions in regard to FEM simulations and optical resonators, Michael Hansen for his help with the frequency comb and his support concerning various things that helped to improve the safety and quality of my laboratory work, Ulrich Rosowski for his help with the stabilization of lab temperature, storage of 500 GB experimental data, support in many IT problems and his maintenance of hydrogen masers and the frequency comb, my office mate Rene Oswald for sharing his experience with work-related and unrelated issues and helping me with the cryostat, Rita Gusek for her aid with the electronics, Franziska Bergstein, Oliver Wyczisk and his workshop team for machining of parts needed for the experiment, secretary Beate Rödding for help with organizational details.

I thank all members of the Institut fr Experimental Physik for their support.

I would also like to extend my thanks to my former colleague Dr. Qun-Feng Chen for designing the 25 cm silicon resonator and helping with the initiation of the experiment, Dr. Ingo Ernsting for sharing his expertise in the operation of the frequency comb, Heiko Luckmann for his work on the cryostat, Dr. Denis Sutyrin for his help with the FEM simulations, Dr. Marco Schioppo for helpful discussions, and Peter Dutkiewich for his help with the electronics.

I would like to acknowledge the scholarship of the Behmenburg-Schenkung and to thank late Professor Wolfgang Behmenburg for his support.

This work was funded by European Space Agency Project No. 4000103508/11/D/JR and by Deutsche Forschungsgemeinschaft Project No. Schi 431/21-1. I would like to thank I. Zayer and J. de Vicente from ESA for their support.

I thank Dr. Thomas Legero from PTB for the optical contacting of the 25 cm Si resonator and for providing me with the design of the biconical Si resonator.

I am grateful to Dr. Timo Müller from Siltronic AG for the silicon material.

Special thanks go to Professor Giorgio Frossati from Leiden Cryogenics and his team. Their continuous help and support made it possible to run the cryostat uninterrupted for a record time of three years.

Finally, I would like to thank my wife Anzhelika, my mother Nina Wiens, and my brother and sister, Peter and Anna, for their love, encouragement, and care throughout the years. I thank my two daughters, Diana and Beatrice for bringing me endless joy that accompanied me during my work on this dissertation.

Contents

1 Introduction

Since the invention of lasers in the second half of the 20th century [1] they became an important tool in the field of physical research, where they are employed e.g. in laser metrology [2, 3, 4], laser spectroscopy [5, 6, 7, 8, 9], the gravitational-wave detectors [10, 11, 12], optical atomic clocks [13, 14, 15, 16, 17, 18, 19], dark-matter detection [20, 21, 22], very long baseline interferometry [23] and astronomy [24, 25], relativistic geodesy [26, 27, 28, 29] and tests of fundamental physics [30, 31, 32, 33, 34, 35, 36, 37]. The precision of these state-of-the-art experiments is directly related to the stability and purity of the applied laser wave and ideally requires a linewidth in the mHz range and the fractional frequency instability on the order of 10^{-17} or below. To satisfy these requirements there is a never-ending commercial quest for improvement of the frequency stability of lasers. However, even last-generation lasers lack the required stability and cannot be used off-the-shelf (see Fig. 1.1). This makes a further frequency stabilization of their output waves necessary for their employment in the aforementioned applications.

Optical resonators represent to date the most common tools for the stabilization of lasers. They usually consist of a pair of mirror substrates, coated for high reflection and low optical losses at the ppm level, which are separated by a hollow spacer machined from a single piece of material with parallel end faces polished to allow for optical contacting of the mirror substrates (see Fig. 1.2). The transmission spectrum of an assembled resonator displays a set of distinctive lines which can be used for the stabilization of lasers. Their frequency stability reflects the dimensional stability of the resonator. A system consisting of a resonator in conjunction with a laser locked to its transmission line using a suitable locking technique, e.g., the Pound-Drever-Hall technique [38, 39, 40], represents a device that translates the length stability of the resonator into the frequency stability of its output optical wave. The requirement for ultra-stability of the laser wave makes it an essential prerequisite to isolate the resonator from all kinds of environmental perturbations which can influence its length, such as vibrations, tilt, temperature, and pressure variations, thermo-elastic deformations of mirrors due to the fluctuating laser power and material creep. This is usually done using passive and/or active isolation/stabilization techniques together with a careful choice of material with a low sensitivity response to the variations of the parameter in question. For instance, in order to reduce the influence of environmental seismic and acoustic vibrations, the resonator is operated inside a vacuum chamber installed on an active vibration isolation platform. In addition to this, the shape of the resonator and the position of the supports are optimized in order to minimize its vibration sensitivity. Temperature variations are reduced using multi-stage isolation, each with separate active temperature stabilization, and by choosing materials with a low coefficient of thermal expansion in the temperature region of future operation. The result of these

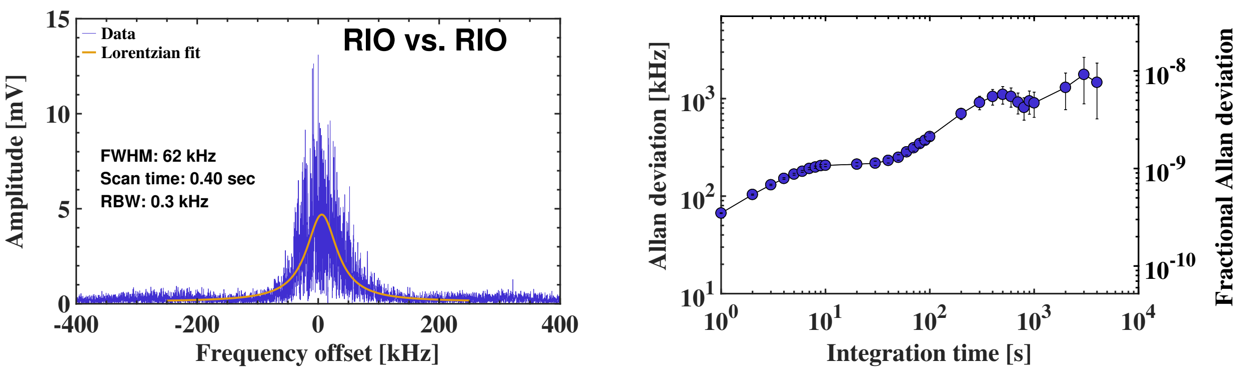

Figure 1.1: Properties of the free-running ORION laser (built by Redfern Integrated Optics Inc.) used in this work. **Left panel:** 62 kHz linewidth of the beat with a second ORION laser, frequency stabilized to an optical resonator. **Right panel:** frequency stability, measured against the hydrogen maser with a frequency comb.

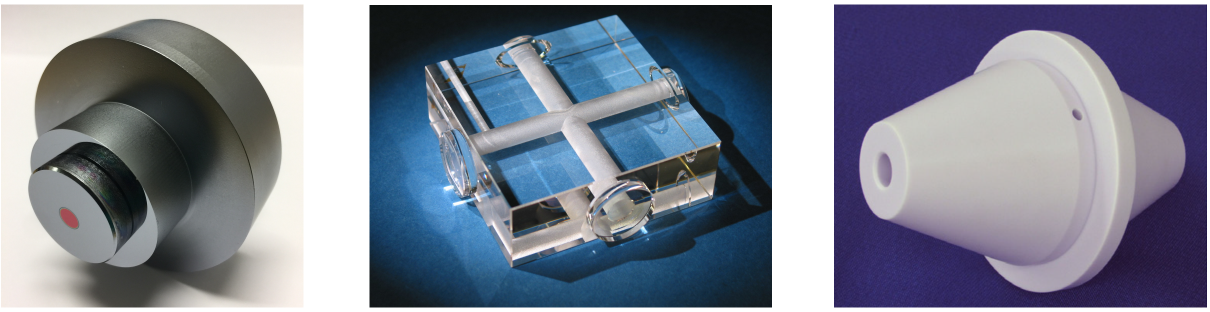

Figure 1.2: Examples of optical resonators. **Left panel:** 50 mm long silicon resonator (used in this work) with a visible anti-reflection coating, designed for 1550 nm, at the top of the front mirror. **Middle panel:** 84x84 mm ULE block with two resonators (from [41]). **Right panel:** 120 mm long Nexcera ceramic spacer before optical contact with mirror substrates (from [42]).

ongoing activities toward the improvement of the length stability of the resonators is a reduction of the frequency instability by more than a factor of 100 over the last three decades (see Fig. 1.3).

While there exists a broad range of resonators with different shapes and dimensions built for a wide variety of applications, there is only a limited choice of materials for usage at or near room temperature. Ultra-low-expansion glass (ULE) has long been the material of choice for resonators at this temperature. The resonators made of ULE, equipped with fused silica mirrors [44], reach the residual frequency instability $\Delta\nu/\nu$ on the order of a few times 10^{-15} on short time scales [45, 46, 47, 48, 49]. This number represents a fundamental limit defined by the fluctuation of the distance between the mirrors due to the Brownian thermal motion of the today's common amorphous tantala/silica Ta_2O_5 and SiO_2 multilayer dielectric mirror coatings, mirror substrates, and the spacer [50, 51]. According to Fig. 1.4 this limit can be lowered into the 10^{-16} instability region either by increasing the distance between the mirrors, thus building longer resonators [52, 53, 54, 55, 56], increasing the beam size by stabilizing the laser to the higher-order modes of the resonator [57, 58, 59, 60, 61], using a different kind of mirror coatings (e.g., crystalline) with the lower mechanical loss [62, 63], or by cryogenic operation of the resonator [30, 35, 64, 65, 66, 67, 68, 69, 70, 71].

Another limitation of the frequency stability of the room-temperature ULE resonators is their relatively large fractional frequency drift on the order of 1×10^{-16}/s due to the creep of the amorphous material. This number can be reduced with a recently developed Nexcera ceramic [72, 73, 74] by one order of magnitude to 1.6×10^{-17}/s [74].

Cryogenic temperatures are expected to allow to lower the residual thermal noise of the resonators

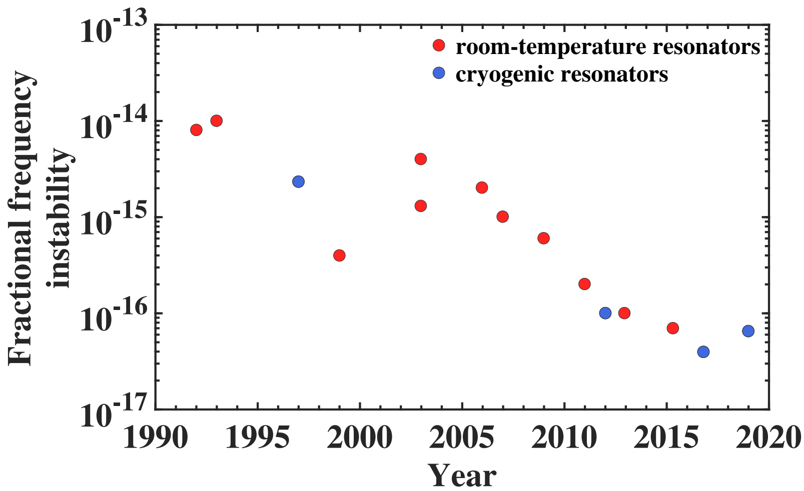

Figure 1.3: Improvement of the frequency instability of the state-of-the-art optical resonators over the last three decades (adapted from [43]).

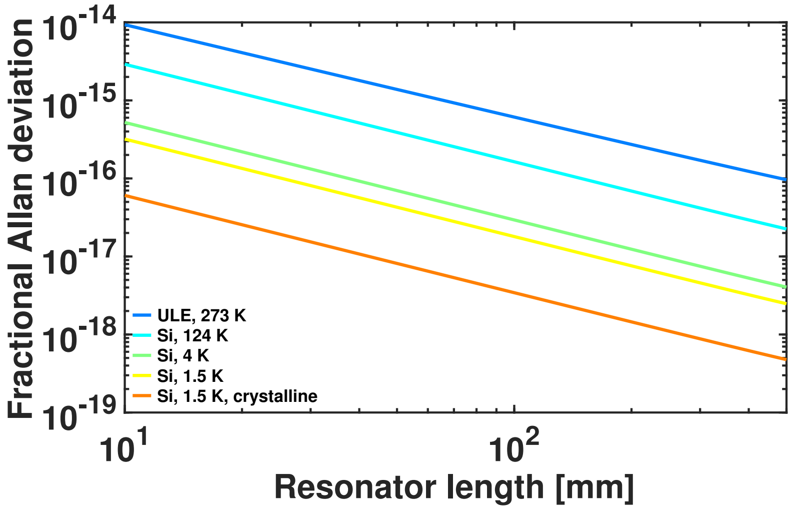

Figure 1.4: Calculation of theoretical thermal noise limit for resonators made of ULE glass or monocrystalline silicon on their length and environmental temperature. All calculations are done for common high-reflective tantala/silica amorphous coatings (SiO_2/Ta_2O_5) except for silicon at 1.5 K, where an additional calculation was done for mirror substrates equipped with crystalline $Al_xGa_{1-x}As$ coating.

down to the level of $< 10^{-17}$. A choice of an appropriate material with high stiffness to survive cooldown to cryogenic temperatures, low thermal expansion, and high thermal conductivity to minimize the response of the resonators to thermal variations at these temperatures becomes crucial and renders the room-temperature ULE material unsuitable. The mentioned criteria are usually satisfied by crystalline materials. Among those, the most outstanding, with excellent thermal and mechanical properties, are sapphire and silicon. They are characterized by a very low thermal expansion coefficient of $\sim 10^{-12}$/K [64, 68] and high thermal conductivity on the order of 1 W/(m·K) [75, 76] below 2 K. They can be grown as a high-purity singe-crystals with a perfect crystal structure and absence of any defects, thus eliminating any possible frequency drift due to the aging of the material. Today, both materials are routinely used in cryogenic optical resonators.

First cryogenic operation of a sapphire single-crystal resonator was demonstrated in 1997 [64], followed by a first long-term operation over a 6-month period with a total frequency drift of 2.7 kHz [77] and an operation at the record-low temperature of 1.4 K [78]. Since then, sapphire single-crystal resonators with an average frequency instability above or equal to 2.3×10^{-15} at low averaging times were successfully applied for tests of fundamental physics [30, 79, 80, 81]. Due to the nature of the sapphire single-crystal growing procedure, the dimensions of the resonators remain at the level of a few cm. Purchase costs set another limiting factor that prevents the further spreading of this type of resonator.

Cryogenic operation of a silicon resonator with a length of 15 cm was first tested by [82] in 1991. After measuring the thermal expansion of the resonator at 4.2 K it was predicted, that with proper temperature stabilization silicon resonators are capable of reaching instability below 1×10^{-15}. However, it took 21 years for the optical resonator community to focus on cryogenic silicon resonators [66]. This was triggered by the need for high-stability frequency sources for the optical clocks and was enabled by recent advances made in cryogenic engineering, vibration isolation techniques, and developments in the semiconductor industry, which enabled cost-efficient production of silicon mono-crystals ingots with a high degree of purity and sufficiently large dimensions.

Today, despite great technological challenges and the required level of complexity, silicon single-crystal optical resonators enjoy an increased degree of popularity. Operated at 124 K, the temperature of the first zero-crossing of the coefficient of thermal expansion of silicon, they demonstrate the lowest, thermal noise limited degree of frequency instability among optical resonators, 4×10^{-17} at short and median integration times [69] and a fractional frequency drift below 5×10^{-19}/s [67]. Operated at 4 K,

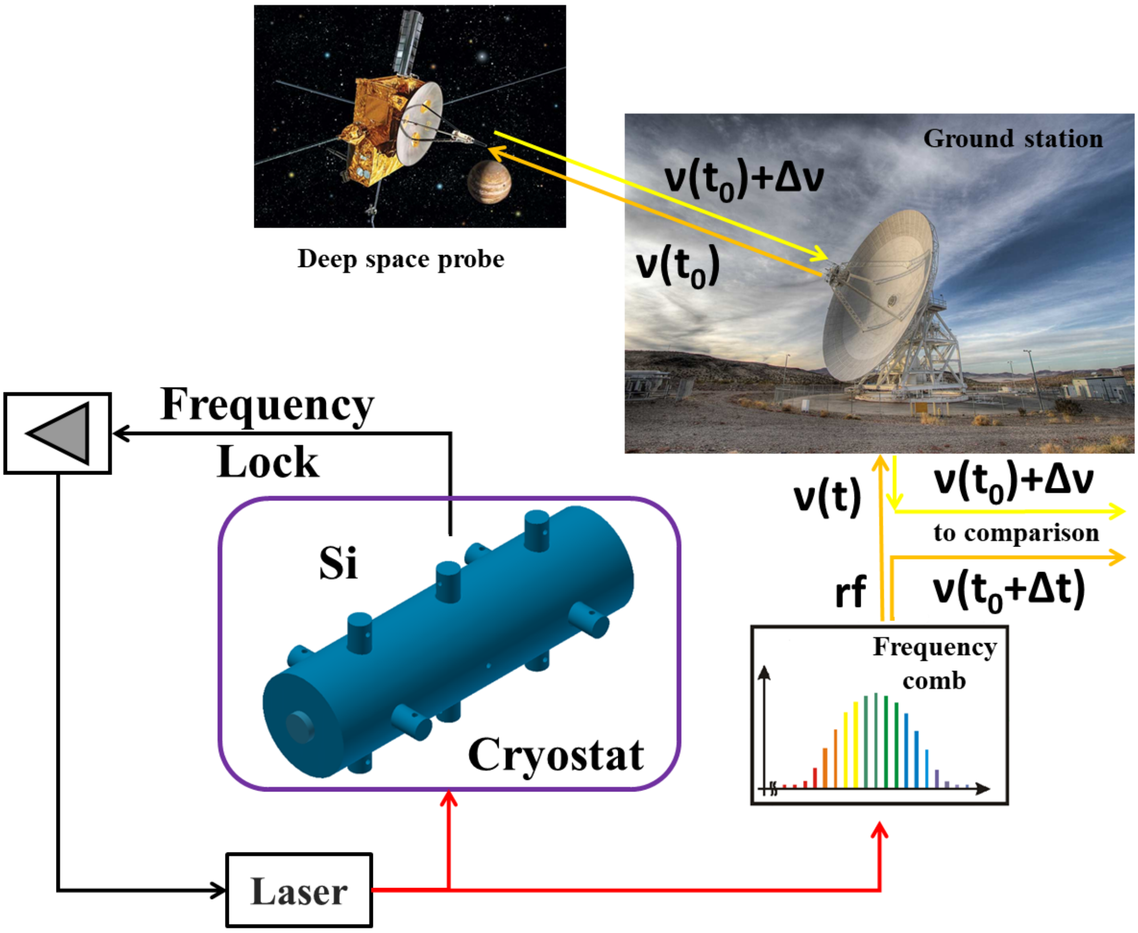

Figure 1.5: Principal schematic for the integration of a cryogenic silicon resonator as reference oscillator into the ESA deep space network used for Doppler tracking of spacecrafts: the frequency stability of a laser locked to the cryogenic silicon resonator is transferred to the microwave frequency domain via frequency comb. The microwave with a frequency $\nu(t_0)$ at a time t_0 is sent toward the deep space probe using the ground station antenna. After the time period Δt the returning wave, reflected by the moving probe and having the frequency $\nu(t_0) + \Delta\nu$, is detected by the ground station. To extract the speed of the spacecraft relative to the ground station along their mutual line of sight, the Doppler-shifted frequency of the detected wave is compared to the frequency $\nu(t_0 + \Delta t)$ of the local oscillator.

another silicon resonator demonstrated a laser light power-dependent frequency drift [70, 71]. These properties make silicon resonators an attractive competitor with hydrogen masers.

The work presented here was done in the group that has gathered large experience with the operation of room-temperature ULE and sapphire cryogenic resonators. Based on the historical context of the year 2012, together with PTB (Braunschweig) we were among the first groups worldwide to explore the properties of silicon resonators at cryogenic temperatures [66, 68]. The goals of our work were defined by the framework of the two following projects:

- **Development of next-generation reference clock for navigation of deep space probes:** The initial work in our group was done in the framework of the ESA funded project aimed at the development of cryogenic silicon resonators as reference clocks for ESAs deep space network with a goal to demonstrate a frequency instability of $1 \times 10^{-14}/\sqrt{\tau}$ on time scales $\tau \leqslant 10\,000$ s. Installed on the ground next to one of the three ESAs deep space network antennas and operated continuously and maintenance-free for over a year inside a closed-cycle cryostat (see Fig. 1.5), silicon resonators could provide a stand-alone system with frequency stability superior to that of hydrogen masers.

- **Further development of ultra-stable silicon resonators:** The follow-up DFG-funded project concentrated on further improvement of the frequency stability of the cryogenic silicon resonator with a goal of 5×10^{-17} fractional frequency instability at integration times τ between 100 s and 10 000 s.

Five resonators using three different home-developed designs were built and operated inside a closed-cycle pulse-tube helium cryostats with the lowest working temperature of 1.4 K. Three of these resonators, most thoroughly investigated, are presented in this work. Their properties are summarized in Tab. 1 and their technical drawings can be found in Appendix E.

Table 1: Summary of the properties of the three mono-crystalline silicon resonators used in this work.

Parameter	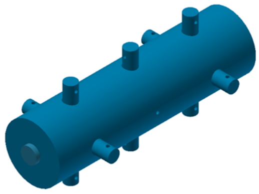	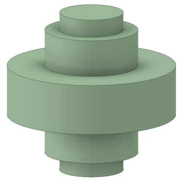	
Length (mm)	250	50	190
Orientation	horizontal	vertical	vertical
Number of supports	10	3	3
Crystal orientation	[100]	[111]	[111]
Crystal resistivity (kΩ·cm)	4000	8000	8000
Linewidth (kHz)	2.1	24.2	3.5
Free spectral range (MHz)	600	3000	789
Finesse	286 000	124 000	225 000
Mirror thickness (mm)	6.3	6.3	6.3
Mirror diameter (mm)	25.4	25.4	25.4
Mirror crystal orientation	[100]	[100]	[100]
Mirror crystal resistivity (kΩ·cm)	4000	4000	4000
Curvature radii of the mirrors (m)	1/∞	1/∞	1/∞
Beam waist at the flat mirror (mm)	0.464	0.329	0.442
Beam waist at the curved mirror (mm)	0.536	0.338	0.491
Thermal noise limit, σ_y (10^{-17})	0.81	2.8	0.8

To be able to successfully operate these three resonators, abbreviated as Si1, Si5, and Si190 in this work, and to reach the specifications proposed by the projects following issues have to be addressed:

1. **Low-vibration sensitivity design:** resonators must be carefully designed for low sensitivity to vibrations using a commercial finite-element-method (FEM) package (Ansys and Comsol). This step is crucial due to the operation of the resonators in the noisy environment of the closed-cycle pulse tube cryostat (see Sec. 3.2).

2. **Supporting frame:** A suitable supporting frame must be designed. The materials for the frame must be carefully chosen to allow for damping of thermal fluctuations transmitted to the resonator, thus acting as a low-pass filter. Due to the different materials used, an additional FEM study must be done to minimize the interplay between the resonator and the supporting frame induced by the difference in their response to temperature changes.

3. **Optical contacting:** to form a resonator, mirror substrates have to be attached to the polished end surfaces of the spacers by optical contact. During this process, the alignment of the symmetry axes of both the mirrors and the spacer has to be insured. Every discrepancy in their position will increase the sensitivity of the resonators to vibrations.

4. **Cryostat characterization and long-term operation:** this step includes the study of the temperature stability at the experimental plate and characterization of the spectrum of vibrations produced by the pulse tube cryocooler (see Sec. 3). Trouble-free long-term operation of the cryostat (at least half a year) should be insured in order to study the long-term frequency drift of the resonators.

5. **Cryogenic vibration sensors:** to measure vibrations in the cryostat and to determine the vibration sensitivity of the resonators suitable commercial sensors must be adapted for use in a cryogenic environment.

6. **Tilt stabilization of the cryostat:** every change in tilt produces an additional compression force on the resonators operated inside the cryostat and thus changes their length and shifts their resonance frequency. To account for this, an active tilt stabilization system has to be implemented (see Sec. 3.3).

7. **All-cryogenic optical system:** to ensure stable, time-independent uncoupling of the laser light into the resonators an all-cryogenic optical setup has to be implemented. This setup should incorporate three motorized mirror mounts to allow for possible corrections of the uncoupling due to the position changes and mechanical stress introduced by the cooldown process. Further, frequency locking of the laser light to the transmission line of the resonators requires a set of cryogenic photodiodes to monitor the amplitude of the reflected and transmitted light. To reduce noise in the reflection signal and to increase the overall bandwidth the cable length between the photodiode in reflection and the corresponding amplifier has to be minimized. This requires a development of a cryogenic amplifier (see Sec. 4).

8. **Phase noise cancellation in cryogenic optical fiber:** due to the operation of the cryostat, the optical cryogenic fiber is constantly twisted and shaken. This produces undesirable linewidth broadening of the laser wave going through it, which should be eliminated using an active fiber noise cancellation technique (see Sec. 10.2).

9. **Temperature stabilization:** to understand the requirements for temperature stability and to characterize the thermal sensitivity of the resonators a technique for active stabilization of temperature should be implemented.

10. **Power stabilization:** fluctuations of the optical power circulating inside the resonators result in changes of the optical absorption at the mirror substrates which leads to changes in temperature and length. Thus, an active power stabilization technique is necessary to ensure a constant level of circulating power inside the resonator and to prevent changes in the mirror distance.

11. **Laser frequency stabilization:** to measure the frequency changes of the resonators an active laser frequency stabilization technique has to be implemented.

12. **Vibration isolation:** to reduce vibrations at the experimental side generated by the cryostat active or passive vibration isolation should be implemented.

This thesis is organized in chronological order. It starts with a thorough description of the first type of resonator with a 25 cm length (Si1) followed by the description of the newly developed 5 cm Si5 and 19 cm Si190 resonators and an application of the achieved frequency stability results for tests of Einstein Equivalence Principle. The work is rounded up by the discussion of possible improvements.

2 A 25 cm silicon resonator

2.1 Design

The resonator consists of a cylindrical spacer, two mirror substrates, and ten additional cylinders cut out of a single, undoped, dislocation-free, float-zone silicon mono-crystal with a resistivity of 4 kOhm·cm and a [100] crystallographic direction oriented along the optical axis of the resonator. For an optimal match of their physical properties, all parts were cut out by preserving their relative orientation in the resonator as in the original crystal. The spacer, with end faces polished for optical contacting, has a length of 250 mm, an outer diameter of 70 mm, and an axial bore of 15 mm. Two super-polished and coated for 1.5 µm wavelength mirror substrates with a target finesse of 300000, a thickness of 7 mm, and a surface curvature radii of $R_1 = 1$ m and $R_2 = \infty$, were optically contacted to the spacer. The resulted free spectral range is 600 MHz (see Fig. 2.1, left panel). Selected curvatures of the mirrors together with chosen resonator length result in a degenerate position of low and high order modes. This issue was not considered during the design process of the resonator.

The resonator is supported by a copper supporting frame with a ten-point support configuration using ten small silicon cylinders glued to the spacer with a stycast epoxy and a set of flexible stranded stainless steel (type 316) wires of 1 mm thickness consisting of 19 braids of 0.2 mm diameter, as seen in Fig. 2.2 (left panel) [83]. Stainless steel wires hold the resonator in place by blocking every movement along their centerline. However, they allow movement perpendicular to their centerlines, due to their flexibility. As can be seen in Fig. 2.2, right, there are three sets of wires (marked with different colors), which are responsible for holding the resonator in one particular direction. Thus, all ten wires together not only effectively prevent the resonator from displacement along the three perpendicular axes, but also allow to block possible rotation of the resonator relative to the supporting frame.

2.2 FEM simulations

To reduce the sensitivity to accelerations the position of the ten small cylinders, which are connected to the frame with the aid of the stainless steel wires, was optimized with FEM software. The resulted total displacement and the displacement along the optical axis of the resonator for a 1g acceleration applied along all three spatial directions consecutively is displayed in Fig. 2.3. For each type of acceleration only cylinders responsible for holding the resonator were set as supports. Their heads can be seen as blue colored in Fig. 2.3 (right column). The results show, that for an optimal position of support cylinders

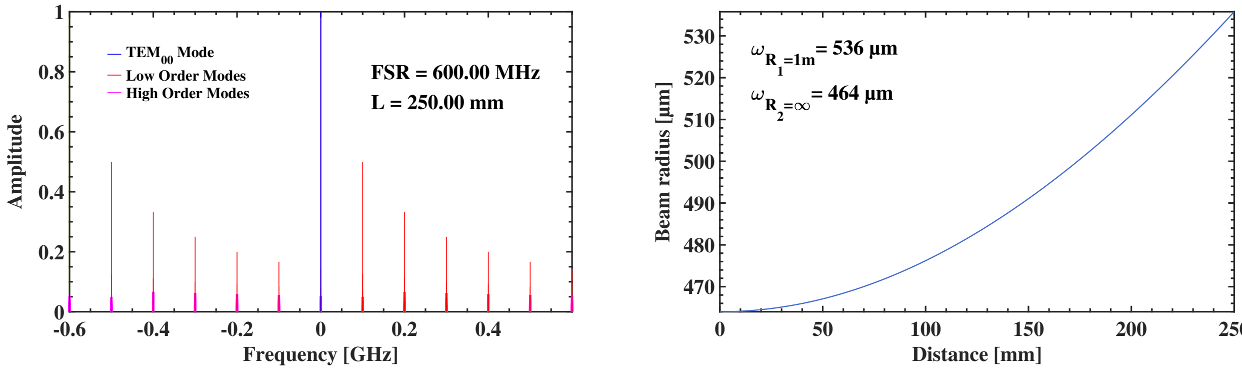

Figure 2.1: **Left panel:** resonator mode spacing. **Right panel:** calculated beam waist radius ω inside the resonator with a flat mirror set at zero mm distance.

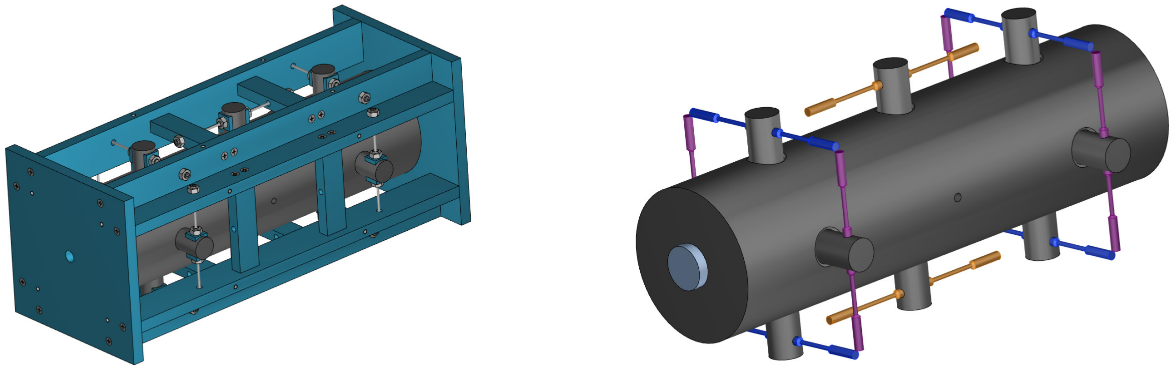

Figure 2.2: **Left panel:** schematic of the resonator with the supporting frame. **Right panel:** schematic view of the resonator with ten supporting wires. Each set of colored wires prevents the resonator against displacement along the corresponding direction. All ten wires effectively prevent rotation of the resonator relative to the supporting frame.

the change in the mirror distance due to the applied accelerations is zero. However, the ideal symmetry of the shape of the resonator is rarely possible due to the finite precision in manufacturing, imprecise optical contacting of the mirror substrates, and errors in the position of the small cylinders due to the gluing process. Another contribution comes from irregularities in the positioning of the resonator inside the supporting frame.

We evaluated the sensitivity to a typical manufacturing error of 0.1 mm in the position of the supports and obtained an increase in sensitivity of 1×10^{-11}/g and 1×10^{-13}/g for the acceleration acting along the optical axis of the resonator and perpendicular to it, respectively.

Imprecise optical contacting of the mirrors results in the shift of the optical axis of the resonator with respect to the symmetry axis. For a shift of 1 mm, our simulations yield an increase in sensitivity of less than 1×10^{-12}/g and 1×10^{-11}/g for the acceleration acting along the optical axis and perpendicular to it, respectively.

We also obtained frequencies of the eigenmodes of vibration of the unsupported and in-frame resonator (see Fig. 2.4). Fist resonance of the free-standing resonator, which corresponds to the bending in the xz-plane, occurs at a frequency of $f = 6.34$ kHz followed by bending in the xy-plane at a frequency of $f = 6.39$ kHz (not shown in Fig. 2.4). Torsional and compressional resonance occurs at a frequency of $f = 10.9$ kHz and $f = 14.43$ kHz, respectively. They are followed by another resonance at $f = 14.54$ kHz which corresponds to a more complicated bending, than the first resonance at $f = 6.34$ kHz.

The in-frame resonator displays eigenmodes of vibration corresponding to the bending in the xz- and xy-plane at the slightly higher frequencies of $f = 6.4$ kHz and $f = 6.45$ kHz, respectively. However, there are three eigenmodes at lower frequencies which corresponds to the pendulum motion of the resonator along the three orthogonal directions inside a frame. The characteristic frequencies of these eigenmodes are equal to $f = 2.5$ kHz for the pendulum motion along the optical axis of the resonator and $f = 3.4$ kHz for the two pendulum motions perpendicular to it.

2.3 Assembly

To assemble the resonator we first optically contacted the mirror substrates to the end faces of the spacer. This step was done by Dr. T. Legero at PTB. The small cylinders were simultaneously glued at one side of the resonator using stycast epoxy (see Fig. 2.5). Both the cylinders and the corresponding spacer surfaces were coated with epoxy before attaching the cylinders. The amount of applied epoxy was tried to be held constant for all cylinders. All cylinders were rotated to ensure proper orientation of the holes designed to hold the steel wires. After attaching the cylinders at one side, the resonator was put on them to ensure the correct orientation of the cylinders with respect to the spacer and to level their height using the weight of the spacer. The resonator was held in this position until the glue was hardened. This process was repeated four times until all cylinders were glued (see Fig. 2.5, middle panel).

To mount the resonator inside the frame we first assembled half of the frame. The horizontally oriented resonator was put inside and the remaining parts of the frame were attached (without the front plates). The steel wires were installed at the top side. Then, the resonator and the frame were rotated 180 degrees to attach the steel wires at the opposite side. During this process, the rule was used to ensure the symmetrical position of the resonator relative to the frame. This procedure was subsequently completed for the two remaining sides. The resulted structure is seen in Fig. 2.5, bottom panel. After attaching the two front plates the resonator is ready for installation inside the cryostat.

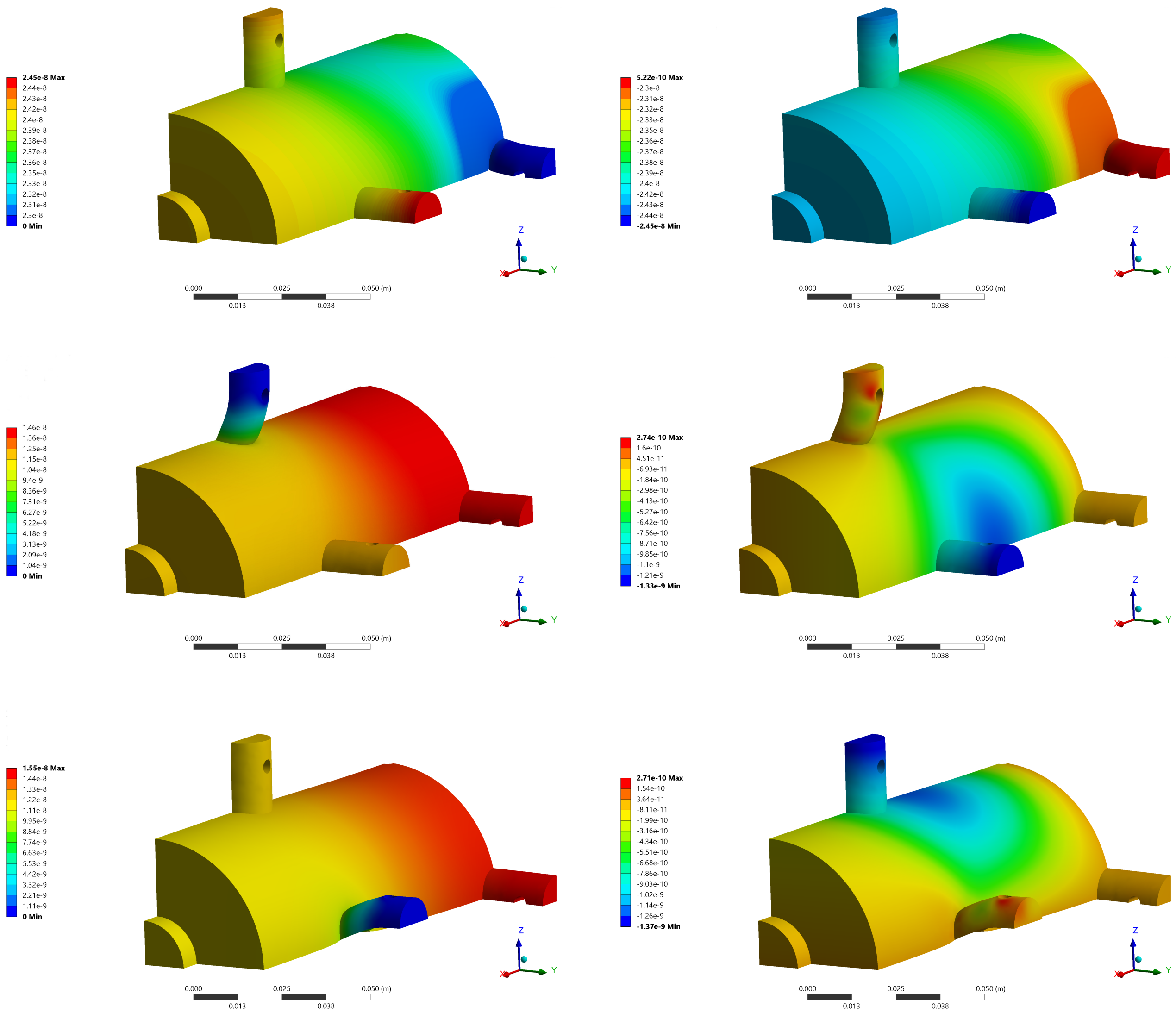

Figure 2.3: Results of the FEM simulation. Total deformation, defined as the cumulative deformation along all spatial directions (**left column**) and the deformation along the optical axis of the resonator (**right column**) for the 1g acceleration applied along the x-axis (**top row**), y-axis (**middle row**), and z-axis (**bottom row**). Cylinders, which act as active supports have zero total displacement at their ends. They can be seen as blue colored in the left column. Due to the symmetry considerations, only one-eighth of the resonator was simulated.

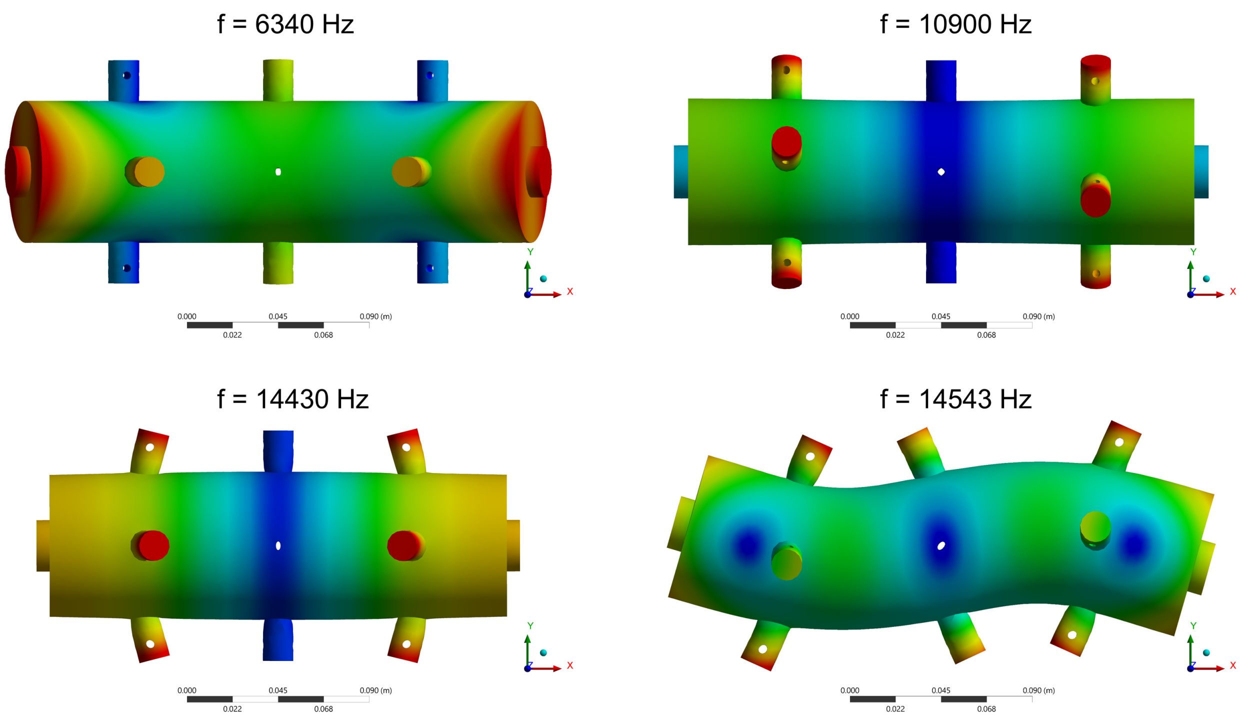

Figure 2.4: First eigenmodes of vibration of the silicon resonator obtained using FEM software. The color indicates the amount of total deformation.

2.4 Calculation of thermal noise

Random Brownian movement of the atoms in the crystal lattice of the spacer and substrates as well as in the amorphous, high reflective coatings results in the random fluctuations of the distance between the mirror substrates. Thus, this motion directly influences the optical path length and sets limits to its stability. We calculate the thermal-noise-induced instability for the resonator at 1.5 K using the parameters summarized in Tab. 3 and compare this result with the thermal noise instability at room temperature and at two CTE zero-crossing temperatures, 124 K and 16.8 K. Results are presented in Tab. 2. We expect a fourteen-fold reduction of thermal noise contribution to the fractional frequency instability for the temperature change from 300 K to 1.5 K. The calculated total Brownian noise contribution to the frequency instability at 1.5 K is 6×10^{-18}. Due to the amorphous nature of the coating, it constitutes 95% of the total contribution to Brownian noise.

Table 2: Results of the calculation of residual fractional frequency instability contributions from thermal noise of the spacer, substrates, and the coating for the wavelength of $\lambda = 1562$ nm and different temperatures of interest expressed with Allan deviation σ_y for dielectric and crystalline coatings.

	σ_y (10^{-17})				
Coating	**Dielectric (SiO_2/Ta_2O_5)**				**Crystalline ($Al_xGa_{1-x}As$)**
Temperature	**300 K**	**124 K**	**16.8 K**	**1.5 K**	**1.5 K**
Spacer	0.06	0.04	0.01	3.9×10^{-3}	3.9×10^{-3}
Substrates	0.31	0.2	0.07	0.02	0.02
Coating	11.13	7.15	2.63	0.79	0.1
Sum	**11.49**	**7.39**	**2.72**	**0.81**	**0.1**

Figure 2.5: **Top and middle panels:** spacer and the small cylinders before and after completion of the gluing process. **Bottom panel:** the resonator mounted inside the frame without front plates.

Table 3: Parameters used for the calculation of thermal noise.

Parameter	Description	Value
λ	laser light wavelength	1562 nm
k_B	Boltzmann's constant	1.381×10^{-23} J/K
f	noise frequency	1 Hz
L	length of the spacer	250 mm
R_{sp}	radius of the spacer	35 mm
r_b	radius of the central bore	7.5 mm
$w_{R=1m}$	beam waist at curved mirror	536 µm
$w_{R=\infty}$	beam waist at flat mirror	464 µm
E	Young's modulus of Si along [100] crystallographic direction[84]	130.1 GPa
ν	Poisson's ratio of Si along [100] crystallographic direction[84]	0.278
$Q_{si} = 1/\phi_{Si}$	Si quality factor[85]	$> 10^8$
ϕ_{ct}	coating loss factor[86]	1 mrad
d_{ct}	coating thickness	9.38 µm

3 Cryostat

3.1 General description

Silicon resonators are operated in a Leiden Cryogenics pulse tube type cryostat with a 1.4 Hz working frequency, pulse tube base temperature of 3 K, and cooling power of 1.38 W at 4.2 K. Pulse tube is complemented by a Joule-Thomson stage operated around 1.4 K with a cooling capacity of 40 mW at 1.5 K. All stages of the cryostat are rigidly connected to each other and to the cryostat's top plate by the G-11 glass fiber rods with very low thermal conductivity. The cryostat has a cylindrically shaped experimental chamber with a length of 690 mm and a diameter of 350 mm attached to the 1.4 K stage by copper rods. It can accommodate an experimental setup with a total mass of 100 kg (see Fig. 3.1).

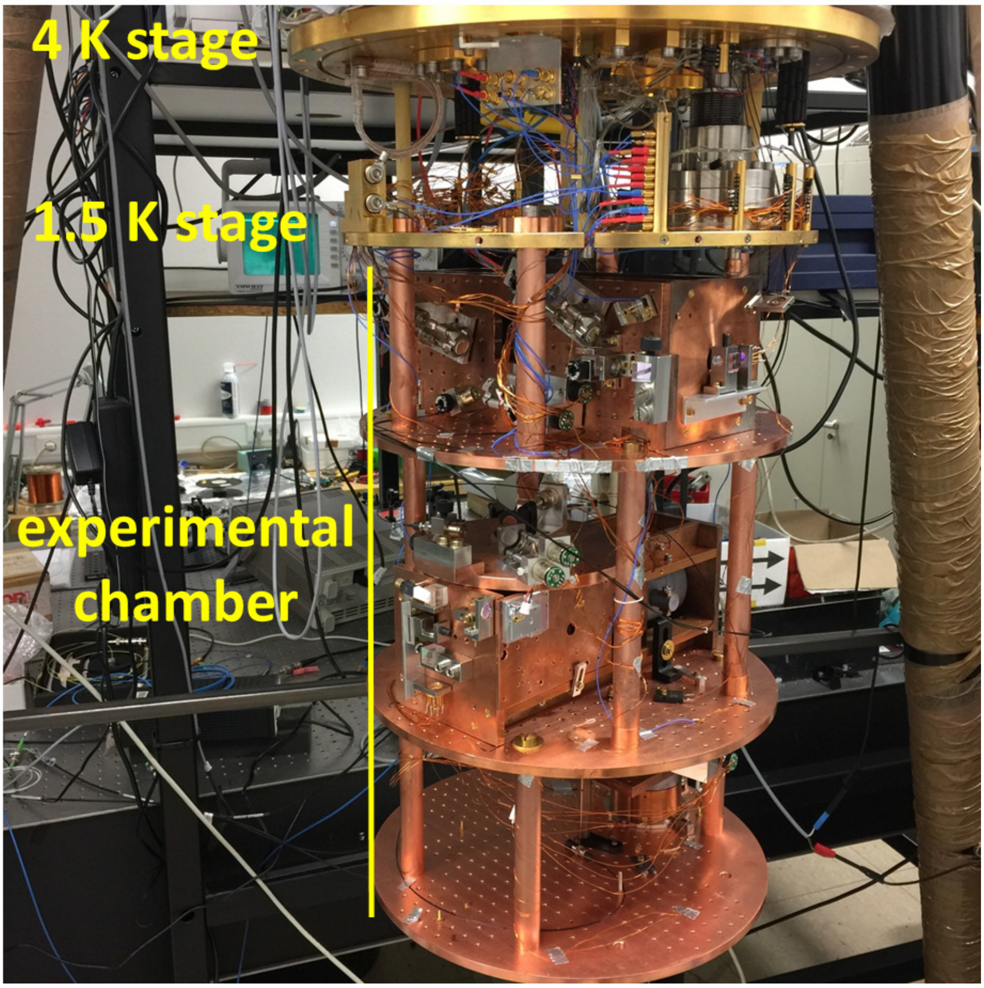

Figure 3.1: Experimental space with installed silicon resonators inside open Leiden Cryogenics cryostat.

The experimental chamber is isolated from the environment by the outer vacuum chamber (OVC) and the three radiative shields connected to the 50 K, 3 K, and 1.4 K cooling stages (see Fig. 3.2). To further improve the isolation and for the reason discussed below, the 3 K shield represents an inner vacuum chamber (IVC) and is held under a separate vacuum. The cryostat is supported by a tripod at a reasonable height allowing for easy access and opening of the experimental chamber. Each leg has a soft rubber base to dampen the transfer of seismic vibrations to the cryostat. The pulse tube is connected via rotary valve and two 20 m long flexible lines to a He gas water-cooler compressor located in a neighboring room, with a nominal power consumption of 9.2 kW in a steady state. It permanently holds two volumes of He at constant low and high pressures of 7.5 bar and 21 bar, respectively. These

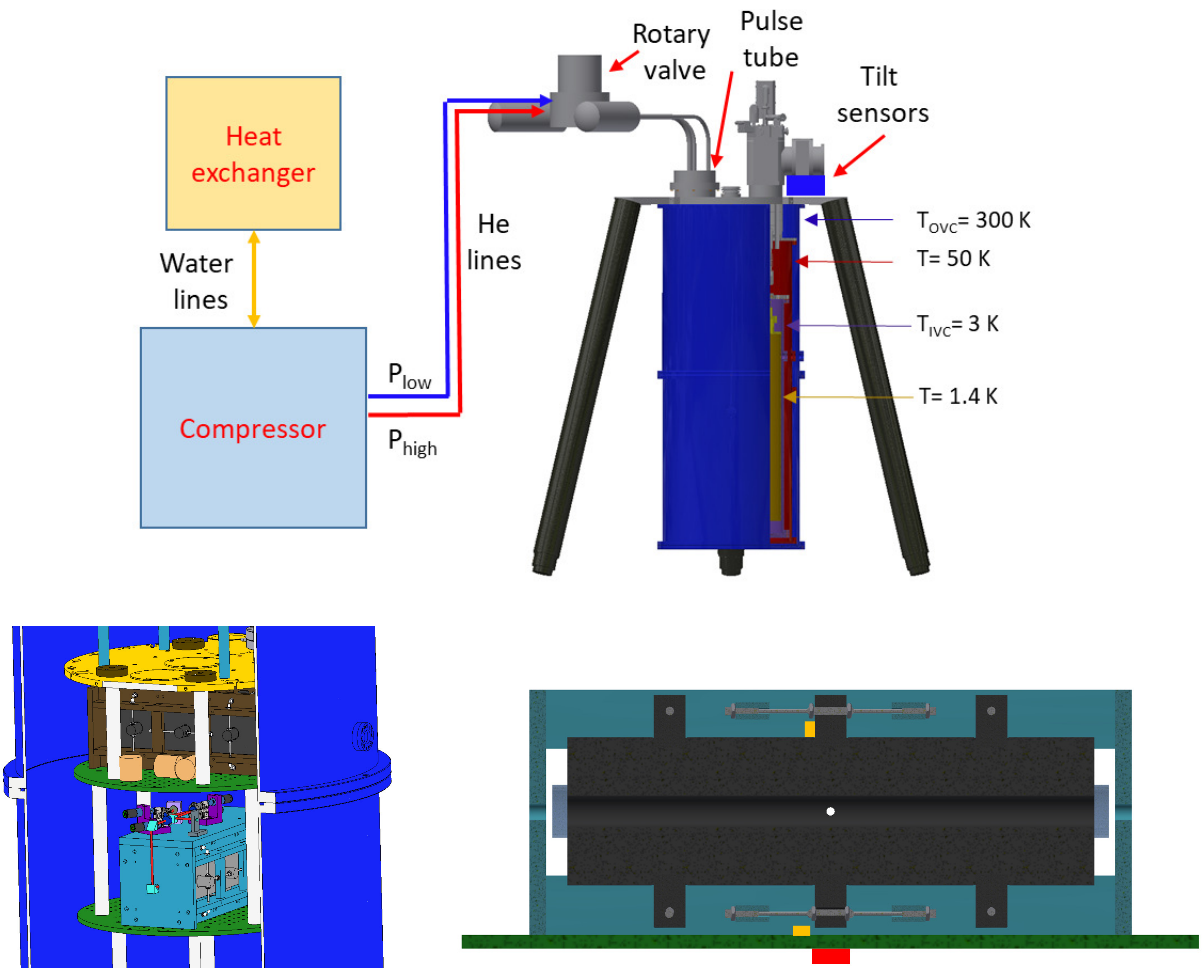

Figure 3.2: **Upper panel:** schematic of the cryostat setup together with compressor and heat exchanger (thermal shields are not shown for clarity); **Bottom left panel:** zoom into the experimental chamber of the cryostat with the two silicon resonators Si1 and Si2, installed at the middle and upper experimental plates, respectively, cryogenic geophones and one cryogenic optical setup for the incoupling of laser light into the resonator; **Bottom right panel:** cross-sectional view at the resonator and the position of temperature sensors (yellow) and a heater (red) at the second optical plate. One of the sensors is temporarily glued to the top middle of the resonator with the Apiezon N grease. The second sensor is bolted to the top of the optical plate and at the side of the resonator. A heater is attached to the bottom of the experimental plate right below the resonator. The sensor and the heater at the experimental plate are used for the active temperature stabilization.

volumes are successively connected with the pulse tube by a rotary valve rigidly attached to the top of the cryostat with a damping material in between and operated at a frequency of 1.4 Hz allowing for the pulse tube to function.

The cryostat setup is complemented by temperature sensors and heaters attached to all cooling stages and at various positions of the experimental setup. The cooldown of the cryostat to the base temperature of 3 K lasts 45 hours (see Fig. 3.3,a). To bridge the thermal isolation between the 3 K stage of the cryostat and the experiment during the cooldown process the IVC is filled with He gas. After the 3 K stage reaches its base temperature the He gas is adsorbed by the charcoal adsorbers attached to the 3 K stage. At this point (marked as P_1 in Fig. 3.3,a) the1.4 K stage and the experimental setup has a temperature of about 20 K, which is decreasing slowly due to the poor thermal connection between the1.3 K and the 3 K stages. The Joule-Thomson cooling is started at a point marked P_2 in Fig. 3.3,a, and the lowest operating temperature of the cryostat is reached 30 hours thereafter (point P_3 in Fig. 3.3,a). It remained stable during the entire operating time of the cryostat except for a two-month span where the pump of the Joule-Thomson stage was in repair (peak between days 400 and 500 in Fig. 3.3,b).

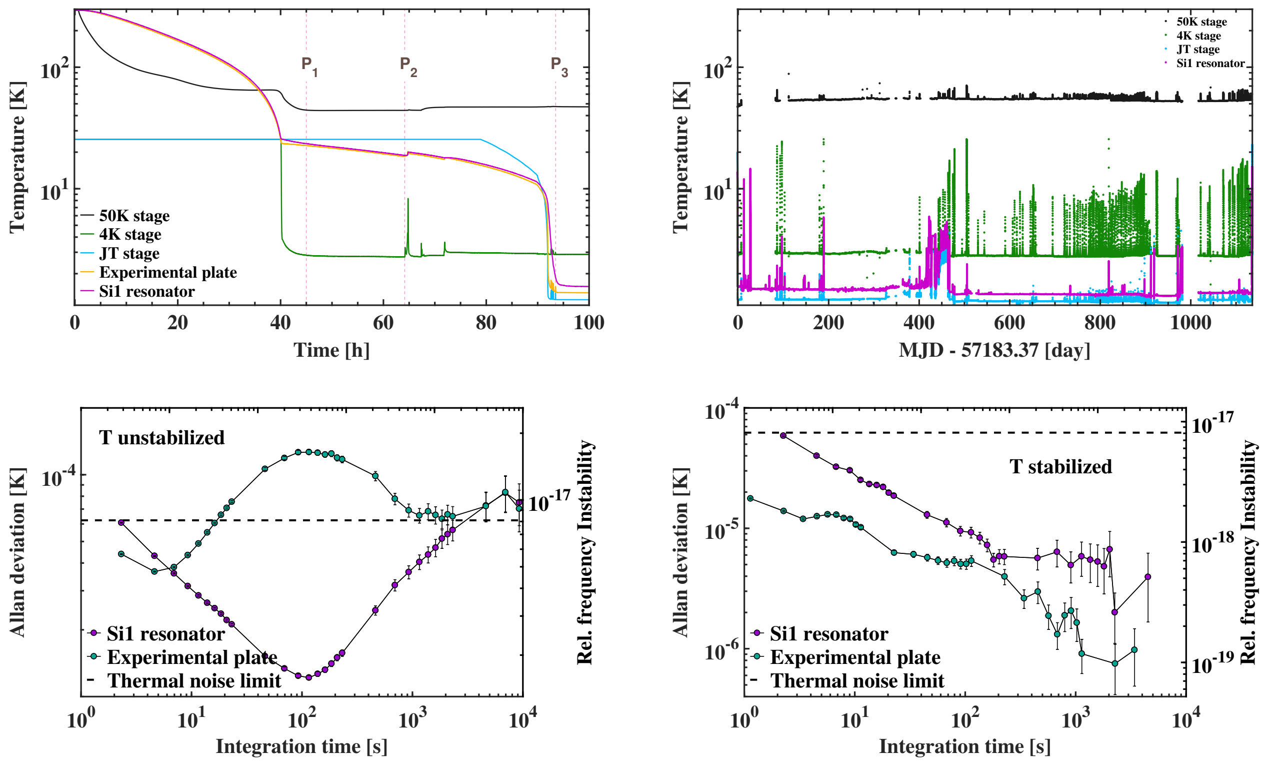

Figure 3.3: **Upper left panel:** temperature of pulse tube stages and the experimental setup during the cooldown. At point P_1 the 50 K and the 3 K stage reaches its base temperature. The operation of the 1.4 K Joule-Thomson stage is started at point P_2. The cooldown is completed at point P_3. **Upper right panel:** long term temperature stability of the cryostat. Sharp peaks are the result of the experimental activity. Temperature rise between days 400 and 500 is due to the malfunction of the Joule-Thomson stage pump. **Bottom left panel:** temperature stability of the optical plate and the resonator with no active stabilization of temperature. **Bottom right panel:** temperature stability of the optical plate and the resonator with active stabilization of temperature. Right hand side of the diagrams in the bottom row displays the frequency stability calculated from the temperature stability data and the value of CTE (see Sec. 8.4) of silicon at these temperatures.

The temperature of the resonator is monitored with a sensor attached to the top middle of the resonator by the means of aluminum wires and additionally glued with the Apiezon N grease, which becomes solid at low temperatures. It also improves thermal contact between the sensor and the resonator by increasing their contact area. A second temperature sensor is bolted to the top of the experimental plate right next to the resonator. Together with the heater attached to the bottom of the experimental plate and centrally and below the resonator it is used for the active temperature stabilization of the setup (see Fig. 3.2). Temperature stability of the resonator and optical plate with and without active temperature stabilization are displayed in Fig. 3.3,c, and d. In case of no active temperature stabilization, there is a discrepancy between the temperature stability of the resonator and the experimental plate. This can be explained by the low thermal conductivity of the steel wires which hold the resonator in the frame. With a relaxation time τ of 20 min, they act as a low-pass filter for the heat transfer between the resonator and plate. This makes the resonator insensitive to the short-term temperature fluctuations of the cryostat.

While the Joule-Thomson stage and thus the experimental setup are thermally isolated from the pulse tube, the 3 K stage is rigidly connected to it. Due to the principle of operation of the pulse tube, the cooling process of the 3 K stage does not occur continuously. This degrades the short-term stability of the 3 K stage, as can be seen in Fig. 3.4 where each pulse of He gas, detected with a cryogenic geophone placed at one of the experimental plates is accompanied by cooling of the 3 K stage by 8 mK. The amplitude of the temperature fluctuations depends on the thermal load of the system.

The AC bridge electronics which is used for the monitoring of temperature has a sensitivity of

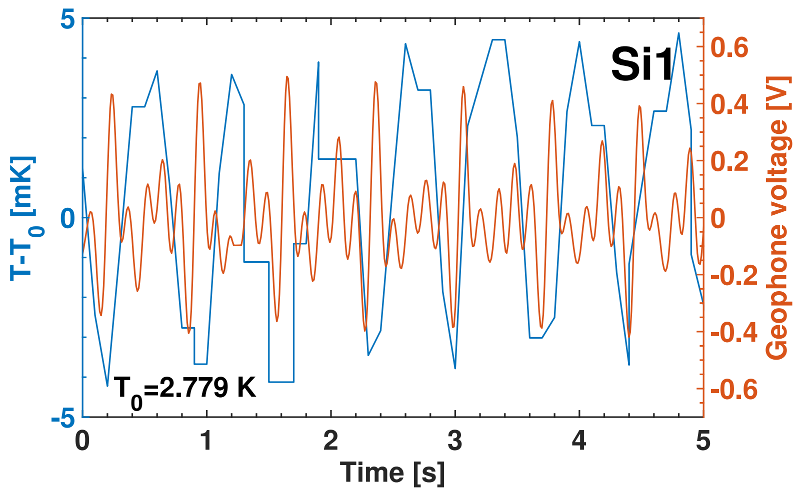

Figure 3.4: Time trace of the geophone signal attached to the upper experimental plate of the cryostat cooled down to the temperature below 3 K (right y-axis), together with the temperature variations at 4 K stage (left y-axis).

1.7×10^{-5} K per degree of lab temperature variation. To reduce these errors, the temperature in the lab was actively stabilized with a commercial air conditioner and associated temperature sensor located near the top of the cryostat. The temperature inside the lab was measured with four sensors at different sensitive locations: near the cryostat, next to the electronics, and near the room-temperature optical setups. An example of temperature time trace measured with a sensor near the room-temperature setup over the course of the entire experiment is displayed in Fig. 3.5, left. The total variation in temperature is approximately 4 K. However, calculated temperature instability over one day is less than 0.3 K (see Fig. 3.5, right). This results in a 6 μK error in cryogenic temperature sensor readings.

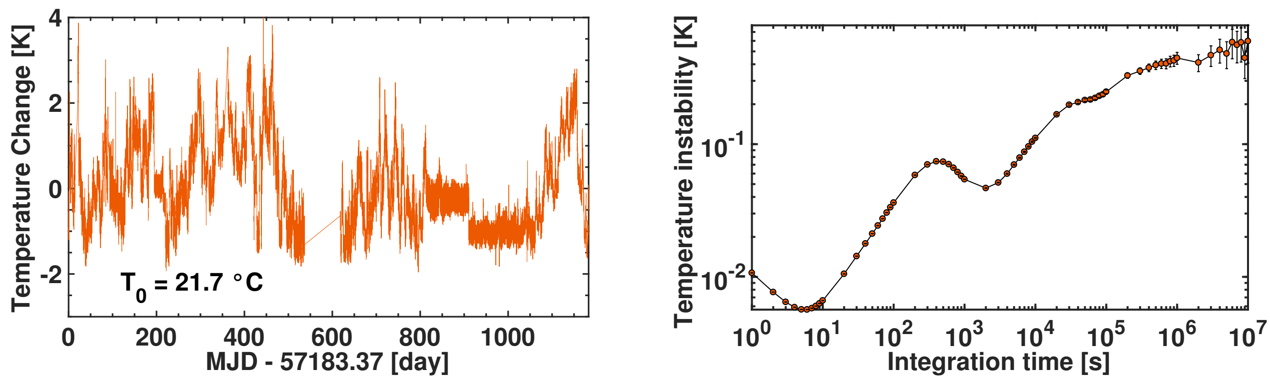

Figure 3.5: Temperature stability in the lab over the whole time span of the experiment. **Left panel:** time trace. **Right panel:** calculated temperature instability. Peak at 400 s is due to the periodicity in the activation and deactivation of the air conditioning during active temperature stabilization.

3.2 Characterization of vibrations

The cryostat is placed on the second floor of the building and has no vibration isolation from the environment. Thus, the experimental setup is sensitive to vibrations of natural and human-made seismic and acoustic activity. Both contributions are detected clearly with cryogenic geophones operated on the 1.5 K stage (see Fig. 3.6).

We measured lab floor vibrations below the operational cryostat along the three orthogonal directions coincident with the orientation of the three silicon resonators inside the cryostat with a high-sensitivity

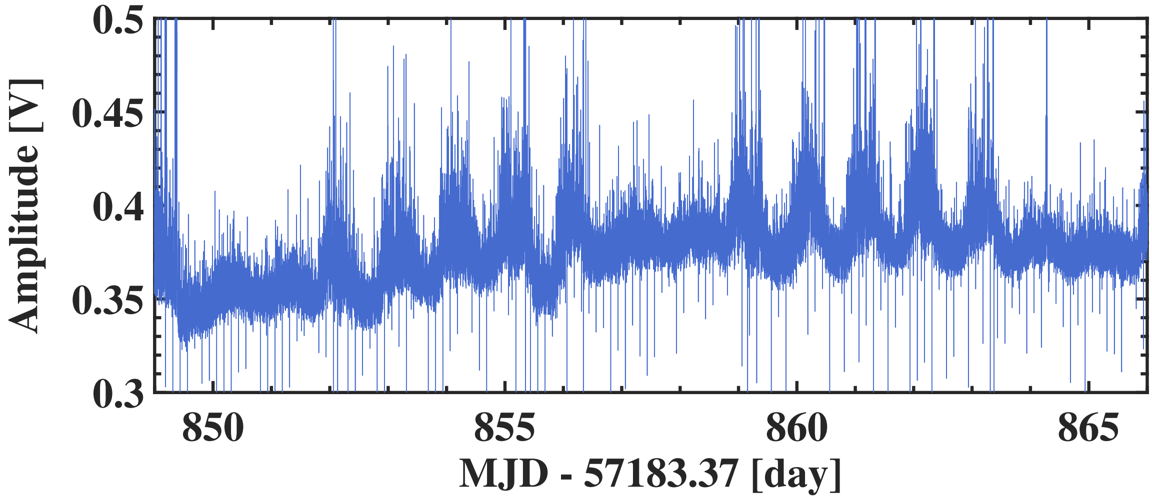

Figure 3.6: Amplitude of a cryogenic horizontal geophone fixed at the 1.5 K stage next to the one of the silicon resonators recorded over a two weeks period. Five working days with high human activity are followed by two quiet weekend days. The slowly changing background level is probably determined by drift of the electronics offset.

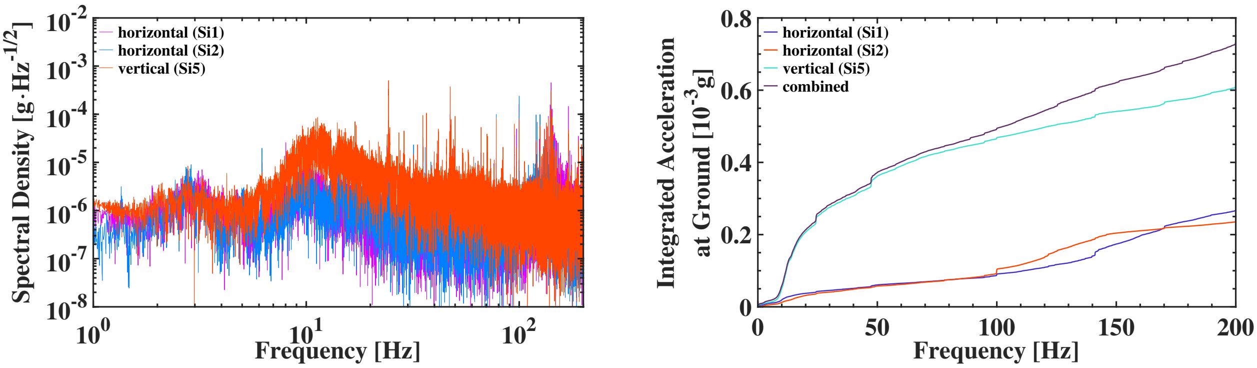

Figure 3.7: **Left panel:** spectral density of ground acceleration measured along the three spacial directions. **Right panel:** total accelerations in the frequency range from 1 Hz to 200 Hz. The combined total acceleration is the root sum-of-squares of the three individual total accelerations.

piezoelectric transducer. The results are presented in Fig. 3.7. The cumulative acceleration in the frequency band from 1 Hz to 200 Hz is 0.7 mg.

Due to the mechanical design and principle of operation, the cryostat adds to this noise by subjecting the experimental setup to characteristic low- and high-frequency vibrations. We measured these vibrations at room temperature and at the temperature of 1.5 K using two different techniques. The results are presented below.

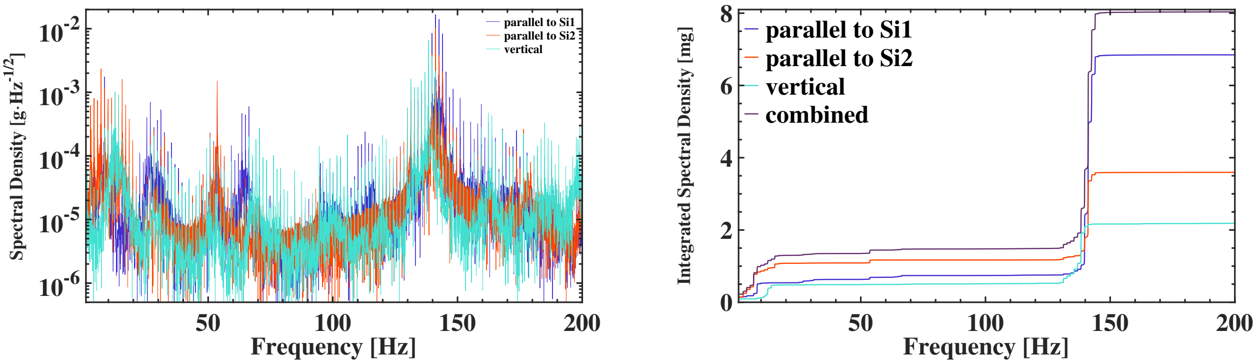

Figure 3.8: **Left panel:** spectral density of vibrations. **Right panel:** integrated spectral density of vibrations of an open and working cryostat measured with a high sensitivity accelerometer (1 kV/g) placed at the experimental plate subsequently along three orthogonal directions. Combined integrated spectral density was calculated by taking the root sum-of-squares of all three contributions.

Measurement with a high sensitivity piezoelectric transducer at 300 K

The vibration spectrum of open and working cryostat was taken with a high sensitivity accelerometer (Wilcoxon 731A/P31) attached to the middle experimental plate, next to the Si1 resonator. The sensor was subsequently oriented along the three orthogonal directions determined by the orientation of the Si1 resonator. The result is presented in Fig. 3.8. The largest contribution to the spectrum of vibrations is made by the stepping motor of the rotary valve. It rotates the rotary valve by making 140 separate steps during one second and adds three fourth or 6 mg to the total amount of acceleration (see Fig. 3.8, left panel). Another noise source is the pressure waves of the He gas inside the pulse-tube. They deform the steel walls of the pulse-tube and bend it as a whole. The latter displaces and accelerates the experimental setup rigidly attached to it. The operational frequency of the pulse-tube (1.4 Hz) and its high-order harmonics can be seen as sharp peaks throughout the spectrum. Integration of all vibration noise contributions in the frequency range from 0 Hz to 200 Hz results in a total acceleration of 8 mg with the vertical direction making the least contribution (see Fig. 3.8, right panel).

Measurement with an optical sensor at 1.5 K

Vibrations inside the cryostat were also measured using reflections from three silicon resonators installed along the three orthogonal space directions of space together with a commercial optical displacement sensor based on laser interferometry (Attocube IDS3010) with a resolution of 1 pm and a bandwidth of 250 kHz. The sensor heads were installed on platforms in front of the cryostat or on the floor below it. All three platforms were not isolated from seismic vibrations. The laser light with a wavelength of 1530 nm was sent through the optical windows of the cryostat to the resonators.

After reflection at the front mirrors of the resonators, the laser beam exited the cryostat and was coupled back into the sensor heads. The resulted displacement time traces are presented in Fig. 3.9, left column. The dominant displacement with a peak to peak amplitude of 20 µm for two horizontal directions and 1 µm for the vertical direction occurs at the frequency of 2.8 Hz, the second harmonic of the cryostat. The displacement amplitude along both horizontal directions is larger for every second peak. This corresponds to the 1.4 Hz frequency of the pulse tube. The distributions of the time trace data are displayed in Fig. 3.9, right column. While the distribution for the displacement along the vertical direction is Gaussian in form, both distributions of the displacement along the two horizontal directions are more complicated in form. At the same time, all three distributions are slightly asymmetrical.

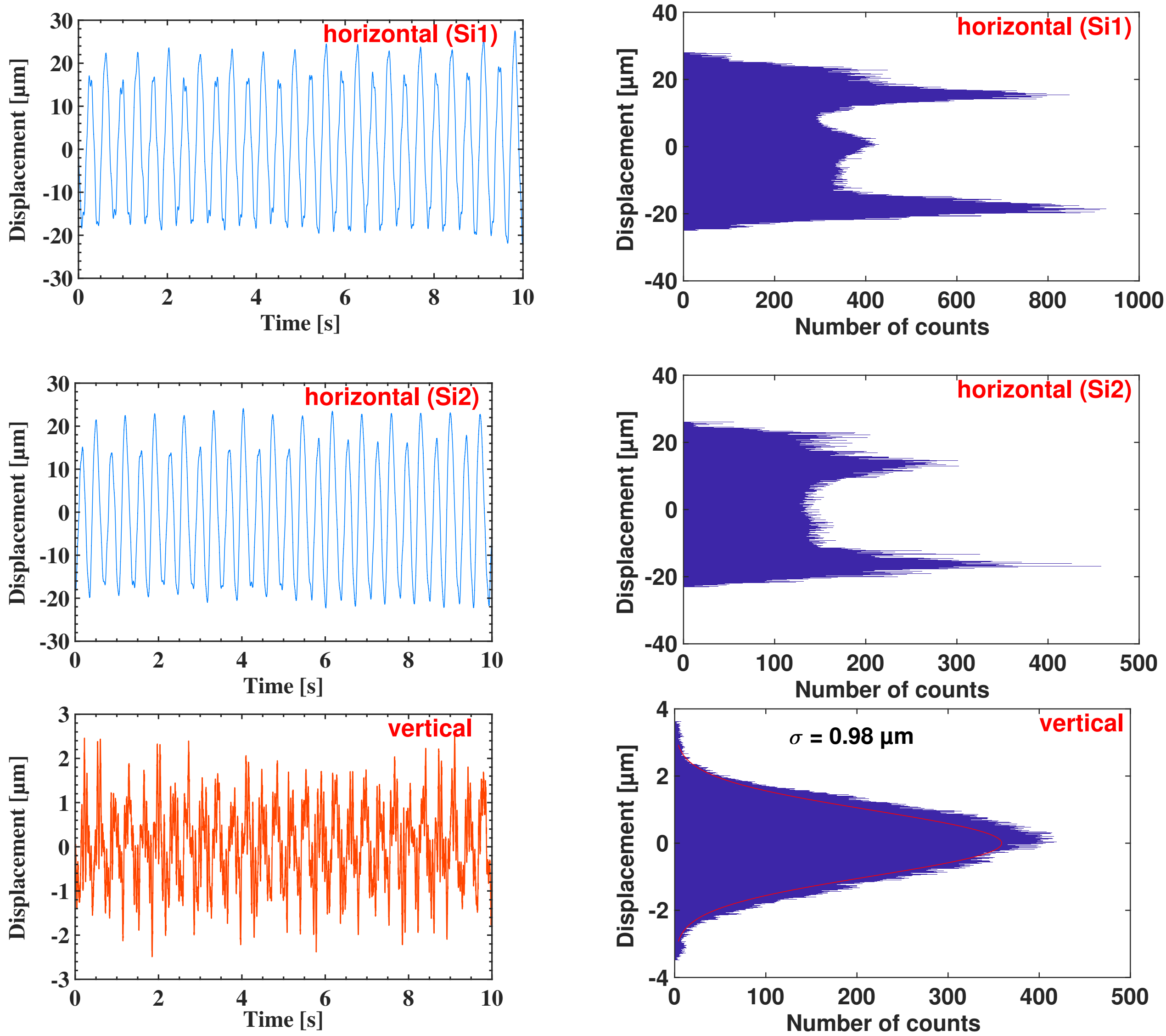

Figure 3.9: Results of the measurement with the optical position sensor: displacement along the three three spatial directions (**left column**) and their distributions (**right column**).

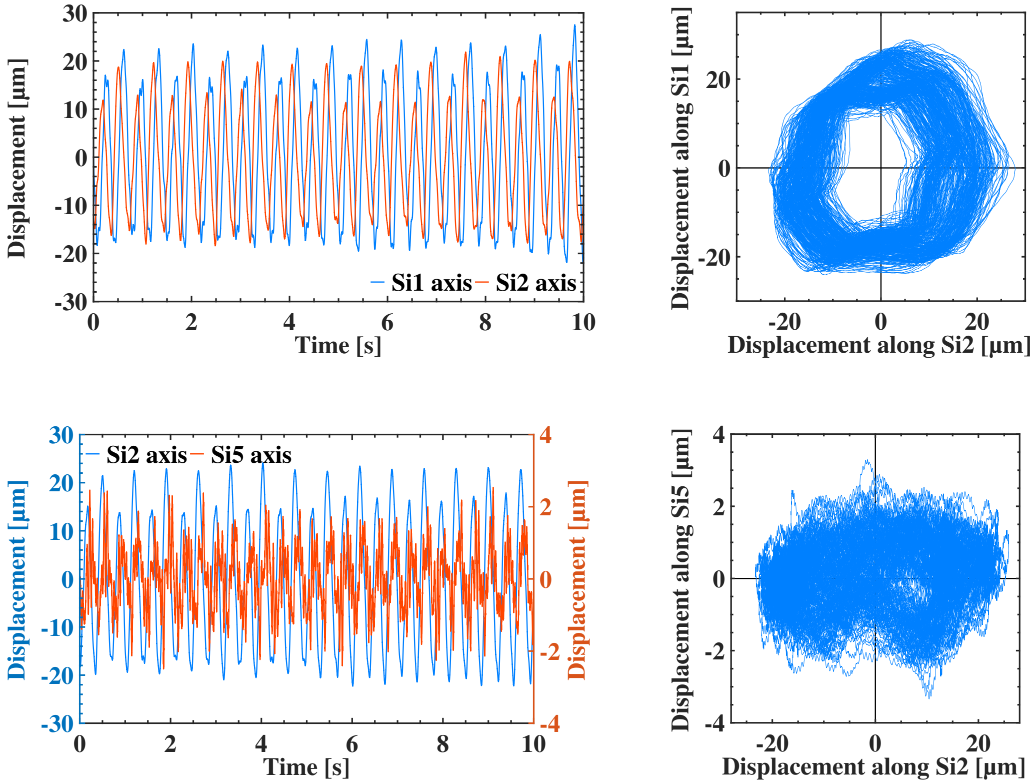

Figure 3.10: Results of the displacement measurement with an optical position sensor in the horizontal and vertical spatial planes: time trace (**left column**) and displacement projection on the corresponding plane (**right column**).

We have also measured the displacement in the two perpendicular spatial planes by a simultaneous reading of two outputs of the interferometer. The results are presented in Fig. 3.10. The vibrations of the pulse tube do not occur simultaneously along three spatial directions. There is a time delay of approx. 0.12 s and 0.1 s between the two axes in the horizontal plane and between the two axes in the vertical plane, respectively (see Fig. 3.10, left column). The motion of the experimental setup in the horizontal plane is almost circular with a radius of approx. 20 µm and a time period of 0.36 s. The corresponding centripetal acceleration is 6×10^{-4} g. Motion in the vertical plane is noisy due to the low amplitude of the displacement along the vertical direction.

Time traces presented in Fig. 3.9, left column, are used for the calculation of the displacement, velocity, and acceleration spectrum using FFT (see Fig. 3.11). The displacement at 1.4 Hz, the base frequency of the rotary valve, is at the level of 3 µm along the two horizontal directions. The highest contribution to displacement, as already seen in Fig. 3.9, comes from the frequency of 2.8 Hz, the first harmonic of the cryostat.

Velocity and acceleration spectra were obtained by single and double integration of the displacement time traces, respectively. We observe peak velocity at the frequency of 2.8 Hz with a value of 0.3 mm/s. As in the case of the measurement at the room temperature, the acceleration is highest at the frequency of 140 Hz. The acceleration along the horizontal directions at the frequency of 2.8 Hz is 6×10^{-4} g and is identical to the value of the centripetal acceleration calculated above.

To compare these results with the measurement done with an accelerometer, we calculated the spectral density (see Fig. 3.12, left panel). It is almost identical to the one measured with the accelerometer (see Fig. 3.8). Cumulative acceleration along all three directions, obtained from the integration of spectral density spectrum is presented in Fig. 3.12, right panel. The calculated combined acceleration is almost 5 mg. This is roughly the half of the cumulative acceleration obtained with the accelerometer. This difference can be explained by the fact, that the accelerometer measurement was done cryostat at

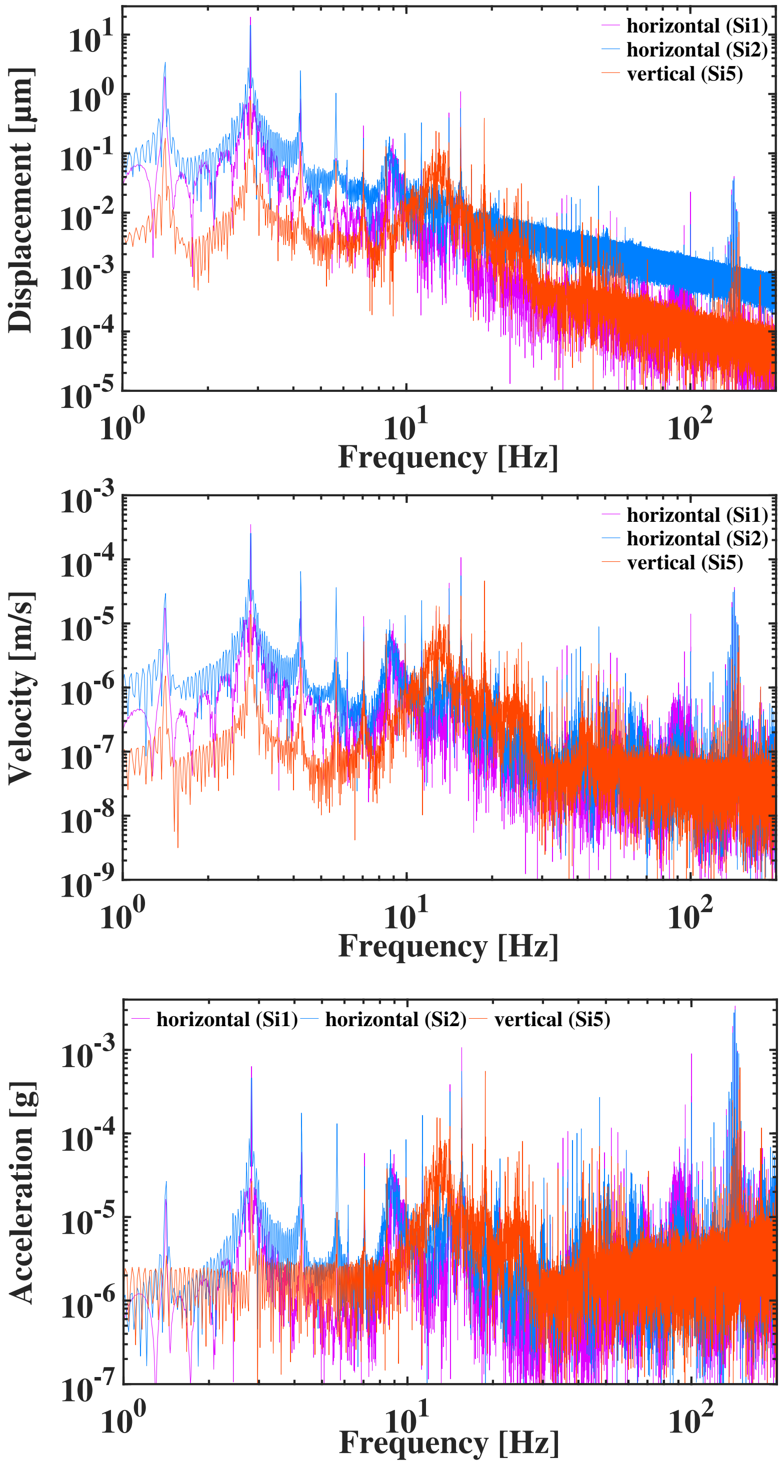

Figure 3.11: **Top, middle, bottom panels:** spectrum of the displacement, velocity and acceleration for all three directions produced from the interferometer time traces presented in Fig. 3.9, left column.

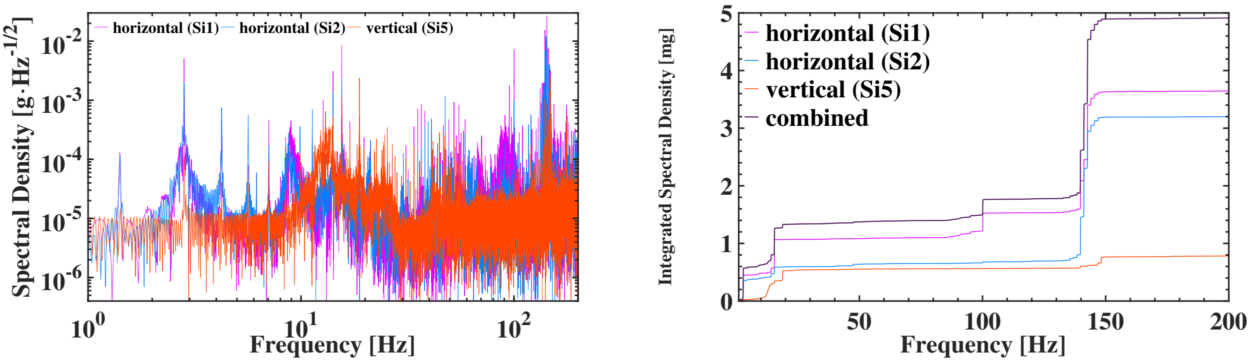

Figure 3.12: **Left panel:** spectral density of vibrations inside the cryostat determined from the time traces of the interferometer for all three spatial directions. **Right panel:** integrated spectral density of vibrations. Combined integrated spectral density was calculated by taking the root sum-of-squares of all three contributions.

room temperature with removed thermal shields. Four shields of the closed cryostat bring an additional weight and damp the vibrations at the experimental plate. At the same time, cryogenic temperatures provide materials with additional stiffness and make the cryogenic setup more robust against vibrations.

3.3 Stabilization of tilt

Due to the changing environmental conditions such as wind or temperature and low-frequency seismic activity of the earth's crust, the tilt of the building is not stable and can vary in our lab by 40 µrad during 24 h period. Variable tilt introduces compression and buckling of the resonator and thus changes its frequency. To minimize this impact we installed an active tilt stabilization system. It consists of two temperature stabilized, orthogonally positioned tilt sensors placed at the top of the cryostat (see Fig. 3.2) with one of the sensors oriented along the optical axis of the silicon resonator. The resolution of the sensors is 0.1 µrad. The signals from the sensors are used by a PC-based PID controller to apply a voltage to the heating wires wrapped around the two legs of the tripod. Changing the length of the legs by heating the tilt change of up to 150 µrad can be compensated. As there is a cross-talk between the legs because of the angular separation of 120 degrees between them, we installed two separate control loops. To allow for an active tilt compensation in both directions the legs are preheated before the beginning of active tilt stabilization. The resulted tilt stability for both axes is displayed in Fig. 3.13. For integration times up to 1000 s, the stability is limited by the temperature stability of the tilt sensors. At 1000 s the resolution limit of the sensors is reached. At longer times stability degenerates due to the noise of the electronics. Right-hand side of the diagram displays the fractional frequency stability of the resonator calculated from the tilt stability data using the experimentally determined conversion factor of 48 mHz/µrad and the frequency of the laser light (see Sec. 8.3).

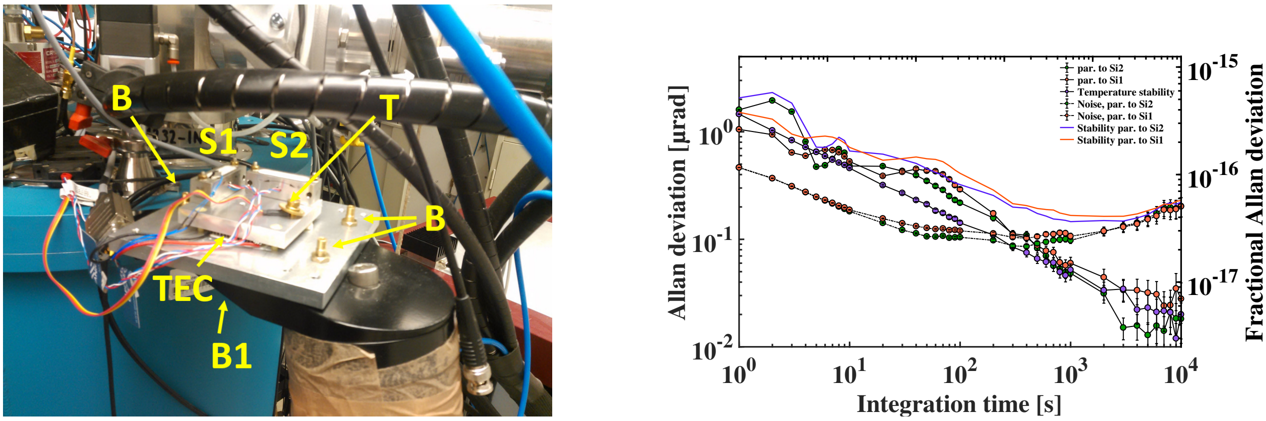

Figure 3.13: **Left panel:** arrangement of the tilt sensors **S1** and **S2** on top of the cryostat. They are positioned orthogonal to each other with sensor **S1** measuring tilt along the optical axis of the resonator. Both sensors are bolted to the plate, which is temperature stabilized using a thermoelectric cooler **TEC** and a temperature sensor **T**. Temperature stability of the sensors can be monitored separately with their own temperature sensors inside them. Due to the narrow effective range of the sensors the tilt of the plate is initially tuned with adjustable bolts **B**. After that the plate is fixed with bolt **B1** to the leg of the cryostat from below and enclosed with a thermally isolating material for improved temperature stability (not shown here). **Right panel:** tilt stability of the cryostat using an active tilt stabilization setup described in the text. Solid lines with green and orange markers are calculated from the time traces of the two sensor readings. Solid line with violet markers was calculated from the temperature data of the sensors using a conversion factor supplied by the manufacturer. Electronics noise was determined from the time tracers and the sensors detached from the electronics. It is represented by dotted lines with green and orange markers. Blue and orange solid lines is the resulted tilt stability for both axes. Right hand side displays fractional frequency stability of the resonator using an experimentally defined conversion factor of 48 mHz/µrad.

4 Cryogenic installations of the resonator

The resonator was successfully operated inside the Leiden Cryogenics cryostat described in Sec. 3. However, over the course of seven years, the resonator was installed in total inside three different pulse-tube cryostats and operated in two. The first cooldown of the resonator was achieved inside a 4 K pulse-tube cryostat from TransMIT Center for Adaptive Cryotechnology. Due to the limitation of the available space the resonator was installed vertically (see Fig. 4.1, left panel). The laser light was coupled from the room-temperature breadboard located below the cryostat through the optical window at the bottom of the cryostat. The transmitted light was detected with a photodiode. However, at that point, we lacked an appropriate InGaAs camera and thus no mode identification was done. This made it impossible to identify the TEM_{00} mode of the resonator during the operation of the cryostat. Despite this, the first cooldown was still considered successful, because of the intact optical contact between the mirrors and the spacer and because no damage was done to the resonator due to the differences in thermal contraction between the silicon spacer and the copper frame. Because of its advanced age, the TransMIT cryostat proved to be maintenance-intensive and was abandoned immediately after taking into the operation the Leiden Cryogenics cryostat.

Another vertically-oriented installation of the resonator was done inside a second 1.5 K pulse-tube cryostat (see Fig. 4.1, right panel). However, this setup was not cryogenically operated due to the problems with the cryostat and had to be disassembled as the cryostat was later reserved for other types of experiments.

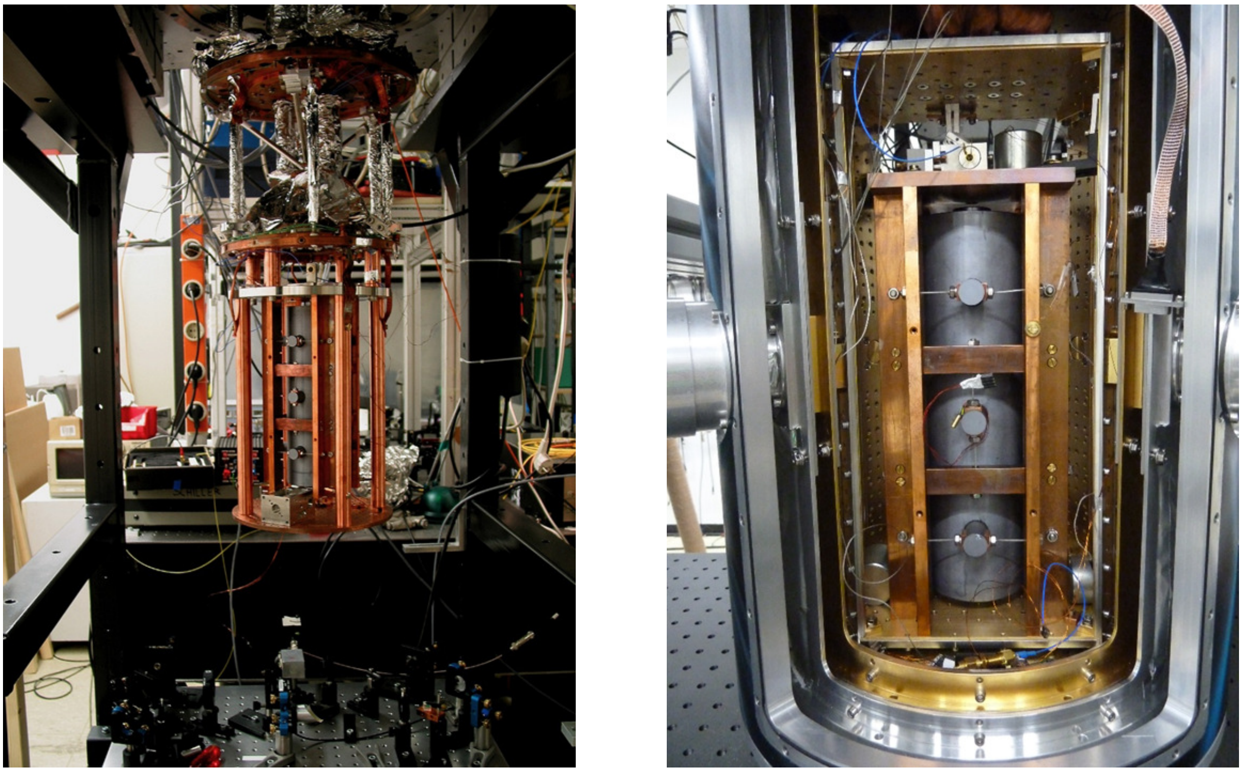

Figure 4.1: **Left panel:** first cryogenic operation of the vertically-oriented resonator inside a 4 K pulse-tube cryostat with the room-temperature optical setup seen below the cryostat. **Right panel:** another installation of the vertically-oriented resonator inside a 1.5 K pulse-tube cryostat that did not went to the cryogenic operation due to the insufficient cryostat performance.

The first operation inside the Leiden Cryogenics cryostat was done with the horizontally oriented resonator and with the light-weight room-temperature optical setup, assembled at an aluminum plate, rigidly attached to the optical window of the cryostat (see Fig. 4.2). A 2 m long optical fiber was used for the transmission of the laser light to the setup. An AOM was installed along the light path to prevent unwanted interferences of the laser light with the back-reflection from the front mirror of the resonator and other optical components along the laser beam path. This optical assembly allowed for the application of the Pound-Drever-Hall locking technique. To identify the correct mode of the resonator a suitable camera was used. As the cryostat lacked a second window at the back of the resonator, the transmitted light was guided to the free window at the bottom of the cryostat using a set of mirrors and lenses (see Fig. 4.2, left panel). This cumbersome detour was removed at the later stage of the experimentation after the second optical window was built directly behind the resonator and along the path of the transmitted light.

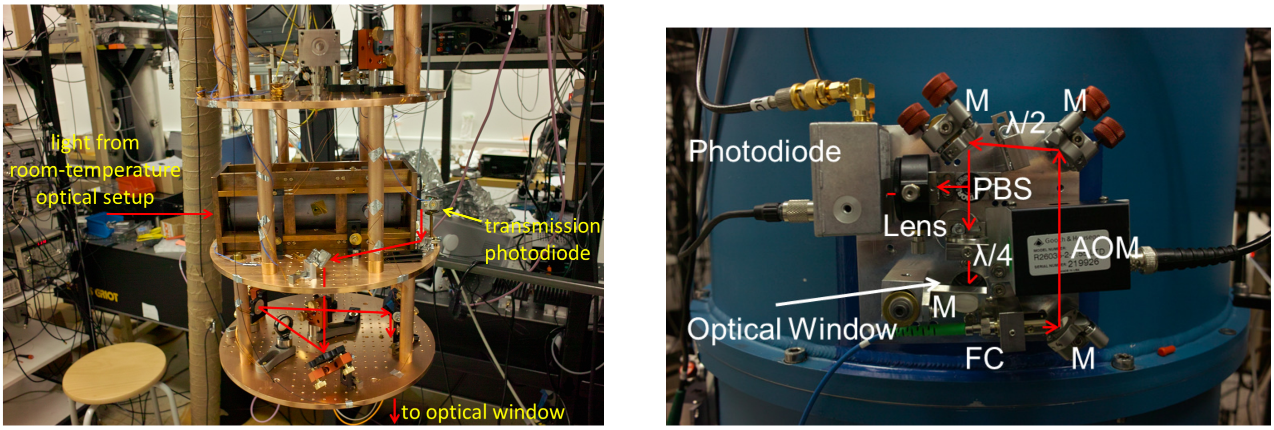

Figure 4.2: **Left panel:** first operation of the horizontally-oriented resonator inside a 1.5 K Leiden cryostat. Red colored is the path of the transmitted light to the bottom window of the cryostat. **Right panel:** corresponding room-temperature optical setup with following abbreviations: **FC**, fiber collomator, **M**, mirror, **PBS**, polarizing beam splitter, and $\boldsymbol{\lambda/4}$, quarter wave-plate.

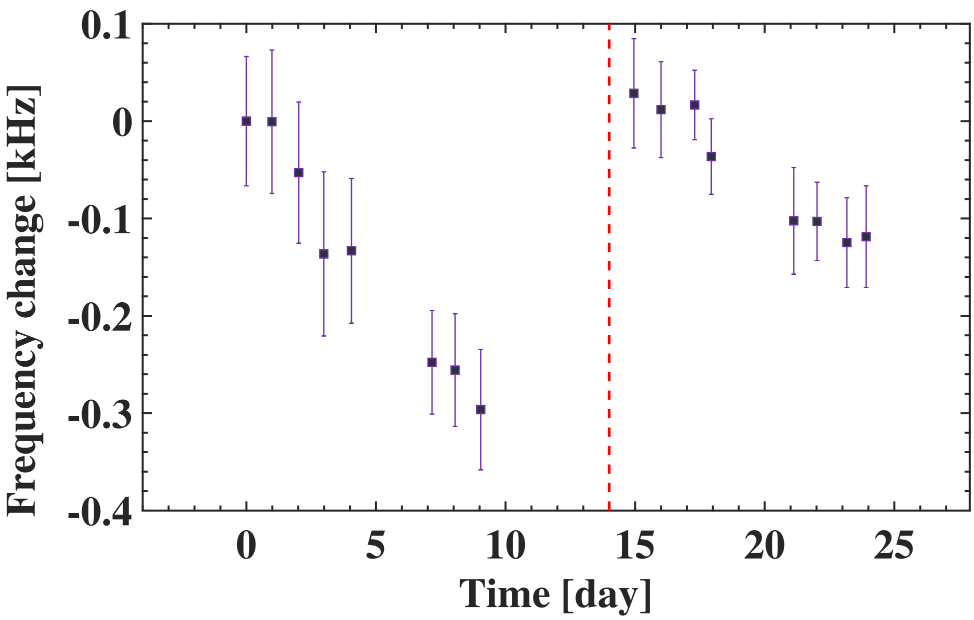

Figure 4.3: Example of the frequency measurement with a room-temperature optical setup displaying a sensitivity of the optical frequency of the resonator to the changes in light incoupling. The red dotted line marks time, where the incoupling was adjusted.

This configuration allowed for the first characterization of the resonator. However, it proved to be insufficient for the characterization of the long-term frequency drift. Variations in lab temperature affect the beam pointing stability of the laser light in the optical setup. They also have an effect on the interplay in the relative orientation of the outer vacuum shield of the cryostat and the cryogenic experimental setup by heating and cooling the vacuum shield. This results in the change of the incoupling. As already mentioned in Sec. 2 we do not observe a pure TEM_{00} mode but an overlap of the TEM_{00} mode with high order modes. Thus, every change in the incoupling changes the intensity of the TEM_{00} mode as well as of all the respective high-order modes. This in turn shifts the frequency of the resonance line. Fig. 4.3 shows the drift of the Si2 resonator measured using the room-temperature optical setup. After initial adjustment of the incoupling at day zero, we observe a continuous drift in frequency. On day 14 another adjustment of the incoupling was done. This procedure removed the accumulated frequency change over the past two weeks. Immediately after the adjustment, we see a repetition of the observed behavior.

To eliminate this issue we moved to the all cryogenic optical setup displayed in Fig. 4.4. Optical fiber feedthrough guides the laser light into the cryostat and to the free space cryogenic optical setup. While the cryostat is open, the cryogenic optical setup is adjusted to optimally couple the light into the resonator. After closing the cryostat and cooling it down to 3 K, the optimal uncoupling of light is usually lost due to the thermal contraction of used materials. We reduced this effect by making a very compact setup with a small path length from the fiber outcoupler to the front mirror of the resonator. Additionally, to be able to adjust the beam path at 3 K, we installed two motorized mirror mounts and mounted the photodiode in reflection on a cryogenic two-dimensional translation stage for possible position optimization. The cryogenic setup was complemented by a photodiode in transmittance, used for mode detection and active stabilization of the optical power circulating inside the resonator.

To increase the bandwidth of the photodiode in reflection we reduced the length of the coax cable from the photodiode to the transimpedance amplifier using a home-built cryogenic amplifier. We installed the latter at the 3 K stage to reduce the heat load at the cryogenic setup. Nevertheless, the temperature of our setup was increased by approximately 0.2 K during the operation of the amplifier.

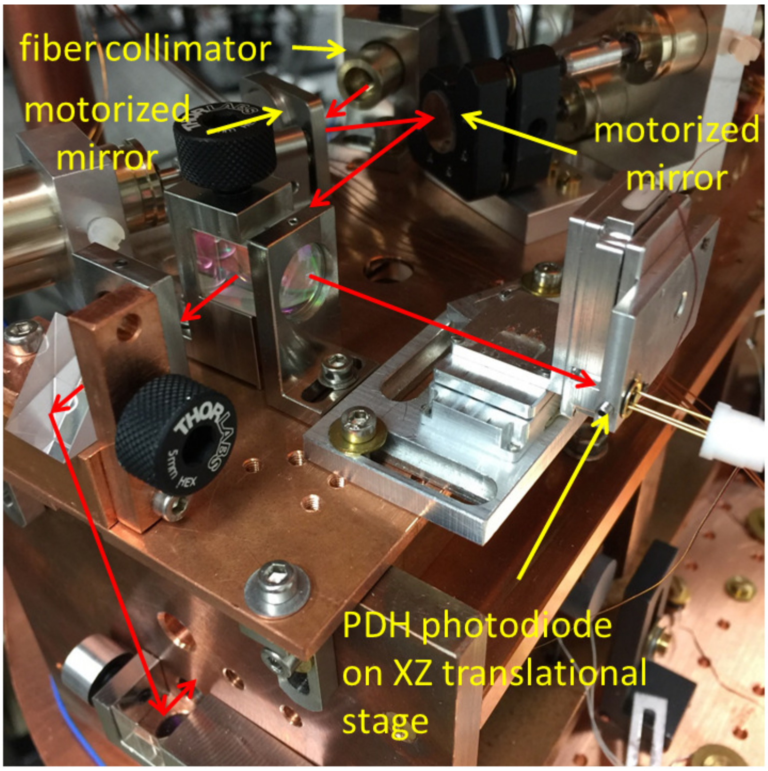

Figure 4.4: Example of a cryogenic optical setup implemented inside the cryostat.

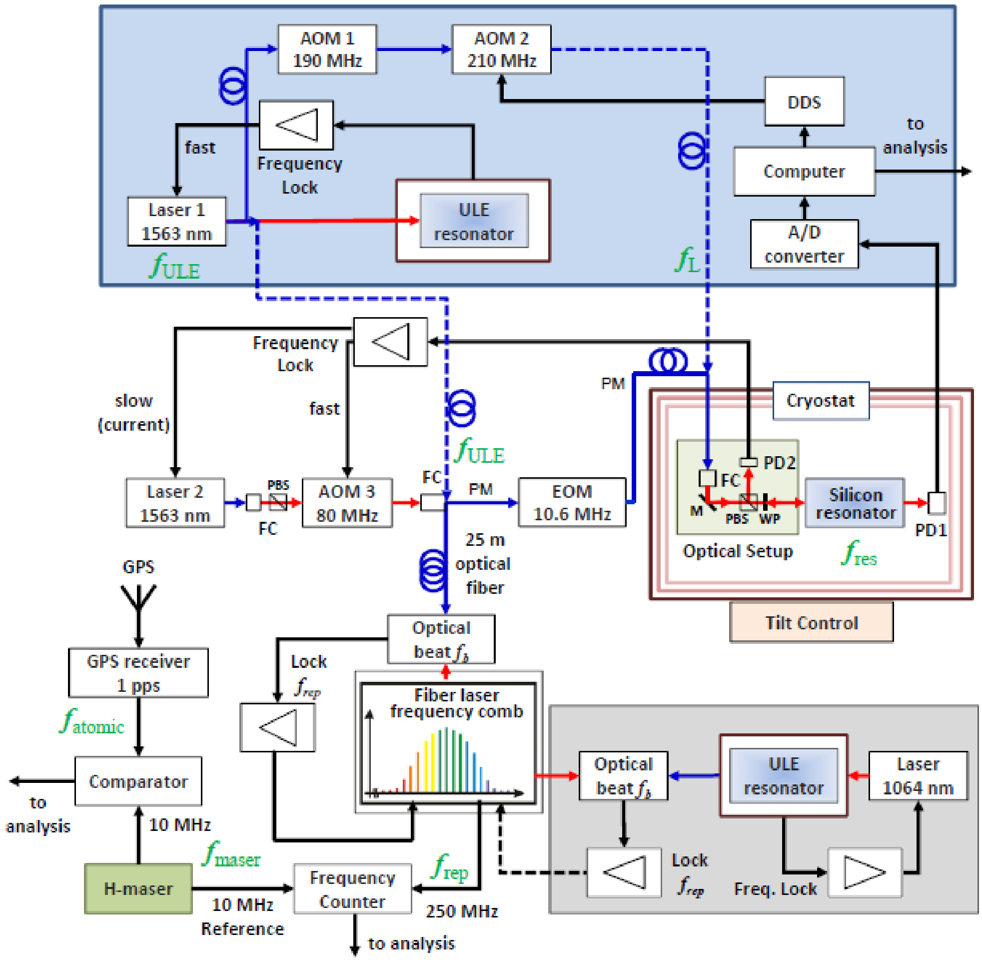

Figure 4.5: Schematic of the overall setup, containing the silicon resonator, three continuous-wave lasers and an optical frequency comb. To reduce the linewidth of the comb's modes, one of its modes was locked either to a 1.06 μm reference laser (modality A, gray background), to the Si-resonator-stabilized laser (modality B, no colored background), or to a 1.5 μm reference laser (modality C, blue background; dashed blue lines indicate connections when this modality is in use). Abbreviations: **FC**, fiber coupler, **AOM**, acousto-optic frequency shifter, **DDS**, synthesizer, **EOM**, electro-optic modulator, **WP**, quarter-wave plate, **PBS**, polarizing beam splitter, **M**, set of motorized mirrors, **PD1** and **PD2**, photodetectors. **Red lines** indicate free-space beams. **Blue lines** indicate optical fibers. All r.f. sources are referenced to the H-maser. (This figure and caption are reproduced from [35]).

5 Optical schematic of the experiment

The overall optical schematic used during the experiment is presented in Fig. 4.5. Depending on the applied techniques, parts of this setup were used interchangeably or in parallel. We use two 1.5 μm external-cavity semiconductor lasers (Rio Orion) with an output power of 20 mW and a linewidth of less than 15 kHz, designated as laser1 and laser2, for the interrogation of our silicon resonators. Laser1 with a frequency f_{ULE}, prestabilized to the room-temperature 10 cm long ULE resonator, is utilized whenever the linescan technique is applied (see Sec. 6 and Sec. 7.2 below). Installed in a comb lab, it is connected with the silicon resonator via a 50 m long polarization-maintaining optical fiber. To trim the frequency of the laser1 at the frequency of the transmission line of the resonator, a set of fiber-coupled acousto-optic modulators is used. Laser2, located at the optical table next to the cryostat, is applied for frequency-locking to the silicon resonator using the Pound-Drever-Hall (PDH) technique (see Sec. 7.1) and a compact all-cryogenic optical setup installed next to the resonator (see Fig. 4.4). Both lasers share a single 6 m long polarization-maintaining optical fiber feedthrough for the guidance of the light to the cryogenic resonator.

The measurement of the absolute optical frequency f of both lasers is done using a frequency comb. It is a sum of a beat frequency $\pm f_B$ between the laser and a comb mode, a repetition rate of the comb $f_{rep} \sim 250$ MHz multiplied by corresponding comb mode number mf_{rep}, and frequency of the carrier-envelope-offset $\pm f_{ceo}$ stabilized at 20 MHz using a commercial synthesizer. Both, the synthesizer and the high-resolution counter used for the measurement of f_{rep} are referenced to the 10 MHz output of a hydrogen maser (Vremya-CH VCH-1005). To reduce the noise of the f_{rep} measurement and to increase the overall precision we reduce the linewidth of the comb modes by optically stabilizing the comb to either one of the two 1.5 µm lasers or to a 1.06 µm laser, stabilized to a separate 10 cm long ULE resonator [47]. For this, the signal of a photodiode detecting the frequency f_b was fed to a servo electronics to stabilize the beat frequency to 50 MHz by acting on the comb's cavity length via an intracavity electro-optic modulator.

6 Characterization of the 1.5 μm room-temperature ULE resonator

To measure the short-term stability of the cryogenic resonator and to be able to scan over its resonance line, a 1.5 µm room-temperature reference resonator was built. Made of a block of ultralow expansion glass (ULE), it has a length of 100 mm and a diameter of 60 mm. End faces of the resonator are optically contacted with fused silicon mirrors with a 1 m and infinitely long radii of curvature. To compensate for the difference in the expansion coefficient between the spacer and mirrors two ULE rings were optically contacted to the mirrors [44]. The resonator was fixed inside the frame with a ten-point support configuration resembling the suspension of a cryogenic resonator (see Fig. 6.1, left). After installing two temperature shields to isolate the resonator from the environmental temperature fluctuations and evacuating the setup, an ultra-narrow laser (RIO) with a 1561.6 nm wavelength was locked to it using the Pound-Drever-Hall technique. The setup is displayed in Fig. 6.1, right. Laser light is splitted into three parts. The first two parts are needed for the lock at the ULE resonator and the measurement of the optical frequency of stabilized laser light with the frequency comb. The third part is used to produce the beat with the light of another laser stabilized at the cryogenic silicon resonator or to scan over its resonance line. To lock the laser to the resonator the light is modulated with EOM and guided, after reflection from the front mirror of the resonator, to the PDH photodiode. An AOM is installed along the beam path to eliminate parasitic interferences inside the path and to prevent the reflected light from reaching the laser. The signal from the photodiode is used by the lock electronics to change the laser current and thus laser frequency to keep it at the resonance line. The complete setup is situated on an optical plate that is actively isolated from seismic vibrations with an AVI system (Table Stable). Prior to its prime usage as the reference resonator for the experiments with the cryogenics silicon resonator, it has to be fully characterized. Results of characterization are presented below.

Relaxation time: relaxation time τ of the resonance frequency due to temperature variations was determined by changing the temperature of the resonator from 29 C to 24 C. and measuring temporal beat frequency variation between the laser light frequency stabilized to the ULE room temperature resonator and laser light stabilized on cryogenic silicon resonator over a course of seven days (see Fig. 6.2, upper left panel). As the frequency of the silicon resonator remains stable over long periods of time all observed frequency changes stem from ULE resonator. For detection, two beams of the ULE and silicon resonator stabilized lasers were overlapped using optical fibers and the beat signal was detected with a photodiode. To find the beat frequency, we used a PC-controlled spectrum analyzer (Signal Hound). The data from the spectrum analyzer were fitted with a Lorentzian function and the frequency of the beat was determined. Recorded change in beat frequency is presented in Fig. 6.2. To extract the relaxation time τ these data were fitted with an exponential:

$$f_{Beat} = a + b\exp(-\frac{x}{\tau}).$$

The relaxation time was found to be:

$$\tau = (0.94 \pm 0.08) \text{ days}.$$

It is surprisingly large and allows good thermal isolation of the resonator from the temperature fluctuations of the surrounding.

Zero CTE temperature: temperature T_0, where the CTE of the ULE resonator α_{reson} is zero was determined over the course of two months by changing the temperature in steps of 1 C to 2 C from 6 C to 0 C and observing beat frequency between the ULE-stabilized laser light and laser light stabilized on silicon cryogenic resonator (see Fig. 6.2, upper right panel). The total change in beat frequency over this period of time, accompanied by a total temperature change of 6 C, is around 3.5 MHz, with a contribution from the silicon resonator of less than 1 kHz. Beat frequency was determined by fitting the Lorentzian function to the data obtained with a spectrum analyzer. Results of the fits were plotted as a

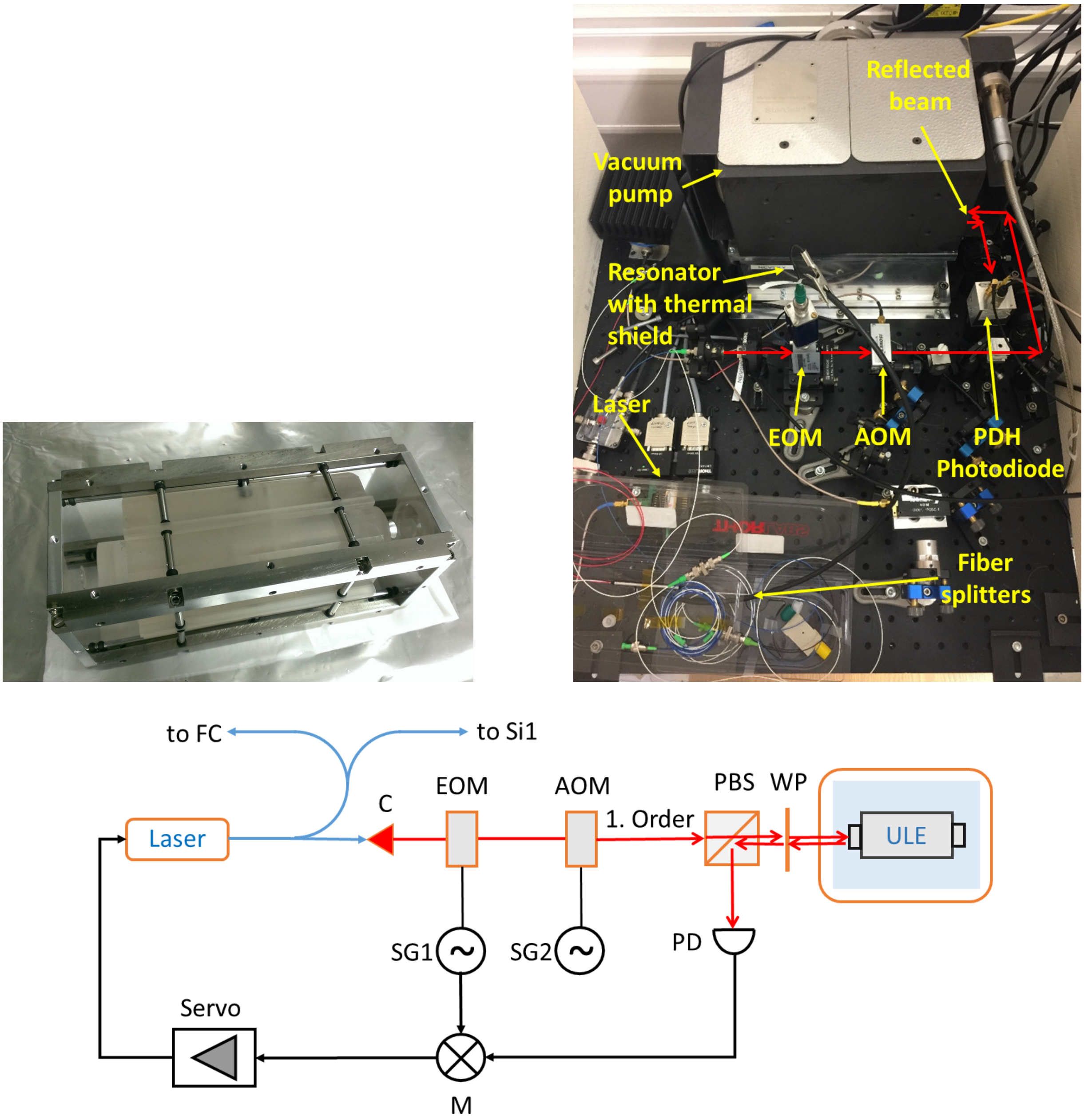

Figure 6.1: **Upper left panel:** ULE room-temperature resonator inside a frame with a ten point support configuration (photo credit: Qun-Feng Chen). **Upper right panel:** PDH setup of the ULE room-temperature resonator installed inside the thermal radiation shield and held under vacuum. **Bottom panel:** the radiation of the laser is divided with fiber splitters in three parts used for the lock at the resonator, beat with cryogenic resonator **Si1**, and optical frequency measurement with frequency comb **FC**, respectively. The light is coupled out of the fiber with collimator **C** and modulated with **EOM**, driven with a signal generator **SG1**. After passing through polarizing beam splitter **PBS**, quarter-wave plate **WP** and reflection at the mirror of the resonator the beam is guided to the PDH photodiode (marked as **PD** in the scheme). The signal from the photodetector is mixed with the output of the signal generator **SG1** with a mixer **M**, and is analyzed with the lock electronics (not showed here) to stabilize the laser at the resonance by driving the laser current. To eliminate the beam path from parasitic interferences and to prevent the back reflection from going back to the laser an **AOM** was installed along the beam path, driven with a signal generator **SG2**. The whole setup is isolated from vibrations with an AVI system. Both **SG1** and **SG2** signal generators are referenced to the maser.

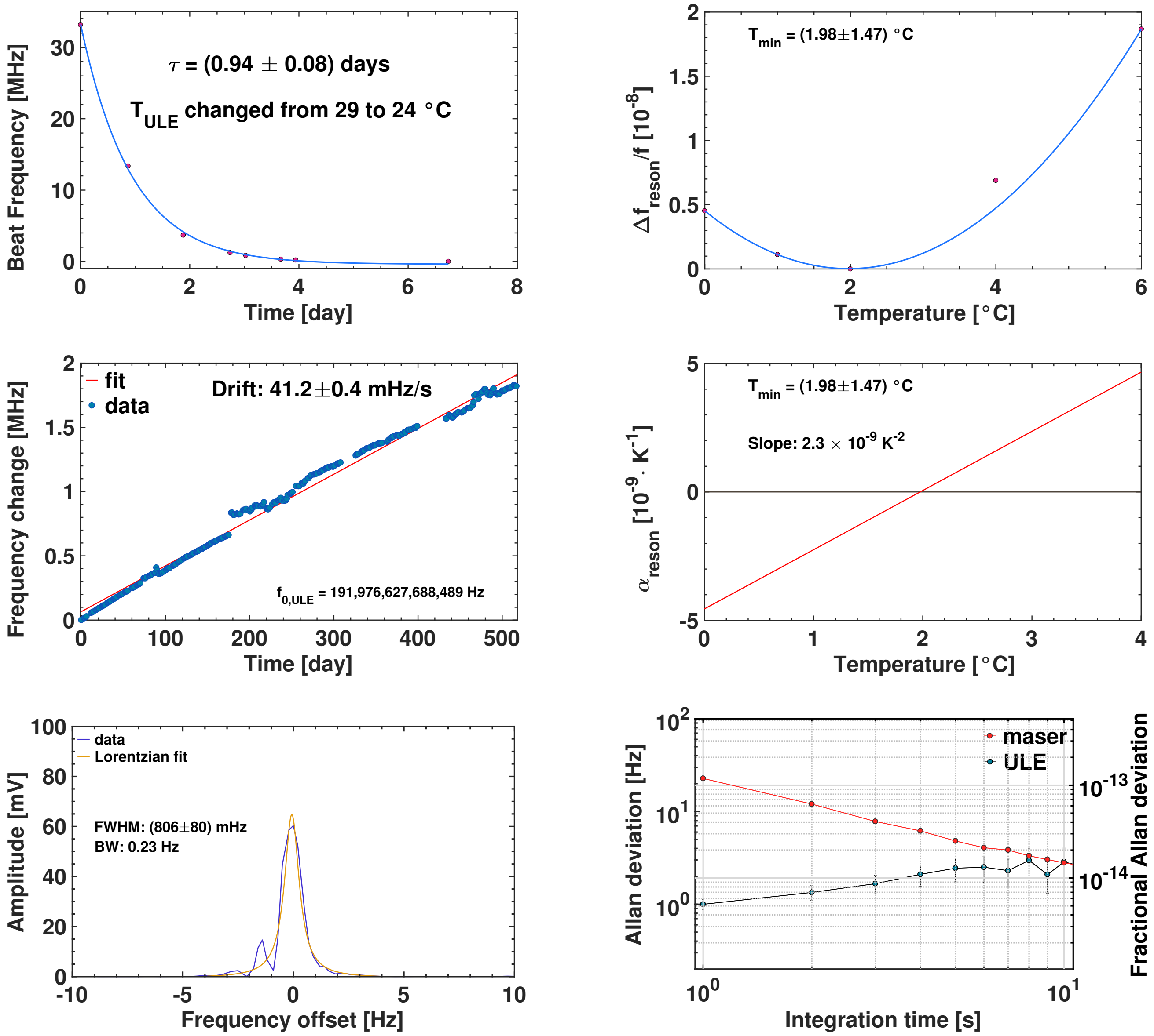

Figure 6.2: Characterization of the ULE room temperature resonator operated at 1561.6 nm. **Upper left panel:** thermal relaxation time constant of the resonator determined from the fit of the ULE vs. cryogenic silicon resonator beat frequency over one week time period after the temperature change from 29 C to 24 C. **Upper right panel:** determination of the zero CTE temperature done by reduction of the temperature of the resonator and monitoring of the corresponding frequency change followed by a fit of the data with a second order polynomial. **Middle left panel:** drift of the resonator frequency measured relative to the hydrogen maser via femtosecond frequency comb. **Middle right panel:** coefficient of thermal expansion $\alpha_{reson}$of the ULE spacer material determined from derivative of the fit function presented in the upper right panel. **Bottom left panel:** linewidth of the optical beat between the ULE-resonator-stabilized laser and the laser light of a second room-temperature ULE resonator at 1064 nm obtained via a frequency comb. **Bottom right panel:** frequency instability of the laser light stabilized at ULE resonator measured relative to a ULE room-temperature resonator at 1064 nm via frequency comb.

function of temperature and were fitted with a polynomial of second order. The zero-CTE temperature corresponds to the minimum of the fit function at $T_0 = 1.98$ C. The slope of the thermal expansion coefficient α_{reson} at this temperature is (see Fig. 6.2, middle right panel):

$$\frac{d\alpha_{reson}(T_0)}{dT} = 2.3 \times 10^{-9}\,\mathrm{K}^{-2}.$$

Frequency drift: the drift of the resonator $d\Delta f/dt$, temperature-stabilized at the temperature of zero CTE, was continuously measured with a frequency comb relative to a hydrogen maser. The result is presented in Fig. 6.2, middle left panel. Jumps in the data were caused by a repeated movement of the resonator to another lab or inside the lab, by unintentional bumps of the supporting table at which the resonator was installed, or by problems with stabilization of lab temperature. From the linear fit to the data we obtain with a 2σ error:

$$\frac{d\Delta f}{dt} = 41.2 \pm 0.4\,\mathrm{mHz/s}$$

Thus, the corresponding fractional frequency drift is $(2.06 \pm 0.02) \times 10^{-16}/\mathrm{s}$.

Linewidth: the linewith $\Delta\nu$ of the laser, actively locked to the ULE resonator was obtained by producing an optical beat with a tooth of a femtosecond frequency comb actively stabilized to a second identical ULE resonator, operated at 1064 nm [47]. Both optical paths for guiding laser light from ULE resonators to the frequency comb were operated with an active fiber-noise cancellation setup [87]. As can be seen from Fig. 6.2, bottom left panel, the linewidth of the beat δf_{Beat} between the two systems is:

$$\delta f_{Beat} = (806 \pm 80)\,\mathrm{mHz}.$$

With the assumption that two ULE resonators are identical, we obtain the linewidth of a single system:

$$\Delta\nu = \frac{\delta f_{Beat}}{\sqrt{2}} = (571 \pm 57)\,\mathrm{mHz}.$$

Short-term instability: Short therm instability was measured with the frequency comb optically stabilized to the second room-temperature ULE system, operated at 1064 nm, with a fractional frequency instability of 1×10^{-15} at the integration times between 1 s and 10 s[47]. Measured instability is presented in Fig. 6.2, bottom right panel. It is equal to $5.2 \times 10^{-15}/\mathrm{s}$. This instability is larger than that of a system operated at 1064 nm and can be further reduced with an implementation of an active power stabilization setup.

7 Laser stabilization techniques

In order to characterize the frequency stability of the resonator and the sensitivity to various disturbances, we need to measure the frequency of the resonance line. This is done using the Pound-Drever-Hall (PDH) lock of the laser to the resonance line of the resonator or by scanning the resonance line of the resonator with laser light of stable frequency. Both techniques together with the corresponding optical setups are presented below.

7.1 Pound-Drever-Hall lock

We implemented the Pound-Drever-Hall lock of a RIO diode laser to the resonance line of the Si1 resonator using the schematic presented in Fig. 7.1. After passing through a free space acousto-optic modulator, used for the fast frequency correction, and fiber-coupled electro-optic modulator, the light with an amplitude of 50 µW is guided into the cryostat and to the free space cryogenic optical setup, using optical fiber feedthrough. After reflection at the front mirror of the resonator, detection with a PD1 photodode, and amplification with the cryogenic amplifier, the signal of the photodiode is mixed with the signal from the local oscillator (SG2 in Fig. 7.1, top panel) and used by the lock electronics for the fast frequency adjustment via the AOM and slow frequency adjustment via the current of the photodiode of the laser.

A scan of the error signal is presented in Fig. 7.2, top left panel. The peak to peak amplitude of the signal is 9 mV and the slope is $a_{PDH} = 6.9\,\mu\text{V}/\text{Hz}$. Due to the high acceleration sensitivity of the Si1 resonator to vibrations, the error signal is highly disturbed, as can be seen in Fig. 7.2, top right panel. These disturbances lead to the fluctuation of the error signal zero point by $\Delta V \approx 10^{-3}$ V (see inset in Fig. 7.2, top right panel). As the lock electronics cannot differentiate between these disturbances and

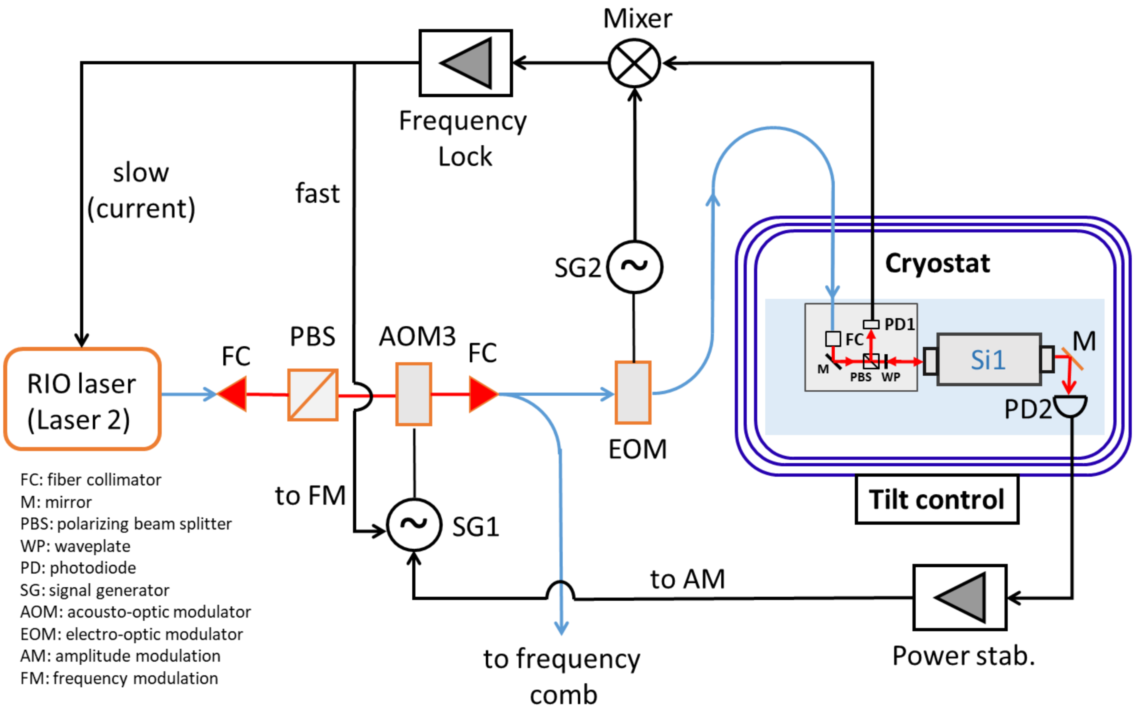

Figure 7.1: Schematic of the Pound-Drever-Hall stabilization setup of a laser source on a resonance of the Si1 cryogenic resonator.

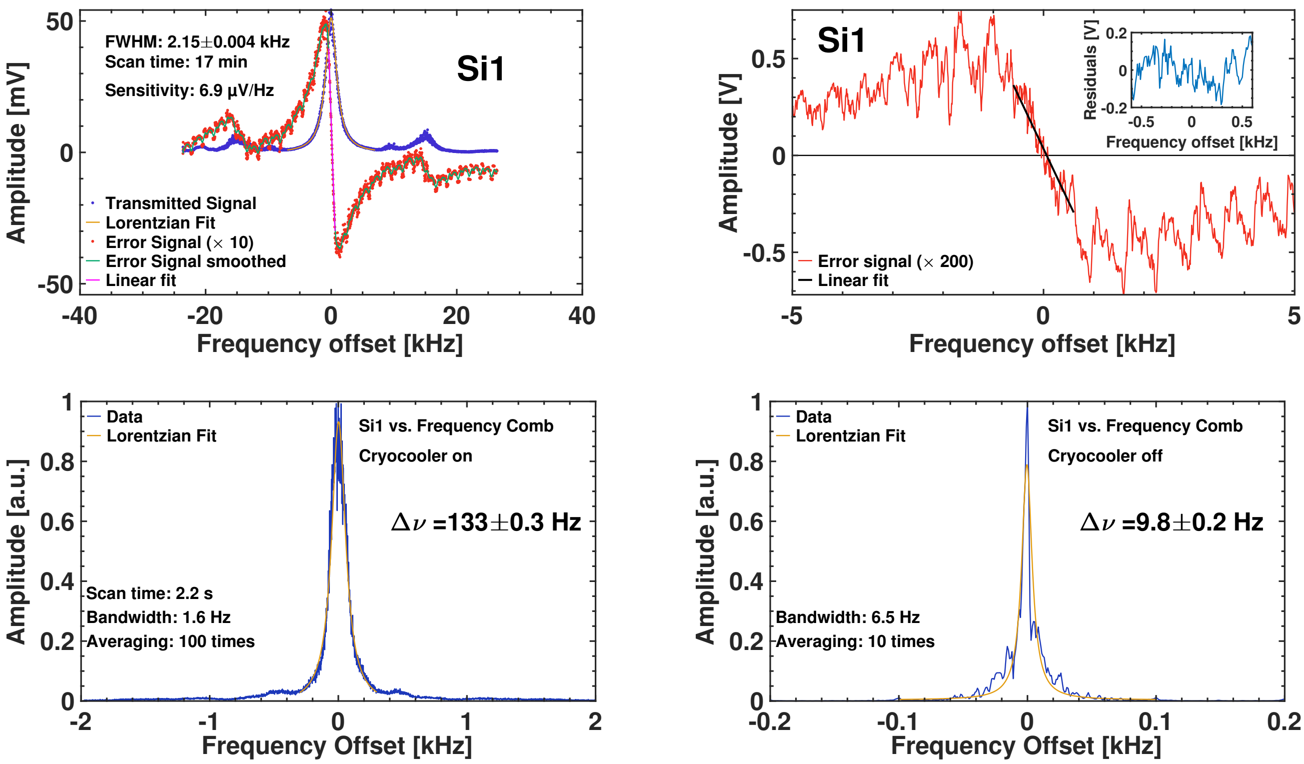

Figure 7.2: **Top left panel:** long time scan of the error signal together with the resonance line of the resonator with a prestabilized laser light. **Top right panel:** fast scan done around the zero crossing of the error signal together with the inset showing the residual fluctuations of the error signal due to vibrations. **Bottom left and right panels:** the linewidth of a beat of the laser frequency-stabiilzed to Si1 silicon resonator with a stable laser source at 1 μm [47] with a linewidth of less than 1 Hz and the cryostat switched on and off.

the real shift in frequency, it directly translates them into the frequency fluctuations Δf using the slope of the central part of the error signal as the conversion factor:

$$\Delta f = \frac{\Delta V}{a_{PDH}}.$$

After inserting the numbers in the above formula we obtain $\Delta f \approx 140$ Hz as the amplitude of frequency fluctuations. Thus, we expect the linewidth of the laser to be in this order of magnitude. To confirm this, we measured it by making the beat with a laser light stabilized to the room-temperature ULE resonator (see the previous section) with a linewidth below 1 Hz via frequency comb. The measurement was done with a cryostat switched on and off. The results are presented in Fig. 7.2, bottom panels. With the cryostat switched on the linewidth is on the order of 130 Hz. This number is in agreement with the above estimation. According to the measurement of vibrations with an optical sensor, switching off the cryostat would reduce the vibrations by one order of magnitude (see Sec. 3). Thus, we expect a reduction of the linewidth to approx 10 Hz. Our measurement result presented in Fig. 7.2, bottom right panel, confirms this.

The frequency stability of the laser stabilized at the Si1 resonance line was measured using a frequency comb referenced against the hydrogen maser and long-term frequency corrected using the GPS signal. As can be seen in Fig. 7.3 we obtain frequency stability of Si1 resonator equal to or better than the frequency stability of our maser. Due to the lack of alternative references, we cannot determine the true Si1 frequency stability.

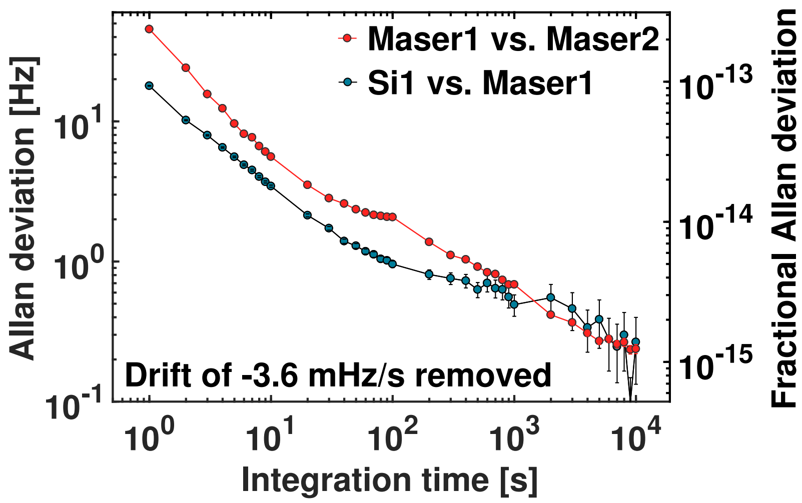

Figure 7.3: Mod. Allan deviation of the frequency instability of the Si1 resonator measured with a frequency comb relative to the hydrogen maser.

7.2 Linescan technique

The drawback of the Pound-Drever-Hall technique is that it is affected by the unwanted residual amplitude modulations of laser light, which occur along the optical path due to the low-order finesse resonators formed by the surfaces of the optical elements inside the setup. These modulations are interpreted by the lock electronics as modulations of frequency and lead to the change in the setpoint and thus change in frequency. To eliminate this effect we introduced a linescan technique, where the resonator is scanned over its resonance line with a light of a laser, frequency stabilized to a transmission line of a ULE room-temperature resonator using the Pound-Drever-Hall technique (see. Sec. 6). The setup is presented in Fig. 7.4, top panel. ULE laser and cryostat are located in different labs. The length of the optical fiber connecting the ULE laser with the cryogenic resonator is 30 m. We apply no fiber noise cancellation. Thus the linewidth of the laser light is expected to widen by $\sim$ 30 Hz, assuming an increase of 1 Hz for a 1 m path length inside the optical fiber. The was also no fiber noise cancellation along the path from the ULE laser to the frequency comb. For that reason, the frequency stability degraded compared with the result presented in Fig. 6.2, bottom right panel (see Fig. 7.4, bottom left panel). We also actively control the power of the light going into the cryogenic optical fiber by splitting a part of light and detecting its amplitude with a room-temperature photodiode PD3. The output of the latter is used to modulate the output amplitude of the DDS connected to the acousto-optic modulator AOM2. Residual instability of optical power, measured with the in-loop photodetector PD3, is presented in Fig. 7.4, bottom right panel. To bridge the difference in frequency between the TEM_{00} modes of the ULE and cryogenic Si1 resonator, we use two AOMs. With the frequency of the AOM2 set to 210 MHz, we manually shift the frequency of the light with AOM1 to get to the middle of the transmission line of the Si1 resonator. Thus, AOM1 frequency is continuously changing over time due to the frequency drift of the ULE resonator. At the maximum of the resonance line, the signals from photodiodes in reflection and in transmission were recorded (see Fig. .7.5, upper left panel). They are modulated by the 1.4 Hz working frequency of the pulse tube with an amplitude variation of $\sim 25\%$ and have mirror symmetry. After the resonance was found, an automated scanning is started using a computer-controlled DDS connected to the AOM2. The duration of one scan was chosen to be approximately 10 s, the time at which the ULE resonator displays the lowest frequency instability (see Fig. 7.4, bottom left panel). The optimal span of the scan, 3 kHz, was found experimentally. We collect 1000 points during each scan, with each point being an average of data collected during 3 ms time interval with a sampling rate of 45 kS/s. The remaining 7 ms is the dead time needed for the labview program to change the frequency of the AOM. An example of a scan is presented in Fig. 7.5, bottom right panel.

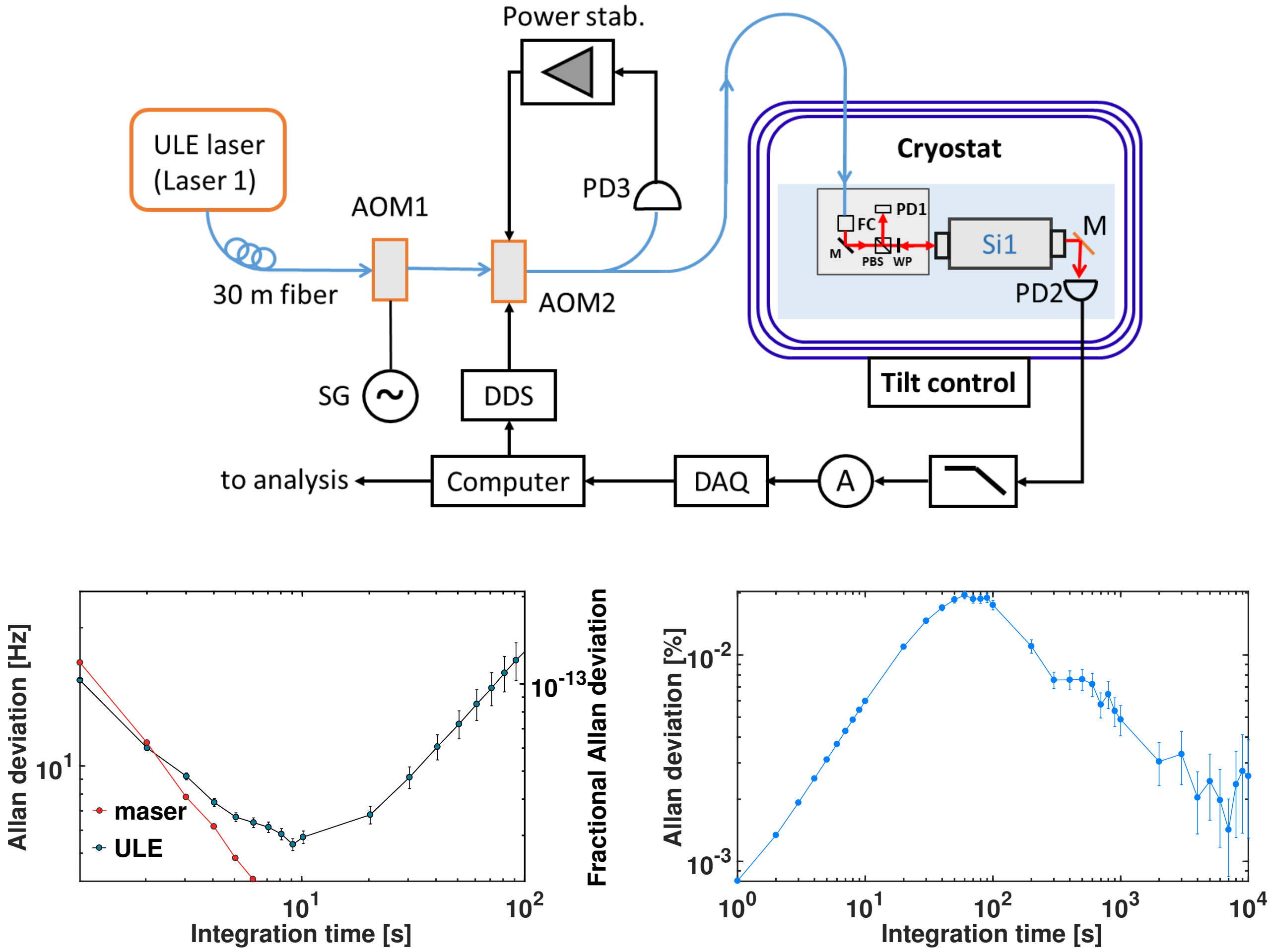

Figure 7.4: **Top panel:** schematic of the setup used for the scan over the Si1 resonance line with a laser light stabilized at the ULE room-temperature resonator: after a passage over the 30 m long optical fiber connecting the two systems in two different labs, the light is manually frequency shifted with **AOM1,** driven by signal generator **SG,** to the middle of the transmission line. Computer controlled **DDS** drives **AOM2** to scan around the resonance. Transmitted light is detected with photodiode **PD2**, filtered with 10 Hz low-pass filter, amplified, and digitized with a DAQ card. After digitizing the signal is analyzed with a computer. The power of the light going inside the cryostat is actively stabilized using photodiode **PD3** and corresponding server electronics used to modulate amplitude of the **AOM2**. **Bottom row panels:** frequency (left) and power (right) stability of the ULE laser light used for scanning.

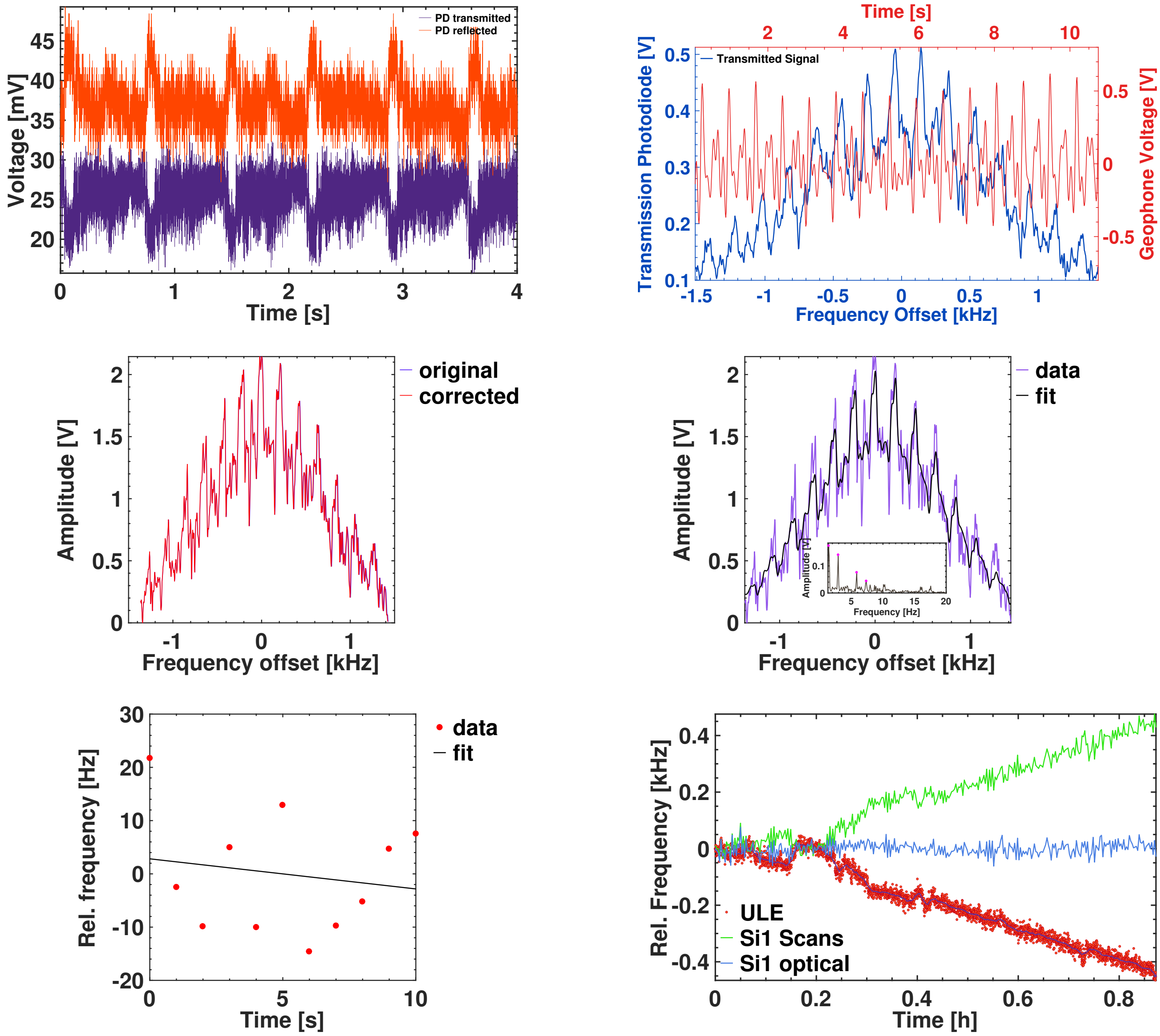

Figure 7.5: **Top left panel:** signal of two photodiodes in transmission and reflection for the laser light put at the peak of the resonance line of the Si1 resonator. **Top right panel:** voltage of the photodiode in transmission during the scan of the resonance line with a span of 3 kHz and scan duration of approximately 10 s (blue) together with geophone data (red). **Middle left panel:** frequency correction of the Si1 scan data for the drift of the room-temperature ULE laser used for scanning. **Middle right panel:** scan data and the corresponding fit with a Lorentzian function together with the FFT of the scan data in the inset. **Bottom left panel:** determination of the ULE frequency drift used for correction of the Si1 scan data. **Bottom right panel:** subtraction of the ULE optical frequency drift (red) from the Si1 line scan data (green) to obtain the absolute optical frequency of the Si1 resonator (light blue).

To obtain the frequency of the transmitted line, each scan is first corrected for the drift of the ULE resonator frequency by fitting the corresponding frequency data of the ULE resonator, simultaneously measured with frequency comb, with a linear fit to obtain the drift in frequency d_{ULE}. This drift is added to the scan data points $f_{i,OLD}$ to obtain the corrected frequency f_i:

$$f_i = f_{i,OLD} + i \cdot d_{ULE},$$

where $i \in [1, 1000]$.

An example of data correction together with the drift data of the ULE resonator are presented in Fig. 7.5, middle left panel, and bottom left panel, respectively. Corrected scans are fitted with a

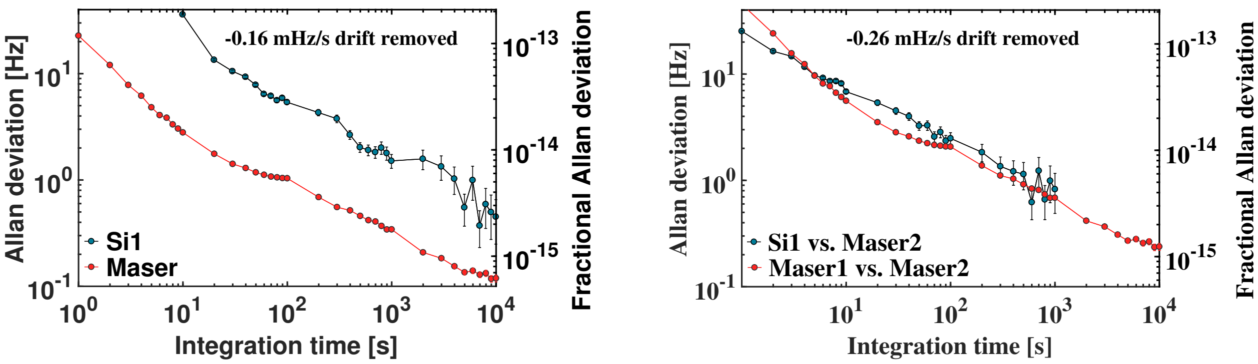

Figure 7.6: **Left panel:** instability of the Si1 resonator frequency determined from the scans of its line with the laser light prestabilized at the room-temperature ULE resonator and after subtraction of -0.16 mHz/s frequency drift. **Right panel:** frequency instability after improvement of the line scanning technique.

Lorentzian function f_L to obtain the frequency of the line peak f_{max}:

$$f_L = a + \frac{2\pi}{b}\frac{c}{4(f - f_{max}) + c^2},$$

where a, b, and c are fit parameters. They correspond to the offset in amplitude, the area under curve, and linewidth, respectively. To improve fit quality we account for the amplitude modulations of linescan data, caused by the operation of the pulse tube, by the introduction of four additional terms to the fit function:

$$f_L' = (a + \frac{2\pi}{b}\frac{c}{4(f - f_{max}) + c^2})(1 + \sum_{i=1}^{4} e_i \sin(2\pi\nu_i t + g_i)). \tag{7.1}$$

While ν_i is readily obtained from the FFT of the linescan data by taking four frequency values with the largest amplitude (see inset in Fig. 7.5, middle right panel), parameters e_i and g_i are to be determined from the fit. An example of the fitting is presented in Fig. 7.5, middle right panel. After the fitting is done for all scans and frequencies of the peak maxima are obtained, we can calculate the absolute optical frequency of the Si1 resonator f_{Si1} by taking a sum of the mean optical frequency of the ULE resonator f_{ULE}during the scans, operational frequency of the AOM1 f_{AOM1}, and the frequency maximum of each scan f_{max}:

$$f_{Si1} = f_{ULE} + f_{AOM1} + f_{max}.$$

An example of this calculation is presented in Fig. 7.5, bottom right panel. As we can see, the drift of the ULE resonator is completely removed from the Si1 optical frequency data. Residual fractional frequency instability of the Si1 resonator is 2×10^{-15} (see Fig. 7.6).

The linescan technique presented above suffers from the long dead time in between the data acquisition points of one linescan. To improve the linescan efficiency we changed the underlying labview algorithm and eliminated the dead time. Simultaneously, we decreased the time of a single linescan to 0.7 s. As seen in Fig. 7.6, right panel, this resulted in the improvement of the measured frequency instability of our resonator at all times.

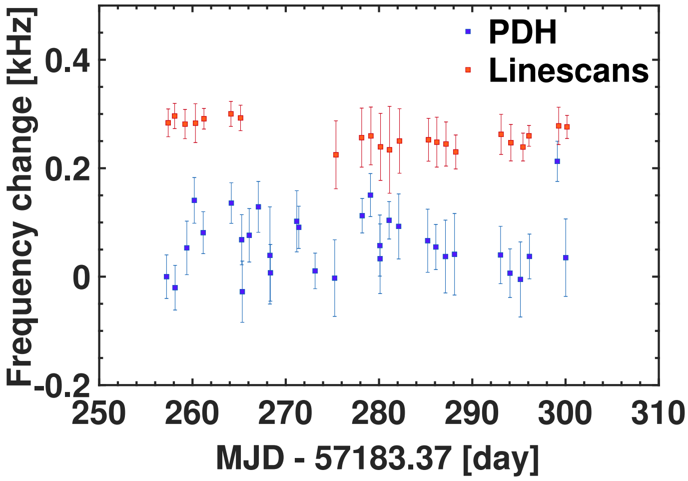

Figure 7.7: Comparison of the frequency measurements done with the PDH lock (blue colored data points) and with linescans (orange colored data points).

7.3 Comparison of the PDH lock with the linescan technique

We compared the frequency stability of the resonator using both techniques presented above for a duration of 40days. The result is displayed in Fig. 7.7. Both techniques differ in the determination of the optical frequency and in the scatter of data points on a day-to-day measurement basis. It is a result of a constant shift of a PDH locking technique offset together with the dependence on lab temperature fluctuations and the time-dependent change in the amplitude of the residual modulations generated by the EOM installed in the optical PDH scheme. Thus, to increase the precision of our measurement we employ the linescan technique for the most time of the experiment.

8 Properties of the 25 cm resonator at 1.5 K

In this section we present experimental results concerning the main properties of the resonator, e.g., sensitivity to vibration, tilt, temperature, and circulating optical power. We have also determined the coefficient of optical absorption of coated silicon mirror substrates. The result of this experiment is presented in Appendix B.

8.1 Optical properties

To determine the incoupling ratio of light into the resonator a scan over the resonance with a frequency stabilized laser light was made and the amplitude of the photodiodes in transmission and reflection was recorded (see Fig. 8.1,left panel). To obtain clear signals, the pulse tube of the cryostat was switched off during the experiment. The incoupling ratio is about 1.7%.

The mode matching is obtained by scanning low-order modes of the resonator with the pulse tube of the cryostat in operation and comparing the mode's amplitudes. As can be seen in Fig. 8.1,right panel, the TEM_{00} mode is the mode with the largest amplitude. TheTEM_{02} mode could not be obtained due to the limitation of the hardware at hand. With the assumption that no high-order modes of the resonator are excited except of the modes TEM_{00} to TEM_{04} and with the amplitude of the TEM_{02} assumed to be ~ 0.15 we obtain approximately 60% for the mode matching factor.

The linewidth of the resonator was determined by a direct scan of the TEM_{00} mode with a pre-stabilized ULE laser. The obtained linewidth is 2.1 kHz, as can be seen in Fig. 8.2, upper panel. This number corresponds to the finesse of 286000.

8.2 Sensitivity to vibrations

In Sec. 2 we presented FEM results regarding the vibrational sensitivity of the resonator inside the supporting frame. Our obtained sensitivities are zero for accelerations along all three directions. However,

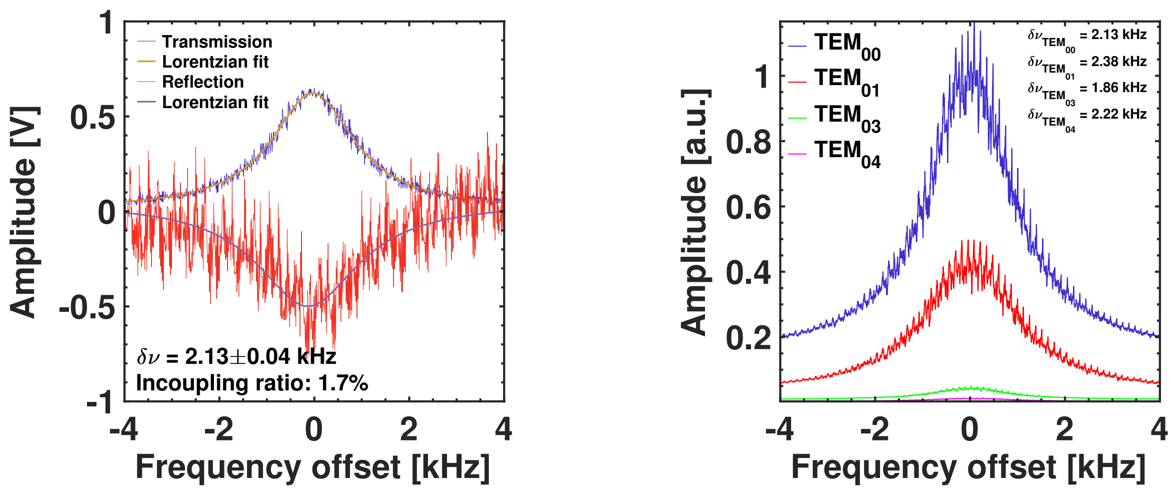

Figure 8.1: **Left panel:** scan of the resonator linewidth and the cryostat switched off. Transmitted signal was shifted to zero for convenience. **Right panel:** amplitude and linewidth comparison of different low order modes of the resonator. TEM_{02} could not be scanned due to the limitation of available hardware. Linewidth of each mode is determined from the fit of the Lorentzian function to the data.

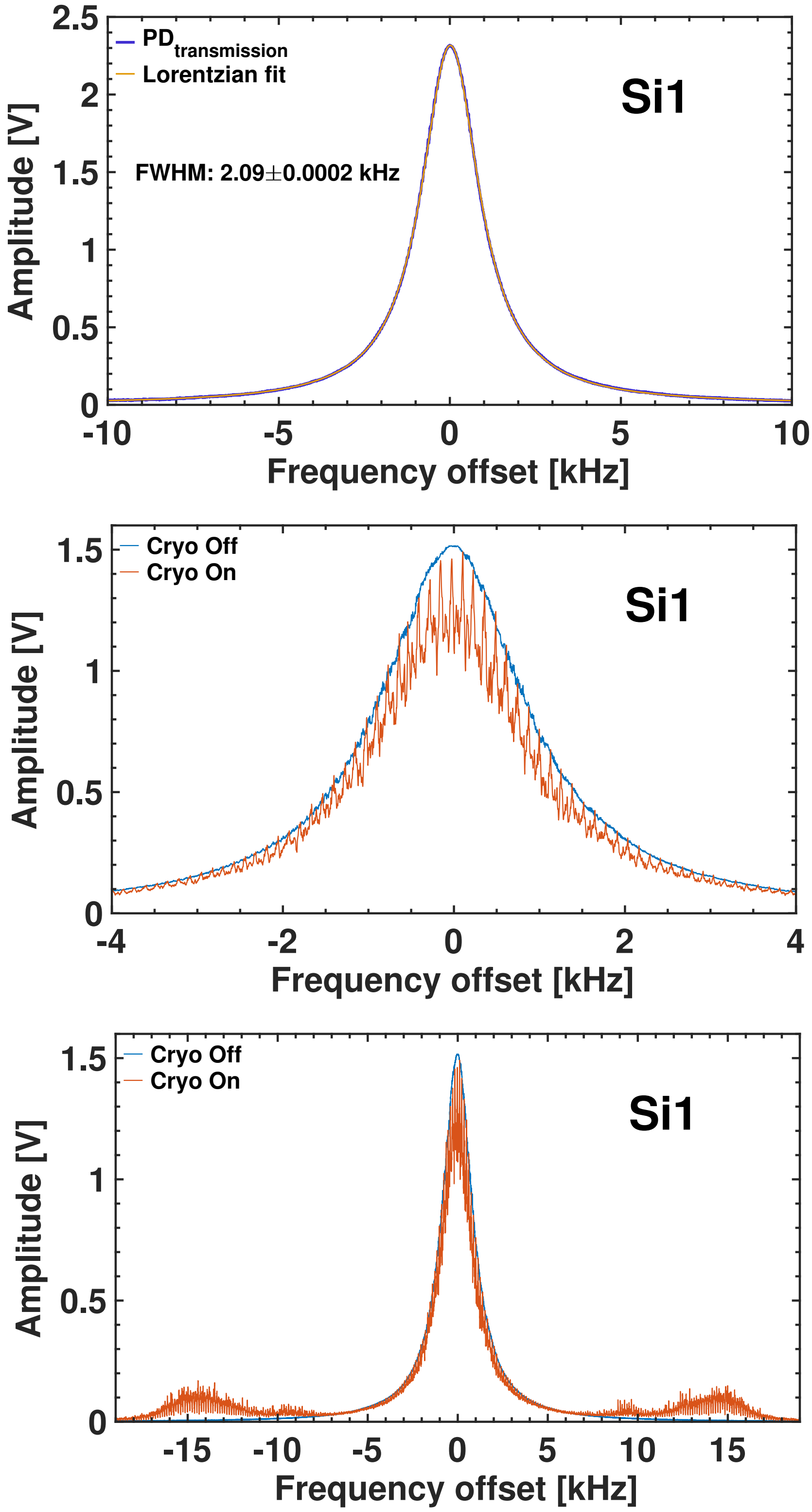

Figure 8.2: **Top panel:** scan of the Si1 transmission line with a ULE pre-stabilized laser and the cryostat switched off. **Middle and bottom panels:** comparison of the shape of the Si1 transmission line with the cryostat switched on and off and the scan span of 8 kHz (middle) and 19 kHz (bottom).

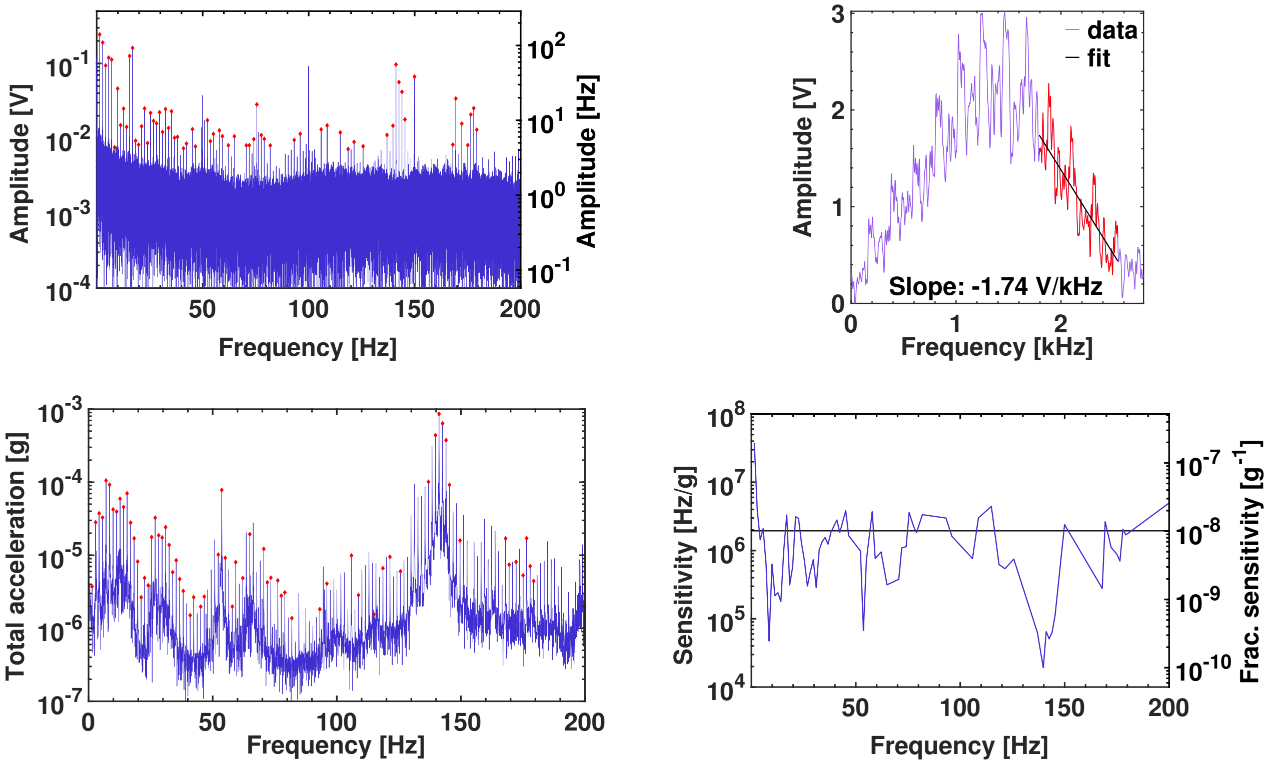

Figure 8.3: **Top left panel:** power spectrum of the photodiode voltage time trace in transmittance with a interrogating laser frequency set at the slope of the transmission line. Local maxima are marked with red markers. The right y-axis was obtained using the slope of the transmission line at set laser frequency (**top left panel**). **Bottom left panel**: total acceleration of open and running cryostat obtained from the time traces of an accelerometer positioned subsequently along three spacial directions. Red points mark the amplitude at the position of local maxima in the top left panel. **Bottom right panel**: calculated acceleration sensitivity of the Si1 resonator.

the ten-point support is heavily affected by a range of factors. The final sensitivity is usually high and is in the range between 1×10^{-11} and 1×10^{-8} Hz/g. To obtain the sensitivity of the resonator to the total acceleration along all three spatial directions we measured amplitude fluctuations of the light of the laser prestabilized to the room-temperature ULE resonator, with its frequency shifted by the AOM to the side of the silicon resonator transmission line, with a photodiode in transmission. Fig. 8.3 (top left panel) shows the power spectrum of the recorded photodiode output voltage amplified by factor 500. The amplitude was recalculated to Hz using the slope of the transmission line, -1.74 V/kHz (see Fig. 8.3 (top right panel)). The amplitude of the local maxima, marked red in Fig. 8.3 (top left panel), was divided by the amplitude of the local maxima of total acceleration measured with an accelerometer in open and running cryostat along three spatial directions (see. Fig. 8.3 (bottom left panel) and Sec. 3). Resulted vibration sensitivity and fractional sensitivity is presented in Fig. 8.3 (bottom right panel). It decreases rapidly from 2×10^{-7}/g at a frequency $f = 1.4$ Hz to 1×10^{-8}/g at a frequency $f = 4.26$ Hz. For higher frequencies, it fluctuates around the mean value of 1×10^{-8}/g. Since the measurement of the acceleration was done with an open cryostat, we expect a reduction in the amplitude of acceleration, due to the additional mass of the four shields, which act as a damper. Another small reduction is likely due to the slight increase of the material stiffness at low temperatures. Therefore, we regard our presented results as an upper limit.

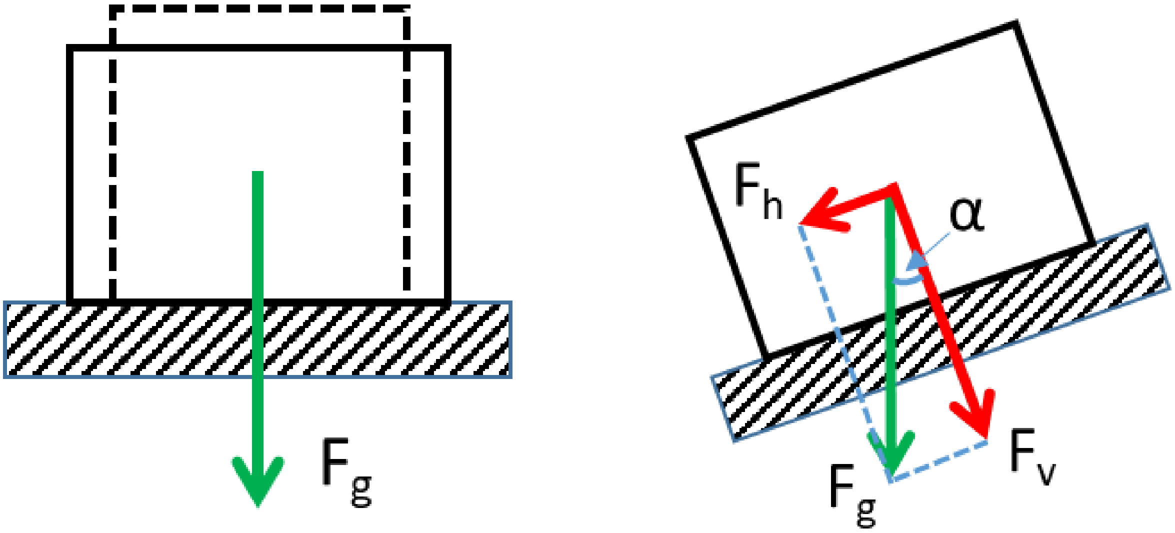

Figure 8.4: **Left panel:** dimensions of a cube of a solid material before (solid line) and after application of gravity force F_g. **Right panel:** schematic depiction of forces acting upon solid cube after introduction of tilt.

8.3 Sensitivity to tilt

Tilt variations of the resonator orientation relative to the Earth's gravity field produce a compression force on the resonator and change its resonance frequency. To understand the influence of tilt on frequency stability we analyze a simple model of a resonator as a cubic piece of material. In the absence of the gravity force F_g the edge length is L_0 and the area of the cross-section is A. After the application of gravity the cube is compressed along the vertical direction (see Fig. 8.4, left panel). To describe the change in edge length ΔL we apply Hook's law

$$\sigma = E\varepsilon,$$

where σ is the stress, ε is the strain and the proportionality factor E is Young's modulus of the cube material. From the last equation we yield:

$$\Delta L = \frac{F_g L_0}{AE}.$$

Together with $F_g = \rho L_0 A g$ and introduction of the Poisson's ratio ν we obtain:

$$L_v = L_0 - \frac{\rho L_0^2 g}{E},$$

and

$$L_h = L_0 + \frac{\rho L_0^2 g}{E}\nu,$$

for the edge length of the cube along the vertical and horizontal direction, respectively.

Tilting the cube changes the amplitude of the vertical force $F_v = F_g \cos(\alpha)$ and generates a force component $F_h = F_g \sin(\alpha)$ acting along the horizontal direction (see Fig. 8.4, right panel). Tilt changes vertical horizontal dimensions of the cube as

$$\Delta L_v = \frac{\rho L_0^2 g}{E}\nu(1-\cos(\alpha)),$$

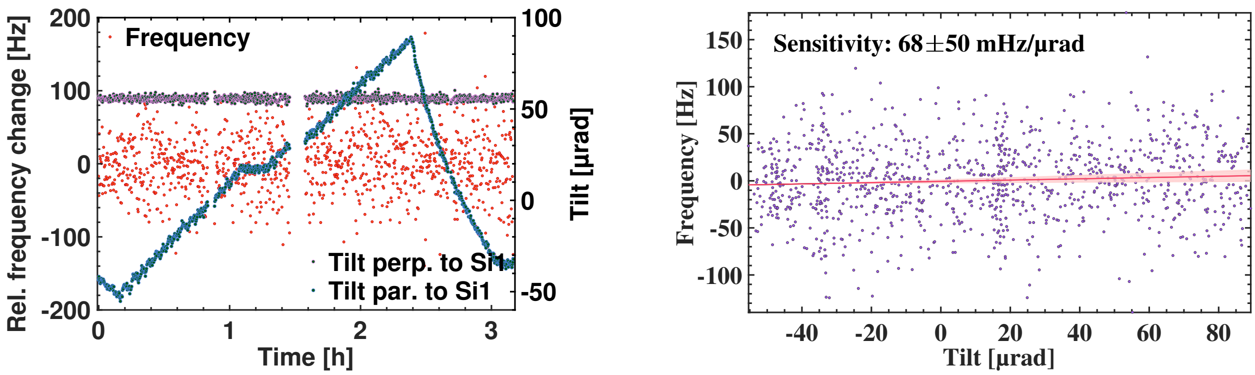

Figure 8.5: **Left panel:** measurement of the Si1 resonator frequency with the linescan technique, while changing the tilt along the optical axis of the resonator and actively stabilizing the tilt along the direction perpendicular to it. **Right panel:** determination of the Si1 sensitivity to tilt by a linear fit of the measurement data.

$$\Delta L_v = \frac{\rho L_0^2 g}{E}(\lambda - 0.5)\sin(\alpha),$$

where factor λ accounts for the way how the resonator is suspended. It equals to 0.5 if the mounting of the resonator is symmetric and elongation and shortening of the length perfectly cancel each other. For small tilt angles α above equations are simplified to:

$$\Delta L_v = \frac{\rho L_0^2 g}{E} v \frac{1}{2}\alpha^2,$$

$$\Delta L_h = \frac{\rho L_0^2 g}{E}\alpha(\lambda - 0.5). \tag{8.1}$$

As we can see ΔL_v is much smaller if compared to ΔL_h. Eq. 8.1 imply that the sensitivity to tilt is dominated by the way how the resonator is mounted inside the frame. This sensitivity is reduced for material with high stiffness. The importance of stabilizing the tilt was stated in Sec. 3.3, where a technique for the stabilization of tilt was presented. In this section we describe our measurement results of the resonator sensitivity on tilt variations along its optical axis obtained with the linescan technique and results on tilt sensitivity along the optical axis and perpendicular to it with the laser locked to the cavity using the PDH method.

Linescan technique: the tilt was changed by heating one of the three legs of the cryostat over a two hours time period with a speed of approx.0.37 µrad/s (see Fig. 8.5, left panel). To ensure tilt stability in the direction perpendicular to the optical axis of the resonator the tilt of the cryostat along this direction was actively stabilized during this experiment. to determine the sensitivity we plot measured frequency against tilt and do linear fitting (see Fig. 8.5, right panel). The resulted sensitivity is 68 ± 50 mHz/µrad. Using this number and eq. 8.1 we can determine the symmetry parameter which is equal to $\lambda = 0.508$. Thus, the suspension of the resonator is symmetrical to within 0.8%.

PDH technique: the tilt was changed by lifting the two legs of the cryostat tripod and observing the frequency change of the locked laser with a frequency comb. In opposite to the results presented in the previous section, the tilt was changed almost instantaneously and over a higher range. Because all legs of the cryostat are 120 deg apart, it is not possible to have a pure tilt change along the optical axis of the resonator or perpendicular to it (see Fig. 8.6). To determine tilt sensitivities s_p and s_r along the optical axis and perpendicular to it we input resulted tilt and frequency change, shown in Fig. 8.6, into a system of two equations:

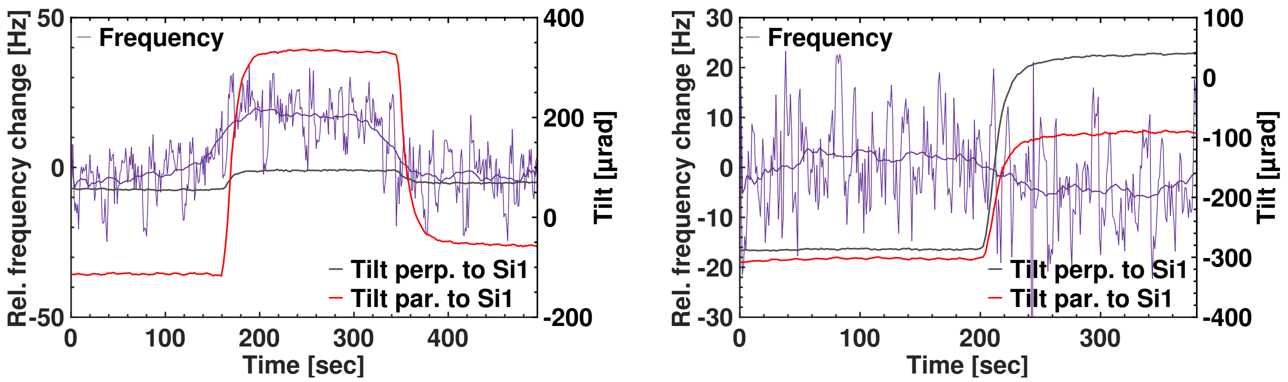

Figure 8.6: Measurement of the Si1 resonator frequency dependence on tilt with the laser locked to it using the PDH method**. Left panel:** Si1 resonator frequency change due to the tilt of the resonator along its symmetry axis. **Right panel:** Si1 resonator frequency change due to the tilt of the resonator perpendicular to its symmetry axis.

$$s_p \Delta T_{p1} + s_r \Delta T_{r1} = \Delta f_{1,}$$
$$s_p \Delta T_{p2} + s_r \Delta T_{r2} = \Delta f_{2,}$$

where ΔT_{pi}, ΔT_{ri}, and $\Delta f_{i,}$ are the tilt changes along the optical axis and perpendicular to it and the measured frequency change of the resonator resulted from the movement of the leg i. After inserting the measured data resulted from the movement of leg 1 (Fig. 8.6, left panel) and leg 2 (Fig. 8.6, right panel) into the above system of equations and resolving for s_p and s_r we obtain:

$$s_p = 48\,\mathrm{mHz}/\mu\mathrm{rad},$$
$$s_r = 3\,\mathrm{mHz}/\mu\mathrm{rad}.$$

The first sensitivity is in very good agreement with the result of the linescan measurement presented above. The resulted fractional frequency change is:

$$(\frac{\Delta f}{f})_p = 2.5 \times 10^{-16}/\mu\mathrm{rad},$$
$$(\frac{\Delta f}{f})_r = 0.16 \times 10^{-16}/\mu\mathrm{rad}.$$

Thus, the sensitivity for tilting the resonator around its optical axis is more the ten times less than sensitivity to tilt along the optical axis.

8.4 Thermal expansion of the resonator

Temperature change ΔT affects the length L of the resonator over the coefficient of thermal expansion (CTE) α_{reson} of the spacer material:

$$\frac{\Delta L}{L} = \alpha_{reson} \Delta T.$$

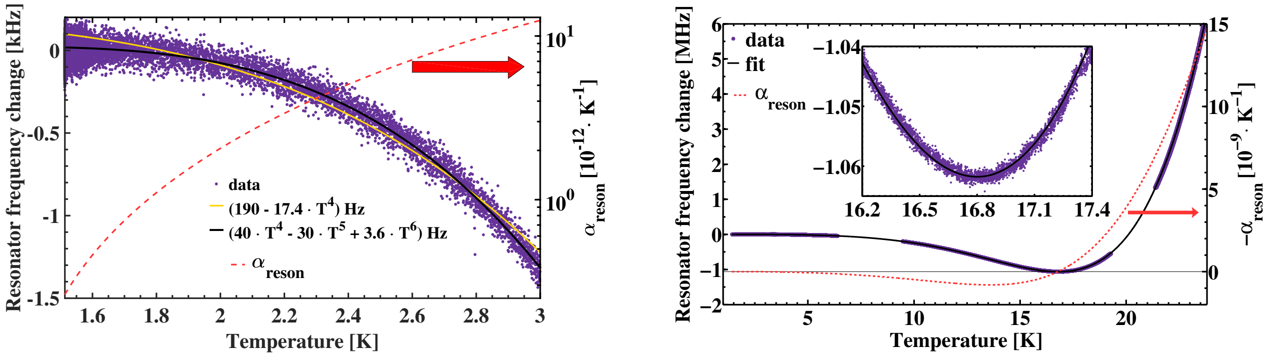

Figure 8.7: Dependence of the Si1 resonator frequency (blue colored lines) and the CTE (dotted red lines) on temperature. **Left panel:** measured dependence in the temperature region from 1.5 K to 3 K. **Right panel:** measured dependence in the temperature region from 1.5 K to 23.8 K. The inset in the right panel shows the frequency dependence around the CTE zero-crossing at 16.8 K. (Diagrams are reproduced from [68], see also Appendix F.1).

The frequency change Δf is directly connected with CTE as:

$$\frac{\Delta f}{f} = -\frac{\Delta L}{L} = -\alpha_{reson}\Delta T. \tag{8.2}$$

We determine the CTE of our resonator by slow cooldown of the setup with a Joule-Thomson stage and simultaneous measurement of the absolute optical frequency of the resonator using both the PDH lock and the linescan technique. The results of the CTE measurement with the PDH lock technique are presented in Fig. 8.7 (see Appendix F.1 for full publication).

The above results for the temperature region from 1.5 K to 3 K were verified four years later using the linescan technique. Two diagrams, presented in Fig. 8.8 (top row), display a temperature change of approximately 1.5 K accompanied by a change in frequency of approximately 2.5 kHz occurred over a time scale of two hours. These two data sets were joined and fitted with a polynomial function (see Fig. 8.8, middle panel). The result is:

$$f(T) = (35.7(1)T^4 - 28.6(1)T^5 + 3.70(1)T^6)\,\text{kHz},$$

with a fit error of the coefficients of less then 1%. Using this result and eq. 8.2 we can calculate α_{reson}:

$$\alpha_{reson} = -\frac{1}{f}\frac{\Delta f}{\Delta T}. \tag{8.3}$$

with a following result:

$$\alpha_{reson} = (-74.3(2)T^3 + 74.5(2)T^4 - 11.40(4)T^5) \times 10^{-14}\,\text{K}^{-1},$$

plotted in Fig. 8.8, middle panel. To evaluate fit quality we plot fit residuals in Fig. 8.8, lower panel. As can be seen, the distribution of fit residuals below 1.6 K is not symmetric. Therefore, the result presented above should be used with caution in this range. To improve the fit quality, we evaluate the range between 1.31 K and 1.6 K separately. The result of the fit, presented in Fig. 8.9 (top panel), is:

$$f(T) = (8.1(1.3) - 1.99(28)T^4)\,\text{kHz}.$$

The fit residuals are distributed evenly (see Fig. 8.9, middle panel). Thus, the CTE in this temperature region can be accurately described with:

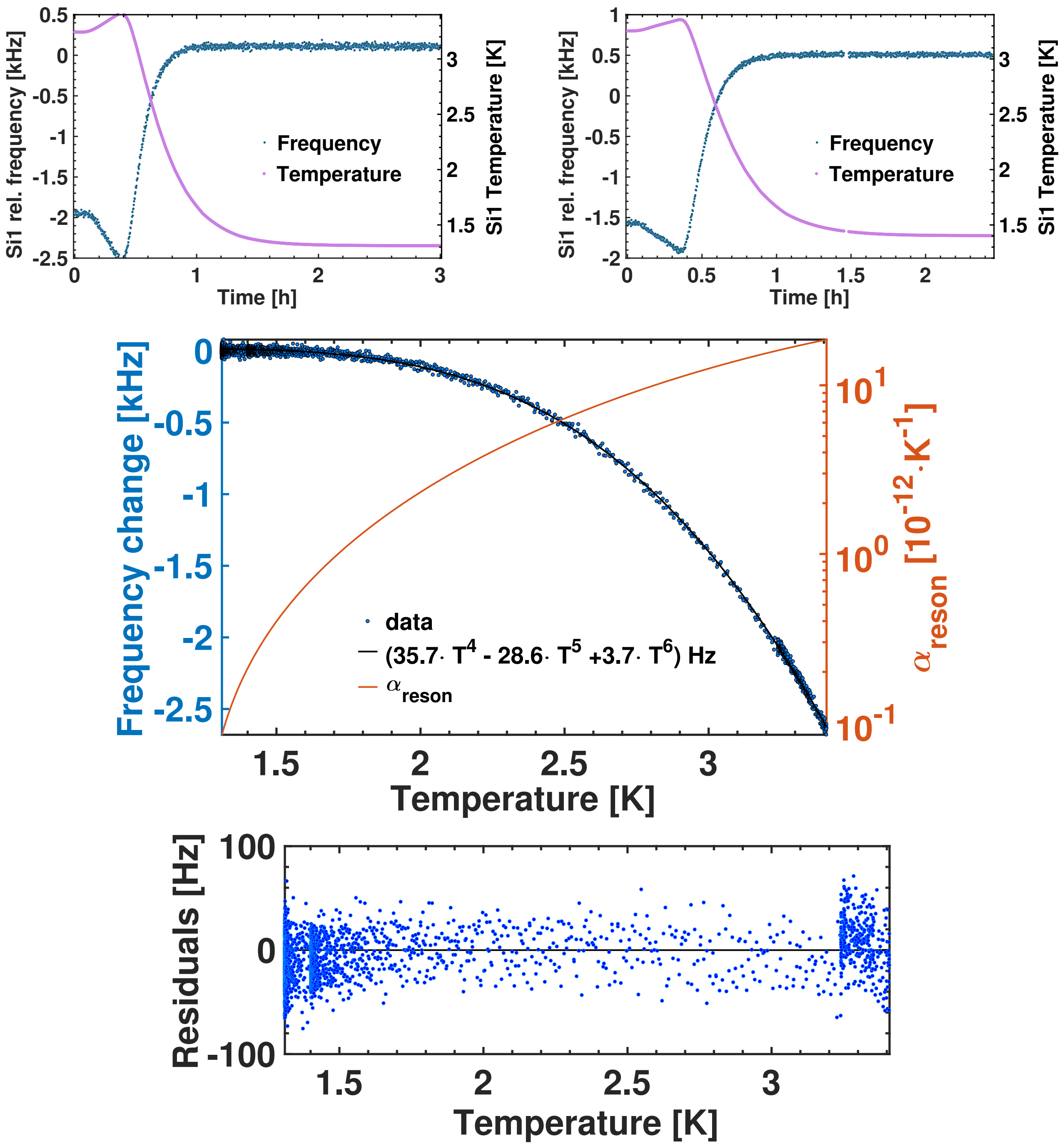

Figure 8.8: **Top row panels:** results of two measurements of the absolute optical frequency of the Si1 resonator with the linescan technique over a time scale of 2.5 h while cooling down the resonator from 3.4 K to 1.31 K **Middle panel:** to obtain the CTE of the resonator α_{reson} the two measurements from the top row panels were merged and fitted with a polynomial to obtain frequency dependence on temperature. **Bottom panel:** fit residuals of the fit in the middle panel.

$$\alpha_{reson} = 4.14(58) \times 10^{-14} T^3 \,\mathrm{K}^{-1}. \tag{8.4}$$

The CTE dependence on temperature in the region between 1.31 K and 1.6 K is presented in Fig. 8.9, lower panel.

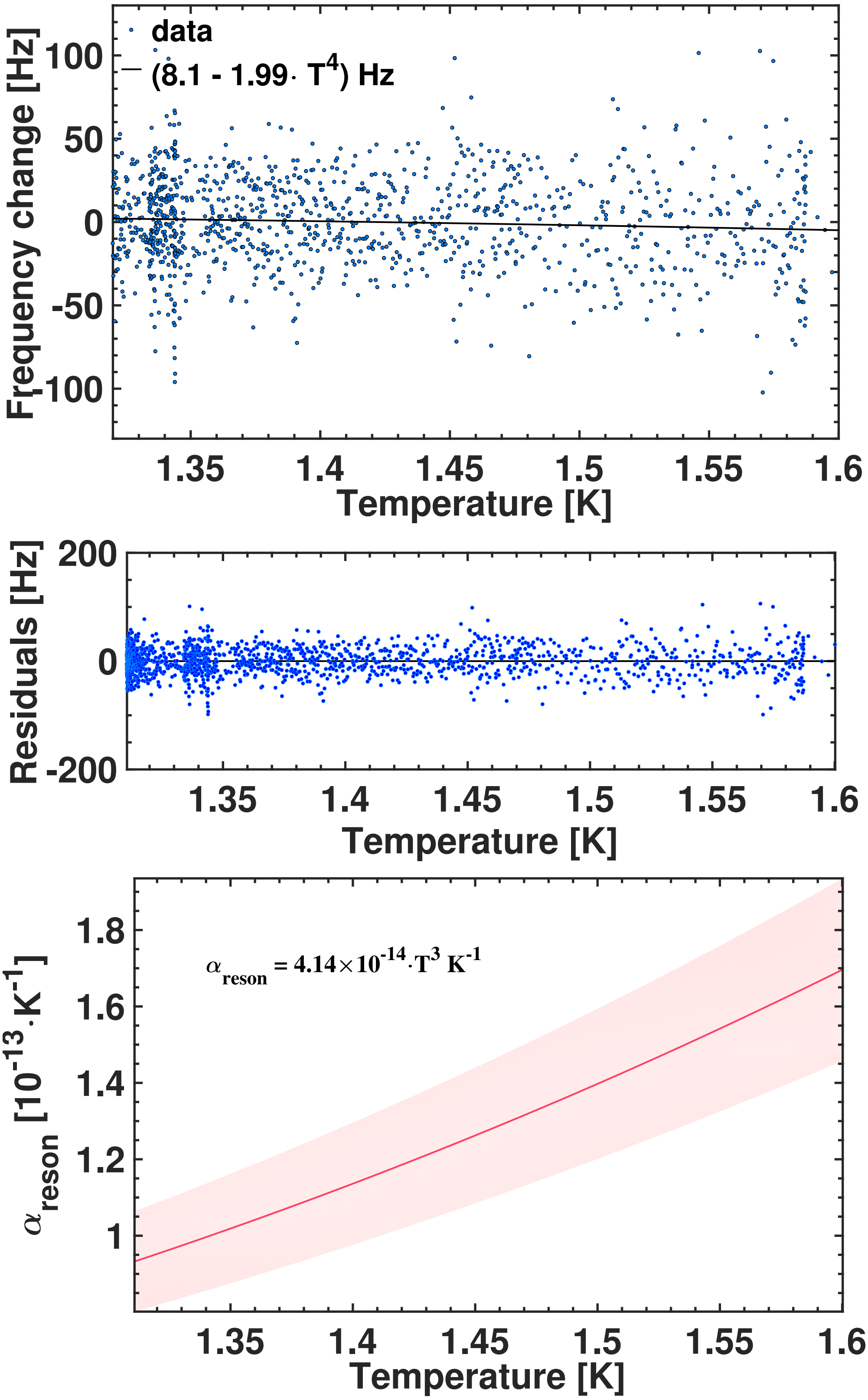

Figure 8.9: **Top panel:** joint evaluation and fitting of three separate measurements of the absolute optical frequency of the Si1 resonator dependence on temperature with the linescan technique for the temperature range between 1.31 K and 1.6 K. **Middle panel:** fit residuals. **Bottom panel:** the resulted CTE of the resonator α_{reson} dependence on temperature.

8.5 Sensitivity to circulating optical power

Fluctuations of the optical power of laser light impinging on and transmitted through the cavity introduce frequency fluctuations by changing the length of the resonator through heating generated by a change in absorption of optical power in the mirrors. We determined the resonator's sensitivity to optical power by scanning over its resonance line with laser light of optical power varying between 16 µW and 40 µW from scan to scan (see Fig. 8.10, upper panel). At the same time, absolute optical frequency of the resonator was determined. It is plotted together with the value of laser optical power for each scan in Fig. 8.10, middle panel. From these data, a distribution of frequency difference from scan to scan was obtained and plotted in Fig. 8.10, lower panel. This distribution was fitted with a Gaussian function. Resulted frequency variation is (-0.16 ± 16.04) Hz with a power variation of 24 µW or

$$\Delta f = (0.007 \pm 0.668)\,\mathrm{Hz}/\mu\mathrm{W},$$

$$\frac{\Delta f}{f} = (0.003 \pm 3.481) \times 10^{-15}/\mu\mathrm{W}.$$

This result is consistent with zero and provides an upper limit for optical power sensitivity.

Another possibility to evaluate the dependence on optical power is to look at the temperature fluctuations during the linescan measurement evaluated above. They are presented in Fig. 8.11. The amplitude of temperature variations is on the order of $\Delta T = 0.1$ mK for 24 µW variation in power, or $\Delta T = 4.2 \times 10^{-6}$ K/µW. Using eq. 8.4 we can obtain the amplitude of frequency variations. With $\alpha_{reson}(T = 1.4\,K) = 1.14 \times 10^{-13}/\mathrm{K}$ it is equal to:

$$\Delta f = 0.002\,\mathrm{Hz}/\mu\mathrm{W},$$

$$\frac{\Delta f}{f} = 1.14 \times 10^{-17}/\mu\mathrm{W}.$$

This result is much lower than the upper limit obtained from the direct evaluation of linescans.

8.6 Sensitivity to inclination of laser beam

Sensitivity to change of the position and angle of the light beam impinging on the front mirror of the resonator was studied by locking the laser to the resonator with the room-temperature PDH setup attached to the flanged window of the cryostat, changing the inclination of one of the mirror mounts in the setup and observing the change in frequency with the frequency comb. The circulating power was kept constant during this experiment. We obtain a sensitivity of 0.6 Hz/µrad to the influence of the laser beam inclination on laser frequency.

8.7 Measurement of the long term frequency drift

One of the expected advantages of silicon material compared to the ULE glass is the absence of the continuous length drift due to the perfect crystal structure with a minimum of defects. This should result in the absence of any frequency drift. To prove this, we have measured the frequency of the resonator continuously over the three years. The following is the update of our results, already published in Wiens

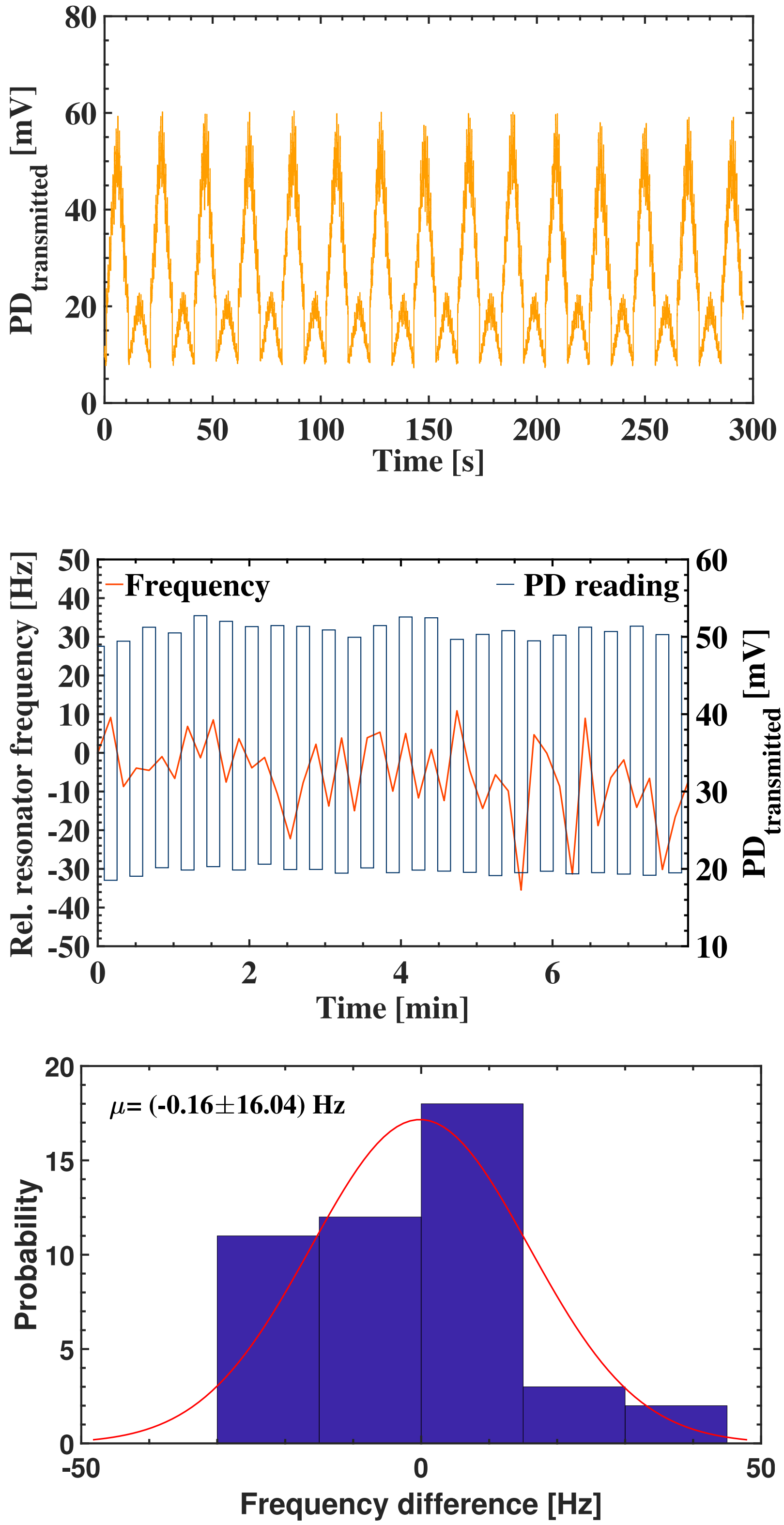

Figure 8.10: **Top panel:** determination of sensitivity to optical power using subsequent scans with different power of 16 μW and 40 μW by monitoring the amplitude of the photodiode in transmittance while measuring the absolute linescan frequency. **Middle panel:** both relative optical frequency of linescans and their amplitude, determined from the fit of the Lorentzian function to the photodiode data are plotted for overview. **Bottom panel:** the resulted distribution of frequency fluctuations due to fluctuations of power.

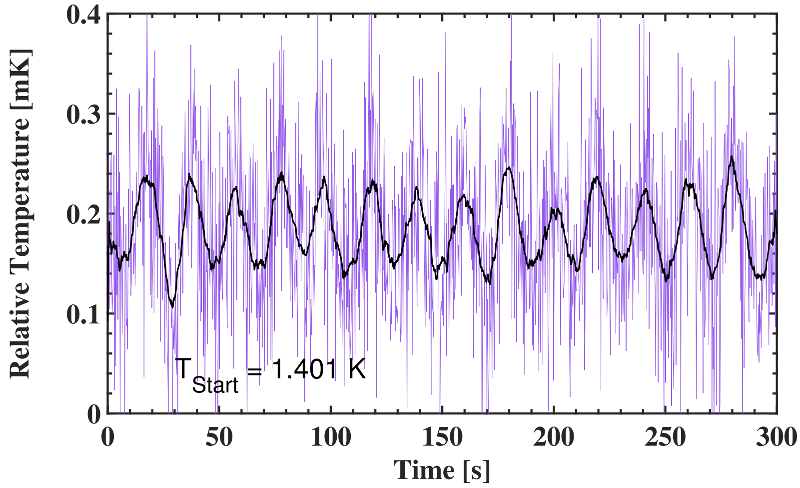

Figure 8.11: Relative temperature variation of the cryogenic resonator caused by scans of its resonance line with a laser light of different optical power. Temperature at the beginning of the experiment was $T_{Start} = 1.401$ K. Temperature drift of $0.6\,\mu$K/s was subtracted from the data before plotting.

et al. [35] (see also Appendix F.2 below). Initially, the PDH lock technique was applied, however, due to the problems connected to this technique (see Sec 7.3) we changed to the linescan technique after 250 days of the experiment. The complete data set is presented in Fig. 8.13. The total frequency change is over 80 kHz. However, most of it is due to frequency jumps triggered by spontaneous relaxation effects, temperature rise, or deliberate bumping of the cryostat. (see points $J_1..J_6$ in Fig. 8.13). After removal of their contribution, we obtain a frequency change of 8.5 kHz or 4.4×10^{-11}/s (see Fig. 8.13, middle panel). The strongest change occurred in the first 250 days of the experiment. As can be seen in Fig. 8.13, bottom panel, this relaxation displays an exponential behavior and is best fitted with a double exponential with the following relaxation times $[\tau_1; \tau_2] = [3.3; 81.8]$ days.

Within the presented measurement we identify the two most stable data sets with a duration of approximately half a year each. They are between the days [257, 420] and [618, 793] and have a measured fractional frequency drift of $(-1.6 \pm 3.8) \times 10^{-21}$/s and $(12.6 \pm 3.2) \times 10^{-21}$/s, respectively. After correction for the slightly time-dependent frequency drift of the H-maser, measured relative to the atomic time of the GPS signal and equal to 7.5×10^{-21}/s, we obtain a fractional frequency drift of $(5.9 \pm 3.8) \times 10^{-21}$/s and $(20.1 \pm 3.2) \times 10^{-21}$/s (with 1σ error) for the two data sets in Fig. 8.14. These are the lowest frequency drifts measured with an optical resonator to date. An upper value of the

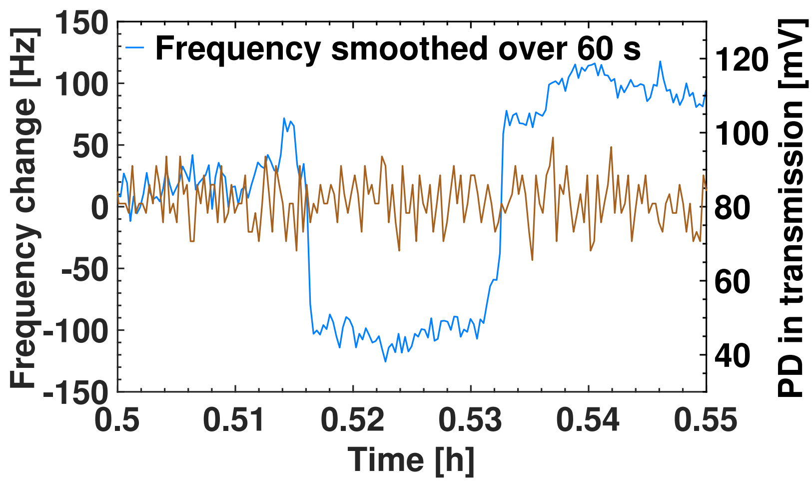

Figure 8.12: Observed frequency change (light blue) after tilting the mirror in the PDH stabilization setup by 250 µrad at time 0.515 h followed by a tilt in the opposite direction by the same angle at time 0.532 h. Power transmitted through the resonator (braun line) was kept constant during the experiment.

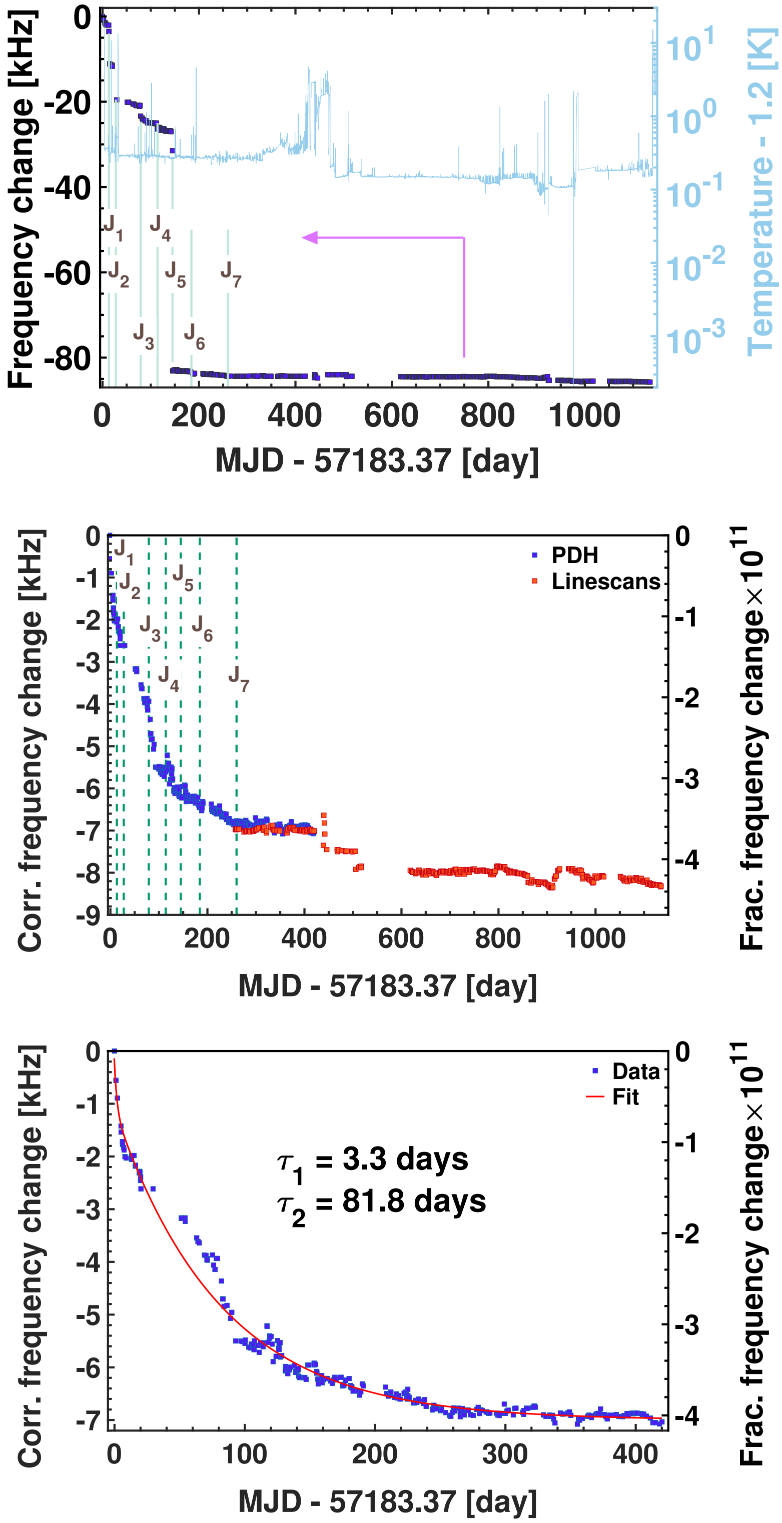

Figure 8.13: **Top panel:** measured change of frequency and temperature of the resonator. **Middle panel:** corrected frequency change after removal of frequency jumps J_1..J_6. Point J_7 marks the introduction of the linescan technique. **Bottom panel:** double exponential fit of the first 400 days.

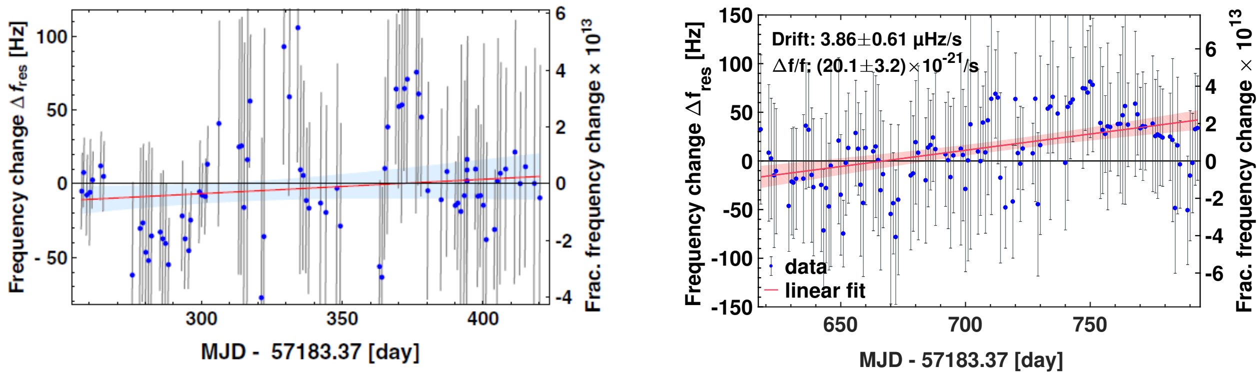

Figure 8.14: Two data sets with the most stable optical frequency of the resonator after correction for maser drift. Left panel is reproduced from [35].

first data set, 1.4×10^{-20}/s (with a conservative 2σ error), corresponds to an absolute length change (expansion) of our resonator being equal to 0.35×10^{-20}m/s. At this rate, it takes almost three days for the resonator to expand over the size of a proton.

8.8 Summary of systematic effects

To estimate the frequency stability that can be reached with our resonator we summarized the influence of all systematic effects in Table 4, described their influence in terms of frequency instability, and added them up. We plot this estimation together with the measurement limited by the maser in Fig. 8.15. Our result suggests, that our resonator can reach fractional frequency instability of 5.5×10^{-16} at one second time scale. The dominant effect, that limits the performance at this time scale is the tilt instability followed by the instability of the circulating optical power. Both contributions decrease with increasing integration times. At the integration time of 1000 s the lowest value of frequency instability is reached, 0.72×10^{-16}. With further increasing integration time, the influence of the drift becomes the dominant effect, and the fractional frequency instability increases to 2.1×10^{-16}. The constant drift of the resonator can be easily corrected. Thus, we can subtract this contribution from our estimation of frequency instability. We obtain 0.58×10^{-16} as the lowest frequency instability calculated for 1000 s integration time. This is equivalent to the absolute frequency instability of 10 mHz. At an integration time of 10 000 s we obtain a slightly higher value, 0.73×10^{-16} .

Table 4 summarizes all systematic effects without vibrations, which however play an enormous role at short times. To evaluate their influence, a beat between two identical resonators Si1 and Si2, operated inside the Leiden Cryogenics cryostat was recorded with a spectrum analyzer (SignalHound, bandwidth of 240 kHz). As can be seen from Fig. 8.16, left panel, the signal is highly disturbed by the presence of cryostat vibrations at 140 Hz. The corresponding modified Allan deviation (see Fig. 8.16, right panel) starts at 20 kHz at 4 μs integration time and averages down to approx. 20 Hz at 0.4 s. This reflects the high vibration sensitivity of the resonator and large accelerations produced by the operation of the cryostat. Thus, to improve the short-term stability we must either design a new resonator with low sensitivity to vibrations or decouple the experimental setup inside the cryostat using passive or active vibration isolation. These two possibilities are discussed in the following chapters.

Table 4: Summary of all measured or calculated systematic effects and their combined contribution to the frequency instability of the 25 cm silicon resonator.

Effect	**Sensitivity**	**Frequency instability $\Delta f/f\,(10^{-16})$**				
		10^0 s	10^1 s	10^2 s	10^3 s	10^4 s
Tilt $\parallel$ to Si1	48 mHz/µrad	3.8	1.8	1.0	0.42	0.57
Tilt $\perp$ to Si1	3 mHz/µrad	0.32	0.1	0.04	0.02	0.03
Temperature	1.6×10^{-13}/K	0.09	0.05	0.02	0.008	0.005
Circulating optical power	0.675 Hz/µW	1.2	0.3	0.1	0.07	0.07
Drift	2.7 µHz/s	1.4×10^{-4}	1.4×10^{-3}	0.014	0.14	1.4
Thermal noise		0.06	0.06	0.06	0.06	0.06
Total		**5.5**	**2.3**	**1.2**	**0.72**	**2.1**
Total without drift		**5.5**	**2.3**	**1.2**	**0.58**	**0.73**

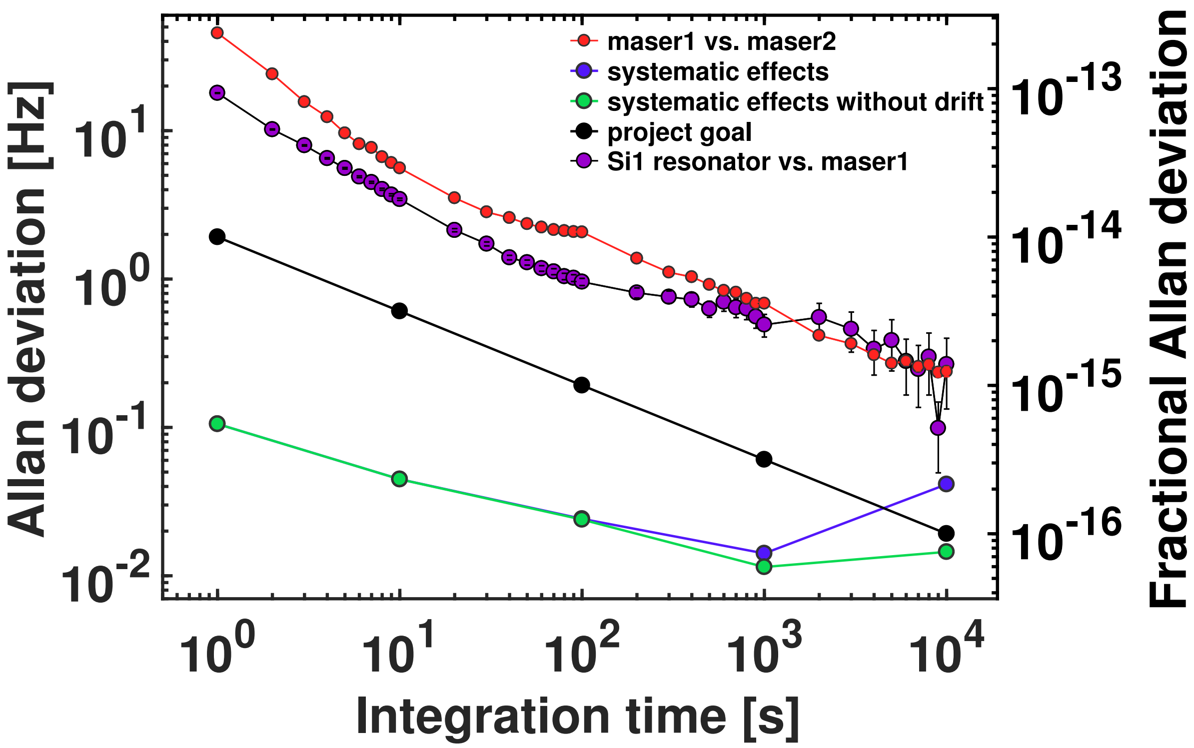

Figure 8.15: Measured frequency instability of the silicon resonator together with the estimation of the summed contributions of all measured and calculated systematic effects and project requirements.

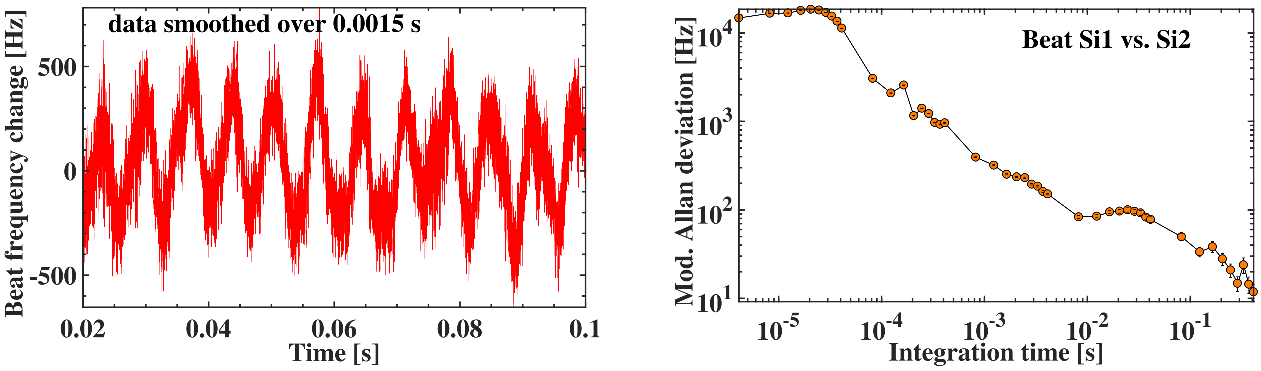

Figure 8.16: Beat frequency between two identical resonators Si1 and Si2 operated inside Leiden Cryogenics cryostat. **Left panel:** smoothed time trace. **Right panel:** corresponding mod. Allan deviation.

9 A 5 cm vertical resonator - summary of properties

As seen from the results presented above, the 25 cm long silicon resonator could reach the instability of a maser for all integration times up to 10 000 s and displayed an impressively low long-term frequency drift of less than 1.4×10^{-20}/s. However, due to the presence of strong vibrations produced by the pulse-tube of the cryostat coupled with the low vibration sensitivity of the resonator on the order of $1 \times 10^{-8}/g$, the short-term frequency stability is highly degraded (see Fig. 8.16). To resolve this issue we decided to build a new resonator, designed for low sensitivity to vibrations. The design process started with a conical shape, which has already proved to provide low vibration sensitivity for vertically oriented silicon resonators operated at cryogenic temperatures [66, 67, 70, 71]. We further simplified the design using FEM simulations to reduce the shape complexity and improve manufacturing efficiency. The so designed spacer has a length of 5 cm and is oriented with the optical axis along the [111] crystallographic direction of silicon (see Fig. 9.1, left panel). After optical contacting of the mirror substrates and integration of the resonator inside the Leiden Cryogenics cryostat with an all-cryogenic optical setup for incoupling of laser light (see Fig. 9.1, right panel), we obtained a linewidth of 24.2 kHz for the TEM_{00} optical mode. This corresponds to a resonator finesse of 120 000.

After the cooldown to 1.5 K the sensitivity of the resonator to various environmental parameters was characterized and its short- and long-term frequency stability was measured. The results are thoroughly described in Appendix F.4. In the following, we summarize only key results. As we used the same procedures and techniques as in the case of the 25 cm horizontal resonator, we avoid the repetition of their description.

Sensitivity to vibrations: Sensitivity to vibrations was determined using the inherent vibrations of the cryostat (compare Sec. 8.2). The mean sensitivity along the three directions in the frequency range $[1, 200]$ Hz is equal to 133 kHz/g or $6.9 \times 10^{-10}/g$ in fractional terms (see Fig. 9.2, a). This is comparable to the sensitivity of another vertically-oriented silicon resonator operated at 4 K [71] and represents a factor 14 improvement compared to the sensitivity of the 25 cm long Si1 resonator.

Sensitivity to temperature: We measured the coefficient of thermal expansion of the resonator α_{res} in the temperature range from 1.5 K to 22 K using the procedure described in Sec. 8.4 and Appendix F.1. The results are presented in Fig. 9.2, b,c. We observe a zero crossing of the α_{res} with a derivative of

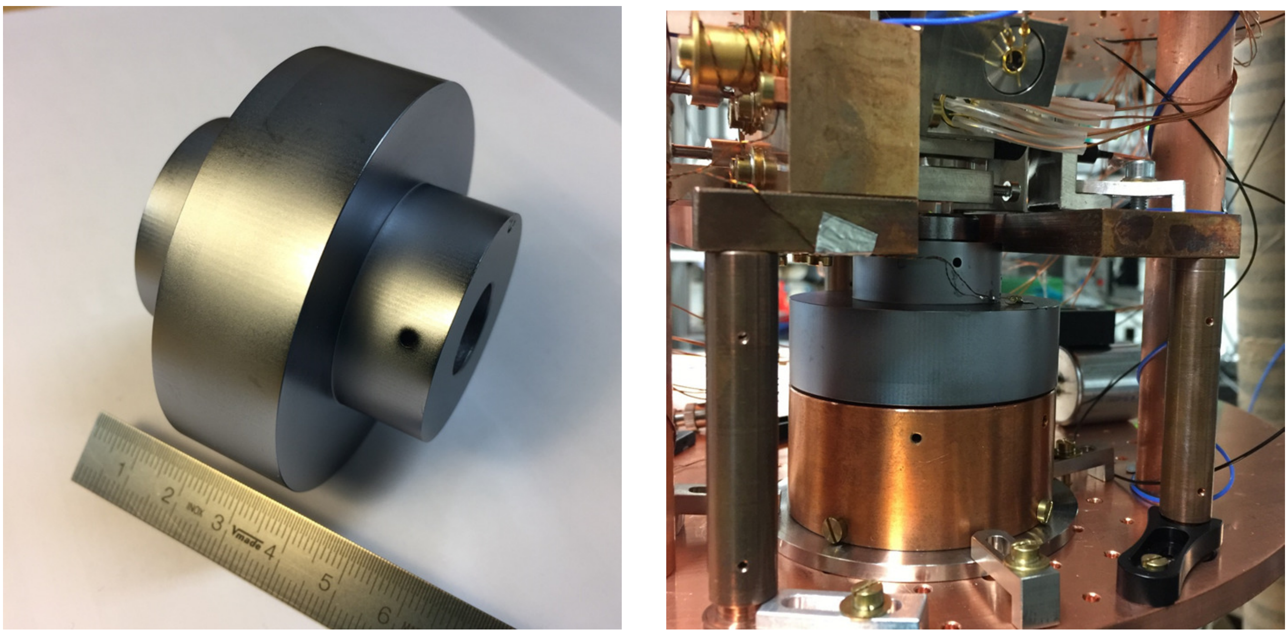

Figure 9.1: **Left panel:** spacer of the 5 cm vertical resonator before optical contacting of the mirror substrates. **Right panel:** resonator installed inside Leiden Cryogenics cryostat.

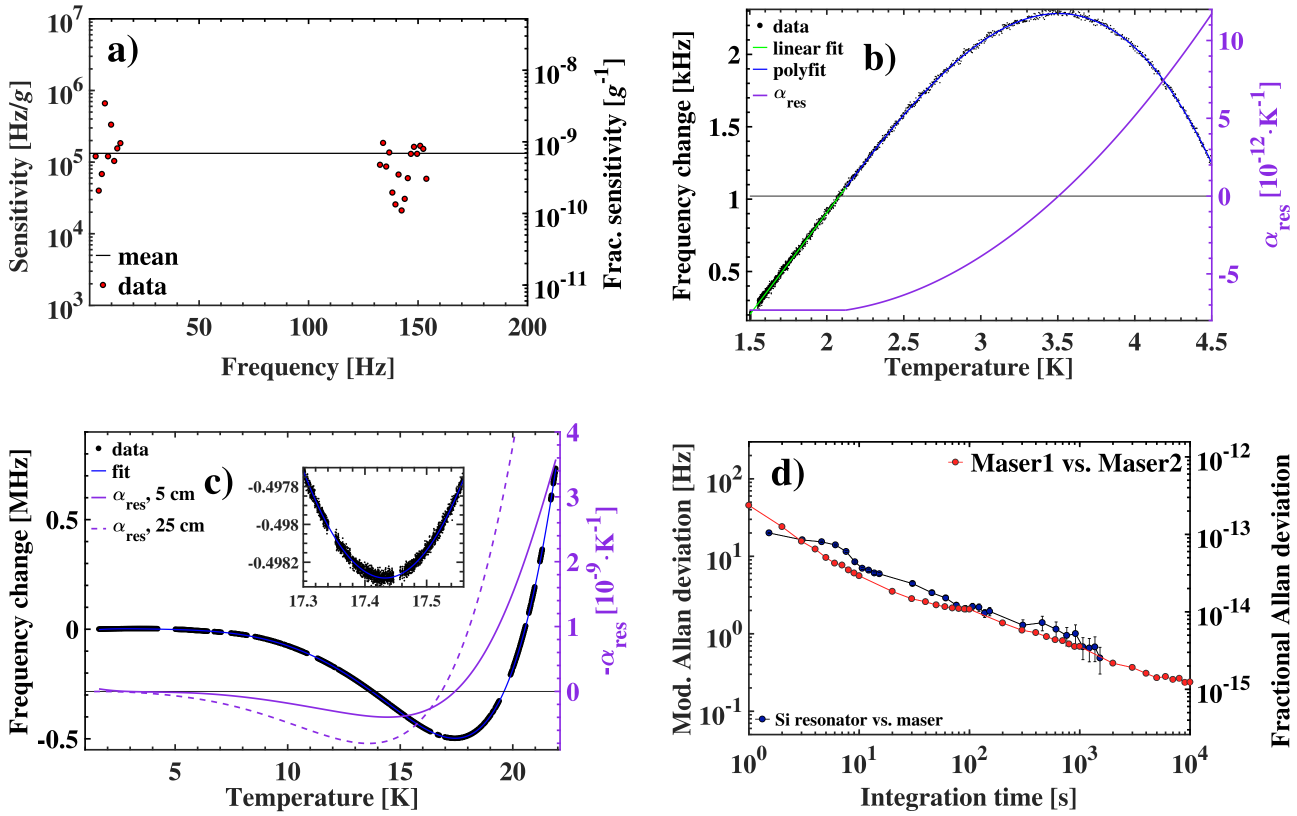

Figure 9.2: Selected properties of the 5 cm Si5 resonator: **a)** Sensitivity to vibrations at different frequencies; **b)** Sensitivity to temperature in the temperature range from 1.5 K to 4.5 K and **c)** in the temperature range from 1.5 K to 22 K. The dashed line represents the results of the 25 cm long Si1 resonator; **d)** Frequency stability measured relative to the hydrogen maser. (All diagrams are reproduced from [88])

$d\alpha_{res}/dT = 8.5 \times 10^{-12}/\mathrm{K}^2$ at the temperature of 3.5 K with a negative α_{res} below this temperature. In the low-temperature region from1.5 K to 2.2 K we observe a constant $\alpha_{res} = -7 \times 10^{-12}$/K. Both results are inconsistent with the results obtained for the 25 cm resonator and are subject to further studies. The behavior of the α_{res} in the extended temperature region from 1.5 K to 22 K is displayed in Fig. 9.2, c, where we compare them with the α_{res} of the 25 cm resonator. The total change of the α_{res} in this region is smaller when compared with the α_{res} of the 25 cm resonator. The second zero crossing was found to be at 17.4 K, a 0.6 K shift when compared to the temperature of the second zero crossing of the 25 cm resonator at 16.8 K. The discrepancies between both resonators may be due to the differences in the resonator suspension inside the frame or different properties of the silicon material.

Short-term frequency stability: Short-term frequency stability of the resonator was measured relative to the hydrogen maser. Fig. 9.2, d depicts the instability for the integration times up to 1000 s, which closely follows the instability of the hydrogen maser with the lowest value of 2×10^{-15} at 1000 s. We expect this number to decrease for a resonator properly isolated from the vibrations of the pulse tube.

Long-term frequency stability: Long-term frequency stability of the resonator was found to depend strongly on the laser light power and interrogation time: As can be seen Fig. 9.3 we monitored the frequency of the resonator and performed simultaneous stepwise reduction of the laser light power, measured before incoupling of the light into the cryogenic fiber, from the initial 550 nW to 100 nW at the end of the experiment. At the same time we observed an almost hundredfold reduction of the frequency drift from $-462(18)$ µHz/s to $-49(4)$ µHz/s. The mean duty cycle was at the level of 30% during the measurement. Our results confirm the previously published results of power-modified frequency drift [71] and allow to null the long-term frequency drift of the resonator by careful adjustment of the laser light power used for interrogation of the resonator.

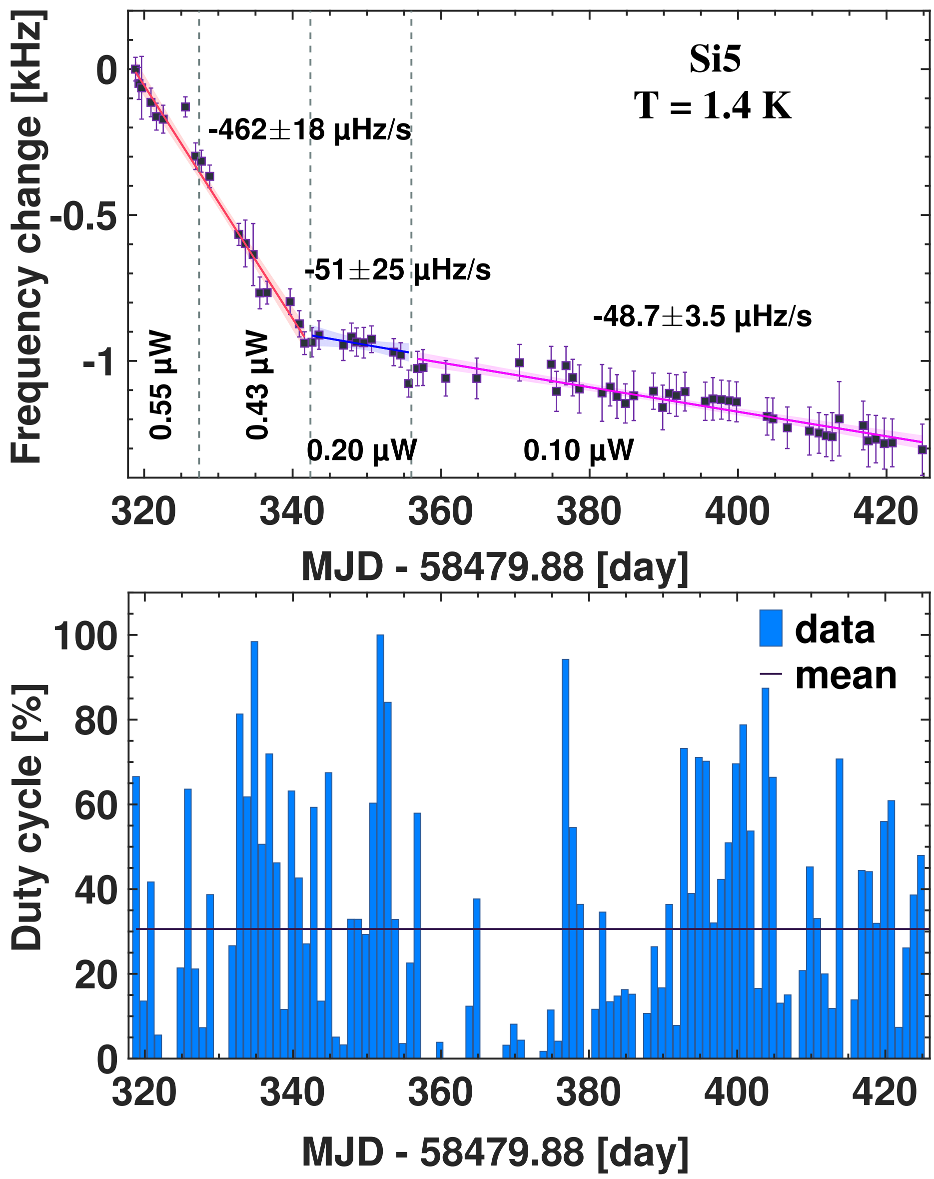

Figure 9.3: **Top panel:** long-term frequency stability of the resonator as function of the laser light power. **Bottom panel:** corresponding duty cycle. (All diagrams are reproduced from [88])

10 A 19 cm vertical resonator

With our vertical 5 cm resonator we have already done the first step towards the reduction of vibration sensitivity. With this resonator we could test the in-house optical contacting procedures and evaluate the optical bonding response to thermal cycling. Meanwhile, the resonator successfully survived three thermal cycles, thus proving the high quality of the optical contacts. While designed for low sensitivity to vibrations, this resonator has a relatively low finesse and correspondingly large linewidth, which makes it difficult to achieve very low frequency instabilities. Further progress in this direction would require a resonator with a longer spacer and high finesse mirrors.

Based on our experience with the 5 cm resonator we built two vertical biconically-shaped resonators with a length of 190 mm and 212 mm. The design of these resonators resembles that of a 212 mm silicon resonator operated by the PTB [66]. We expect both resonators to possess an equivalent sensitivity to vibrations equal to $< 1 \times 10^{-10}/g$ [66] for horizontal accelerations and $< 1 \times 10^{-11}/g$ for vertically projected accelerations [69]. Both resonators are already built and optically contacted with high-finesse mirrors. They are currently installed and operated inside the Leiden Cryogenics cryostat with an installed passive vibration isolation (see Fig. 10.1), which is discussed in the next section.

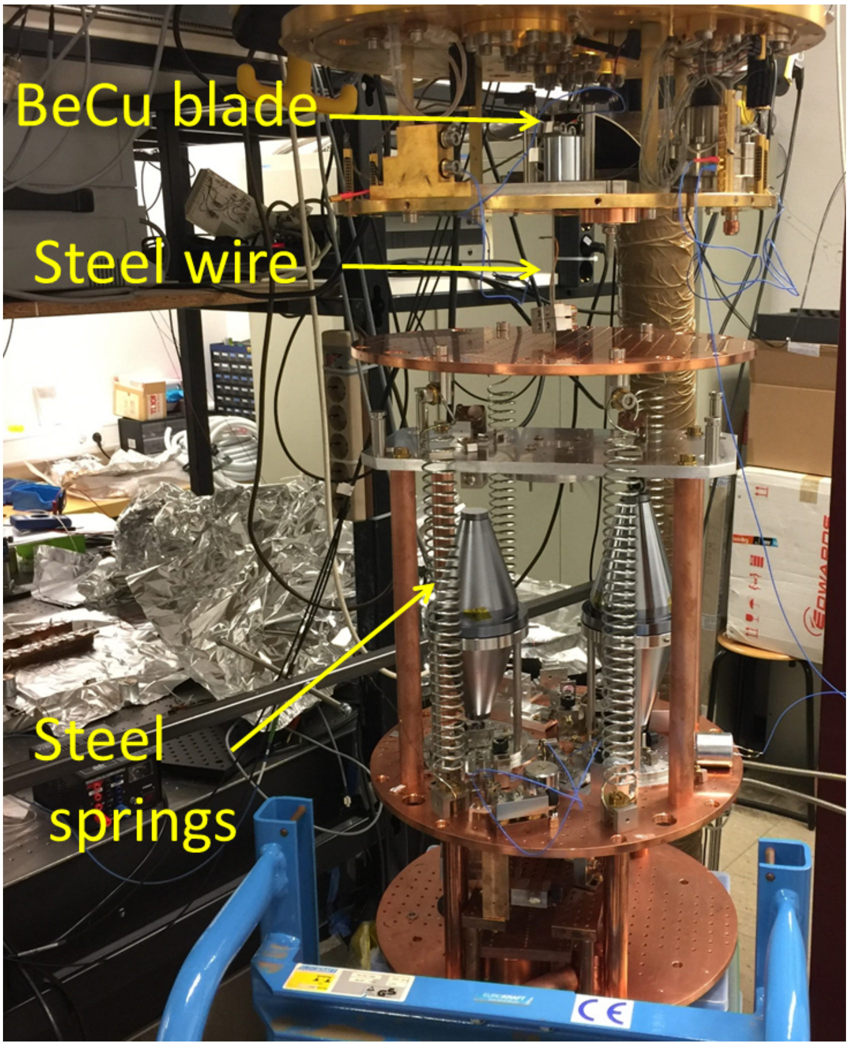

Figure 10.1: Installation of the 212 mm and 190 mm long silicon resonators inside our Leiden Cryogenics cryostat equipped with two stages of passive vibration isolation.

10.1 Passive damping of cryostat vibrations

In parallel with the development of low-vibration-sensitivity resonators, a passive isolation of the experimental payload from the pulse-tube generated vibrations was installed. Passive vibration isolation in cryostats using springs was already successfully demonstrated [89, 90, 91, 92]. This approach is facilitated inside our cryostat using two stages of damping: a home-built BeCu blade spring designed for 2.5 Hz resonance frequency (see Appendix C for detailed description) with the 30 kg payload attached to it via a steel wire and a set of four steel springs with an extended length of 370 mm and a resonance frequency of 1 Hz (see Fig. 10.1). The horizontal resonance frequency is defined by the total length of the suspension of 590 mm and is equal to 0.65 Hz.

The vibration spectrum along the two and three spatial directions, measured with two sets of cryogenic geophones attached to the cold plate and experimental plate of the cryostat, respectively, and calibrated at room temperature, is presented in Fig. 10.2. We observe a good reduction of vibrations above 5 Hz. The cumulative acceleration was reduced from 25 mg. for the cold stage of the cryostat to 0.12 mg measured at the experimental plate (see Fig. 10.2, right panels). This represents a factor 200 of reduction. When compared to the accelerations measured during the previous cooldown with Si1 and Si5 resonators the reduction factor is equal to 40 (see Fig. 3.12). This is due to the large mass of the previous setup acting as a damper. (see Fig. 3.12).

From the Fig. 10.2, bottom left panel, we can see, that the resonance frequency of the four steel springs and the BeCu blade increased from 1 Hz to 1.33 Hz and from 2.5 Hz to 2.7 Hz, respectively due to the improvement in the strength of the materials and their thermal contraction upon the cooldown.

10.2 Cryogenic fiber noise cancellation

The optical setup of the resonator was upgraded with a partially reflective mirror installed at the output of the cryogenic optical fiber with a length of 5 m and with a corresponding optical setup at the room temperature end of the fiber to allow for active cancellation of frequency noise generated in the fiber by mechanical stress due to cryostat vibrations using a technique described in [87]. The linewidth broadening of the laser light after a double pass through the fiber is presented in Fig. 10.3, left panel, where the beat with the unperturbed laser wave is shown. The broadening is estimated to be ~ 50 Hz and is completely eliminated by the active noise suppression setup (see Fig. 10.3, right panel)

10.3 Summary of the resonator properties

The sensitivity of the resonator to some environmental parameters was characterized and its short- and long-term frequency stability was measured. In the following, we present only results that were available at the time of writing this work. Again, we use the same procedures and techniques here as in the case of the 25 cm horizontal resonator and the 5 cm vertical resonator.

Linewidth: After the cooldown of the resonator to 1.5 K the resonator linewidth was determined to be 3.5 kHz. This corresponds to a finesse of 225 408.

Sensitivity to temperature: The coefficient of thermal expansion of the resonator α_{res} was measured in the temperature range from 1.7 K to 4.2 K using the procedure described in Sec. 8.4 and Appendix F.1. The result is presented in Fig. 10.4. The behavior of the α_{res} can be described by: $\alpha_{res} = (-2.04T^5 + 18.6T^4 - 4.92T^3) \times 10^{-14}$/K. As can be seen, it is comparable to that of Si1.

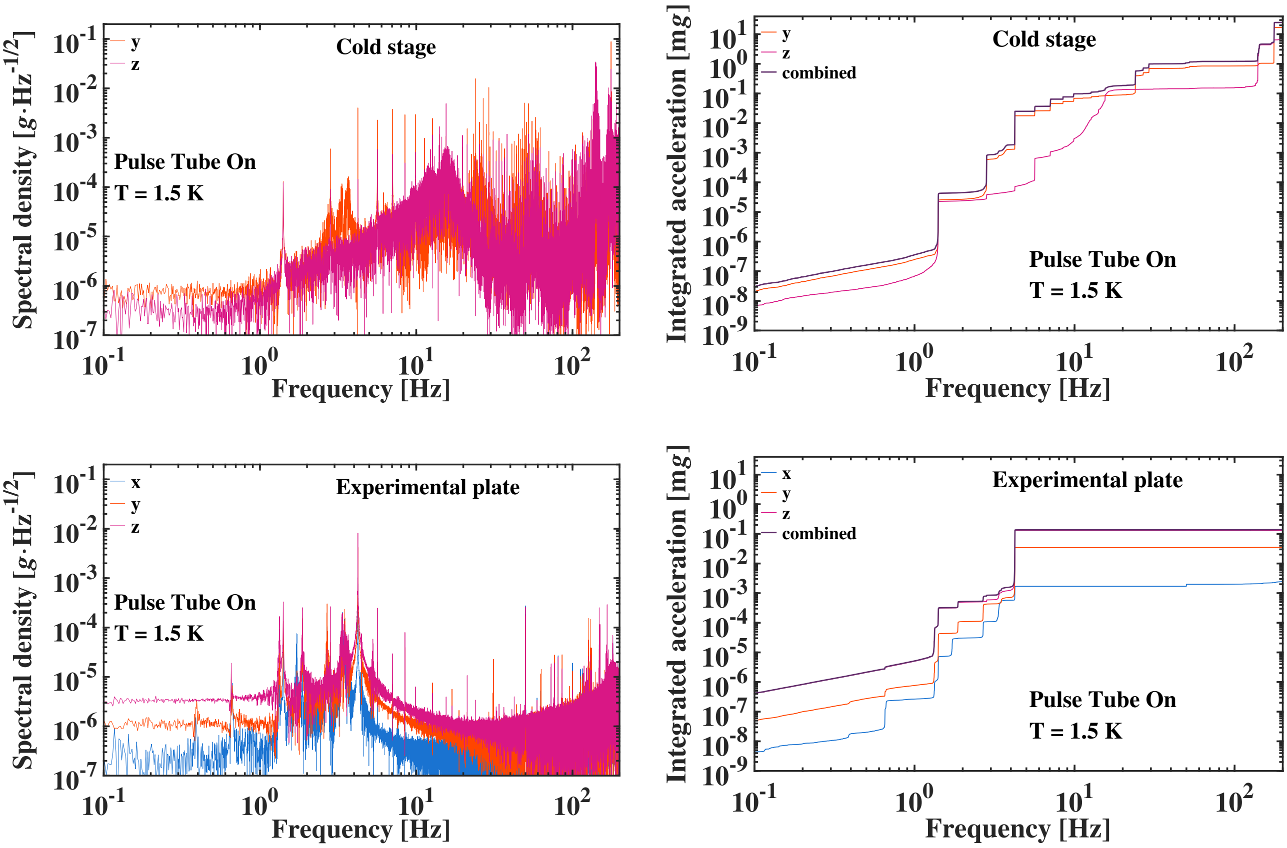

Figure 10.2: Vibrations at the Joule-Thomson cold stage and at the experimental plate of the cryostat measured with cryogenic geophones at $T = 1.5$ K. **Left panels:** spectral density. **Right panels:** the cumulative acceleration along three orthogonal directions. One of the horizontal geophones attached to the cold stage failed to operate at cryogenic temperatures. The calculate the combined integrated acceleration in the upper right panel we used twice the data of the second horizontal geophone.

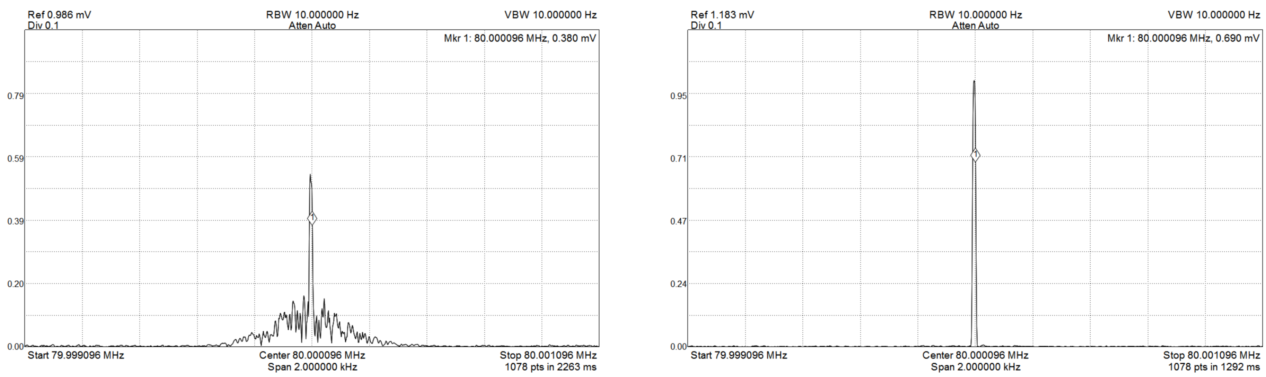

Figure 10.3: Linewidth broadening of the laser wave after a double passage through the cryogenic optical fiber and beat with the unperturbed laser wave with an active noise suppression switched off (left) and on (right).

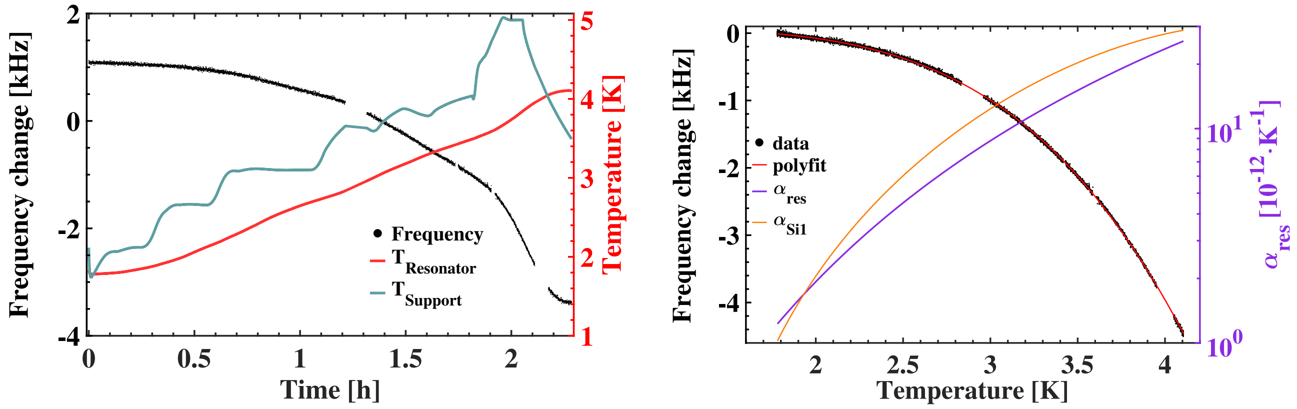

Figure 10.4: Sensitivity of the Si190 resonator to temperature in the range from 1.7 K to 4.2 K. **Left panel:** raw data. **Right panel:** extracted frequency (left y-axis) and coefficient of thermal expansion (right y-axis) dependence on temperature. Orange line represent the CTE of Si1 taken from [68].

Sensitivity to vibrations: Frequency-dependent sensitivity was determined using the procedure described in [93] (see Appendix F.4, Sec. 8.2, and Sec. 9). We recorded time traces of the photodiode signal in transmission by parking the laser light at resonance and at the half-maximum of the resonance line (see. Fig. 10.5, upper left panel). After subtraction of the spectrum taken with the laser tuned to the resonance from the spectrum at half-maximum and application of a conversion factor S = 0.53 a.u./kHz (slope of the transmission signal at the half-maximum value) we obtain a spectrum with the amplitude in Hertz (see. Fig. 10.5, upper right panel). Applying a cumulative summation of this spectrum we obtain a contribution of vibration to the broadening of the transmission line, 60 Hz. As can be seen from Fig. 10.5, bottom left panel, the largest contribution is observed in the low-frequency band below 5 Hz, where the damping of vibrations is not effective. To obtain the frequency-dependent sensitivity of the resonator to vibrations we must compare the spectrum from Fig. 10.5, upper right panel with the acceleration spectrum. Due to the problem with the calibration of geophones at cryogenic temperatures described in the previous section we used an interferometric sensor (IDS3010, Attocube) to obtain the spectrum of vibrations in vertical and in one horizontal directions. For this, we used a set of two mirrors installed for this purpose at the experimental plate inside the cryostat. As the sensor was mounted next to the cryostat windows at a separate platform with no active or passive vibration isolation we use only low-frequency data at 1.4 Hz and 4.2 Hz, operational frequency of the cryostat and the third harmonic, respectively (red marked in Fig. 10.5, upper right panel). The result is presented in Fig. 10.5, bottom right panel. We obtain a sensitivity of 11 kHz/g and 28 kHz/g with a mean of 20 kHz/g or $1 \times 10^{-10}/g$ in fractional terms. This is a factor 7 less than the sensitivity of the Si5 resonator and a factor 100 below the sensitivity of Si1.

Short-term frequency stability: Short-term frequency stability of the resonator was measured relative to the hydrogen maser. As can be seen in Fig. 10.6 the instability follows the instability of the hydrogen maser with the lowest value slightly below the 2×10^{-15} at integration time above 1000 s.

Long-term frequency stability: Long-term frequency stability was measured relative to the hydrogen maser from the start of the experiment. Initially, the drift was measured to be -3.5 mHz/s. However, starting on day 76 after the end of the cooldown the measured drift is not more than $-0.9(1.3)$ µHz/s. This corresponds to the fractional frequency drift of 11.4×10^{-21}/s (see Fig. 10.7).

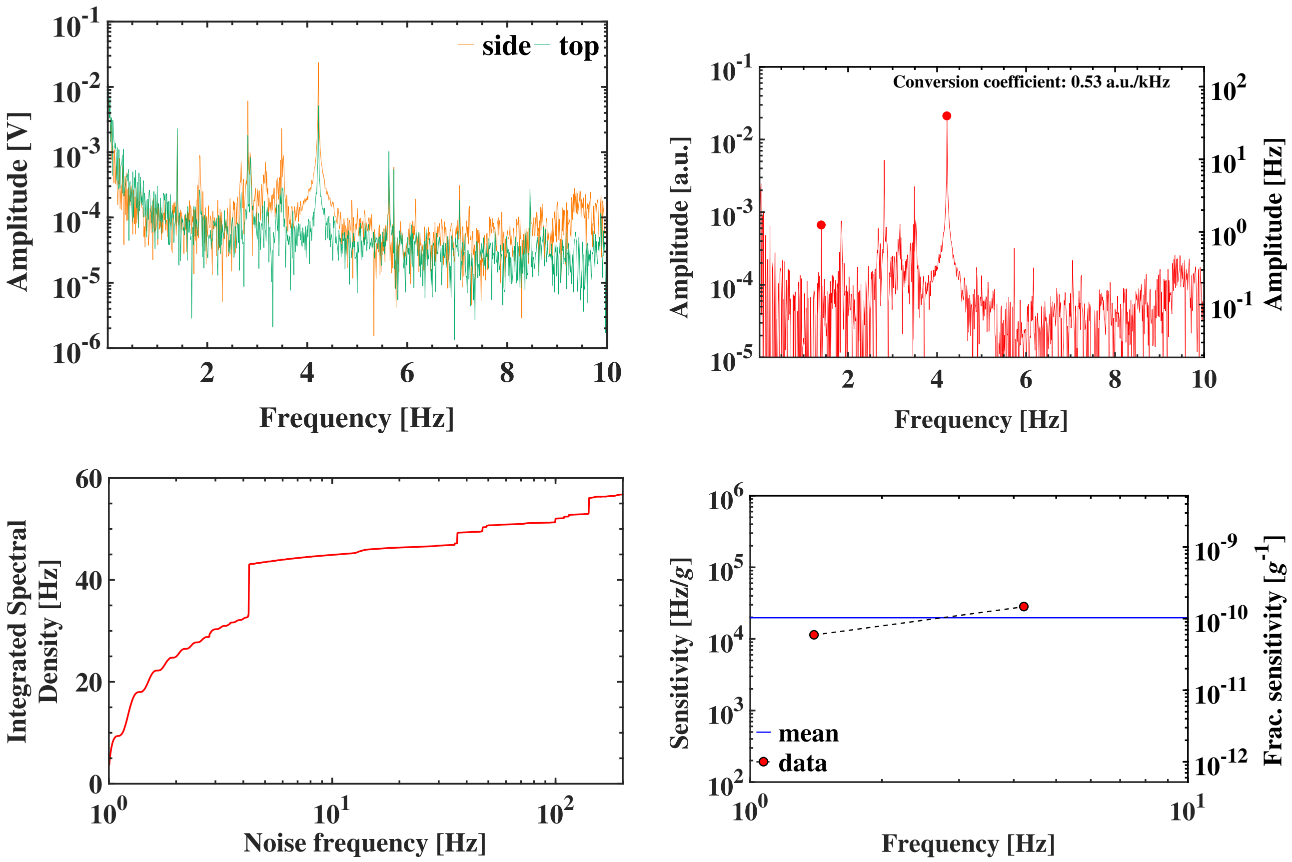

Figure 10.5: Determination of the Si190 resonator sensitivity to vibrations. **Upper left panel:** Spectra of time traces of the resonator transmission signal measured with the laser frequency tuned to the half-transmission of the resonance (orange) and on-resonance (green). The green time trace includes a factor of 1/2 to account for the larger transmitted power. **Upper right panel:** Spectrum calculated by subtraction of the spectrum taken with the laser tuned to the resonance from the spectrum at half-maximum. Right y-axis gives the frequency fluctuation level after applying the conversion factor S = 0.53 a.u./kHz (slope of the transmission signal at the half-maximum value). **Bottom left panel:** Contribution to the linewidth from vibrations in the frequency region from 1 Hz to 200 Hz. **Bottom right panel:** Sensitivity of the resonator to vibrations at 1.4 Hz and at 2.8 Hz obtained by division of the spectrum from upper right panel by the spectrum of cryostat accelerations defined as root sum-of-squares of the three individual accelerations. The black line indicates the mean of the two data points.

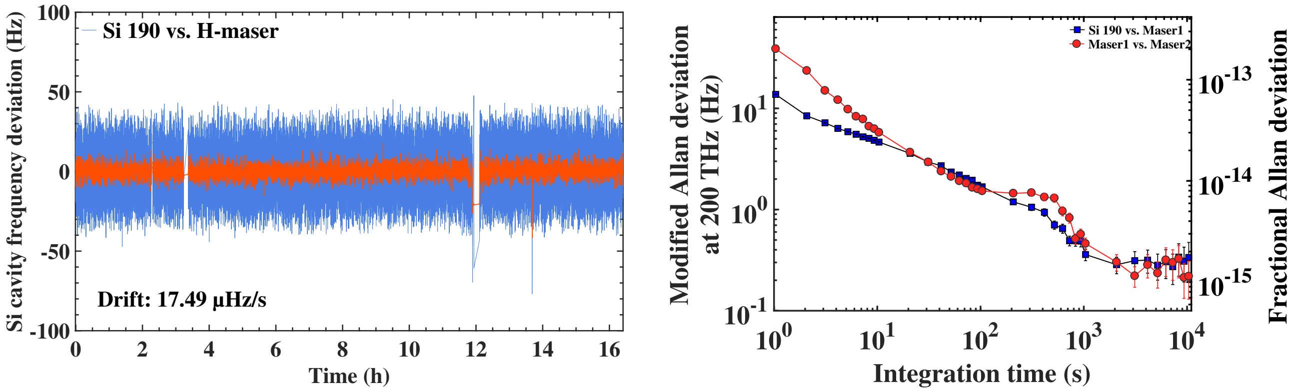

Figure 10.6: Si190 frequency stability measured relative to the hydrogen maser. **Left panel:** raw data. **Right panel:** modified Allan deviation in absolute (left y-axis) and in fractional terms (right y-axis).

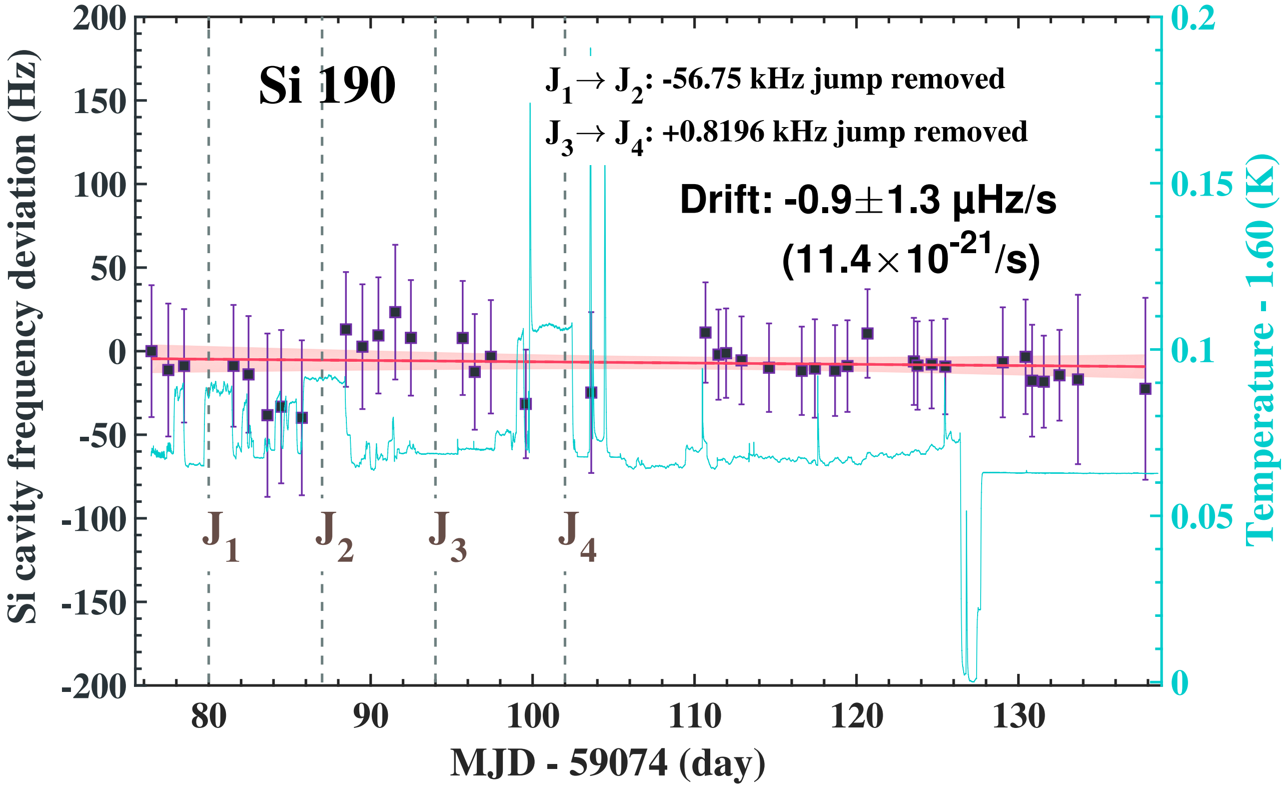

Figure 10.7: Si190 long-term frequency drift measured over two months relative to the hydrogen maser.

11 Summary

The goals of this work were to develop mono-crystalline silicon resonators designed for low-vibration sensitivity, equip them with high-finesse mirrors, and operate them in the deep cryogenic regime at 1.5 K. Their suitability for the next generation of high-stability frequency sources with possible implementation as reference clocks for navigation of deep-space probes with a required residual frequency instability of $1 \times 10^{-14}/\sqrt{\tau}$ on time scales $\tau \leqslant 10\,000$ s (ESA funded project) was evaluated. Further reduction of their instabilities down to 5×10^{-17} at integration times τ between 100 s and 10 000 s (DFG funded project) was achieved with the Si190 resonator. In the following, the summary of all three resonators is presented

First, we built and operated an optical silicon resonator with a length of 250 mm in a closed cycle cryostat at 1.5 K nonstop over a time period of three years. To our knowledge, this is the first time, that an optical resonator was operated at this low temperature and for so long. We built a complete cryogenic optical setup with motorized mirror mounts, thus removing possible influences of the environment and eliminating changes in the laser light incoupling during the cooldown process. The result is a system with the lowest length drift measured so far among optical resonators, $< 1.4 \times 10^{-20}$/s in fractional terms. During the cryogenic operation, we measured the linewidth and the finesse of the resonator, 2.1 kHz and 2.86×10^5, respectively, and determined key sensitivities to temperature, tilt, vibrations, and optical power. At the same time, we applied active stabilization techniques to minimize their influence. The vibrations inside the cryostat at 1.5 K were carefully measured and their influence on the length stability of the resonator was utilized to determine its sensitivity to vibrations, which we found to be quite high, 2 MHz/g or $1 \times 10^{-8}/g$ in fractional terms. This severely limits the short-term length stability of the resonator.

The frequency of the resonator was monitored continuously over the whole span of the experiment using a frequency comb referenced to the GNSS atomic signal and applying two experimental techniques: a Pound-Drever-Hall lock of the laser to the TEM_{00} line of the resonator and the linecan technique, where an external light of a prestabilized laser is used to continuously interrogate the resonance line of the silicon resonator. We found the PDH lock to be less precise due to two parameters: the thermally driven fluctuations of the lock electronics offset and the influence of the residual time-dependent amplitude modulations generated by the electro-optic modulator. These modulations are sensed by the electronics as modulations of frequency and affect the locking point stability of the lock. Another possible limitation is presence of parasitic interference effects inside the cryogenic optical setup, generated by the back reflections from optical elements.

The medium-term frequency stability, measured using the PDH lock technique was limited by the stability of our hydrogen maser. To estimate the frequency stability that can be reached with our resonator we summarized the influence of all systematic effects (see Fig. 11.1). The result suggests, that our resonator can reach fractional frequency instability of 5.5×10^{-16} at one second time scale. The dominant effect, that limits the performance at 1 s time scale is the tilt instability followed by the instability of the circulating optical power. However, their effect is reduced at longer integration times. At the integration time of 1000 s the lowest value of predicted frequency instability is estimated, 0.72×10^{-16}. With further increasing integration times, the influence of the drift becomes the dominant component, and the fractional frequency instability increases to 2.1×10^{-16}. However, the constant drift of the resonator can be easily corrected. Thus, we can subtract this contribution from our estimation of frequency instability. We obtain 0.58×10^{-16} as the lowest frequency instability calculated for 1000 s integration time. This is equivalent to the absolute frequency instability of 10 mHz. At an integration time of 10 000 s we obtain a slightly higher value, 0.73×10^{-16} .

The results summarized above and in Fig. 11.1 indicate, that resonator Si1 has the capability to meet the ESA project goals if it is installed in an environment with a level of vibrations reduced by a factor of 10 compared to that of the present cryostat A high level of vibrations inside the Leiden Cryogenics

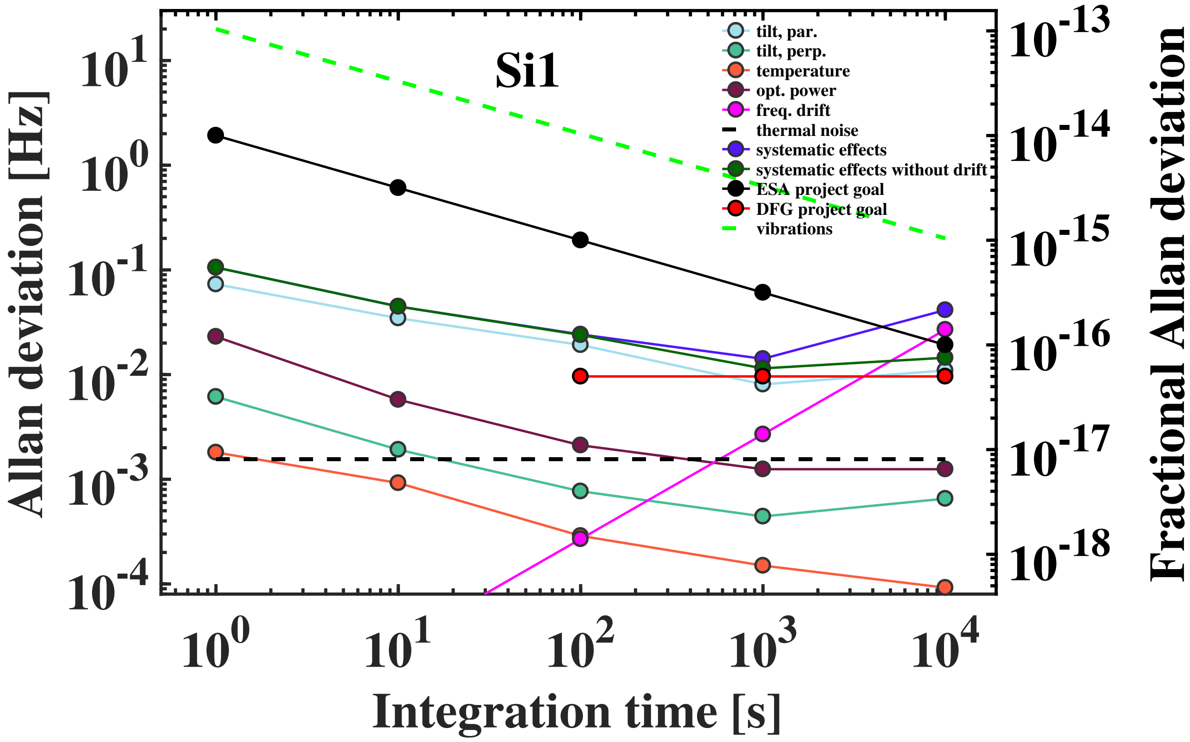

Figure 11.1: Si1 resonator: estimation of contributions of all measured and calculated systematic effects together with project requirements (Influence of vibrations (dashed green line) is not included in the sum of systematic effects (blue line)).

cryostat coupled with high vibration sensitivity of our 250 mm long resonator compelled us to build two other vertically-oriented resonators designed for low vibration sensitivity.

With a length of 50 mm, a linewidth of a 24.2 kHz, and a finesse of 1.2×10^5, the Si5 resonator has a vibration sensitivity of 133 kHz/g ($6.9 \times 10^{-10}/g$), a factor of 14 improvement compared with the 250 mm resonator. The frequency instability of this resonator was found to match the instability of the hydrogen maser with the lowest instability of 2×10^{-15} at 1000 s integration time with a potential to reach 1×10^{-15} at 100 s in a low-vibration environment.

In addition to the zero crossing of temperature sensitivity at 17 K, this resonator exhibits a zero crossing of thermal sensitivity at 3.5 K with a temperature derivative of $8.5 \times 10^{-12}/\mathrm{K}^2$ thus making it very attractive for future operation in low-cost 4 K cryostats.

Lowering the intensity of the laser wave used for the interrogation and maintaining a 30% duty cycle we could reduce the frequency drift rate to $-49(4)$ µHz/s ($< 3 \times 10^{-19}$/s). A further reduction of intensity might allow to null the frequency drift rate.

Operation of the Si5 resonator successfully proved the accuracy of the low-vibration sensitivity design and the high quality of the in-house done optical contacting of the mirror substrates which survived several thermal cycles. With this resonator, we did the first step towards the reduction of vibration sensitivity. However, due to a relatively low finesse and correspondingly large linewidth, it is difficult to achieve low frequency instabilities with this resonator.

Si190 resonator, designed for low-vibration sensitivity, built and incorporated into the setup inside the Leiden Cryogenics cryostat represents further progress in this direction. With a linewidth of 3.5 kHz this resonator was installed at a two-stage vibration isolation platform inside the Leiden Cryogenics cryostat. Constrains on available volume inside the cryostat made a custom in-house development of a BeCu cantilever blade with a resonance frequency of 2 Hz as a first stage for isolation of the setup in the vertical direction necessary. The second stage for isolation in vertical direction is comprised by four helical springs with a resonance frequency of 1 Hz. The resulted cumulative acceleration along vertical direction for the frequency band [1,200] Hz is 0.12 mg. The isolation along the two horizontal directions was facilitated by the total length of suspension formed by two vertical vibration isolation stages. With a total length of suspension equal to 590 mm the horizontal resonant frequency is 0.65 Hz. This effectively dampens vibrations and results in lower cumulative accelerations along two horizontal directions, when compared to the damping in the vertical direction. On the overall, we measure a fortyfold reduction of vibrations in the frequency band [1,200] Hz, compared to the vibrations measured inside the cryostat with an installed rigid frame.

The sensitivity to vibration of the Si190 resonator was measured at two frequencies, 1.4 Hz and 4.2 Hz, where the passive vibration isolation is not effective, and obtained a sensitivity of 11 kHz/g and 28 kHz/g with a mean of 20 kHz/g or $1 \times 10^{-10}/g$ in fractional terms. This is a factor 7 less than the sensitivity of the Si5 resonator and a factor 100 below the sensitivity of the Si1 resonator.

Si190 resonator also exhibits a low long-term frequency drift and has a medium-term frequency instability comparable or better to that of a hydrogen maser.

With the already obtained results we can make an estimation of the best theoretical performance of the Si190 resonator in Leiden Cryogenics cryostat by adapting the Fig. 11.1 as follows:

1. Low vibration sensitivity of the Si190 resonator together with the reduction of vibrations due to the passive vibration isolation allows to reduce the influence of vibrations on the Si190 frequency instability by a factor of 140 if compared to the Si1 resonator.

2. Due to the nature of the passive isolation the tilt of the experiment is always zero. Thus, its influence can be skipped.

3. Through the studies performed with the Si5 resonator we know, that the long-term frequency drift can be set to zero using appropriate laser power.

4. The frequency dependence of the Si190 resonator on optical power was not studied. Due to the almost identical size and the usage of identical mirrors, we assume that the Si190 response to power fluctuations is equal to that of the Si1 resonator, 0.675 Hz/μW.

Estimation of contributions of all measured and calculated systematic effects of the Si190 resonator with the incorporation of the issues discussed above is presented in Fig. 11.2 together with project requirements. The sum of systematic effects is well below the requirements of the two project goals and approaches the thermal noise limit for integration time above 100 s. The sensitivity to optical power limits stability at shorter integration times and requires further studies. Another limitation is the presence of vibrations inside the cryostat. To satisfy the DFG project requirements vibrations must be reduced by at least factor two. A further hundred-fold reduction of the influence of vibrations is required to reach the thermal noise limit of the resonator. The issues discussed in this passage are addressed in the outlook.

To reach presented frequency stability and long-term drift following technical issues were addressed during this work:

1. **Low-vibration sensitivity design:** all three resonators were designed for low sensitivity to vibrations. However, contrary to the FEM simulations Si1 resonator performed poorly due to the complexity of the ten-point support configuration.

2. **Supporting frame:** Designed supporting frames allowed damping of thermal fluctuations sensed by the resonators and were not found to introduce any additional mechanical stress on the resonators.

3. **Optical contacting:** Both Si5 and Si190 were optically contacted in-house. The bonding between the substrates and the spacers was proved to be insensitive to thermal cycling.

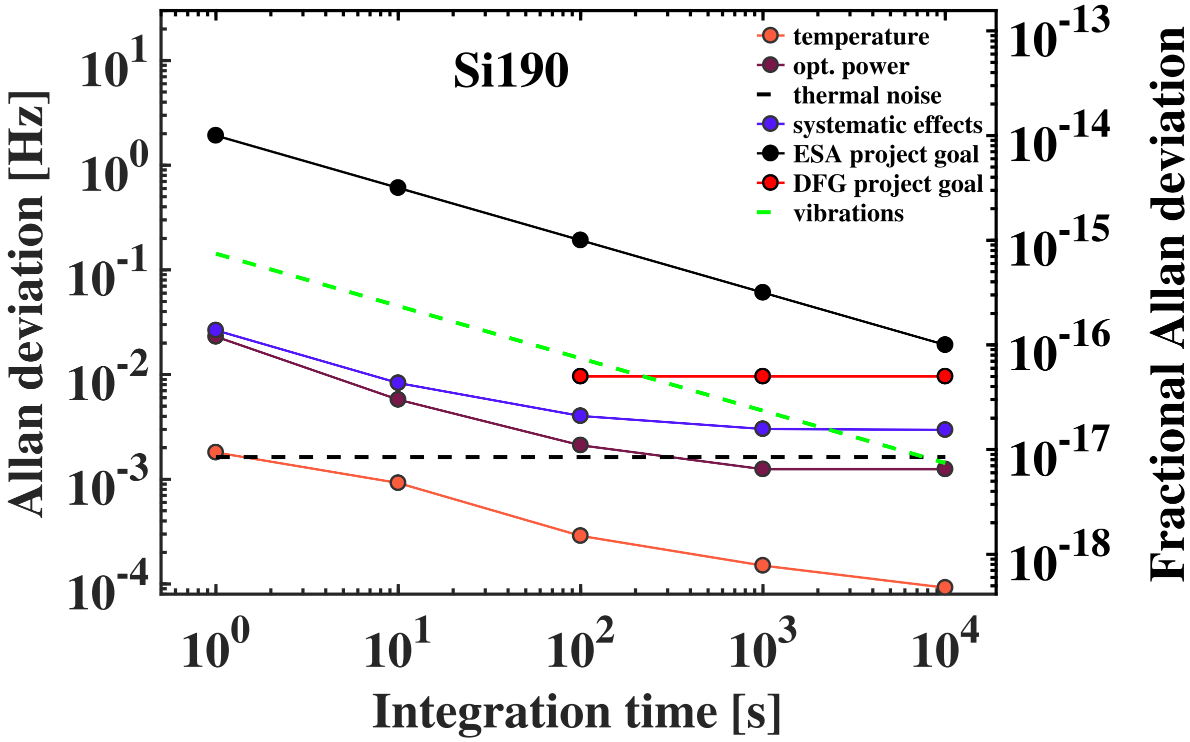

Figure 11.2: Si190 resonator: estimation of contributions of all measured and calculated systematic effects together with project requirements (Influence of vibrations (dashed green line) is not included in the sum of systematic effects (blue line)).

4. **Cryostat characterization and long-term operation:** Study of the temperature stability at the experimental plate and characterization of the spectrum of vibrations produced by the pulse tube cryocooler was done Trouble-free long-term operation of the cryostat over a time span of three years was insured.

5. **Cryogenic vibration sensors:** Cryogenically operated geophones and room-temperature inteferometer were used for the characterization of cryostat vibrations and the determination of vibration sensitivity of our resonators.

6. **Tilt stabilization of the cryostat:** Both Si1 and Si5 resonators were operated inside the cryostat with implemented tilt stabilization. Due to modification of the cryogenic setup tilt stabilization became obsolete for the Si190 resonator.

7. **All-cryogenic optical system:** All three resonators were operated together with an all-cryogenic optical setup.

8. **Phase noise cancellation in cryogenic optical fiber:** This step was implemented for the Si190 resonator. However, due to very low power levels used for the interrogation of the resonator, it became impossible to use in practice.

9. **Temperature stabilization:** Temperature stabilization was implemented for all three resonators, where necessary.

10. **Power stabilization:** Power stabilization was implemented for all three resonators, where necessary.

11. **Laser frequency stabilization:** Three different frequency stabilization techniques were implemented. All three were successfully shown to reach the frequency instability of our hydrogen maser as a limiting factor.

12. **Vibration isolation:** A passive cryogenic vibration isolation system was implemented. Further improvements are considered.

All the above issues represent essential solutions toward the realization of optical resonators with low-vibration sensitivity and thermal-noise-limited instability.

The frequency stability of the presented resonators was used to study the material properties of silicon and found applications in fundamental physics:

1. All three resonators were used to study the thermal expansion of the silicon. Their high thermal sensitivity allowed us to determine their thermal expansion coefficients with a resolution on the order of 10^{-12}/K.

2. We applied the frequency stability of our resonator for the study of the material absorption of the front-coated mirror and determined a lower boundary for the coefficient of optical absorption $\alpha \geq (1440 \pm 120)$ ppm/cm. We found that our system is capable of resolving absorption powers on the level of 1 nW, thus making the resonator a very sensible calorimeter.

3. We interpret the frequency stability of the 25 cm long horizontal resonator to put an upper limit to possible violations of Lorentz Local Invariance and Local Position Invariance. The analysis of LLI is done within the Robertson-Mansouri-Sexl kinematic test theory, assuming the Cosmic Microwave Background (CMB) as a reference frame. The violation parameter is $P_{KT} = (0.9 \pm 1.1) \cdot 10^{-5}$. The analysis of LPI is done by a null redshift test, using the natural motion of the Earth in the sun's gravitational potential. We obtain the violation parameter $\beta = (1.0 \pm 1.1) \cdot 10^{-5}$. The 1 σ upper limit for $|\beta|$ is better than the best previous result obtained with an electromagnetic resonator.

12 Outlook

The ultimate goal of the work with optical resonators is to reach their lowest, thermal-noise-limited instability. Achieving this goal requires the necessary implementation of the following changes and improvements to the present Si190 resonator setup:

1. Further improvement of the vibration sensitivity of resonators or reduction of vibrations inside the cryostat by means of passive or active isolation of the experimental setup or by switching to a new generation of cryostats.

2. Precise monitoring of vibrations at the experiment.

3. Miniaturization of the cryogenic optical setup.

4. Improvement of the reliability of the motorized mirror mounts.

5. Simultaneous operation of multiple cryogenic resonators.

All these approaches are currently pursued by our group and are discussed below.

Damping of cryostat vibrations

As can be seen from Fig. 10.2 (bottom right panel), the total amplitude of acceleration, measured at the experiment, is dominated by the vertical component. To mitigate this situation we are adopting the usage of quasi-zero stiffness technique to cryogenics, which is successfully employed in gravity-wave detectors, where it is used to isolate test masses with a resonance frequency on the order of 0.5 Hz or lower, well below 1.4 Hz, the working frequency of the cryostat [94, 95, 96]. It is worth trying this technique at cryogenic temperatures. However, it requires careful adaptation of the setup for the change in the stiffness of the materials and the overall length contraction during the cooldown.

Active vibration isolation using e.g., hexapods allows for cancellation of vibrations to start already at the DC level. This technique was already applied in cryogenics for scanning probes microscopes [97], where piezoelectric actuators were used as struts (see Fig. 12.2). The difficulty of this approach is the drastic reduction of the displacement amplitude of piezoelectric actuators at low temperatures. To successfully cancel vibrations inside the present cryostat with a typical displacement amplitude equal to 20 µm (no passive damping) would require piezoelectric actuators with a length of approx. 300 mm. Together with the limited availability of space inside the experimental chamber of the cryostat, this fact prevented an application of this type of active vibration isolation in the past. However, with the implementation of the passive vibration isolation, the amplitude of the displacement was reduced by one order of magnitude or more. This makes the use og the hexapod attractive.

Another approach to reduce vibrations is the usage of a new-generation-type cryostat with an experimental chamber physically separated from the cryocooler by placing it in a separate tower (see Fig. 12.1). Flexible s are employed to prevent the transfer of vibrations to the experiment. Further reduction is achieved using flexible heat links or helium buffer gas for heat transfer instead of a rigid connection between the cryocooler and the experiment. These results in residual acceleration amplitudes at the experiment of 0.3 μg at the frequency of 1 Hz [70].

Resonators with improved vibration sensitivity

A promising approach with a demonstrated acceleration sensitivity of $2.5 \times 10^{-11}/g$ is based on the force-insensitive spacer design proposed by Webster and Gill for the room-temperature ULE resonators with a side length of 50 mm [98]. This design was already adopted by other groups to produce room-temperature ULE resonators with a length of 87 mm [99] and 75 mm [100]. As ULE material is unsuitable for cryogenic applications, the design has to be adapted for silicon. Due to the anisotropic

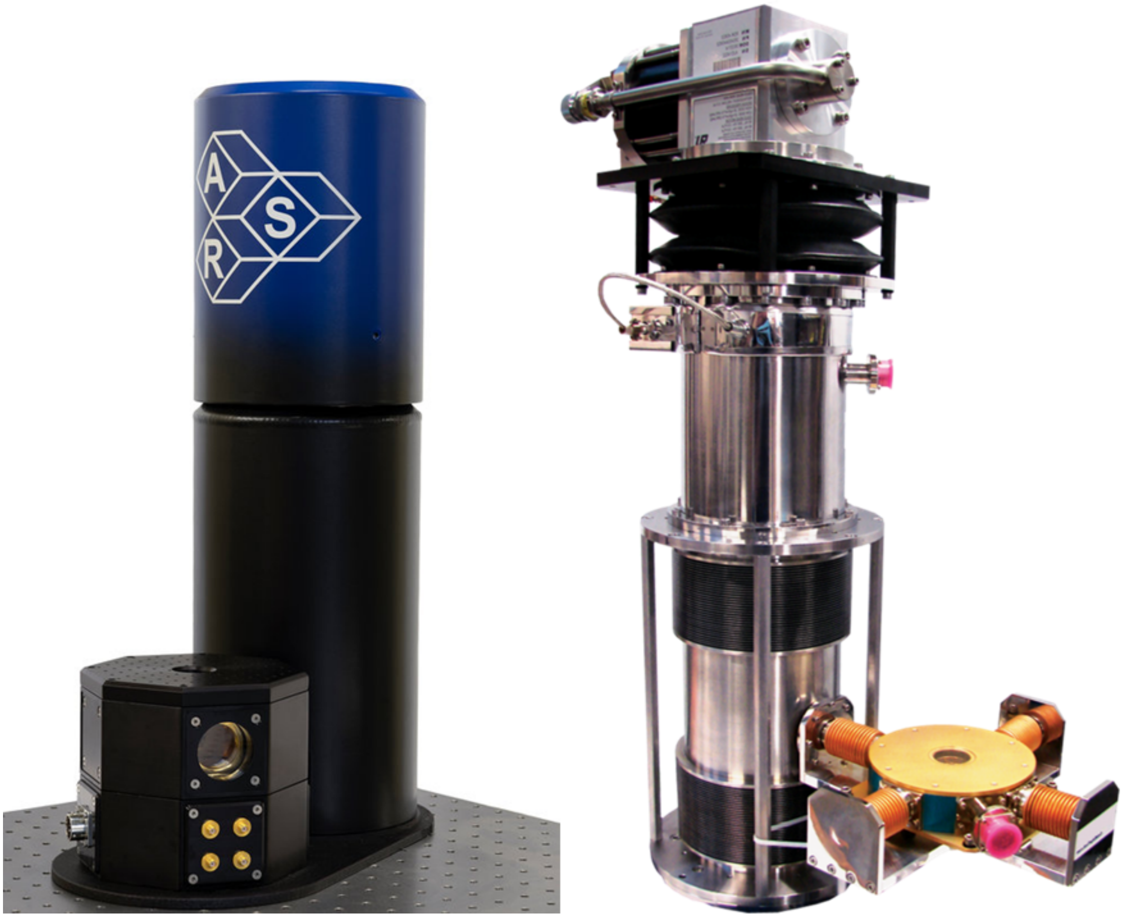

Figure 12.1: Two examples of commercially available cryostats with experimental chambers separated from the cryocoolers (ARS µDrift platform (left) and Cold Edge cryostat (right))

nature of the silicon crystal, this represents a nontrivial task. We performed a thorough investigation of all possible silicon crystal orientations relative to the cubic spacer and identified two suitable orientations [88]. From these two, the [100] orientation of the crystal allows for simultaneous operation of all three cavities inside the resonator in a force-insensitive and vibration-insensitive regime with a precise mounting of the resonator inside a suitable supporting frame.

Precise monitoring of vibrations at the experiment

Monitoring of vibrations at the experiment is essential for the evaluation of the performance of the installed vibration isolation and for precise characterization of the vibration sensitivity of resonators. This is currently done with cryogenically operated geophones and with an interferometric sensor, operated from outside of the cryostat. Both techniques are problematic and need to be improved. Geophones were calibrated at room temperature. Their response is likely to change in cryogenics due to the changes in the material properties. This makes their cryogenic recalibration necessary. The interferometric sensor is usually not isolated from the background vibrations. For precise monitoring of cryostat vibrations, it requires an active vibration isolation platform. Once isolated, it would allow for simple calibration of geophones by comparing the output of the sensor with the output of the co-axially oriented geophones.

Miniaturization of the cryogenic optical setup

Optical setups with long paths for laser beams are sensitive to the thermal contraction of the materials during the cooldown. This makes a degradation of the incoupling of the laser light into the resonator likely and requires constant correction during the cooldown. We already did a large step toward miniaturization of the setups. However, further miniaturization is needed to reduce the amount of active correction of the incoupling to the minimum. This issue can be addressed by replacing the commercial optical mounts with the home-built elements.

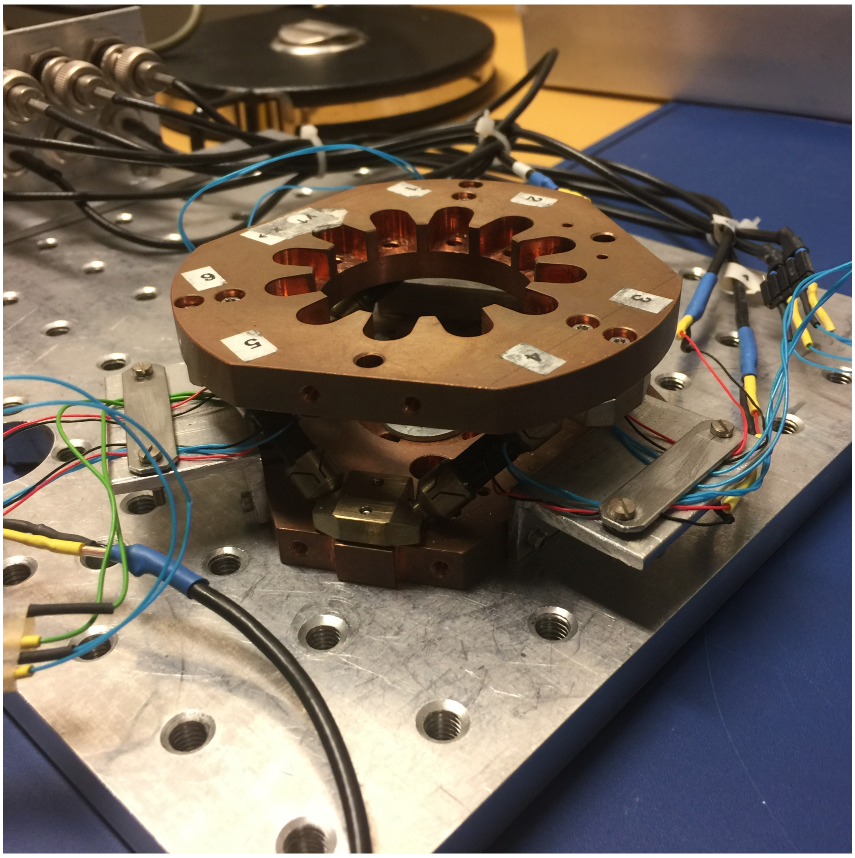

Figure 12.2: Overview of the hexapod platform used for the development of active vibration isolation for the cryostat.

Improvement of the reliability of the motorized mirror mounts

Motorized mirror mounts are required for possible corrections of the incoupling during and after completion of the cooldown. Each of them contains two commercially available stepper motors, designed to operate at room temperature. To extend their operation range into the cryogenic we manually disassemble the motors, remove the lubricant, grease them with MoS_2 power, assemble them and prove their functionality at room temperature before installing them into the cryogenic setup. After cooldown, we observe a failure rate of approximately 40%. This makes it difficult to achieve optimal light incoupling into the resonator. The reliability of motorized mirrors can be dramatically improved by replacing stepper motors with piezoelectric motors (e.g., from JPE) that have a zero failure rate. This upgrade would also help to improve scientific output and accelerate the work, as it would reduce the risk of "losing" resonators after cooldown.

Simultaneous operation of multiple cryogenic resonators

All three resonators presented in this work demonstrated a hydrogen-maser-like performance. However, based on their measured sensitivities to environmental perturbation they are likely to perform better. To be able to demonstrate their best performance, it is necessary to measure their frequency stability relative to comparable frequency sources. An ideal source would be another silicon resonator. This resonator could also be installed inside the Leiden Cryogenics cryostat. However, to exclude a common-mode behavior they should be ideally installed inside different cryostats. The cryostats should be operated in different labs to exclude the influence of air conditioning. An optical beat of two lasers would potentially be more stable than a beat of a laser versus hydrogen maser. However, it would only allow for the characterization of the beat frequency. To characterize the frequency stability of the involved resonators would require a three-cornered hat method [101]. However, this technique needs to compare three resonators and thus is difficult to implement.

A Tests of the Einstein Equivalence Principle

In this section we interpret the frequency stability of our 25 cm long resonator in terms of a potential violation of the two core postulates of the Einstein Equivalence principle (EEP) which are:

- The postulate of Local Lorentz Invariance (LLI). It states that the outcome of any experiment performed in a non-gravitational environment does not depend on velocity.
- The postulate of Local Position Invariance (LPI). It states that the outcome of any experiment performed in a non-gravitational environment does not depend on location in space and time.

A.1 Analysis of LLI in the Mansouri-Sexl framework

Theory

To interpret the experiment in terms of a potential LLI violation we use the well-known RMS framework developed by Robertson [102] and Mansouri, and Sexl [103]. This kinematic test theory assumes that there is a preferred reference frame S defined by $(\mathbf{X}, T)$, in which the speed of light c is constant and isotropic. In any other inertial reference frame S' defined by $(\mathbf{x}, t)$, moving with a velocity $\mathbf{v}$ with respect to the frame S, the speed of light is $c(\mathbf{v}, \theta)$ is a function of both velocity $|\mathbf{v}|$and the angle between $\mathbf{v}$ and the direction of light propagation. The transformation between the two frames is defined by [103]:

$$T = \frac{1}{a}(t - \epsilon \mathbf{x}),$$

$$X = \frac{1}{d}\mathbf{x} - (\frac{1}{d} - \frac{1}{b})\mathbf{v}\frac{\mathbf{x} \cdot \mathbf{v}}{\mathbf{v}^2} + \mathbf{v}T,$$

where the parameters a, b, d, and ϵ depend on velocity $\mathbf{v}$. In special relativity $a = b = \gamma = 1/(1 - v^2)^{1/2}$ and $d = 1$. ϵ is a function of the clock synchronization procedure. Both the Einstein synchronization procedure and the slow moving clock synchronization procedure require $\epsilon = -\mathbf{v}$. In the case of small velocity $\mathbf{v}$, the parameters a, b, and d can be Taylor expanded as $a = 1 + \alpha v^2$, $b = 1 + \beta v^2$, and $d = 1 + \delta v^2$. Inserting the above transformations into the equation of the light cone, $X^2 = T^2$, we obtain the relation between the velocity of light c in the S frame and $c(\mathbf{v}, \theta)$ in S' [103]:

$$\frac{c}{c(\mathbf{v}, \theta)} = 1 + (\beta + \delta - \frac{1}{2})\frac{v^2}{c^2}\sin^2(\theta) + (\alpha - \beta + 1)\frac{v^2}{c^2}. \tag{A.1}$$

In special relativity this relation is always equal to one. Thus, the two coefficients are equal to zero:

$$\beta + \delta - \frac{1}{2} = 0,$$

$$\alpha - \beta + 1 = 0.$$

These requirements set the coefficients to:

$$(\alpha, \beta, \delta) = (-\frac{1}{2}, \frac{1}{2}, 0) \tag{A.2}$$

We can expand the relation in eq. A.1 for small variations of $c(\mathbf{v},\theta)$ with respect to c:

$$\frac{c}{c(\mathbf{v},\theta)} = \frac{c}{c+\Delta c(\mathbf{v},\theta)} \approx 1 - \frac{\Delta c(\mathbf{v},\theta)}{c}.$$

Eq. A.1 can then be written as:

$$\frac{\Delta c(\mathbf{v},\theta)}{c} = -(\beta+\delta-\frac{1}{2})\frac{v^2}{c^2}\sin^2(\theta) - (\alpha-\beta+1)\frac{v^2}{c^2}.$$

In order to find possible deviations of the coefficients from these values we can perform either a Michelson-Morley type experiment, testing for the anisotropy of the speed of light, and determine the coefficient

$$P_{MM} = -(\beta+\delta-\frac{1}{2}),$$

or a Kennedy-Thorndike type experiment in the search for a possible boost (v) dependence of the speed of light and determine the coefficient:

$$P_{KT} = \beta - \alpha - 1. \tag{A.3}$$

Reference frame

The application of the RMS theory described in the preceding section requires the choice of a reference frame $(\mathbf{X},T)$. We test relativity using the J2000 frame of reference (see Fig. A.1) with respect to the velocity of cosmic microwave background (CMB) radiation [104] as seen in that frame.

To determine the possible dependence of the light speed on v, we must account for the movement of the Earth around the Sun and for Earth's rotation. The total boost $\mathbf{b}$ is defined in the reference frame $\mathbf{X}$ as the sum of the velocity $\mathbf{u}$ of our planetary system with respect to the CMB, of the orbital velocity of the Earth $\mathbf{v}_\mathrm{o}$, and of the velocity of the laboratory with respect to the Earth's center of mass, $\mathbf{v_r}$ divided by the speed of light,

$$\mathbf{b} = \frac{\mathbf{v}}{c} = \frac{(\mathbf{u}+\mathbf{v}_\mathrm{o}+\mathbf{v}_\mathrm{r})}{c}, \tag{A.4}$$

where $c = 299\,792\,458$ m/s is the speed of light.

The velocity $\mathbf{u}$ with respect to CMB is described in the J2000 frame by the right ascension α, the declination δ, and the speed u (see Fig. A.2, left panel)

$$\mathbf{u} = u \times \begin{pmatrix} \cos(\delta)\cos(\alpha) \\ \cos(\delta)\sin(\alpha) \\ \sin(\delta) \end{pmatrix}. \tag{A.5}$$

To obtain the orbital velocity $\mathbf{v_o}$ in the J2000 frame we first consider its value at the time point of the autumnal equinox in the frame where the x-axis is coincident with the x-axis of the J2000 frame, but the y-axis and the z-axis are in the ecliptic plane and perpendicular to it, respectively. Orbital velocity $\mathbf{v_o}$ is parallel to the y-axis in this frame. Thus we can state:

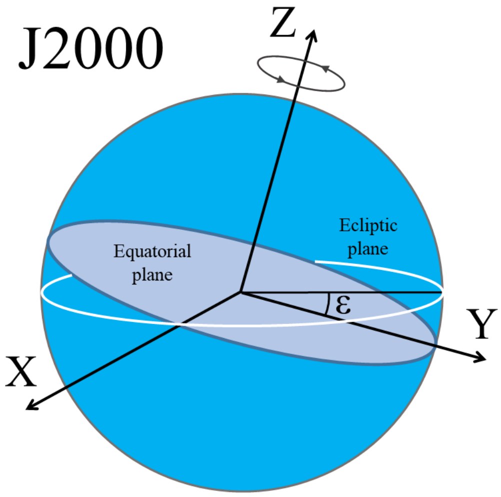

Figure A.1: Definition of the J2000 equatorial celestial reference frame with the origin at the Earth center: x-axis is defined by the mean equinox at epoch J2000 (01.01.2000 at 12:00, universal time); z-axis is the mean rotational axis of the Earth; y-axis is defined by the cross product of x- and z-axis and is lying in the mean equatorial plane of the Earth at epoch J2000, which is inclined with respect to Earth orbital plane by an angle ε.

$$\mathbf{v_o} = v_o \cdot \begin{pmatrix} -\sin(\lambda_o) \\ \cos(\lambda_o) \\ 0 \end{pmatrix},$$

where v_o is the orbital speed of the Earth, and the phase λ_o is the determined by the Earth's orbital angular frequency ω_o and time t elapsed since the autumnal equinox, $\lambda_o = \omega_o t$. The Ecliptic plane is tilted with respect to the equatorial plane of the Earth by an angle ε, called the obliquity of the ecliptic. Thus the transformation of the above equation into the J2000 frame yields:

$$\mathbf{v_o} = v_o \cdot \begin{pmatrix} -\sin(\lambda_o) \\ \cos(\lambda_o) \\ 0 \end{pmatrix}' \times \begin{pmatrix} 1 & 0 & 0 \\ 0 & \cos(\varepsilon) & \sin(\varepsilon) \\ 0 & -\sin(\varepsilon) & \cos(\varepsilon) \end{pmatrix} = v_o \cdot \begin{pmatrix} -\sin(\lambda_o) \\ \cos(\lambda_o)\cos(\varepsilon) \\ \cos(\lambda_o)\sin(\varepsilon) \end{pmatrix} \tag{A.6}$$

For the vernal equinox as the starting point, this expression is modified as follows,

$$\mathbf{v_o}' = v_o \cdot \begin{pmatrix} \sin(\lambda_o') \\ -\cos(\lambda_o')\cos(\varepsilon) \\ \cos(\lambda_o')\sin(\varepsilon) \end{pmatrix}.$$

The velocity of the Earth's surface at the location of Düsseldorf is given as (in the J2000 frame)

$$\mathbf{v_r} = \omega_r R \cos(\chi) \cdot \begin{pmatrix} -\sin(\lambda_r) \\ \cos(\lambda_r) \\ 0 \end{pmatrix}, \tag{A.7}$$

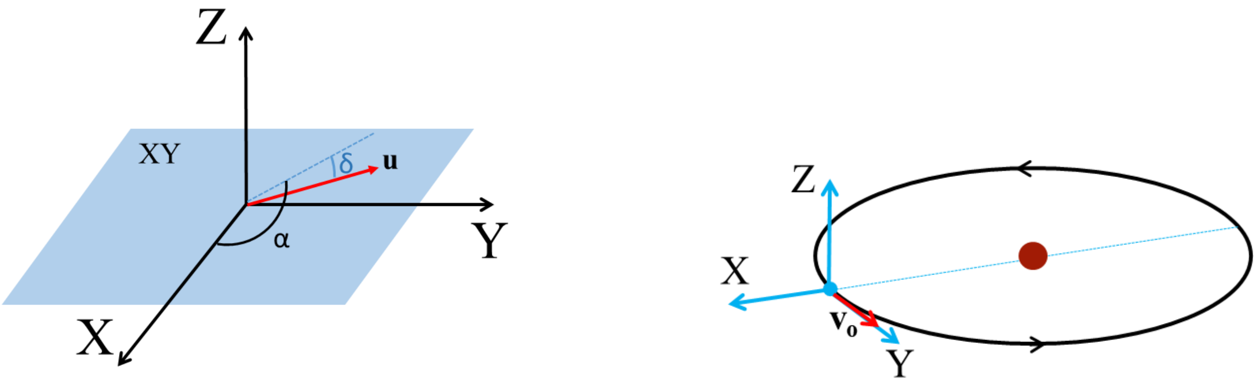

Figure A.2: **Left panel:** direction of the velocity **u** of the solar system with respect to CMB, in the J2000 frame **X**. **Right panel:** definition of the Earth orbital velocity $\mathbf{v}_\mathrm{o}(t=0)$ with respect to the Sun.

where ω_r is the Earth sidereal angular rotation frequency, R is the Earth radius, χ is the latitude of the laboratory in Düsseldorf. Finally, the phase $\lambda_r = \omega_r t + \varphi$, where φ is the phase offset set by an angle between the longitude of the laboratory and the right ascension of the CMB velocity α.

The final expression for the velocity **v**, is:

$$\mathbf{v} = u \times \begin{pmatrix} \cos(\delta)\cos(\alpha) \\ \cos(\delta)\sin(\alpha) \\ \sin(\delta) \end{pmatrix} + v_\mathrm{o} \times \begin{pmatrix} -\sin(\lambda_o) \\ \cos(\lambda_o)\cos(\varepsilon) \\ \cos(\lambda_o)\sin(\varepsilon) \end{pmatrix} + \omega_r R \cos(\chi) \times \begin{pmatrix} -\sin(\lambda_r) \\ \cos(\lambda_r) \\ 0 \end{pmatrix}. \tag{A.8}$$

The expression for the boost **b** can be obtained using eq. A.4.

Fig. A.3 shows both quantities (middle and bottom panels) calculated for the whole duration of the experiment. The relative position of the Earth with respect to the Sun and the direction of the solar system velocity **u** with respect to the CMB at the start of the experiment at 10.06.2015 (57183.37 MJD) is depicted in the top panel of Fig. A.3. A summary of the parameters entered in the above equation is given in Tab. 5.

The direction of the velocity **u** of the solar system relative to the CMB is by no means a preferred direction. It is a result of historical development. Therefore, below we extend our data analysis and

Table 5: Definition of parameters used.

Parameter	Description	Value
α	Right Ascension of CMB velocity	167.9287 deg
δ	Declination of CMB velocity	-6.9269 deg
u	CMB speed	369 km/s
v_o	Earth orbital speed	29.78 km/s
ω_o	Earth annual angular rotational frequency	0.017203 rad/day
ε	Obliquity of the ecliptic	23.439 deg
ω_r	Earth sidereal angular frequency	2π/23 h 56 min 4.09 s
R	Earth radius	6370 km
χ	Lab latitude in Düsseldorf	51.1867 deg
η	Lab longitude in Düsseldorf	6.7965 deg

introduce other reference directions $\mathbf{u_i}$, which we obtain by rotating $\mathbf{u}$ around the z-axis by an angle γ in the range between 0 and 180 deg (see Fig. A.4).

We use eq.A.8 and eq.A.4 to set an upper limit for the Kennedy-Thorndike coefficient P_{KT} by comparing the frequency of cryogenic silicon resonator $\Delta\nu_{Si}$ with a frequency of hydrogen maser $\Delta\nu_{H-Maser}$ and using the following equation:

$$\frac{\Delta\nu_{Si} - \Delta\nu_{H-Maser}}{\nu_0} = P_{KT}|b(t)|^2, \tag{A.9}$$

where ν_0 is equal to 191976.629 GHz.

Analysis of daily variations

To analyze the LLI with respect to daily variations we collected a set of data by recording the frequency of a cryogenic silicon resonator with respect to the hydrogen maser at 28 distinct days with a duration ranging from 5.8 h to 20.68 h. A summary of the data sets is presented in Fig. A.5. We fit all data sets according to eq. A.9 to obtain the coefficient P_{KT} . Due to the short duration of data sets we can set the first two parts in eq. A.4 as constant and fit the data with a function:

$$\Delta\nu_{Si} - \Delta\nu_{H-Maser} = a + bx + C' \sin^2(2\pi t + \varphi), \tag{A.10}$$

Here, the first and second term accounts for a frequency offset and a possible linear frequency drift of the resonator and of the hydrogen maser, respectively. We define $C' = C\cos(\varepsilon)$. To project the velocity change on the direction of $\mathbf{u}$ we introduce the phase shift φ, which is equal to α or 167.9287 deg. The squared sin function in Eq. A.10 implies that one tests for modulation with a frequency equal to the double rotational frequency of the Earth with a rotational period of 12 h. This is due to the resonator's mirror symmetry. The coefficient C is equal to:

$$C = P_{KT} \cdot \nu_0 \frac{\omega_r^2 R^2 \cos^2(\chi)}{c^2}.$$

The Kennedy-Thordike parameters is obtained from C via

$$P_{KT} = C \frac{c^2}{\nu_0 \omega_r^2 R^2 \cos^2(\chi)}.$$

Time t in the Eq. A.10 is the mean sidereal time at the location of the experiment. It is calculated using an algorithm described in USNO Circular No. 163 (1981).

To apply the algorithm we need to calculate the mean sidereal time as the angle relative to the vernal equinox. We first transfer from our local time to Greenwich mean time by taking into account the summer time. Then we transform all dates D_i into the Julian dates JD_i and calculate the number of days NoD_i elapsed since the epoch J2000:

$$NoD_i = JD_i - 2451545.0.$$

The mean sidereal time at Greenwich is then given by:

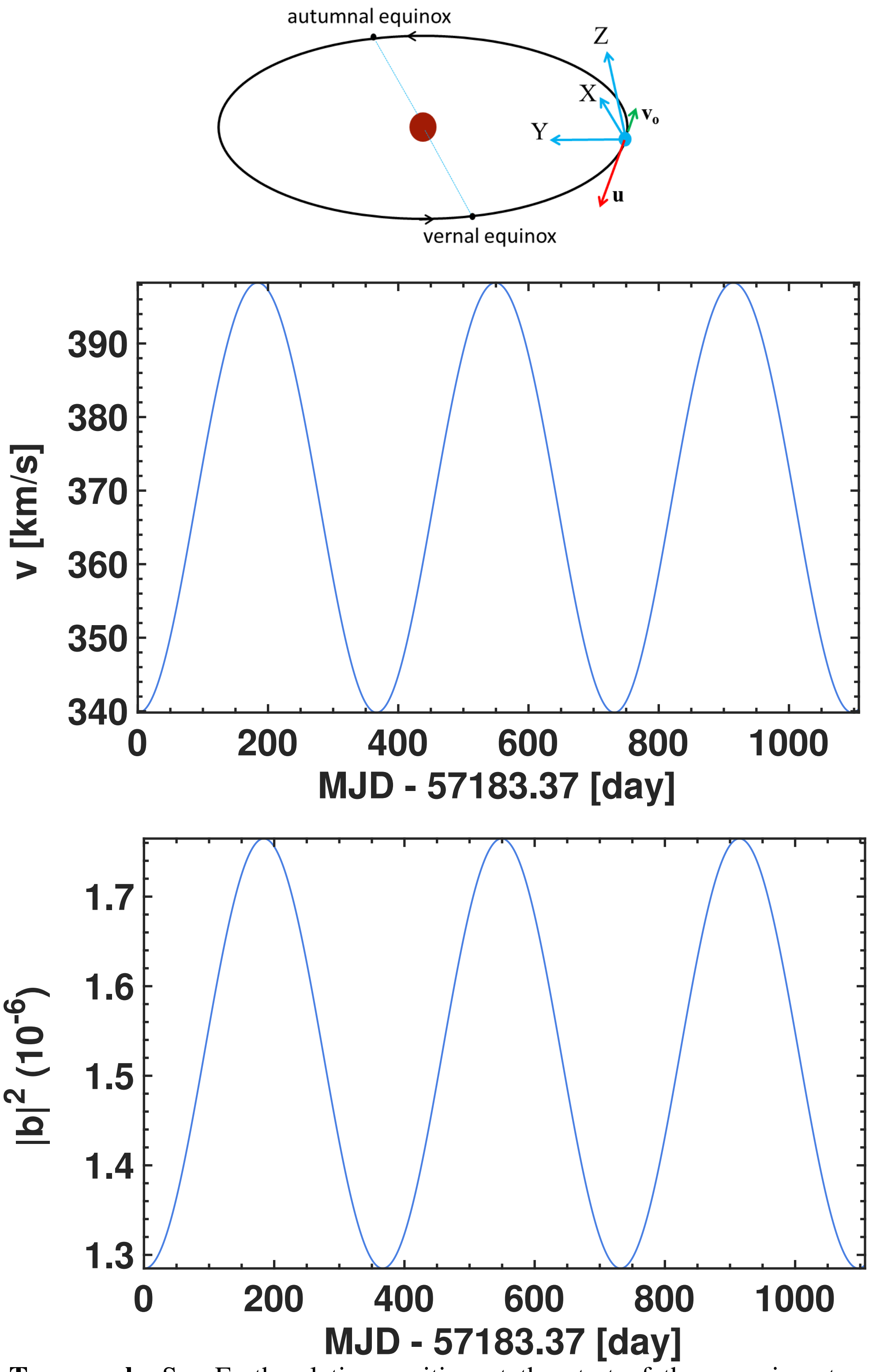

Figure A.3: **Top panel:** Sun-Earth relative position at the start of the experiment on 10.06.2015 (57183.37 MJD).The orbital velocity $\mathbf{v_o}$ is approximately opposite to the velocity $\mathbf{u}$ of the solar system with respect to CMB. **Middle and bottom panels:** speed of the Earth and the squared norm of the boost with respect to the CMB during the data interval, calculated using eq. A.8 and eq. A.4, with the Earth's rotation neglected.

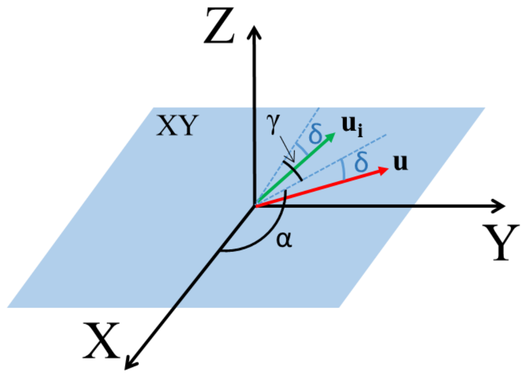

Figure A.4: Definition of a new preferred direction $\mathbf{u_i}$ obtained by rotation of vector $\mathbf{u}$ clockwise around the z-axis as seen along the axis by an angle γ from the original direction. This is equivalent to an increase of the right ascension of $\mathbf{u}$ by an angle γ.

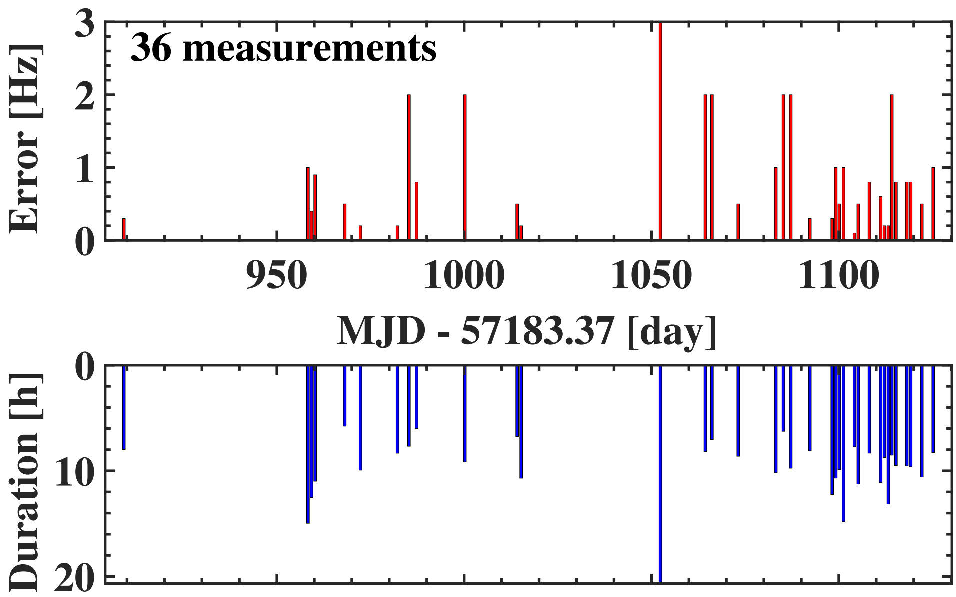

Figure A.5: Properties of all data sets used in the evaluation. Top: error defined by the Allan deviation at longest time τ. Bottom: duration of each data set.

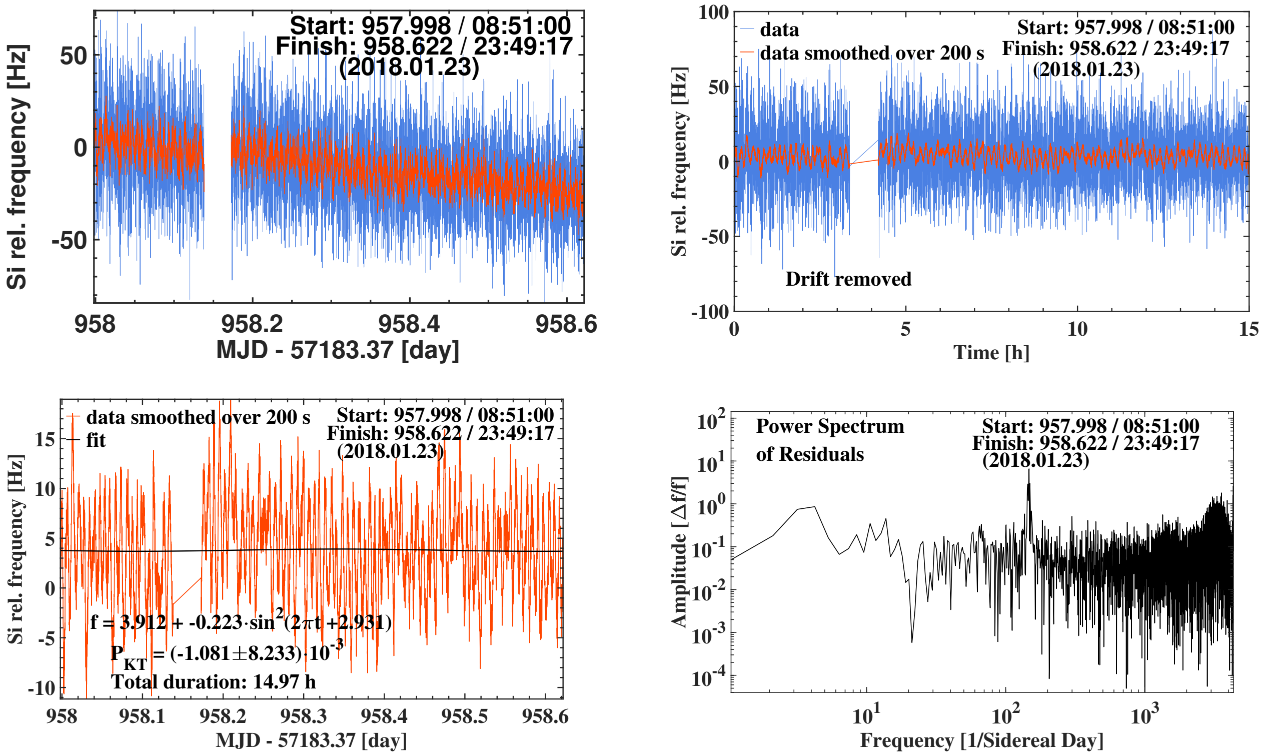

Figure A.6: Example of a data sets. **Top left panel:** initial data. **Top right panel:** data set after removal of a linear drift of the frequency ratio **Bottom left panel:** fit of data with eq. A.10 to obtain the parameter P_{KT}. **Bottom right panel:** power spectrum of fit residuals showing the white nose. Peak at a frequency of approximately 150 $1/(\text{Sidereal day})$ is due to the modulation of laser frequency in the lab by the air conditioner.

$$t_G = 18.697374558 + 24.06570982441908 \cdot NoD_i.$$

The local mean sidereal time t_i with a precision of 1.1 s is calculated using the longitude η of the lab position (see tab. 5):

$$t_i = t_G + \eta/15.$$

Fig. A.6 shows the step-wise evaluation of one data set, where the linear drift removal and fitting are separated for clarity. In actual evaluation, these two steps are merged according to eq. A.10. Fit results are evaluated by calculating the power spectrum of the fit residuals (Fig. A.6, bottom right panel). They are dominated by white noise and therefore prove the validity of fit errors. Fig. A.7 (right panel) presents the distribution of resulted coefficient P_{KT} from fits of individual data sets presented in the right panel of Fig. A.7. We differentiate between all data sets and data sets with a total duration of more than 9 h, which is equivalent to the $3/4$ of one-period duration. Our results are:

$$P_{KT} = (2.02 \pm 3.49) \cdot 10^{-3}$$

from all data sets, and

$$P_{KT} = (6.15 \pm 3.67) \cdot 10^{-3}$$

for data sets with duration longer then 9 h and the standard 1σ error of the mean.

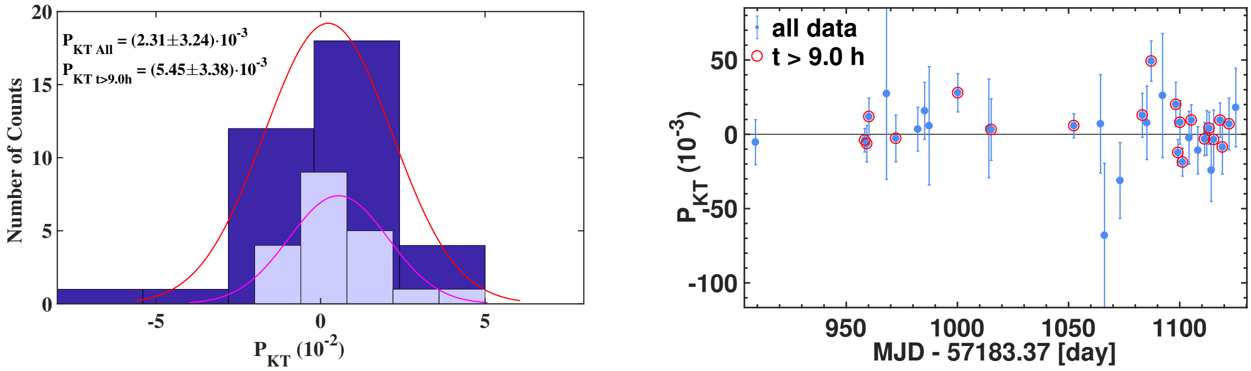

Figure A.7: **Left panel:** distribution of fit results for all data sets (blue colored histogram) and for data sets with a duration of longer then 9 h (light blue colored histogram) together with corresponding normal fits. **Right panel:** resulted parameter P_{KT} from fits of all data sets. Data sets with duration of more then 9 h are additionally marked with red circle.

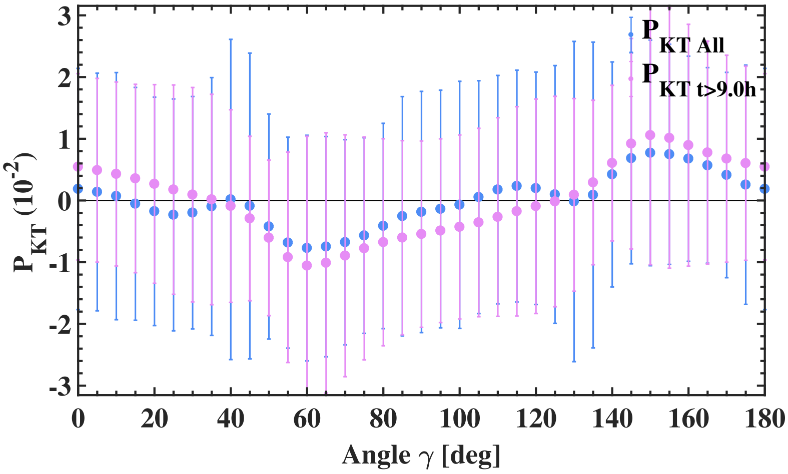

Figure A.8: Kennedy-Thordike coefficient P_{KT} determined from fits of all data sets (light blue) or only data sets with a duration longer then 9 h (magenta) for a solar system velocity with respect to CMB $\mathbf{u}$ rotated clockwise by an angle γ around the z-axis of the J2000 reference frame.

We also performed an analysis with respect to the reference direction rotated clockwise around the z-axis by a variable angle γ with respect to $\mathbf{u}$ as described in Sec. A.1. Results of the fits are presented in Fig. A.8. As in the previous case they are all consistent with zero.

Analysis of annual variations

Earth orbits the Sun with a velocity which is almost two orders of magnitude higher then the velocity at the Earth surface due to rotation (30 km/s vs. 0.46 km/s). To test the LLI, we collected data over two half-year long periods (see Fig. A.9). Data sets were fitted with according to Eq. A.9 where the expression for boost is based on the second term from eq. A.4 and eq. A.8, orbital velocity of the Earth:

$$\Delta\nu_{Si} - \Delta\nu_{H-Maser} = a + bx + C' \sin^2(\omega_o t + \varphi), \tag{A.11}$$

where the phase φ is defined by the right ascension of CMB velocity $\mathbf{u}$ and $C' = C\cos(\varepsilon)$. The Kennedy-Thorndike coefficient P_{KT} can be expressed by the fit coefficient C:

$$P_{KT} = C\frac{c^2}{v_o v_0}.$$

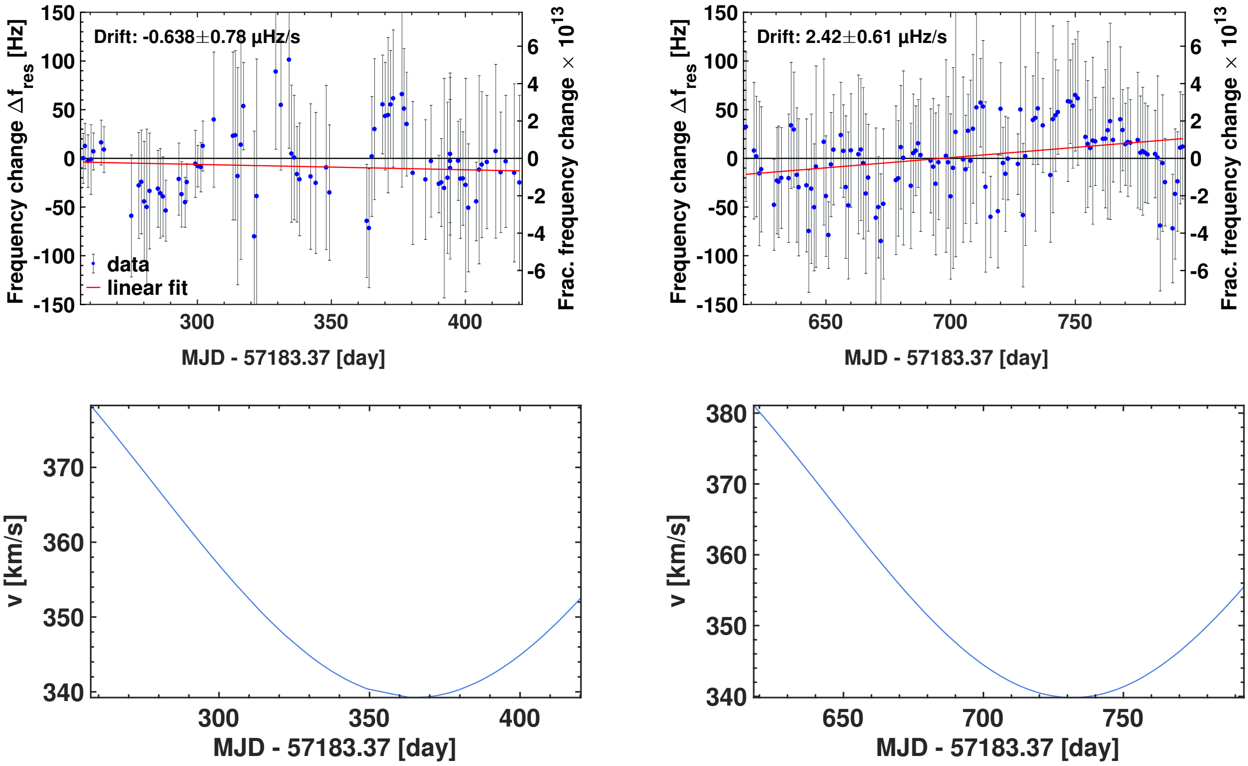

Figure A.9: Two data sets with a duration of approximately 0.5 year each, used for the evaluation of LLI inside the RMS kinematic framework (**top row**) together with corresponding velocity change (**bottom row**).

We obtain (see Fig. A.10, top row):

$$P_{KT} = (0.855 \pm 1.055) \cdot 10^{-5}$$

for the first data set, and:

$$P_{KT} = (3.722 \pm 0.672) \cdot 10^{-5}$$

for the second data set. The error equals 1σ for both datasets. The error for the second data set is smaller than the mean implying possible dependence of the light velocity on boost. To evaluate the quality of the results we fitted the residuals of the fits with a Gaussian function (see Fig. A.10, bottom row). In both cases, the residuals are distributed around zero as a mean value. Thus, errors error estimates for the results presented above can be considered valid. As expected, the coefficients obtained from the evaluation of the two half-year data sets are smaller then the coefficient obtained from the sidereal variation (see Sec. A.1). The difference is approximately equal to the difference in velocities. The waited mean average of the above results is:

$$P_{KT} = (2.894 \pm 0.567) \cdot 10^{-5}$$

We also evaluated the dependence of the Kennedy-Thorndike coefficient with respect to rotation of the reference direction as described in Sec. A.1. The results are presented in Fig. A.11. Both data sets have angles where the coefficient P_{KT} is nonzero. However, the corresponding angles are different. There is also no agreement with the results of the similar evaluation of sidereal data.

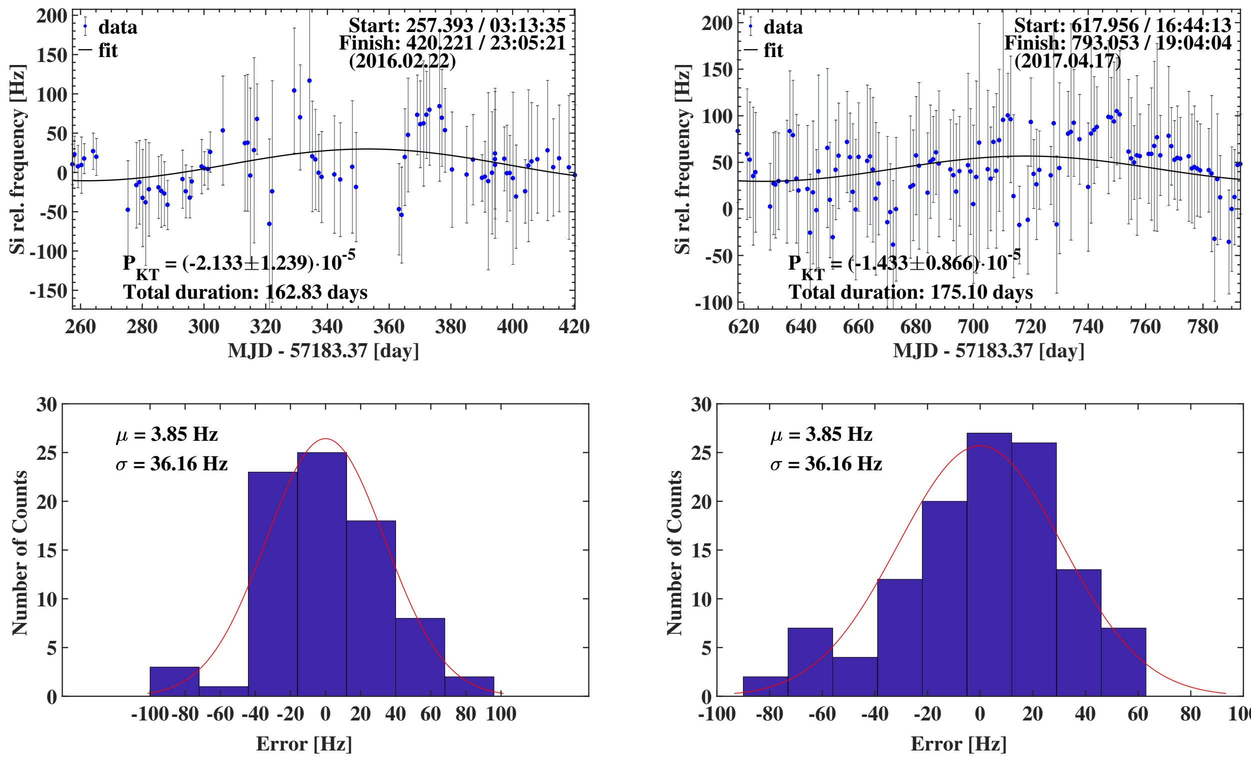

Figure A.10: **Top row panels:** fit of the two half-year data sets with a function defined by eq. A.11. This two data sets with a duration of approximately 0.5 year each, used for the evaluation of LLI inside the RMS kinematic framework on an annual scale. **Bottom row panels:** corresponding distribution of fit residuals.

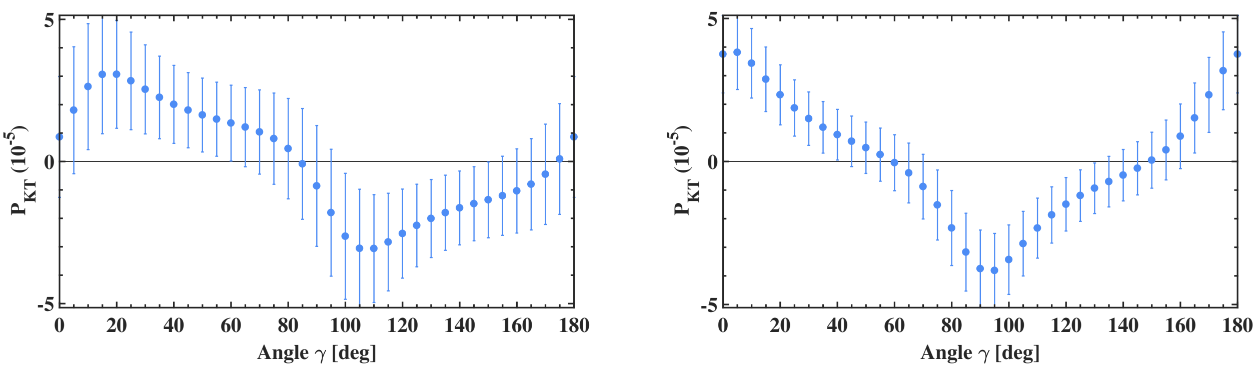

Figure A.11: Kennedy-Thorndike coefficient P_{KT} determined from the fit of the two half-year data sets with a function defined by eq. A.11 for different orientation of the hypothetical preferred direction.

In Table. 6 we compare our best result with a selected number of published results. It is three orders of magnitude worse than the best result by Tobar et al. However, the accumulation of data occurred over a factor of 12 shorter time period. Comparison with another experiment run with a cryogenic optical resonator over an approximately equal time period yields a factor two improvement.

A.2 Analysis of LPI

Theory

Local position invariance can be tested using two nonidentical clocks at the same location subjected to the variations of the Sun's gravitational potential due to the orbital motion of the Earth and its rotation. In this varying potential, both clocks experience frequency drift. However, their common position requires the ratios of their frequency drifts to be equal. A clock in a gravitational field experience a shift of its frequency ν from its unperturbed value ν_0:

$$\nu = \nu_0(1+\frac{U}{c^2})$$

where U is the Sun potential and c is the speed of light. Change of the Sun potential results in fractional frequency change:

$$\frac{\Delta\nu}{\nu} = \frac{\Delta U}{c^2}$$

Possible violation of this law can be expressed by an introduction of coefficient β:

$$\frac{\Delta\nu}{\nu} = (1+\beta)\frac{\Delta U}{c^2}.$$

We expect β to be different for different types of clocks. Hence, the difference in the fractional frequency of two nonidentical clocks in varying Sun potential results in:

$$\frac{\Delta\nu_1}{\nu_1} - \frac{\Delta\nu_2}{\nu_2} = (\beta_1-\beta_2)\frac{\Delta U}{c^2}.$$

with $\frac{\Delta\nu}{\nu} = \frac{\Delta\nu_1}{\nu_1} - \frac{\Delta\nu_2}{\nu_2}$ and $\beta = \beta_1 - \beta_2$ we simplify this equation to:

Table 6: Comparison of the obtained parameter P_{KT} with published results.

Reference	P_{KT}	Duration	description
Hils and Hall 1990 [105]	$< 6.6\times10^{-5}$	105 days	I_2 line and optical cavity
Braxmaier et al. 2002 [30]	$(1.9\pm2.1)\times10^{-5}$	190 days	cryo. optical sapphire resonator vs. I_2
Wolf et al. 2004 [106]	$(1.6\pm3.0)\times10^{-7}$	1 year	cryo. sapphire oscillator vs. H-maser
Tobar et al. 2010 [32]	$(-1.7\pm4.0)\times10^{-8}$	6 years	cryo. sapphire oscillator vs. H-maser
This work	$(0.86\pm1.06)\times10^{-5}$	163 days	cryo. optical Si resonator vs. H-maser

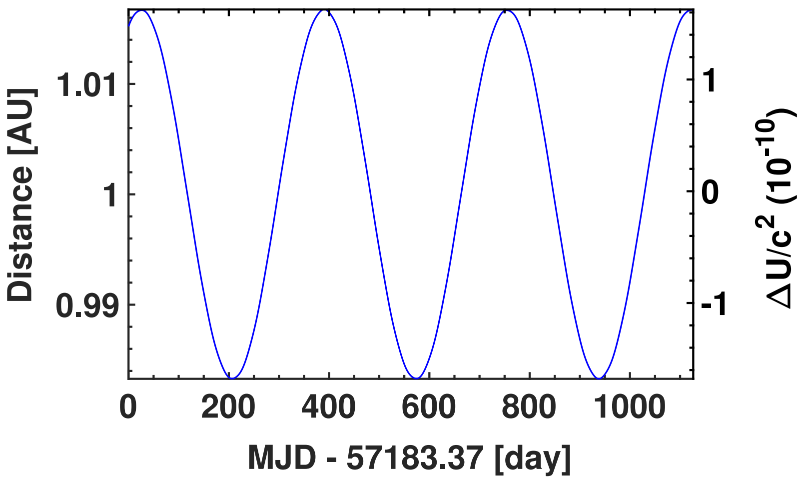

Figure A.12: Absolute Earth-Sun distance (left) and the Sun gravitational potential change (right) during the experiment.

$$\frac{\Delta\nu}{\nu} = \beta \frac{\Delta U}{c^2}. \tag{A.12}$$

Sun gravitational potential is equal to:

$$\frac{U}{c^2} = -\frac{Gm}{Dc^2}, \tag{A.13}$$

where G is the gravitational constant, m is the mass of the Sun, and D is the Earth-Sun distance. To calculate the Sun potential on Earth for the time of the experiment we compute the Earth-Sun distance D using the VSOP 87 algorithm [107] with a precision of 2.5×10^{-8} AU (see Fig. A.12). With the amplitude of Sun-Earth distance change of 3.35×10^{-2} AU the amplitude of the annual potential variation is equal to:

$$\frac{\Delta U}{c^2} = \frac{Gm}{\Delta D c^2} = 1.65 \times 10^{-10}. \tag{A.14}$$

In case of the diurnal variation of the potential the expression in Eq.A.13 is:

$$\frac{U}{c^2} = -\frac{Gm}{D^2 c^2} R\cos(\chi)\cos(\varepsilon)\cos(2\pi t). \tag{A.15}$$

The time t is set to zero when the lab position crosses the imaginary Sun-Earth line at midday. With the parameters R, χ, and ε, defined in Tab. 5, the amplitude of the diurnal potential change at the lab location in Düsseldorf is equal to:

$$\frac{Gm}{\Delta D^2 c^2} R\cos(\chi)\cos(\varepsilon) = 1.21 \times 10^{-13}. \tag{A.16}$$

This amplitude is three orders of magnitude smaller than the amplitude of the annual Sun potential variation (see Eq. A.14).

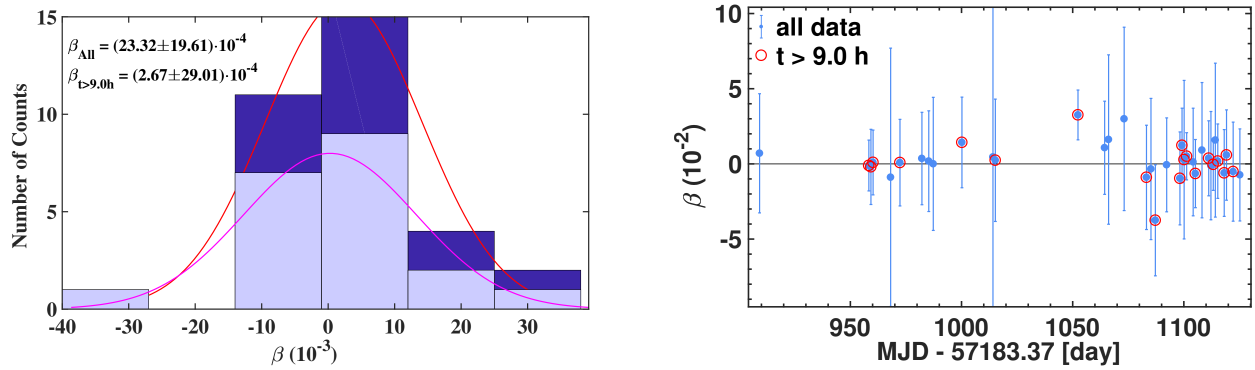

Figure A.13: **Left panel:** distribution of fit results for all data sets (blue colored histogram) and for data sets with a duration of longer then 9 h (light blue colored histogram) together with corresponding normal fits. **Right panel:** resulted parameter β from fits of all data sets. Data sets with duration of more then 9 h are additionally marked with red circle.

Sensitivity to diurnal variations of Sun potential

We analyze sensitivity to diurnal variations by fitting data sets with Eq. A.12, where we use Eq. A.15 for the Sun potential. The drift of the frequency is subtracted before fitting. The results of the fits are presented in Fig. A.13. We obtain:

$$\beta = (27 \pm 21) \cdot 10^{-4}$$

from all data sets, and

$$\beta = (3 \pm 32) \cdot 10^{-4}$$

from data sets with duration longer than 9 h, where the error is equal to the error of the mean ($\sigma/\sqrt{n}$).

Sensitivity to annual variations of Sun potential

Sensitivity to annual variation of sun potential is analyzed by fitting the two detrended data sets with following equation (see Fig. A.14, top row):

$$\Delta\nu = a - C\cos(\omega_o t - \varphi), \tag{A.17}$$

where ω_o is the angular frequency of the Earth rotation around Sun. The time t is counted from the last Perihelion (first data set 2016.01.02, 22:49, second data set: 2017.01.04 at 14:18 GMT). The phase φ is defined by the time difference between the last Perihelion and the start of the measurement campaign. The coefficient β is obtained by comparison of the amplitude of the cosine term C, divided by the absolute optical frequency, with the amplitude of the Sun potential (see Eq. A.12, Eq. A.13 and Eq. A.14):

$$\frac{C}{\nu} = \beta \frac{\Delta U}{c^2}.$$

Table 7: Comparison of the obtained parameter β with published results.

Reference	β	Duration	frequency comparison made
Turneaure et al. 1983 [108]	$\leq 1.7 \times 10^{-2}$	10 days	two H-masers vs. three SCSO's
Godone et al. 1995 [109]	$\leq 7 \times 10^{-4}$	430 days	Magnesium standard vs. cesium clock
Tobar et al. 2010 [32]	$(-2.7 \pm 1.4) \times 10^{-4}$	6 years	cryogenic sapphire oscillator vs. H-maser
Ashby et al 2018 [110]	$(2.2 \pm 2.5) \times 10^{-7}$	>14 years	H-masers at metrology labs
This work	$(1.02 \pm 1.13) \times 10^{-4}$	1 year	cryogenic optical Si resonator vs. H-maser

This comparison yields for the first data set:

$$\beta = (6.65 \pm 18.57) \cdot 10^{-5},$$

and

$$\beta = (12.28 \pm 14.20) \cdot 10^{-5}$$

for the second data set. The weighted average with a 1σ error is:

$$\beta = (10.2 \pm 11.28) \cdot 10^{-5}$$

These constraints are one order of magnitude better than the constraints obtained from the evaluation of the diurnal data sets (see the previous section). Table. 7 shows a selection of published results from other groups. Though our result is worse by two orders of magnitude when compared with the current best estimation of β made by Ashby et al., it is better than the best previous result achieved with an optical resonator. The improvement is by a factor of more than two with a total duration of the experiment reduced by a factor of 6.

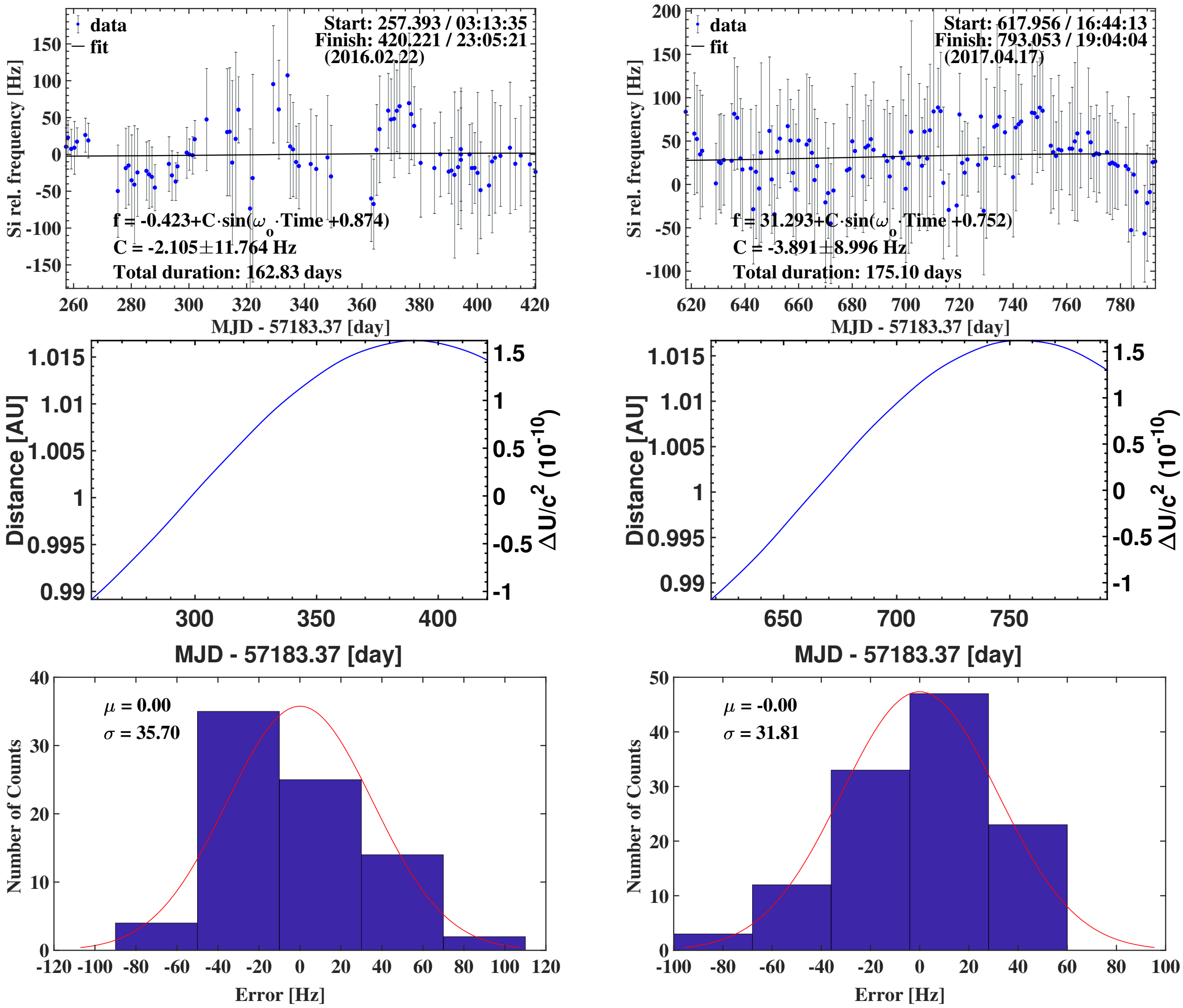

Figure A.14: Two data sets with a duration of approximately 0.5 year each, used for the evaluation of LPI. **Top row panels:** fit of both data sets with eq. A.17. **Middle row panels:** corresponding change of the Sun-Earth distance and of the Sun gravitational potential. **Bottom row panels:** distribution of the fit residuals fitted with a Gaussian function.

B Determination of the silicon optical absorption

Si bulk optical absorption α at the wavelength of $\lambda = 1562$ nm was determined from measurements of thermal relaxation of Si optical resonator operated at approximately 1.4 K by illuminating the front mirror of the resonator with the ULE prestabilized laser light of stable amplitude and frequency (compare Sec. 6). The schematic in Fig. B.1 displays the absorption process in the front mirror substrate of the resonator. Due to the antireflection coating at the front end of the mirror, all laser radiation is inserted into the mirror substrate. After passing the distance equal to 6.3 mm the light is reflected at the high-reflection coating at the backside of the substrate and returns back to the front end of the mirror, where it exits the resonator. This results in the total path length inside the silicon mirror substrate being equal to 12.6 mm. As the frequency of the laser light does not match the resonance frequency of the resonator no light is coupled inside the spacer. Due to the large heat conductivity of silicon (~10 W/mK)[75], the absorbed heat is instantly distributed inside the resonator and the corresponding increase in temperature is detected by the sensor attached to the middle of the resonator. As the resonator is supported by steel wires with very low thermal conductivity compared to that of silicon, the resonator is only loosely thermally connected to the experimental plate acting as a bath of constant temperature. Thus, in this experiment, the resonator plays a role of a calorimeter.

In the following we state the governing equation of the mathematical model of the resonator:

$$\frac{\mathrm{d}Q_{Si}}{\mathrm{d}t} = C_{Si}\frac{\mathrm{d}T_{Si}}{\mathrm{d}t} = P_{Ab} - k(T_{Si} - T_{BB})\,,$$

where P_{In} is the power of the light impinging on the cavity, C_{Si} and T are the heat capacity and temperature of silicon, respectively, P_{Ab} absorbed optical power, T_{BB} temperature of the cavity frame and optical

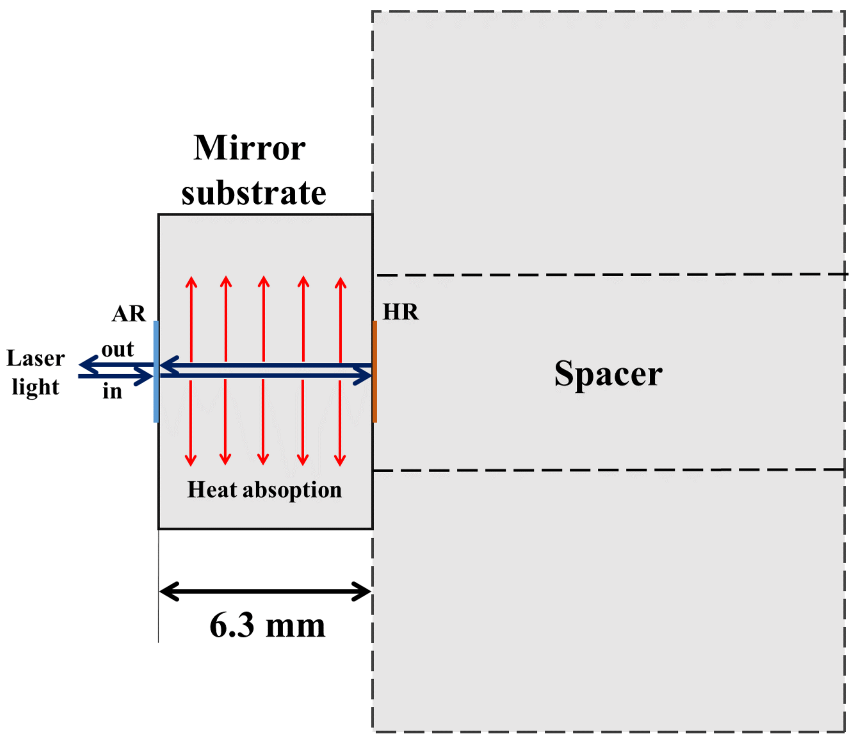

Figure B.1: Schematic of the experiment for the determination of optical absorption of silicon mirror substrates coated with the antireflection (**AR**) and high reflection (**HR**) coating at the front and the back, respectively.

breadboard, and, k the thermal conductance of the supporting steel wires. We integrate this equation:

$$\int_{T_{BB}}^{T_{Si}} \frac{\mathrm{d}T'}{P_{Ab} - k(T' - T_{BB})} = \frac{1}{C_{Si}} \int_0^t \mathrm{d}t' ,$$

$$-\frac{1}{k} \int_{T_{BB}}^{T_{Si}} \frac{\mathrm{d}(P_{Ab} - k(T' - T_{BB}))}{P_{Ab} - k(T' - T_{BB})} = \frac{1}{C_{Si}} \int_0^t \mathrm{d}t' ,$$

$$\ln\left(P_{Ab} - k(T' - T_{BB})\right)|_{T_{BB}}^{T_{Si}} = -\frac{k}{C_{Si}} t ,$$

$$\ln\left(P_{Ab} - k(T_{Si} - T_{BB})\right) - \ln P_{Ab} = -\frac{k}{C_{Si}} t ,$$

$$T_{Si} - T_{BB} = \frac{P_{Ab}}{k}(1 - \exp(-\frac{k}{C_{Si}} t)) . \tag{B.1}$$

Experimental data were fitted with the above equation B.1 to extract values for absorbed power P_{Ab}, the relaxation time of the system $\tau_{\nearrow} = \frac{C_{Si}}{k}$, and thermal conductance of steel wires $k_{\nearrow}$. The heat capacity of the resonator was determined from the Debye model for the specific heat:

$$C = 9Nk_B(\frac{T}{\Theta_D})^3 \int_0^{\Theta_D/T} x^4 e^x (e^x - 1)^{-2} \mathrm{d}x ,$$

with $\Theta_D = 640$ K the Debye temperature of Si and the mass of the resonator ($m = 2.23$ kg). Fit results are summarized in the Table 8.

After reaching the equilibrium temperature the laser light was blocked to allow the resonator to cool down back to the cryostat base temperature. This process of releasing heat stored in the resonator to the cryostat surrounding can be described mathematically as follows:

$$\frac{\mathrm{d}Q_{Si}}{\mathrm{d}t} = C_{Si}\frac{\mathrm{d}T_{Si}}{\mathrm{d}t} = -k(T_{Si} - T_{BB}) ,$$

where $T_{Si}(t)$ is time dependent and minus in the right part of the equation signifies that the rate of temperature change is negative. The general solution of the above equation is:

$$T_{Si}(t) - T_{BB} = C\exp(-\frac{k}{C_{Si}} t) ,$$

with the starting condition at $t = 0$ we obtain

$$T_{Si}(t) = T_{BB} + (T_{Si}(t = 0) - T_{BB})\exp(-\frac{k}{C_{Si}} t) . \tag{B.2}$$

The fit of the above Newton's cooling law equation to the experimental data was done to obtain relaxation time $\tau_{\searrow} = \frac{C_{Si}}{k}$ and thermal wire conductance $k_{\searrow}$.

To fit the data with eq. B.1 and eq. B.2 heat capacity of the resonator was determined using Debye model for the specific heat:

$$C = 9Nk_B(\frac{T}{\Theta_D})^3 \int_0^{\Theta_D/T} x^4 e^x (e^x - 1)^{-2} \mathrm{d}x , \tag{B.3}$$

were $\Theta_D = 640$ K is the Debye temperature of Si. Heat capacity of our Si resonator with a mass of $m = 2.23$ kg is displayed in Fig. B.3. Fit results are summarized in the Table 8.

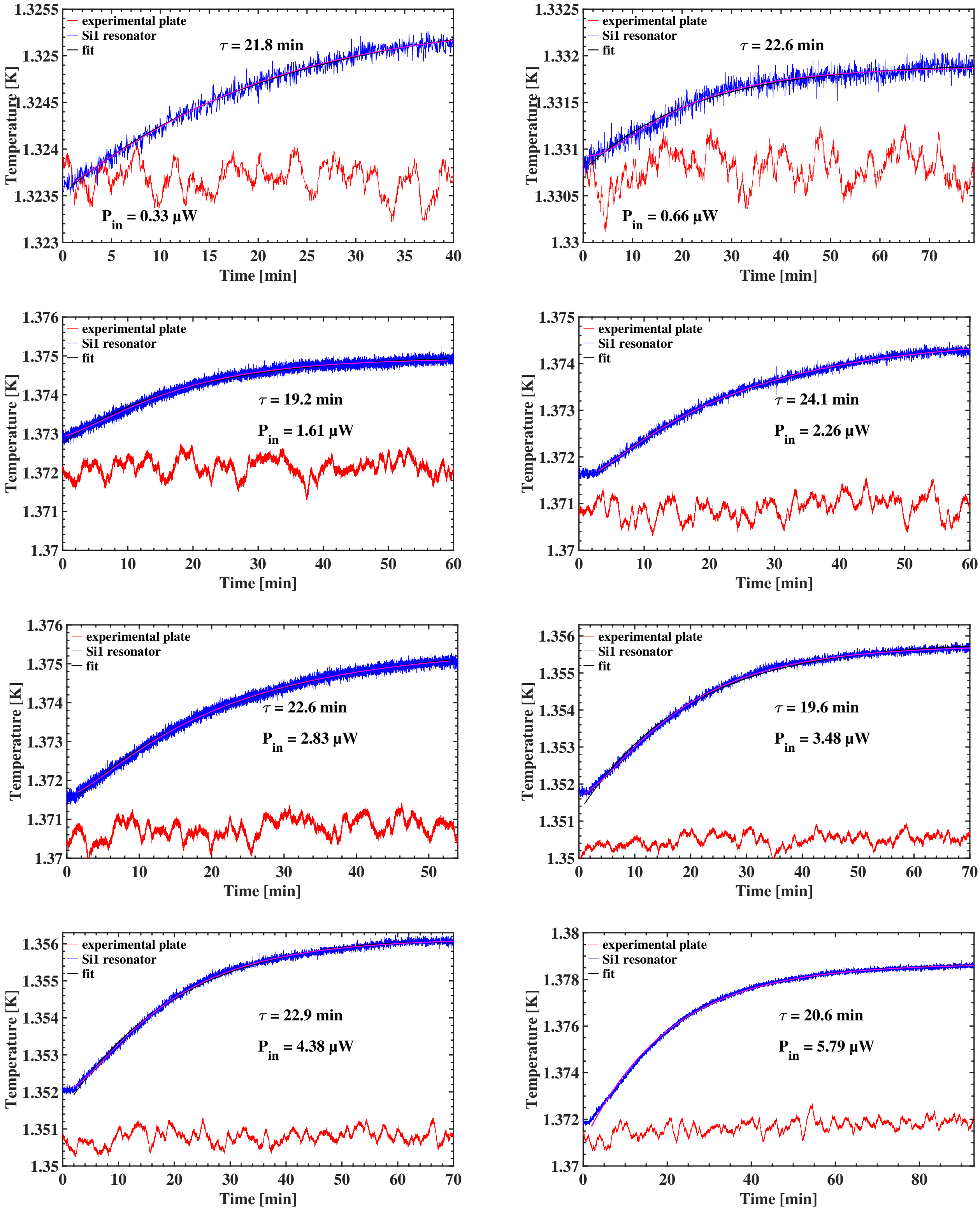

Figure B.2: Temperature data of the Si resonator and its supporting frame taken by illuminating the cavity front mirror with laser light of stable frequency and different optical powers away from cavity resonance together with the fit result using fitting equation B.1.

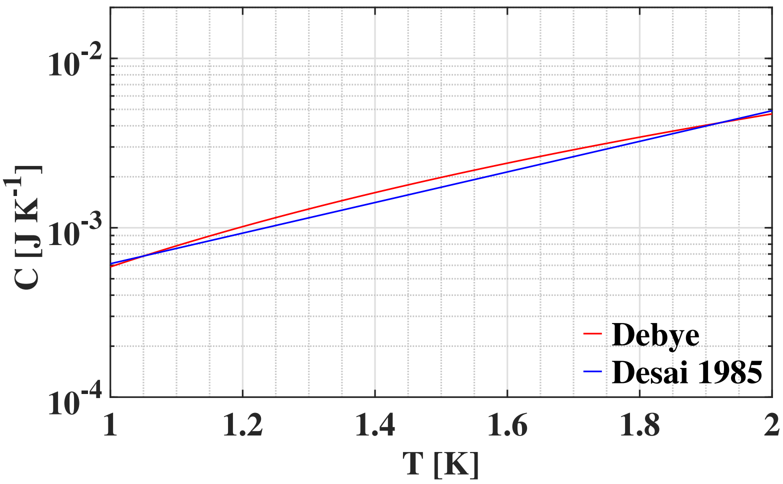

Figure B.3: Heat capacity C of the silicon resonator with a total mass of $m = 2.23$ kg in the temperature range of interest calculated using Debye model in the eq.B.3.

Table 8: Absorbed power P_{Ab} together with the 2σ fit error, relaxation time of the system at heating $\tau_{\nearrow}$ and cooling $\tau_{\searrow}$ and the mean relaxation time τ, thermal conductivity of the supporting wires from the fits during heating $k_{\nearrow}$ and cooling $k_{\searrow}$, determined from the fits of the experimental data with eq. B.1 and different impinging light powers P_{In}, and the fits with eq.B.2.

P_{In}, µW	P_{Ab}, nW	$\tau_{\nearrow}$, min	$\tau_{\searrow}$, min	τ, min	$k_{\nearrow}$, µW/K	$k_{\searrow}$, µW/K
0.5	1.96±0.11	21.8	17.1	19.45	1.04	1.33
1.0	1.12±0.04	22.6	17.6	20.1	1.02	1.31
2.44	2.94±0.02	19.2	19.2	19.2	1.32	1.32
3.44	3.09±0.03	24.1	18	21.05	1.05	1.41
4.3	4.38±0.02	22.6	17.4	20.0	1.11	1.45
5.2	5.19±0.03	18.8	20.7	19.8	1.29	1.17
6.65	5.39±0.03	18.8	20.4	19.6	1.29	1.19
8.85	8.59±0.02	20.6	19.3	19.95	1.23	1.31

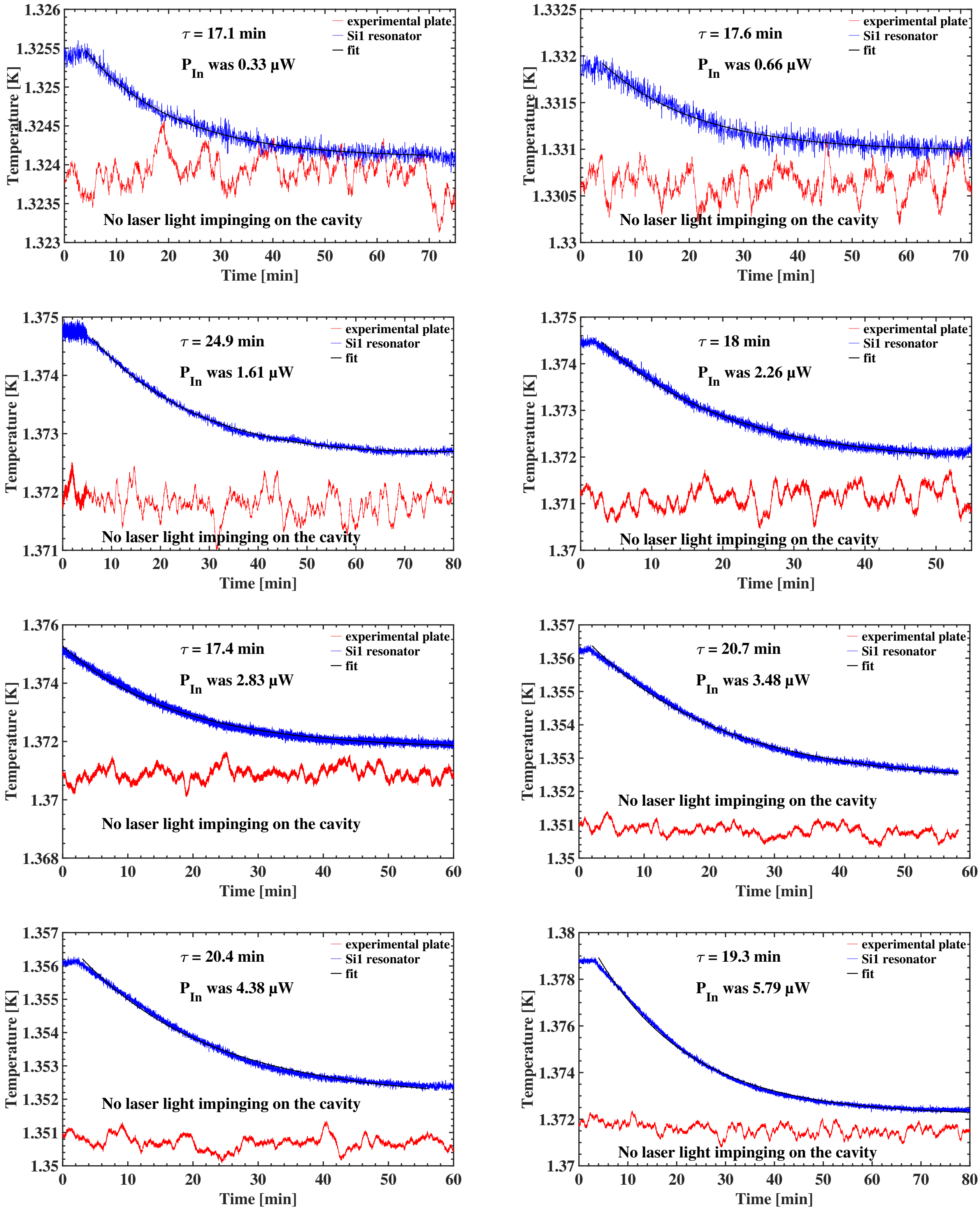

Figure B.4: Temperature data of the Si resonator and its supporting frame taken after blocking the laser light of different optical powers (Fig. B.2) together with the fit result using fitting equation B.2.

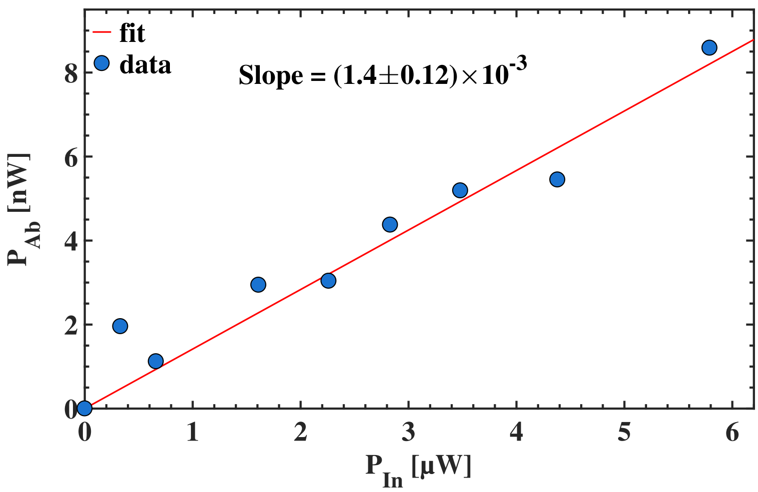

Figure B.5: Relation of the optical power absorbed in a substrate P_{Ab}, to the total input optical power P_{In}.

The amount of optical power absorbed in a bulk sample can be described by the following formula:

$$P_{In} - P_{Ab} = P_{In} e^{-\alpha x},$$

with absorption coefficient α and a path length of light inside the sample x. Solving this equation for α results in:

$$\alpha = -\frac{1}{x} \ln(1 - \frac{P_{Ab}}{P_{In}}).$$

Together with the total optical path inside the substrate of $x = 1.26$ cm, which equals to the double pass of the substrate, and the relation of P_{Ab} to P_{In}, determined from the slope of the linear fit to the data presented in Table 8 (see Fig. B.5), we thus obtain:

$$\alpha = (1400 \pm 120)\, \frac{ppm}{cm}$$

P_{In} is an ideal case of no absorption of light on its way to the resonator. Assuming that losses at the fiber connector which connects the cryogenic optical fiber as well as losses during the passage of light through the cryogenic optical setup are possible, an effective optical power impinging on the resonator is smaller than P_{In}. Thus, our result sets the lower limit for the absorption coefficient:

$$\alpha \geq (1440 \pm 120)\, \frac{ppm}{cm}$$

This result is a factor 300 higher than the value measured by another group (5 $\frac{ppm}{cm}$)[111]. However, such a simple comparison is not appropriate, as the optical absorption is also a function of the purity of the silicon material used for the experiment.

C Development of the BeCu cantilever blade for passive vertical vibration isolation

To dampen vibrations in a vertical direction inside a cryostat a cantilever blade was developed. The resonance frequency of the blade should be below the working frequency of the cryostat, 1.4 Hz. Damping of a typical vibration isolator starts from the frequency $f = \sqrt{2} f_{res}$ [112]. Thus, the resonance frequency of the cantilever blade should not exceed 1 Hz. In the following, we derive formulas for the resonance frequency and the deflection of the cantilever blade under the load of mass m.

C.1 Analytical calculations

Fig. C.1 depicts a schematic of a cantilever blade of length L under load F, applied to the tip of the blade. The curvature of the blade ρ can be described as [113]:

$$\frac{1}{\rho} = \frac{M(x)}{EI}, \tag{C.1}$$

with $M(x)$ the bending moment, E Young's modulus, and I is the moment of inertia. The curvature is also equal to

$$\frac{1}{\rho} = \frac{\frac{d^2y}{dx^2}}{[1+(\frac{dy}{dx})^2]^{3/2}},$$

for small deflections the derivative $\frac{dy}{dx} = \tan\theta$ and the above formula simplifies to

$$\frac{1}{\rho} = \frac{\frac{d^2y}{dx^2}}{[1+(\tan\theta_0)^2]^{3/2}} = \frac{d^2y}{dx^2}\cos^3\theta_0.$$

We insert this expression in eq. C.1 together with $M(x) = -F(L\cos\theta_0 - x)$ and obtain:

$$EI\frac{d^2y}{dx^2}\cos^3\theta_0 = -F(L\cos\theta_0 - x). \tag{C.2}$$

With a cantilever of rectangular cross section, the length a, and thickness d, the moment of inertia is constant:

$$I = \frac{ad^3}{12}. \tag{C.3}$$

Moment of inertia of the triangular cantilever blade is:

$$I = \frac{ad^2}{18}. \tag{C.4}$$

With constant I we can integrate eq. C.3:

$$EI\frac{dy}{dx}\cos^3\theta_0 = -F(xL\cos\theta_0 - \frac{1}{2}x^2) + C.$$

With the boundary condition $x = 0$, $\frac{dy}{dx} = \tan\theta_0$ the constant of integration is $C = EI\tan\theta_0\cos^3\theta_0$. Inserting this in the above equation we obtain:

$$EI\frac{dy}{dx}\cos^3\theta_0 = -F(xL\cos\theta_0 - \frac{1}{2}x^2) + EI\tan\theta_0\cos^3\theta_0. \tag{C.5}$$

Integrating this equation a second time, and resolving for y yields

$$y = -\frac{F}{2EI\cos^3\theta_0}(x^2L\cos\theta_0 - \frac{1}{3}x^3) + x\tan\theta_0, \tag{C.6}$$

where we used the boundary condition $x = 0$, $y = 0$ to obtain the constant of integration. To obtain the deflection δ at the tip of the blade we define its coordinates (x_t, y_t) as [114] :

$$(x_t, y_t) = (L\cos\theta_0 + \delta\sin\theta_0,\ L\sin\theta_0 - \delta\cos\theta_0).$$

We first insert x_t into eq. C.6 and neglect all higher order terms of δ:

$$y_t = -\frac{FL^3}{3EI}(1 + \frac{3\delta\tan\theta_0}{2L}) + L\sin\theta_0 + \delta\sin\theta_0\tan\theta_0.$$

Inserting the expression for y_t in the above equation yields:

$$\delta = \frac{FL^3}{3EI}(1 + \frac{3\delta\tan\theta_0}{2L})\cos\theta_0,$$

We solve for δ:

$$\delta = \frac{2}{3}\frac{FL^3}{2EI - FL^2\sin\theta_0}\cos\theta_0. \tag{C.7}$$

for the absolute deflection. For the cantilever blade fixed at $\theta_0 = 0$ deg this formula simplifies to the known formula from the textbook:

$$\delta = \frac{FL^3}{3EI}.$$

With the eq. C.3) the above equation becomes

$$\delta = \frac{2}{3}\frac{FL^3}{\frac{Ead^3}{6} - FL^2\sin\theta_0}\cos\theta_0. \tag{C.8}$$

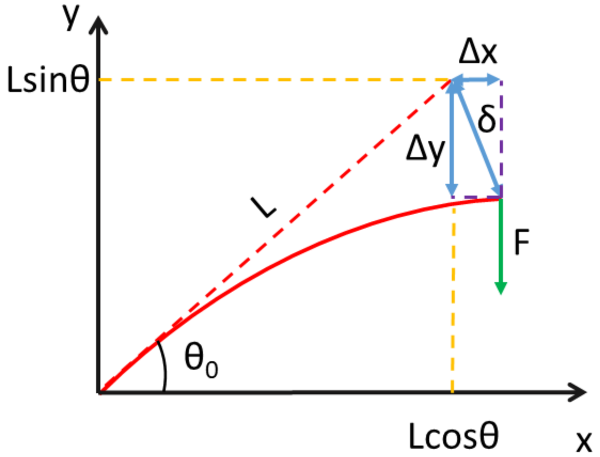

Figure C.1: Schematic of the cantilever blade of length L fixed at an angle θ_0 with respect to the horizontal x-axis before (red dashed line) and after (red line) application of force F, which deflects the blade by amount δ with projection Δx and Δy on the x- and y-axis, respectively.

In the definition of the moment of inertia (see eq. C.3) we set the length of the cross section of the blade a constant. To allow for blade profile with the coordinate dependent length $a(x)$ of the cross section we introduce an additional shape factor α [115]:

$$\alpha = \frac{3}{2(1-\beta)}(3 - \frac{2}{1-\beta}(1 + \frac{\beta^2 \log\beta}{1-\beta})), \tag{C.9}$$

where β is the ratio between the short and wide ends of the blade. α changes from 1.0 to 1.5 for the transition of the blade shape from rectangular to triangular, respectively. Inserting α in eq. C.8 we obtain the final expression for the maximal blade deflection:

$$\delta = \alpha \frac{4FL^3}{Ead^3 - 6FL^2 \sin\theta_0} \cos\theta_0. \tag{C.10}$$

From this equation we can extract the stiffness k of the blade:

$$k = \frac{Ead^3 - 6FL^2 \sin\theta_0}{4\alpha L^3 \cos\theta_0}. \tag{C.11}$$

We can use this expression to calculate the resonance frequency of the blade

$$f_{res} = \frac{1}{2\pi}\sqrt{\frac{Ead^3 - 6FL^2 \sin\theta_0}{4\alpha m L^3 \cos\theta_0}}. \tag{C.12}$$

The resonance frequency is thus proportional to:

$$f_{res} \sim (\frac{d}{L})^{3/2}$$

That means, that to have low resonance frequency, the blade must be thin and long. To calculate the maximal tensile stress on the material we use [113]:

$$\sigma_{max} = \frac{6FL}{ad^2} \cos\theta_0,$$

where the force moment is modified by the angle θ_0. If the angle is $\theta_0 > 0$ the material of the blade experiences additional compression stress, which must be added to the above equation:

$$\sigma_{max} = \frac{6FL}{ad^2} \cos\theta_0 + \frac{F}{ad} \sin\theta_0.$$

C.2 FEM simulations

FEM simulations are performed to verify the above formulas and to obtain the stress distribution over the blade profile. Usually, cantilever blades used for the damping of vibrations work under high steady stress to obtain larger deflections, and therefore to lower the resonance frequency of the blade. At high stress rates, the creeping of the material is a problem. It renders materials such as stainless steel unsuitable. According to [116] only beryllium copper and maraging steel can sustain high stress levels for long times without creep. We have selected BeCu because of its availability. Relevant BeCu material properties are summarized in Tab. 9. Due to the geometry constraints of the cryostat we have chosen the trapezoidal shape of the blade with a length of $L = 170$ mm. The length of the fixed end a, thickness d , and the length of the free edge of the blade have to be derived. The FEM simulations are performed with

Table 9: Properties BeCu with a number of other materials displayed for comparison.

/	AISI 304 [118]	Alu 2024-T4 [118]	BeCu [119]	Cu [118]
Density [kg/m^3]	8000	2780	8260	8930
Elastic modulus [GPa]	193	73.1	115	110
Poisson ratio	0.29	0.33	0.30	0.343
Ultimate tensile strength [MPa]	505	469	483	210
Yield strength ($R_{p0.2}$) [MPa]	215	324	1130-1420	33.3

a load of mass $m = 50$ kg applied to the free end of the blade. An acceleration equal to the acceleration of gravity is acting at the setup. The angle θ_0 is set to 0 deg during the simulation and the deflection of the tip of the blade and the maximum stress is recorded. Expected large deformation of the material requires working with the modulus "large deflections" switched on in the simulation software. The comparison of the FEM simulation results with the analytical results yields a 12 % difference between the results for deflection of 73 mm. This difference is readily explained by the fact, that derivation of analytical expression was made under the assumption, that deflection is low. The stress level is slightly underestimated by the simulation. As in the case of deflection, this difference is explained by inappropriate assumptions made for analytical expressions. To validate the simulation results we have also simulated the cantilever blade developed for the GEO 600 detector [117] and achieved a good agreement with their results.

After FEM and analytical results were proved consistent we performed an extensive search for the suitable shape of the cantilever blade by setting the angle θ_0 equal to zero and modifying the thickness of the blade d and length of the blade base a, and calculating the resonance frequency and material stress. The results are presented in Fig. C.2. They suggest that it is impossible to obtain a BeCu cantilever blade with a resonance frequency of 1 Hz and a material stress level not higher than 90 % of the allowable yield strength $R_{p0.2}$ with constraints posed by the available space in the cryostat. The lowest frequency is in the range of 1.6 Hz. We have also investigated the influence of angle θ_0. Both deflection and stress increase with angle θ_0 until reaching the maximum at an angle of approximately $\theta_0 \approx 40$ deg. After that, they decrease with higher angles (see Fig. C.3). This feature can be used to decrease the resonance frequency of the blade but at a cost of additional material stress.

To finalize the design of the blade we set the blade thickness at a constant value of $d = 2$ mm predetermined by the manufacturer. From Fig. C.2 we can infer, that by holding the thickness of the blade constant we can decrease the resonance frequency by reducing the base length of the blade. Thus, we perform simulations with a base length of the blade varying in the range from 150 to 120 mm. For each base length we change the tilt θ_0. Results of the simulations are presented in Fig. C.3. They suggest that the optimal base length and tilt angle of the blade is 130 mm and 40 deg, respectively. The resulted resonant frequency is 1.66 Hz and the stress of the material amounts to 89 % of the allowable yield strength.

The distribution of material stress for the cantilever blade with an optimal geometry determined above is displayed in Fig. C.4.While the stress levels are highest along the edges of the upper surface, the lower surface displays the highest stress near the middle and at the fixed end of the blade.

We also determined the frequency of the eigenmodes of vibration of the cantilever blade with geometry parameters determined above. We depict the first three eigenmodes of vibration in Fig. C.5. With $f_1 = 79$ Hz, $f_2 = 350$ Hz, and $f_3 = 424$ Hz they are far away from the regions with the most disturbance from the pulse tube (see Fig. 3.8).

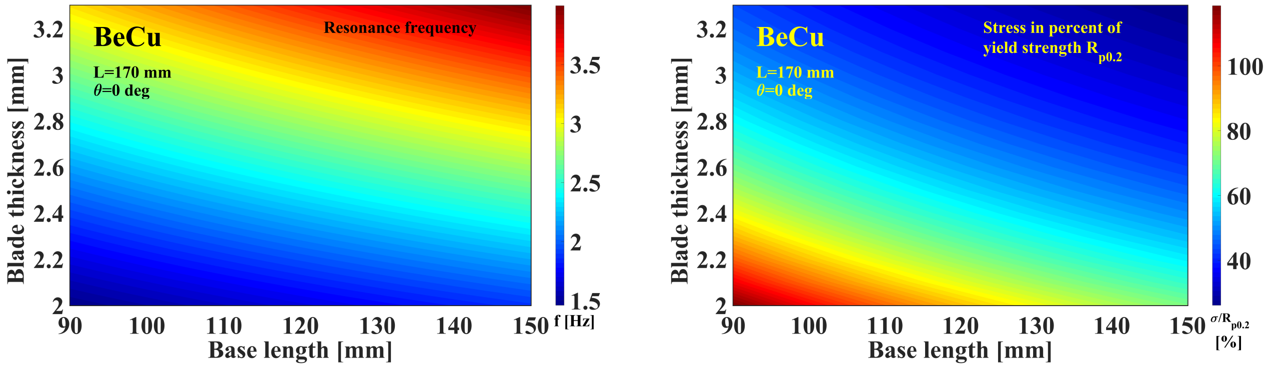

Figure C.2: Resonance frequency of the BeCu cantilever blade (**left panel**) and stress of the material in percent of the maximum allowable stress (**right panel**) as function of blade length and blade thickness for tilt angle $\theta_0 = 0$ deg of the blade at the clamped side.

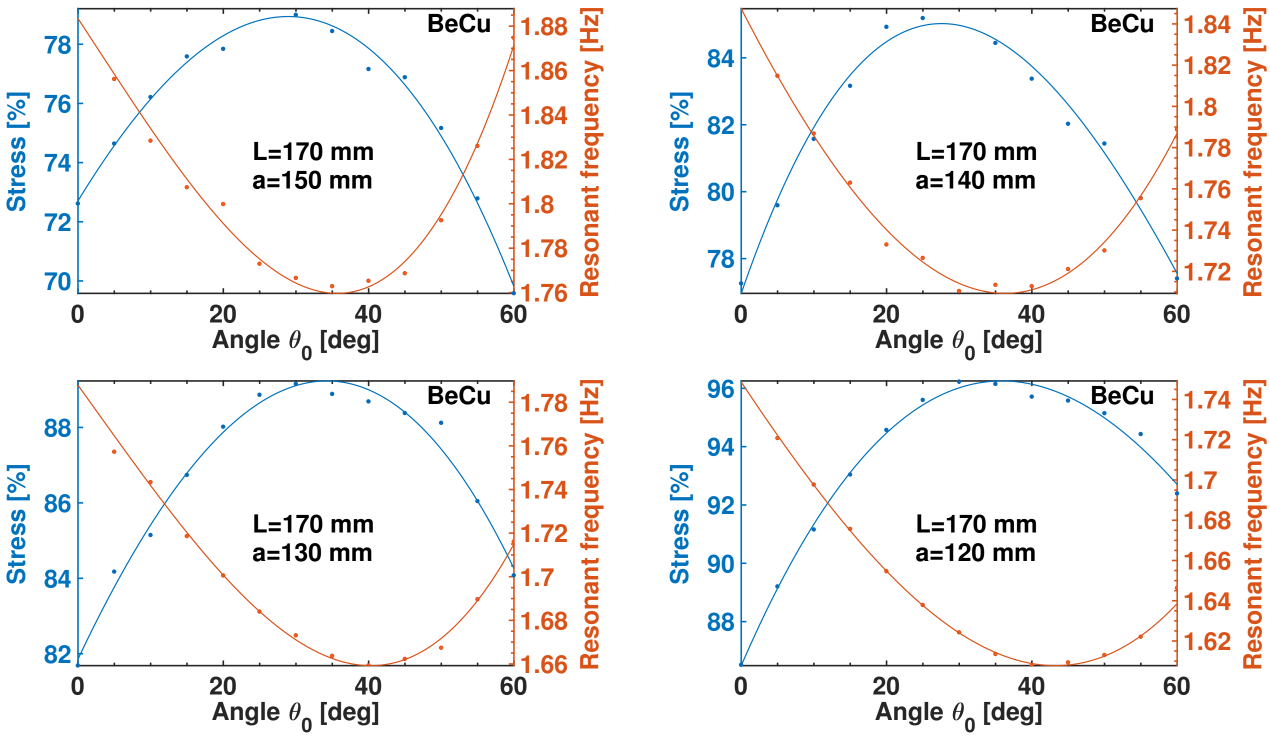

Figure C.3: Results of the FEM simulation used to determine the lowest resonant frequency and material stress for the optimal blade base length a and tilt angle θ_0.

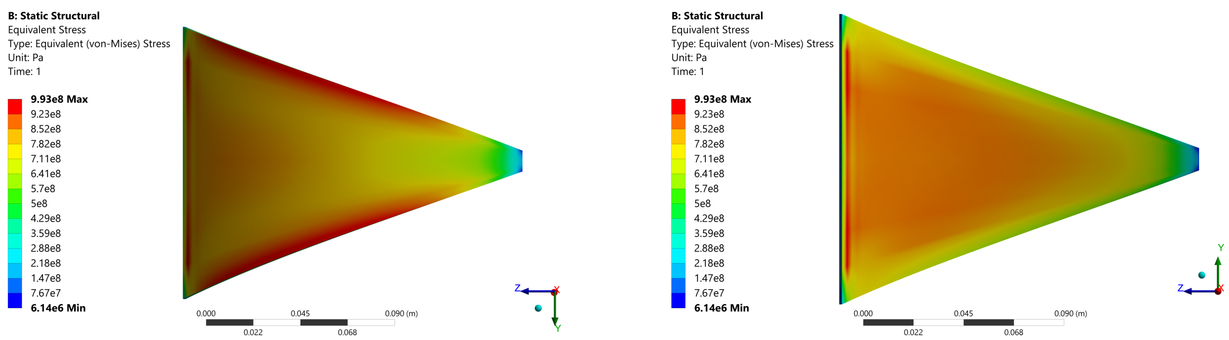

Figure C.4: Material stress distribution over the top (**left**) and bottom (**right**) surface of the cantilever blade with a length of $L = 170$ mm, thickness $d = 2$ mm, and length of the base side $a = 130$ mm determined from the FEM simulations with the base clamped at 40 deg tilt angle and a force equivalent to a load of 50 kg applied to the blade's tip.

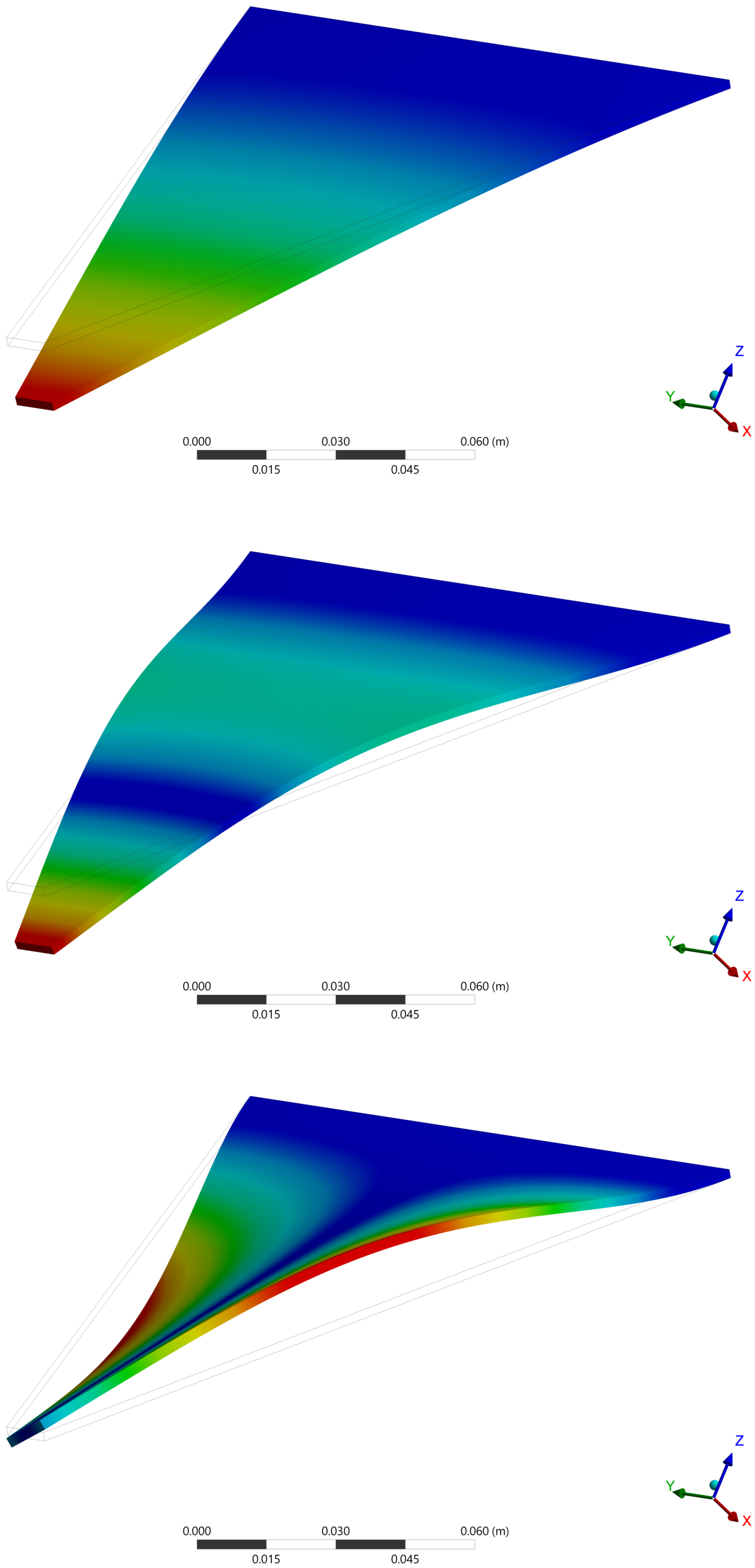

Figure C.5: First three eigenmodes of vibration of cantilever blade with optimal geometry and fixed base determined from FEM simulations corresponding to the frequency of $f = 79$ Hz (**top**), $f = 350$ Hz (**middle**), and $f = 424$ Hz (**bottom**).

D Calibration of geophones

Geophones represent inexpensive and sensitive sensors for the monitoring of the velocity changes. For continuous measurements of vibrations at the experiment inside the cryostat we use a set of three GS-11D geophones (Geospace Technologies) with a natural frequency of 4.5 Hz, coil resistance of 4000 Ohms, and a sensitivity of 28.8 V/m/s and 32 V/m/s along a horizontal and vertical direction, respectively. To be used in the measurements of acceleration we calibrated geophones at room temperature by comparing their output with the output of a calibrated acceleration sensor with a sensitivity of 1000 V/g (Wilcoxon, 731A/P31), while attached next to each other at a moving platform able to produce periodic displacement along all three orthogonal directions in the frequency range from 1 Hz to 200 Hz. To increase the sensitivity of geophones in the frequency range below their natural frequency a home-built amplifier was used.

We compare the frequency-dependent voltage output of the geophones with the acceleration measured with the calibrated sensor. The result is presented in Fig. D.1. We observe a decrease in the sensitivity of geophones to vibrations with increasing frequency. Using a fit of the 9th order polynomial $poly(f)$ to the data we can obtain the frequency-dependent acceleration spectrum $A(g)$ from the spectrum in Volts $A(V)$ using the following expression:

$$A(g) = \frac{A(V)}{poly(f)},$$

where f is the excitation frequency and $poly(f)$ is defined for the vertical and horizontal geophones as follows:

$$poly(f)_{Horizontal} = -9.45\times10^{-16}f^9 + 9.14\times10^{-13}f^8 - 3.76\times10^{10}f^7 + 8.59\times10^{-8}f^6 - \\ -1.19\times10^{-5}f^5 + 1.05\times10^{-3}f^4 - 5.81\times10^{-2}f^3 + 2.02\times10^{0}f^2 - 4.37\times10^{1}f^1 + 5.84\times10^{2}f^0,$$

$$poly(f)_{Vertical} = -3.65\times10^{-16}f^9 + 3.51\times10^{-13}f^8 - 1.43\times10^{10}f^7 + 3.24\times10^{-8}f^6 - \\ -4.47\times10^{-6}f^5 + 3.9\times10^{-4}f^4 - 2.22\times10^{-2}f^3 + 8.68\times10^{1}f^2 - 2.53\times10^{1}f^1 + 5.17\times10^{2}f^0.$$

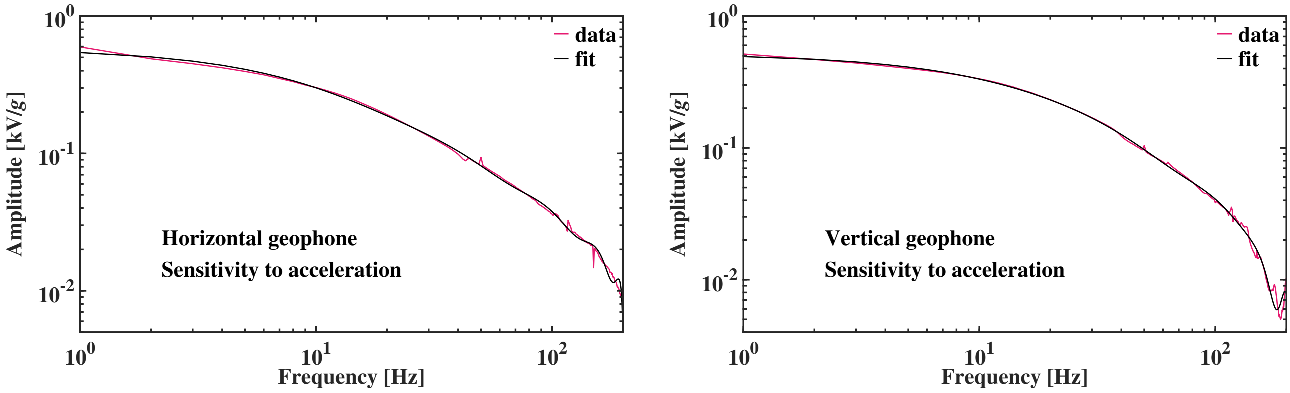

Figure D.1: Calibration of geophones by comparing their voltage output with the output of a calibrated acceleration sensor and applying a 9th order polynomial fit.

E Dimensions of the resonators

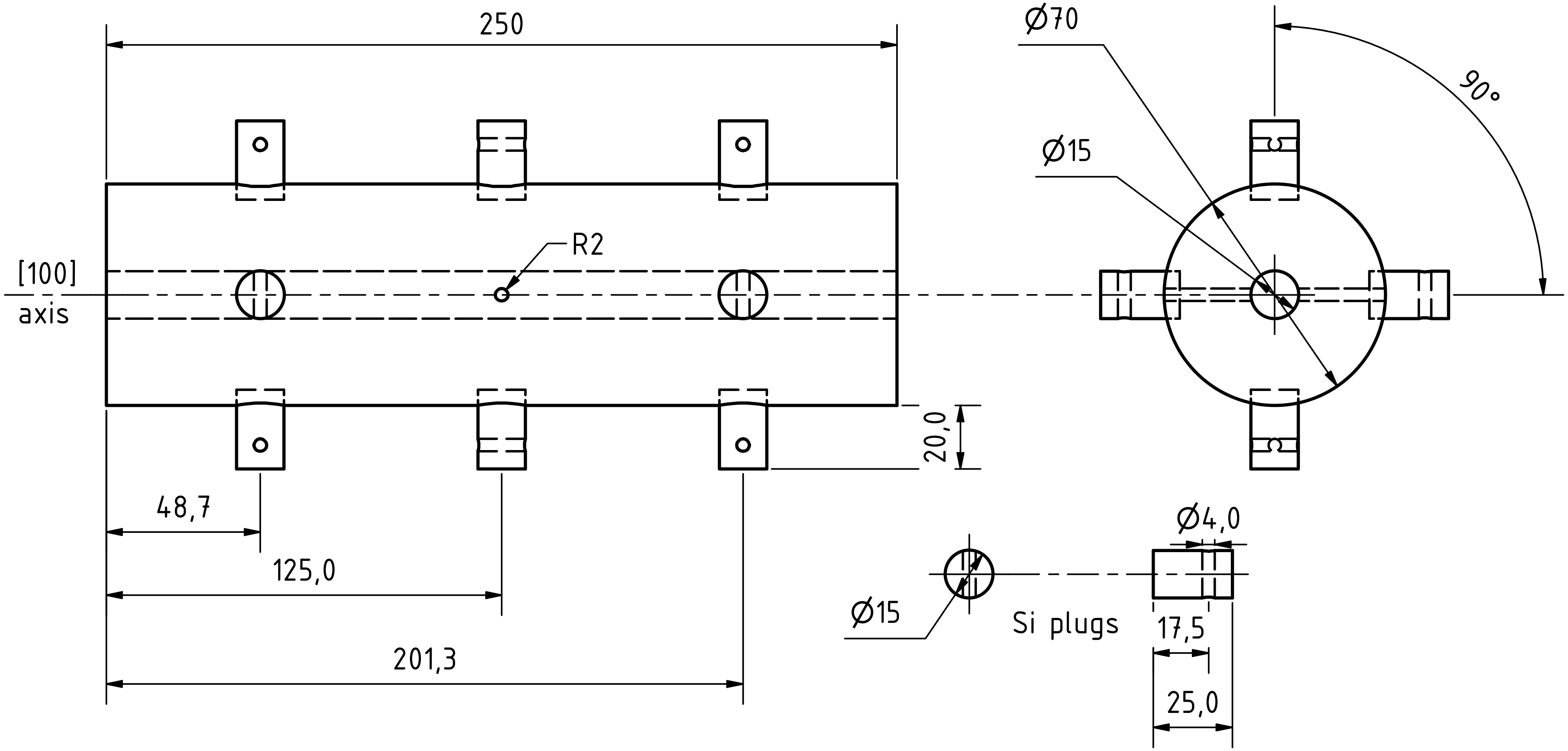

General tolerance ISO 2768-fH		Scale: 1:2
		Silicon, [111] orientation
	Date	Name
Drawn	1/9/2021	Wiens
Checked		
Standard		

Si1 spacer

1

A4

State	Changes	Date	Name

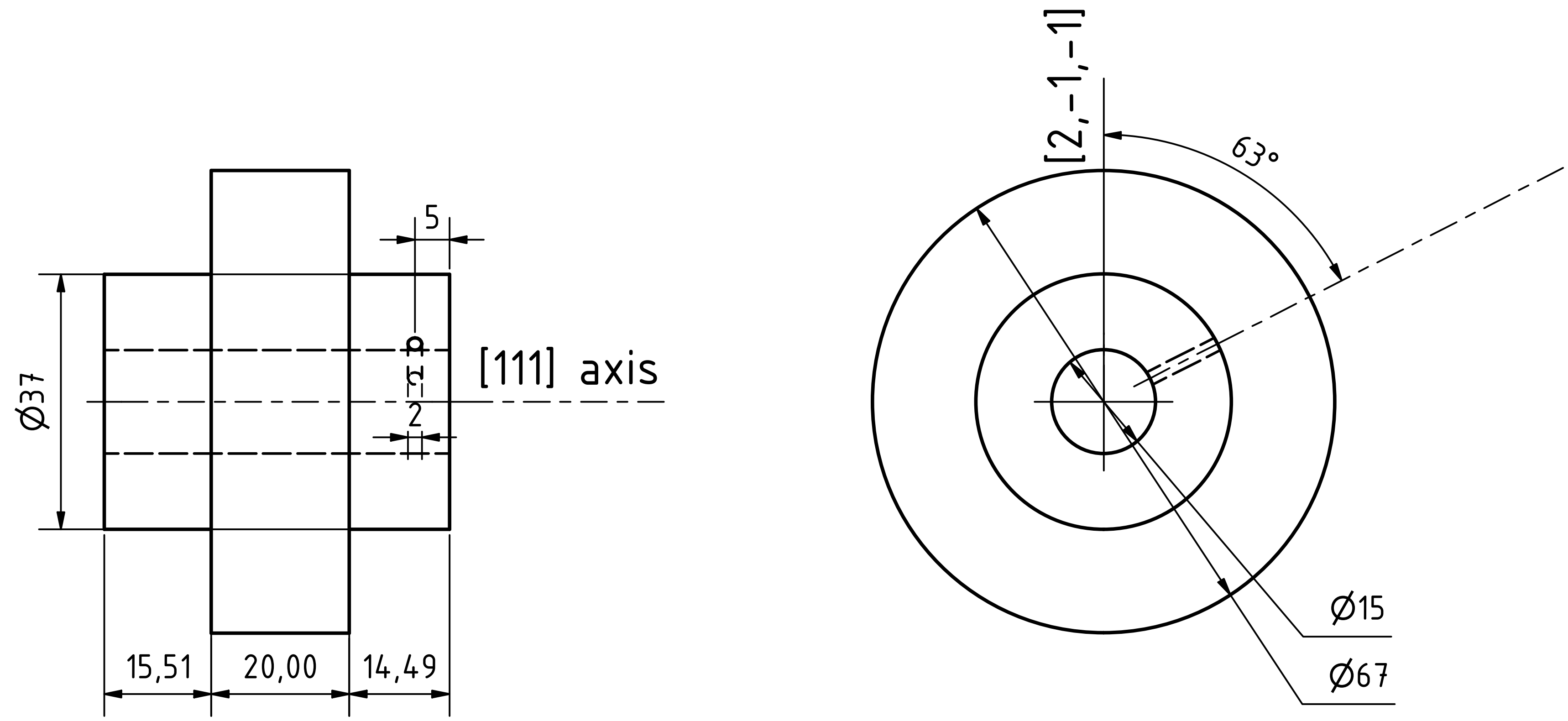

General tolerance ISO 2768-fH		Scale: 1:1	
		Silicon, [111] orientation	
	Date	Name	
Drawn	8/15/2017	Wiens	
Checked			
Standard			
		Si5 spacer	1 A4

State	Changes	Date	Name

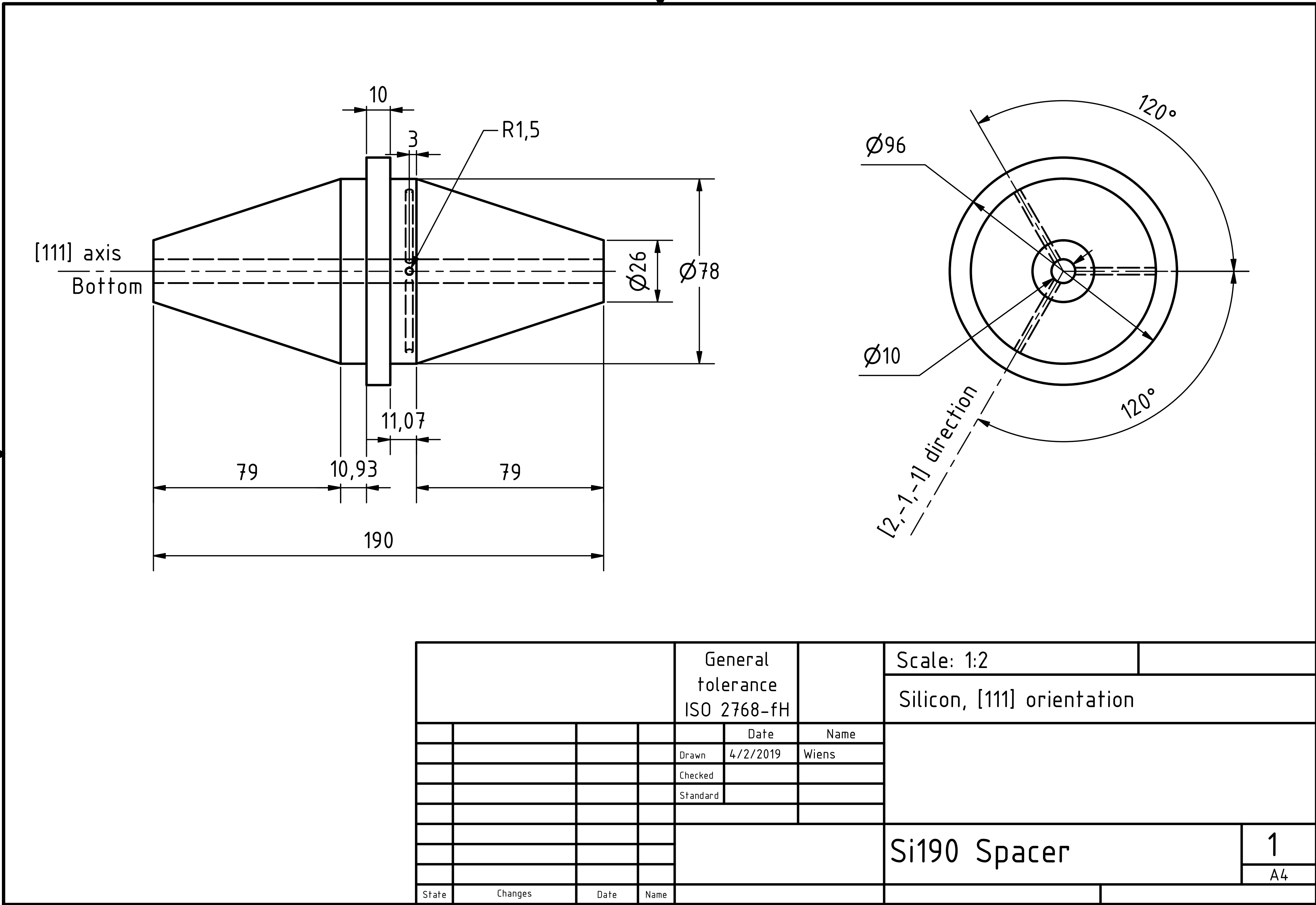

10
3
R1,5
[111] axis
Bottom
Ø26
Ø78
11,07
79
10,93
79
190
Ø96
Ø10
120°
120°
[2,-1,-1] direction
General tolerance ISO 2768-fH
Scale: 1:2
Silicon, [111] orientation
Date
Name
Drawn
4/2/2019
Wiens
Checked
Standard
Si190 Spacer
1
A4
State
Changes
Date
Name

F Publications

F.1 Publication: Silicon single-crystal cryogenic optical resonator

Reproduced from

Eugen Wiens, Qun-Feng Chen, Ingo Ernsting, Heiko Luckmann,

Ulrich Rosowski, Alexander Nevsky, and Stephan Schiller

Silicon single-crystal cryogenic optical resonator

Optics Letters **39**, 3242 (2014)

DOI: https://doi.org/10.1364/OL.39.003242

Corrections:

Optics Letters **40**, 68 (2015)

DOI: https://doi.org/10.1364/OL.40.000068

Author's contributions

All authors contributed to the work. My contributions to this work are:

- Assembling the resonator and the supporting frame.
- Installation of the resonator inside the cryostat.
- Operation of the cryostat.
- Measurement of the coefficient of thermal expansion and evaluation of the results.
- Co-writing the publication.

A silicon single-crystal cryogenic optical resonator

Eugen Wiens, Qun-Feng Chen, Ingo Ernsting, Heiko Luckmann, Ulrich Rosowski, Alexander Nevsky, and Stephan Schiller*

Institut für Experimentalphysik, Heinrich-Heine-Universität Düsseldorf, Düsseldorf, Germany
**Corresponding author: Step.Schiller@uni-duesseldorf.de*

Compiled March 28, 2014

We report on the demonstration and characterization of a silicon optical resonator for laser frequency stabilization, operating in the deep cryogenic regime at temperatures as low as 1.5 K. Robust operation is achieved, with absolute frequency drift less than 20 Hz over 1 hour. This stability allows sensitive measurements of the resonator thermal expansion coefficient (α). We find $\alpha = 4.6 \times 10^{-13}\mathrm{K}^{-1}$ at 1.6 K. At 16.8 K α vanishes, with a derivative equal to $-6 \times 10^{-10}\mathrm{K}^{-2}$. The temperature of the resonator could be stabilized to a level below 10 μK for averaging times longer than 20 s. The sensitivity of the resonator frequency to a variation of the laser power was also determined. The corresponding sensitivities, and the expected Brownian noise indicate that this system should enable frequency stabilization of lasers at the low-10^{-17} level.

OCIS codes: 120.3940, 120.4800, 140.3425, 140.4780.

Optical resonators with low sensitivity to temperature and mechanical forces are of significant importance for precision measurements in the optical and microwave frequency domain. In the optical domain, they serve to stabilize the frequencies of lasers for spectroscopic applications, notably for optical atomic clocks, and for probing fundamental physics issues such as the properties of space-time. Also, by conversion of ultrastable optical frequencies to the radio-frequency domain via an optical frequency comb, radio-frequency sources with ultra-low phase noise can be realized [1], leading to e.g. radar measurements with improved sensitivity.

The conventional approach for ultra-stable optical resonators is the use of ULE (ultra-low expansion glass) material, operated at temperatures near room temperature, where the coefficient of thermal expansion (CTE) exhibits a zero crossing. While ULE resonators with optimized designs (long length, acceleration-insensitive shape) have reached impressive performance [2], their operating temperature near 300 K necessarily leads to a level of Brownian length fluctuations which imposes a fundamental limit to the achievable frequency stability [3], [4]. Cryogenic operation of a resonator provides one avenue towards reduction of these fluctuations. The linear spectral density of length fluctuations decreases proportional to $\sqrt{T}$ [3], if the mechanical dissipation of the resonator elements, in particular of the mirror coatings, is independent of temperature. Measurements performed thus far indicate that the dissipation of mirrors with crystalline substrates at cryogenic temperature are indeed similar to those of fused silica mirrors at room temperature [5], [6]. Nowadays, robust cryogenic solutions exist for continuous operation of even fairly large objects, such as optical resonators, at temperatures as low as 0.1 K. This offers the possibility of reduction of resonator length fluctuations by more than one order of magnitude compared to today's lowest levels realized at room temperature, with a corresponding reduction in frequency instability of the laser stabilized to the resonator. A second outstanding feature of crystalline cryogenic optical resonators is the absence of length drift due to the near-perfect lattice structure.

Cryogenic optical resonators made of single-crystal sapphire have been developed early on [7] and operated at temperatures as low as 1.4 K [8]. Extremely small thermal expansion [7] and long-term drift were achieved [9]. Such resonators have been applied for tests of Lorentz invariance [10], local position invariance [11] and quantum space-time fluctuations [12]. Silicon, a machinable optical material available with high purity and large size, having interesting CTE properties [13], high stiffness and low mechanical dissipation [14], has first been used for an optical reference resonator by Richard and Hamilton [15]. Recently, Kessler et al. [16] developed a laser frequency stabilization system based on a vertically supported silicon resonator operated at a temperature of zero CTE, 124 K, and achieved a high frequency stability (1×10^{-16}), less than 40 mHz laser linewidth, and an extremely low long-term drift.

In this work, we present the first silicon optical resonator for absolute laser frequency stabilization operated at cryogenic temperature and discuss its thermal properties. We find that they are compatible with the goal of achieving frequency instability at the 1×10^{-17} level.

Our silicon resonator consists of a cylindrical spacer of 250 mm length, 70 mm diameter and 15 mm diameter central hole. One mirror is flat, while the other has 1 m curvature radius. Spacer and mirror substrates were manufactured from a dislocation-free float-zone silicon crystal with [110] orientation along the cylinder axis. The substrates and spacer faces were super-polished to a residual surface roughness less than 0.1 nm. The mirror substrates were coated with a high-reflectivity coating for 1.5 μm, and optically contacted to the spacer with the same orientation as in the spacer crystal. By evaluation of a ring-down of the laser power transmitted through the resonator at 1.5 K, the finesse and the linewidth of the resonator were determined to be 200 000 and 3 kHz, respectively. The coupling efficiency into the resonator is 15%.

A special structure for horizontal support of the resonator was implemented. It was designed for small acceleration sensitivity of the resonator's length and small stress imposed by the different CTE of resonator and supporting structure, and for blocking thermal radiation entering the cryostat through the optical window. The design is based on the concept developed by PTB [17] (see Fig. 1). The resonator is attached to a copper frame by three sets of 1 mm diameter stainless steel wires at 10 points. Their position was optimized by finite-element method (FEM, Comsol) in order to minimize acceleration sensitivity along the three axes. The estimated sensitivities are $3 \times 10^{-10}/g$ and $3 \times 10^{-11}/g$ along the resonator optical axis and perpendicular to it, respectively. We also simulated the influence of the supporting structure on the CTE of the resonator. It is a function of temperature, due to the temperature dependence of the CTE of both the resonator and the frame. The results indicate negligible dependence of the CTE of the resonator (α_{reson}) on a change in frame temperature at temperatures below 16.8 K. The CTE zero crossing points at 17 K and 124 K are shifted by 2 mK and 10 mK, respectively, due to the contribution from the frame.

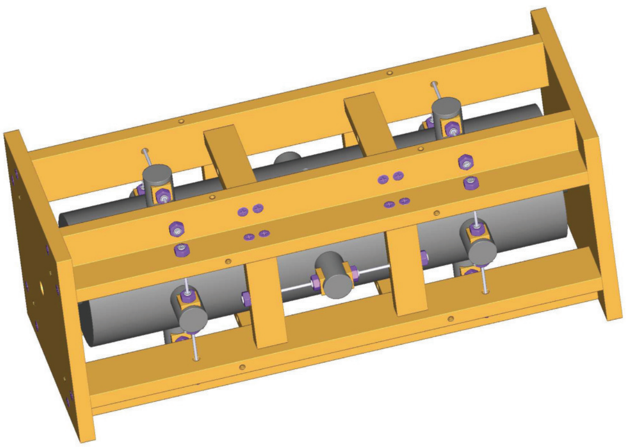

Fig. 1. Schematic of the copper support structure with mounted silicon resonator (grey).

The frame was rigidly attached to an optical breadboard inside a cryostat. A 1.5 μm fiber laser was coupled to the resonator through an optical window. The frequency was stabilized to a TEM_{00} mode of the resonator using the Pound-Drewer-Hall (PDH) technique [18], with a standard optical scheme and using a waveguide phase modulator. The laser power circulating inside the resonator was stabilized by detection of the light transmitted through the resonator and applying a feedback signal to an acousto-optical modulator in the optical setup.

The resonator unit was installed inside a low-vibration, two-stage pulse tube cooler cryostat with Joule-Thomson stage. It allows a lowest operating temperature of 1.4 K and a cooling power of 20 mW. Two calibrated Cernox sensors (inaccuracy less than 10 mK at temperatures below 30 K) were available for controlling and/or monitoring the temperature of the supporting breadboard and of the resonator. One sensor was attached to the center of the breadboard, while the other was attached to the upper central part of the resonator. An AC resistance bridge was used to read out the temperature sensors. A resistance heater installed on the center of the breadboard was used for setting and maintaining a desired operating temperature. When the temperature of resonator is stabilized by controlling the resistance of the resonator sensor, the measured instability at the sensor location is 3.6×10^{-5} K at $\tau = 1$ s averaging time, dropping as $3.6 \times 10^{-5}/(\tau/1s)^{1/2}$ K for τ up to 10^4 s. We estimate that the temperature instability of the average temperature of the resonator is within a moderate factor of the above number, since the very high thermal diffusivity of silicon at cryogenic temperature allows for a rapid thermal equilibration within the resonator. The AC bridge electronics contributes a specified systematic error of 1.7×10^{-5} K per degree variation of the ambient temperature. Thus, in a laboratory stabilized to 0.5 K, the resonator temperature systematic shift is less than 1×10^{-5}K.

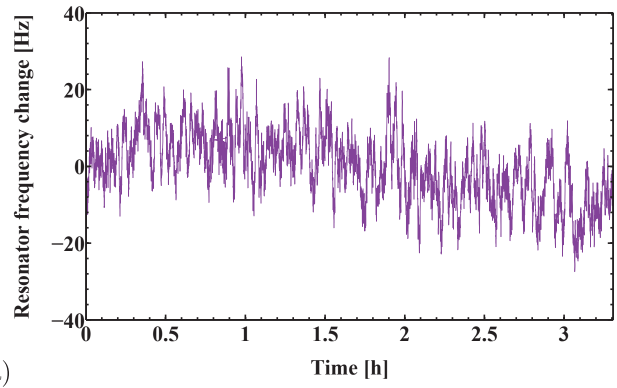

a)

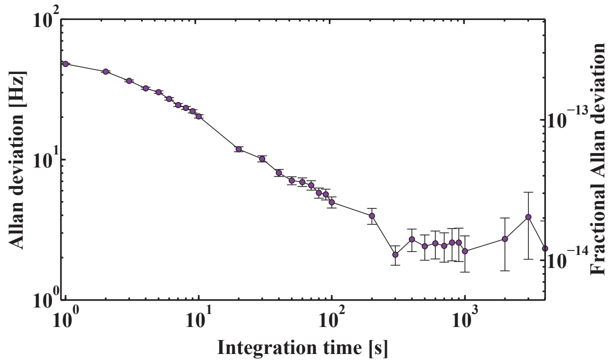

b)

Fig. 2. a) Time trace averaged over 60 s of a typical resonator frequency measurement relative to a hydrogen maser. Each point corresponds to a 1-s average. The black line is an average over 60 s, b) corresponding Allan deviation.

Measurements of the absolute optical resonator frequency were done with respect to a hydrogen maser, using a fiber laser femtosecond frequency comb. It was phase-locked to an optical reference operating at 1064 nm having 1×10^{-15} frequency instability, in order to reduce its short-term fluctuations. The laser light was sent from the laser to the comb via a 150 m length-stabilized fiber. A typical resonator frequency time trace and the corresponding instability, with all parameters including temperature held constant, is depicted in Fig. 2. For integration times longer than 1000 s the frequency instability was approximately 3 Hz (2×10^{-14}), the value being limited by the operating conditions of our hydrogen maser, as determined by an independent characterization of the latter.

Given this level of absolute frequency instability and the good resolution of the temperature sensors, the resonator's thermal expansion coefficient can be accurately measured. The measurements were done either by heating the resonator or by letting it cool down to 1.5 K after heating it up to a desired temperature. The rate of temperature change was approximately 1.5 K/h at temperatures above 1.8 K and much lower for temperatures below 1.8 K, where it was limited by the cooling capacity of the cryostat. No significant discrepancies were found between two measurement procedures.

The temperature dependence of the resonator frequency is presented in Fig. 3. The total change in frequency from 1.5 K to 23.8 K is 6 MHz, with most of the shift occurring in the region above 20 K. A minimum of the frequency occurs at $T_{\alpha=0} = 16.81$ K with negative frequency derivative df/dT (length expansion) below this temperature and positive (length contraction) above it [19]. Between 1.6 K to 2 K the shift in frequency is only 100 Hz (5×10^{-13}).

Whereas the CTE of an insulating crystal at low temperatures is expected to be positive and proportional to T^3 [13], in the case of silicon its thermal expansion behaviour (expansion turns into contraction between 16.8 K and 124 K) necessarily implies that such a dependence can accurately hold only for $T \to 0$. The value predicted from compressibility and heat capacity measurements is $\alpha_{Si} = 4.8\times10^{-13}\mathrm{K}^{-1}(T/\mathrm{K})^3$ [13]. As displayed in Fig. 3 a pure T^3 dependence does not fit the data well. Therefore, the data were fitted with a function containing additional high-order terms. At the lowest temperatures, we find $\alpha_{reson}(T \to 0) = (1.1\times T^3 - 7.8\times T^4 + 8.4\times T^5)\times10^{-13}$, where T is the temperature in Kelvin. Our measured α_{reson} is thus lower then the theoretical value for bulk silicon. At 1.6 K, the value is $\alpha_{reson} = 4.6\times10^{-13}/\mathrm{K}$.

The frequency data around the frequency minimum at $T_{\alpha=0} = 16.8\,\mathrm{K}$ were accurately fitted by a fourth-order polynomial from which we obtain the resonator expansion coefficient $\alpha_{reson}(T \simeq T_{\alpha=0}) = \sum_{n=0}^{2} B_n(T/\mathrm{K})^n$ with $B_n = (37\times10^{-9},\ -4.94\times10^{-9},\ 1.64\times10^{-10})\,\mathrm{K}^{-1}$. The complete dataset from 1.6 K to 23.8 K was fitted with a ninth-order polynomial (black line in Fig. 3), from which we obtain the resonator thermal expansion coefficient $\alpha_{reson}(T)$ shown as red line in Fig. 3 b). It is given by $\alpha_{reson}(T) = \sum_{n=0}^{8} A_n(T/K)^n$, with $A_n = (-9\times10^{-22},\ 4\times10^{-20},\ -7\times10^{-19},\ 2\times10^{-17},\ -3\times10^{-16},\ 2\times10^{-15},\ -1\times10^{-14},\ 3\times10^{-14},\ -2\times10^{-14})\,\mathrm{K}^{-1}$.

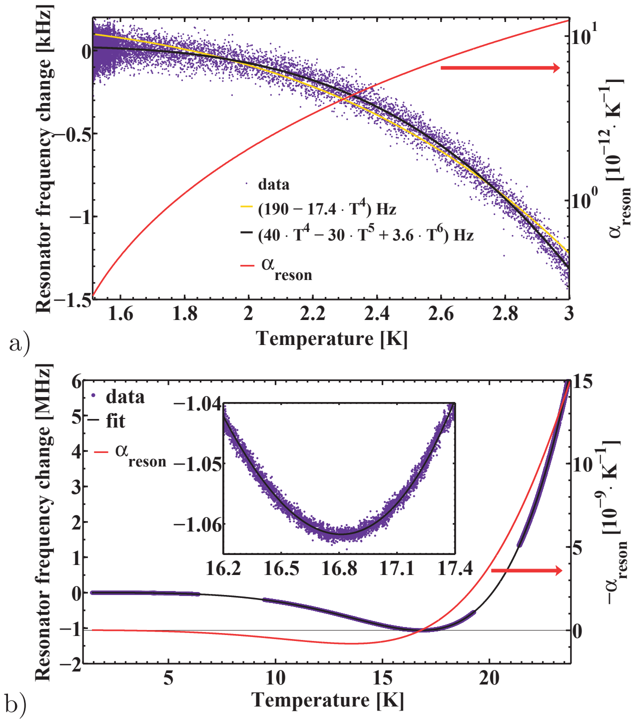

Fig. 3. Temperature dependence of the silicon resonator frequency in two temperature intervals. a) Interaval 1.5 K to 3 K, with fit results in the legend and corresponding expansion coefficient α_{reson} calculated from the second fit (black line). b) Interval from 1.5 K to 23.8 K with a polynomial fit (black) and calculated expansion coefficient α_{reson} (blue). The inset in b) shows a zoom of the interval where the CTE crosses zero.

To our knowledge, only two measurements of thermal expansion of silicon at cryogenic temperature, down to 12 K and 6 K [13] were performed previously. However, due to the difficulty of measuring the corresponding small CTEs, accurate CTE values were only given above 13 K [13], where the values are larger than $1\times10^{-9}/\mathrm{K}$. Our value of $T_{\alpha_{reson}=0} = 16.8\,\mathrm{K}$ is similar, but not identical to that of Ref. [13], where 17.8 K was measured. Our expansivity temperature derivative at 16.8 K is $d\alpha_{reson}(T_{\alpha_{reson}=0})/dT = -6.0\times10^{-10}/\mathrm{K}^2$, which is comparable to $-8.9\times10^{-10}/\mathrm{K}^2$ at 17.8 K in Ref. [13].This expansivity derivative at 16.8 K is nearly a factor 20 smaller than the at the second zero-CTE temperature 124.2 K, namely $1.7\times10^{-8}/\mathrm{K}^2$ [16]. This means that 16.8 K could also be a candidate operating temperature, with the advantage of less temperature sensitivity, and possibly smaller thermal noise, as compared to 124 K. Note that a cryostat for operation at 16.8 K can be of relatively simple construction. As mentioned above, the mirror coating dissipation at this temperature is similar to the room-temperature values for conventional mirror substrates.

With an estimated upper limit of 1×10^{-4} K resonator temperature instability at 1 s (discussed above) and the measured thermal expansion $\alpha_{reson}(T = 1.6\,\mathrm{K}) = 4.6\times10^{-13}\,\mathrm{K}^{-1}$, the corresponding fractional frequency instability is about 5×10^{-17} at 1 s and drops to 1×10^{-17} at $\tau = 30\,\mathrm{s}$. The fractional frequency shift error due to AC bridge temperature shift is expected to be less than 1×10^{-17}.

Fluctuations of the laser power incident on the resonator introduce changes in the power dissipated on the resonator mirrors and result in unwanted fluctuations in resonator length due to the thermal expansion of the mirrors and of the spacer. We measured the resonator frequency change caused by a varying level of intraresonator power at two different operating temperatures. We could not observe any effect, setting an upper limit of 20 Hz change for a 30% power change, both at 1.6 K and at 16.8 K. This upper limit corresponds approximately to $3\times10^{-14}/\mu$W.

Because of the absence of measurable effect, we also simulated the effect of laser heating using FEM and found a 1.4 fm mirror distance change for 10 μW power dissipated on each mirror at 1.5 K, i.e. a fractional resonator frequency change of $3\times10^{-16}/\mu$W total dissipated power. The simulation also shows that thermal equilibrium of the heated mirrors and the spacer is reached with a time constant of approximately 1 s in case of good thermal contact with the breadboard. For our experiment, the power level dissipated in the resonator is estimated as 1.5 μW. If the transmitted laser power is actively stabilized to 1% or better, a level that is expected to be well feasible using an advanced detector, the corresponding fractional frequency fluctuations would be 5×10^{-18} or less.

In summary, we demonstrated a silicon optical resonator for laser frequency stabilization that can be operated at temperatures between 1.5 K and 24 K and investigated its thermal properties. Stable, long-term operation was achieved at temperature as low as 1.4 K. The support structure for the resonator allows to take advantage of the low CTE of bulk silicon. The thermal expansion measurement was performed both at the lowest absolute temperature and with the highest sensitivity for a silicon object so far. The influence of finite thermal expansion coefficient and residual temperature instability on the cavity frequency was determined to be at the 5×10^{-17} fractional level and below, depending on averaging time. The sensitivity to changes in circulating laser power is expected to be controllable to the level better than 1×10^{-17} using an appropriate power stabilization unit. For this resonator, at the temperature 1.6 K, the expected total Brownian noise-induced frequency instability is calculated to be 6×10^{-18}, assuming a coating loss angle $\varphi = 1$ mrad, as determined for silicon mirrors at 20 K in Ref. [6].

We conclude that the thermal properties of the described system should allow to stabilize the frequency of a laser to an instability of less than 2×10^{-17} for integration times larger than 30 s, taking into account that the instability arising from the laser frequency locking system itself can be reduced to the level of 1×10^{-17} [20].

We are very grateful to Timo Müller (Wacker Chemitronic) for providing the crystal and to T. Legero and U. Sterr (PTB) for important help on the resonator. This work has been funded by ESA project no. 4000103508/11/D/JR.

References

1. Y. Y. Jiang, A. D. Ludlow, N. D. Lemke, R. W. Fox, J. A. Sherman, L.-S. Ma, and C. W. Oates, Nat. Phot. **5,** 158–161 (2011)
2. T. L. Nicholson, M. J. Martin, J. R. Williams, B. J. Bloom, M. Bishof, M. D. Swallows, S. L. Campbell, and J. Ye, Phys. Rev. Lett. **109,** 230801 (2012)
3. K. Numata, A. Kemery, und J. Camp, Phys. Rev. Lett. **93,** 250602 (2004).
4. G. D. Cole, W. Zhang, M. J. Martin, J. Ye, M. Aspelmeyer, Nature Photonics **7,** 644–650, (2013).
5. K. Yamamoto, S. Miyoki, T. Uchiyama, H. Ishitsuka, M. Ohashi, K. Kuroda, T. Tomaru, N. Sato, T. Suzuki, T. Haruyama, A. Yamamoto, T. Shintomi, K. Numata, K. Waseda, K. Ito, und K. Watanabe, Phys. Rev. D **74,** 022002 (2006).
6. M. Granata, K. Craig, G. Cagnoli, C. Carcy, W. Cunningham, J. Degallaix, R. Flaminio, D. Forest, M. Hart, J.-S. Hennig, J. Hough, I. MacLaren, I. W. Martin, C. Michel, N. Morgado, S. Otmani, L. Pinard, und S. Rowan, Opt. Lett. **38,** 5268–5271 (2013).
7. S. Seel, R. Storz, G. Ruoso, J. Mlynek, und S. Schiller,Physical Review Letters **78,** 4741–4744 (1997).
8. R. Storz, Dissertation, Univ. Konstanz (1998).
9. R. Storz, C. Braxmaier, K. Jack, O. Pradl, und S. Schiller, Optics Letters **23,** 1031–1033 (1998).
10. P. Antonini, M. Okhapkin, E. Goklü, S. Schiller, Physical Review A **71,** 050101, (2005).
11. C. Braxmaier, H. Müller, O. Pradl, J. Mlynek, A. Peters, S. Schiller, Physical Review Letters **88,** 010401 (2002).
12. S. Schiller, C. Lammerzahl, H. Müller, C. Braxmaier, S. Herrmann, A. Peters, Physical Review D **69,** 027504 (2004).
13. K. G. Lyon, G. L. Salinger, C. A. Swenson, and G. K. White, J. Appl. Phys. **48,** 865 (1977).
14. D. F. McGuigan, C. C. Lam, R. Q. Gram, A. W. Hoffman, D. H. Douglass, H. W. Gutche, J. Low Temp. Phys. **30,** 621–629 (1978).
15. J.-P. Richard, J. J. Hamilton, Rev. Sci. Instr. **62,** 2375–2378 (1991).
16. T. Kessler, C. Hagemann, C. Grebing, T. Legero, U. Sterr, and F. Riehle, Nature Photonics **6,** 687, (2012).
17. U. Sterr (PTB Braunschweig), German patent DE 10 2011 015 489.2, (2011).
18. R. W. P. Drever, J. L. Hall, F. V. Kowalski, J. Hough, G. M. Ford, A. J. Munley, and H. Ward, Appl. Phys. B **31,** 97 (1983).
19. T.F. Smith, G.K. White, J. Phys. C **7,** (1975).
20. Q.-F. Chen, A.Yu. Nevsky, and S. Schiller, Appl. Phys. B **107,** 679–683 (2012).

Silicon single-crystal cryogenic optical resonator: erratum

Eugen Wiens, Qun-Feng Chen, Ingo Ernsting, Heiko Luckmann, Ulrich Rosowski, Alexander Nevsky, and Stephan Schiller*

Institut für Experimentalphysik, Heinrich-Heine-Universität Düsseldorf, Düsseldorf, Germany
** Corresponding author: Step.Schiller@uni-duesseldorf.de*

Compiled November 7, 2014

We correct fit formulas for the coefficient of thermal expansion $\alpha_{reson}(T)$.

OCIS codes: 120.3940, 120.4800, 140.3425, 140.4780.

The fit formulas for the resonator fractional thermal expansion coefficient $\alpha_{reson}(T) = -f^{-1}d\,f(T)/d\,T$ on p. 3244 of our letter [1] were incorrectly reported.

1. The correct expression for $\alpha_{reson}(T \to 0)$ is $\alpha_{reson}(T \to 0) = (-1.14\,T^5 + 7.72\,T^4 - 8.32\,T^3) \times 10^{-13}\,\mathrm{K}^{-1}$, with 17% average fractional fit error for the coefficients. This function was plotted in Fig. 3a as a red curve. The fit was made on data combined from two independent low-noise frequency measurements performed between 1.51 K and 3 K with a total duration over 6 h.

Note that the fit function for $\alpha_{reson}(T \to 0)$ has a zero at a temperature close to 1 K. However, such an extrapolation is not supported by the data.

Experimentally, we find the 2σ upper bound $|\alpha_{reson}(T = 1.55\,\mathrm{K})| < 1.0 \times 10^{-12}\,\mathrm{K}^{-1}$.

2. The coefficients in the list B_n given after the expression for $\alpha_{reson}(T \simeq T_{\alpha=0})$ are: $(B_2, B_1, B_0) = (-1.647(2) \times 10^{-10}, 4.935(5) \times 10^{-9}, -36.42(2) \times 10^{-9})\,\mathrm{K}^{-1}$.

3. The coefficients A_n are as follows: $(A_8, A_7, \ldots, A_0) = (1.79 \times 10^{-6}, -116.8 \times 10^{-6}, 3.17 \times 10^{-3}, -58.6 \times 10^{-3}, 727.2 \times 10^{-3}, -5.07, 24.34, -51.46, 38.1) \times 10^{-12}\,\mathrm{K}^{-1}$. The errors of the coefficients are 5% for the T^0 coefficient and 1% for all other coefficients. The fit function with these coefficients was plotted in Fig. 3b.

References

1. E. Wiens, Q.-F. Chen, I. Ernsting, H. Luckmann, U. Rosowski, A. Yu. Nevsky, and S. Schiller, Opt. Lett. **39**, 3242–3245 (2014).

F.2 Publication: Resonator with Ultrahigh Length Stability as a Probe for Equivalence-Principle-Violating Physics

Reproduced from

E. Wiens, A. Yu. Nevsky, and S. Schiller

Resonator with Ultrahigh Length Stability as a Probe for Equivalence-Principle-Violating Physics

Phys. Rev. Lett. **117**, 271102 (2016)

DOI: https://doi.org/10.1103/PhysRevLett.117.271102

Author's contributions

All authors contributed to the work. My contributions to this work are:

- Assembling the resonator and the supporting frame.
- Installation of the resonator inside the cryostat and building an all-cryogenic optical setup for incoupling of laser light.
- Operation of the cryostat non-stop for over three years and doing the required maintenance.
- Measurement of the long-term frequency drift of the resonator using different experimental techniques with the aid of the frequency comb.
- Analysis of the experimental data.
- Co-writing the publication.

Resonator with Ultrahigh Length Stability as a Probe for Equivalence-Principle-Violating Physics

E. Wiens, A. Yu. Nevsky, and S. Schiller*

Institut für Experimentalphysik, Heinrich-Heine-Universtität Düsseldorf, 40225 Düsseldorf, Germany

(Received 25 September 2016; published 29 December 2016)

In order to investigate the long-term dimensional stability of matter, we have operated an optical resonator fabricated from crystalline silicon at 1.5 K continuously for over one year and repeatedly compared its resonance frequency $f_{\rm res}$ with the frequency of a GPS-monitored hydrogen maser. After allowing for an initial settling time, over a 163-day interval we found a mean fractional drift magnitude $|f_{\rm res}^{-1} df_{\rm res}/dt| < 1.4 \times 10^{-20}/{\rm s}$. The resonator frequency is determined by the physical length and the speed of light and we measure it with respect to the atomic unit of time. Thus the bound rules out, to first order, a hypothetical differential effect of the Universe's expansion on rulers and atomic clocks. We also constrain a hypothetical violation of the principle of local position invariance for resonator-based clocks and derive bounds for the strength of space-time fluctuations.

DOI: 10.1103/PhysRevLett.117.271102

In this Letter, we address experimentally the question about the intrinsic time stability of the length of a macroscopic solid body. This question is related to the question about time variation of the fundamental constants and effects of the expansion of the Universe on local experiments. It may be hypothesized that, in violation of the Einstein equivalence principle (EP), the expansion affects the length of a block of solid matter and atomic energies to a different degree. The length, defined by a multiple of an interatomic spacing, can be measured by clocking the propagation time of an electromagnetic wave across it. This procedure effectively implements the Einstein light clock or, in modern parlance, an electromagnetic resonator. The hypothetical differential effect would show up as a time drift of the ratio of the frequency $f_{\rm res}$ of an electromagnetic resonator and of an atomic (or molecular) transition ($f_{\rm atomic}$). A resonator and an atom are dissimilar in the sense that the former's resonance frequency intrinsically involves the propagation of an electromagnetic wave, while the latter does not. Specifically, the time drift would violate the principle of local position invariance (LPI) of the EP. A natural scale of an effect due to cosmological expansion, here the fractional drift rate $D_{\text{res-atomic}} = (f_{\rm atomic}/f_{\rm res}) d(f_{\rm res}/f_{\rm atomic})/dt$, could be the Hubble constant $H_0 \simeq 2.3 \times 10^{-18}/{\rm s}$. Extensive work in the past decade has ruled out that an effect of this order exists between different *atomic and molecular* frequency standards [1].

The suitable regime in which to investigate the dimensional stability of matter is at a cryogenic temperature, when the thermal expansion coefficient and the thermal energy content of matter are minimized. Ideally, during the cooling down and then permanence at a cryogenic temperature, a stable energy minimum of the solid is reached. The expected high dimensional stability and the magnitude of H_0 lead to a challenging measurement problem: how to resolve tiny length changes and how to suppress the influence of extrinsic disturbances. The problem can be addressed by casting the solid matter into an electromagnetic resonator of appropriate shape, by supporting it appropriately, and by measuring its resonance frequency using atomic timekeeping and frequency metrology instruments, which indeed permit ultrahigh measurement precision and accuracy.

Cryogenically operated resonators [2] have been developed for microwave and optical frequencies. These represent a viable approach for realizing oscillators having ultrahigh stability both on short and on long time scales (months). Therefore, they have found applications for tests of the EP [2–7] and as local oscillators in connection with microwave and optical atomic clocks [8,9].

Recent cryogenic microwave sapphire resonators exhibit nonzero fractional drifts ($D = f^{-1} df/dt$) of $-1.7 \times 10^{-18}/{\rm s}$ [7] and $4 \times 10^{-19}/{\rm s}$ [10] and the lowest value reported was $-1.9 \times 10^{-20}/{\rm s}$ during a 9-day long interval [11]. For a sapphire cryogenic optical resonator [12], a mean drift smaller than $6.4 \times 10^{-19}/{\rm s}$ was measured [13]. Recently, silicon resonators (first studied in Ref. [14]) were investigated at 123 K [9] and at 1.5 K [15,16]. Silicon's advantages are the availability of single crystals of large size at an affordable cost, its easy machinability, a flexibility in the choice of resonator shape, and superpolished mirror substrates allowing high-reflectivity mirrors. Important properties of silicon resonators, such as the thermal expansion coefficient, thermal response, resonator linewidth, and throughput, have already been described in the references given. The 123 K silicon resonator system exhibited an average drift of less than $5 \times 10^{-19}/{\rm s}$ over an interval of 70 d [17].

In earlier work on cryogenic resonators, cryostats using liquid coolants were often employed. With the advent of "dry" cryostats, first applied to optical resonator experiments in Ref. [5], the operation of cryogenic resonators has become possible with reduced maintenance effort and without the disturbances due to the periodic refill of cryogens, opening up new opportunities. Using this technology, the present study was therefore able to investigate a silicon resonator operated at 1.5 K continuously for 420 d. This low temperature is attractive not only for reducing thermal expansion (and consequently reduced requirements for active temperature stabilization) and thermally activated processes but also for reducing the thermal noise of the resonator's components: spacer, mirror substrates, and mirror coatings [15].

We demonstrate here that a crystalline resonator can exhibit outstanding dimensional stability. This performance can be used to test for EP-violating effects. It also has technological potential as an oscillator with a performance improved compared to the well-established masers.

Overview of the apparatus.—Figure 1 (see also [18]) shows the concept of the experiment, which is an extension of our previous work [15]. A silicon resonator is operated in a pulse-tube cooler (PTC) cryostat with a Joule-Thomson (JT) cooling stage, providing a base temperature of 1.5 K.

The silicon resonator is 25 cm long and consists of a cylindrical spacer and two optically contacted silicon mirror substrates [18]. Its linewidth is 2.0 kHz. The resonator is oriented horizontally and supported by wires inside a copper frame [18]. The supports' symmetry is such that to first order the thermal expansion or length drift of the frame does not affect the resonator length.

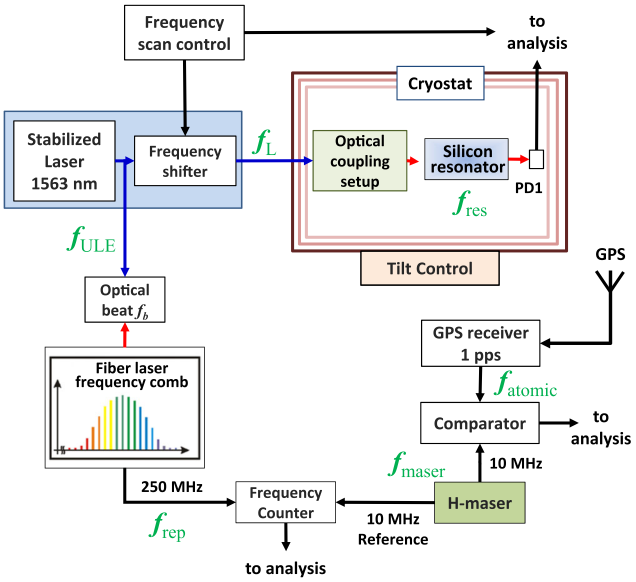

FIG. 1. Principle of the experiment. The optical resonance frequency f_{res} of a silicon resonator is compared with a radio frequency f_{maser} provided by a hydrogen maser. This is done via the intermediary of a laser whose wave of frequency f_L interrogates the resonator and is also measured by an optical frequency comb (pulse repetition rate f_{rep}). The maser frequency is itself compared with a 1-Hz signal (f_{atomic}) obtained from GPS satellites.

In the frequency-scan interrogation technique (Fig. 1), the resonator's TEM_{00} mode frequency f_{res} is read out by a 1.56 μm (192 THz) external-cavity semiconductor laser ("laser 1" in Ref. [18]), which is frequency stabilized to a room-temperature reference resonator (frequency f_{ULE}), having short-time fractional frequency instability 5×10^{-15} and drift 6×10^{-16}/s. During readout, the laser frequency is offset to f_L and is repeatedly scanned in time over a range of a few kilohertz across the silicon resonator resonance (line center frequency f_{res}). We record on the photodetector PD1 the power of the laser wave transmitted through the resonator, fit a line shape model to each scan's data, and extract the frequency offset $f_{res} - f_{ULE}$. Simultaneously, the laser frequency corresponding to f_{ULE} is measured by an erbium-fiber-laser-based femtosecond frequency comb, using a hydrogen maser (f_{maser}) as a reference. From these two measurements, we obtain f_{res} in units of f_{maser}. If f_{maser} was constant in time, the long-term variation of f_{res} would mainly be given by the long-term variation of the length l of the silicon crystal resonator spacer and (hypothetically) of the speed of light c, $\Delta f_{res}/f_{res,0} = \Delta c/c_0 - \Delta l/l_0$, where $f_{res,0}$, l_0, and c_0 are the resonance frequency, the spacer length, and the speed of light at a reference time t_0, respectively.

Systematic effects.—The experiment requires maintaining the operating parameters of the system as stable as possible. Several systematic effects were investigated.

(i) *Temperature.*—The cryostat was operated at its base temperature, and no active temperature stabilization of the resonator was used, since it was unnecessary in the present context. Figure 2 shows the temperature over a period of approximately 420 d with a typical peak-peak variation of 30 mK. The thermal sensitivity of the resonator being $|f_{res}^{-1} df_{res}/dT| < 1 \times 10^{-12}$/K at 1.5 K [15,16], this corresponds to a peak-peak fractional frequency deviation $< 4 \times 10^{-15}$, which is not of importance here. On day 327, the operating temperature had to be raised to 1.55 K because of a pressure increase in the JT stage. The calculated shift of 20 Hz was taken into account in the data analysis.

(ii) *Resonator deformation due to gravity.*—The sensitivity to tilt was measured to be $2.5 \times 10^{-16}/\mu$rad and $1.5 \times 10^{-17}/\mu$rad for tilt around the longitudinal and transverse axis, respectively. A tilt control system actuated two of the legs supporting the whole cryostat and reduced the tilt instability to a level below 0.5 μrad for integration times between 100 and 10^4 s.

The time variation of the local gravitational acceleration (tides, etc.) has a negligible effect on the resonator.

(iii) *Laser power.*—The laser power incident onto the resonator during line scan interrogation was 30 μW or less and was not actively stabilized. The power actually coupled into the resonator was 1.5% of the incident power. The power absorbed in the mirror substrate as the laser wave

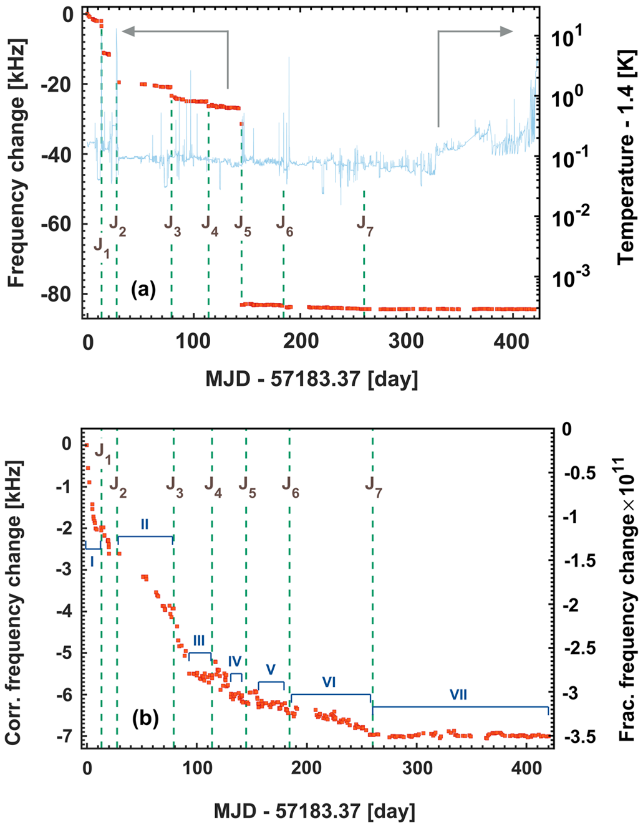

FIG. 2. (a) Variation $\Delta f_{\rm res}$ of the optical frequency of the silicon resonator (left scale) and its temperature (right scale) over time. During intervals I–VI, the Pound-Drever-Hall locking technique was used. The shown data of interval VII were obtained using the frequency scan technique. Time zero corresponds to the first measurement, performed 4 d after reaching the base temperature (1.5 K). (b) Corrected Si resonator frequency change, obtained by removing frequency jumps that occurred at $J_1, \ldots, J_6$.

traverses it before entering the resonator and the power dissipated inside it could be detected via the concomitant resonator temperature changes. However, the corresponding thermal expansion is negligible. No effect on the resonator frequency could be detected directly.

(iv) *Vibrations.*—They are caused by the periodic (0.7 s) pulsing of the PTC and were characterized at room temperature by motion sensors attached to a plate close to the plate supporting the resonator. All spatial components of the acceleration have complex time evolutions (Fourier frequencies up to a few hundred hertz) and rms values of $(1-8)\times 10^{-3}g$ within a sensor bandwidth of 200 Hz. The accelerations cause resonator deformations that lead to fractional frequency shifts on the order of 10^{-12}, periodic in time. We also performed an interferometric measurement of the periodic axial displacement of a second, identical silicon resonator inside the cryostat. The amplitude is approximately 10 μm.

(v) *Resonator interrogation by the frequency-scan technique.*—This technique (Fig. 1 and Ref. [18]) leads to an Allan deviation of the line center frequency of 2×10^{-14} at 1000 s integration time. During each frequency scan across the resonator mode, the signal recorded by detector PD1 is modulated (25% fractionally) in time in synchronism with the PTC pulsing, probably due to variations in the coupling efficiency caused by the pulsing. The modulation is complex, with pulse-to-pulse variations. These signal disturbances lead to variations of the line center frequencies fitted from individual scans. These variations are of the order 3×10^{-13} (2σ of the data) (gray bars in Fig. 3).

(vi) *Long-term effects of laser light.*—The laser intensity circulating in the resonator might cause photochemical or structural changes in the mirror coatings, with a consequent resonator frequency change. We did not keep any laser frequency resonant for an extended duration, in order to limit the irradiation of the mirrors [18].

(vii) Although it is known that maser frequency drift magnitude can be below $1\times 10^{-21}/{\rm s}$ [20], it is fundamental to determine the influence of our particular maser on the optical frequency measurement. The maser was monitored by comparison with a 1-pulse-per-second signal delivered by GPS, which is derived from the international atomic time scale, defined by the cesium hyperfine transition. During the period days 225–264, the mean fractional drift was $8.2\times 10^{-21}/{\rm s}$. During the period days 293–415, the mean drift was $D_{\text{maser-GPS}} = 7.5\times 10^{-21}/{\rm s}$. This level is relevant in comparison with the drift of the resonator's optical frequency with respect to the maser, $D_{\text{res-maser}}$, and thus must be accounted for. The error of $D_{\text{maser-GPS}}$ is negligible for the present discussion.

Measurement of the resonator drift.—Measurements were performed daily, when possible. In practice, each measurement of $f_{\rm res}$ was taken as a time average over several minutes so as to suppress disturbances occurring over short time scales. The long-term behavior of the resonator frequency $f_{\rm res}$ is depicted in Fig. 2(a). Frequency jumps J_1–J_4 were caused by large temperature variations or by unintentional knocks on the cryostat. On day 149 (J_5), we deliberately knocked on the cryostat's outer vacuum chamber and observed a 56 kHz frequency change. The frequency jump after J_6 was probably caused by a power shutdown [18]. To compensate for these jumps, we shifted all frequency values after each jump by an amount equal to the difference between the last measurement before and first measurement after each jump. In Fig. 2(b), we display the resulting time series of the corrected frequency $f_{\rm res}$, the offsets for $[J_1, \ldots, J_6]$ being $[9.1, 7.8, 2.5, 1.4, 56.1, 0.4] \pm 0.1$ kHz.

We find that, within 2 weeks after each disturbance J_1–J_6, the drift has dropped back to nominally zero. The data intervals III–VI are intervals between frequency jumps during which the resonator remained undisturbed. During these intervals, the drift rates were compatible with zero with upper limits of $4\times 10^{-19}/{\rm s}$. Interval VII is the period of longest undisturbed duration, 163 d. Starting

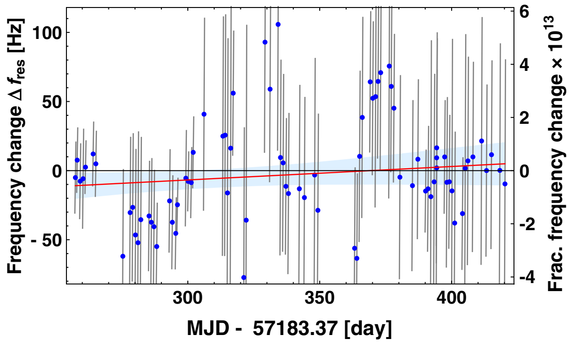

FIG. 3. Resonator optical frequency variation Δf_{res}, corrected for maser drift, during time interval VII, defined in Fig. 2. Each data point (blue) is the average frequency value obtained during a measurement interval i. The bars indicate the range $\pm$ twice the standard deviation of each data set i. Red line, time-linear fit, exhibiting a drift rate $D_{\text{res-atomic}} = 5.9 \times 10^{-21}$/s; blue shaded area, 2σ uncertainty range of the time-linear fit. The zero ordinate value is defined as the mean of the data points.

with this interval, the frequency-scan interrogation technique was used. The f_{res} data thus obtained are shown in Fig. 3. The variations of Δf_{res} are mostly due to the systematic effects (i)–(vi); a possible additional contribution are long-term (time scale of days) maser frequency fluctuations, which we cannot independently identify via GPS, due to the latter's low stability.

Given the long overall measurement duration of 163 d, we can assume that the variations are approximately randomly distributed. A time-linear fit of the optical frequency data f_{res} yields $D_{\text{res-maser}} = (-1.6 \pm 3.8) \times 10^{-21}$/s ($1\sigma$). We then obtain the drift of the silicon resonator frequency with respect to atomic time as $D_{\text{res-atomic}} = D_{\text{res-maser}} + D_{\text{maser-GPS}} = (5.9 \pm 3.8) \times 10^{-21}$/s. The systematic effects disturbing the laser frequency scan data and the finite overall measurement time span determine the uncertainty of $D_{\text{res-atomic}}$.

Interpretation.—We interpret the zero drift in three ways: (a) as a test of LPI [2], (b) as a test for effects related to the expansion of the Universe, and (c) as a test of the existence of space-time fluctuations. Local Lorentz invariance is assumed to hold.

(a) One test of LPI is a null clock redshift test that tests for deviations from the clock-type independence of the gravitational time dilation. It consists in measuring the ratio of the frequencies of two dissimilar clocks $C1$ and $C2$, colocated at $\mathbf{r}$, as they are transported through a region of varying gravitational potential $U(\mathbf{r})$. The change of the frequency ratio is written as

$$(f_{C1}/f_{C2})(\mathbf{r}) = (f_{C1}/f_{C2})_0[1 + (\xi_{C1} - \xi_{C2})\Delta U(\mathbf{r})/c^2], \quad (1)$$

where ξ_{C1} and ξ_{C2} are the gravitational coupling constants of the two clock types, $(f_{C1}/f_{C2})_0$ is the frequency ratio measured for the arbitrary reference value U_0, and $\Delta U(\mathbf{r}) = U(\mathbf{r}) - U_0$. If general relativity holds, $\xi = 1$, independent of the type of clock. For two colocated clocks on Earth, $\Delta U(\mathbf{r}) = \Delta U_{\text{solar}}(\mathbf{r})$ is time-varying because of rotational and orbital motion. The Δf_{res} data in Fig. 3 essentially correspond to $\Delta(f_{res}/f_{\text{atomic}})$, the variation of the ratio of the resonator frequency, and the frequency corresponding to the atomic unit of time (delivered via GPS). A fit of Eq. (1) to the data, neglecting the rotational contribution to ΔU_{solar}, yields $\xi_{res} - \xi_{\text{atomic}} = (-2.8 \pm 1.6) \times 10^{-4}$ for the clock coupling to the Sun's gravitational potential, which is compatible with zero (the error given is the standard error). The upper bound $|\xi_{res} - \xi_{\text{atomic}}|_{2\sigma} < 6 \times 10^{-4}$ is nearly equal to the result of Ref. [7] (accounting for the result of Ref. [21]), where a cryogenic microwave sapphire oscillator (CSO) was used. However, our work achieved this result with a measurement duration of 5 months compared to 6 years.

(b) The second interpretation provides a limit for (hypothetical) linear-in-time effects on measuring rods, caused by the expansion of the Universe, if general relativity is violated. Reference [22] discusses that such an effect is absent if general relativity holds. To arrive at such a bound, we first discuss how bounds of LPI violation and time variation of fundamental constants contribute.

We assume that the LPI bound of Refs. [7,21], $|\xi_{\text{CSO}} - \xi_{\text{atomic}}|_{2\sigma} < 5.5 \times 10^{-4}$, holds also for standing-wave optical resonators, like the one used here. This implies that during the interval from day 258 to day 420 the mean resonator drift from a LPI violation is smaller than $|D_{\text{LPI}}|_{2\sigma} = 1.2 \times 10^{-20}$/s. Note that Ref. [7] derives the LPI bound from the CSO's annual frequency modulation amplitude only. The CSO's frequency drift, -1.7×10^{-18}/s, was removed before data analysis; therefore, the value of D_{LPI} is independent of any expanding-universe effect. Furthermore, we recall that, within conventional physics, $f_{res}/f_{\text{atomic}}$ (where f_{atomic} is derived from the Cs hyperfine transition) can, in principle, be expressed in terms of the fine-structure constant, m_e/m_p, nuclear parameters, the number of lattice planes in the silicon resonator, and numerical coefficients. The current experimental limits for the drifts of these constants and parameters, derived from comparisons between atomic clocks [1], lead to a bound much smaller than our $|D_{\text{res-atomic}}|_{2\sigma}$ and $|D_{\text{LPI}}|_{2\sigma}$.

Thus, the results of $D_{\text{res-atomic}}$ and D_{LPI} can be combined to set the bound 2.8×10^{-20}/s for the magnitude of linear-in-time drifts of the length of a solid, when measured by effectively clocking the propagation of electromagnetic waves across its length. This is a factor of 82 smaller than the natural scale H_0 and thus rules out any effect that is of first order in H_0.

(c) Space-time fluctuations (or "foam") is a concept that describes the possibility that repeated measurements of a particular time interval or a particular distance do not give a constant result but fluctuate due to fundamental reasons. The measurement of the resonator frequency f_{res}

performed here ultimately corresponds to a measurement of a particular distance (the mirror spacing l_0), in units of the wavelength of an electromagnetic wave resonant with the cesium hyperfine transition. Simple models for the noise power spectral density $S(f)$ (f is the fluctuation frequency) of the fractional length fluctuations $\Delta l/l_0$ have been introduced [23], leading to flicker frequency noise $S_{\mathrm{flicker}}(f) = \alpha/f$ or random-walk frequency noise $S_{\mathrm{rw}}(f) = \beta/f^2$. Experiments are required to place upper limits on α and β.

We compare our time series of f_{res} with simulated time series generated from flicker and random-walk noise and therefrom deduce $S_{\mathrm{flicker}}(f) < 4\times10^{-27}/f$ and $S_{\mathrm{rw}}(f) < 9\times10^{-33}\ \mathrm{Hz}/f^2$. These limits are weaker than our previous measurements [6,24] but are here established from data at significantly lower Fourier frequencies, $f \simeq 1\ \mu\mathrm{Hz}$.

Summary and outlook.—In this work, we have demonstrated that a silicon crystal exhibits an extremely small length drift at a cryogenic temperature. The mean fractional drift $D_{\mathrm{res\text{-}atomic}}$ measured during a time span of 5 months of nearly undisturbed operation was $(5.9 \pm 3.8)\times10^{-21}/\mathrm{s}$. This is the lowest value measured so far for resonators, to the best of our knowledge. The uncertainty of the value $D_{\mathrm{res\text{-}atomic}}$ is due to the systematic effects caused by the cryostat cooler and by the finite measurement time span. Both aspects could be improved in the future. The measurement rules out local consequences of the expansion of the Universe which are of the order of the Hubble constant H_0. In addition, the data provide the best upper limit for violations of local position invariance for an optical resonator and for the existence of space-time fluctuations with frequencies in the μHz range.

To illustrate the smallness of the drift, we note that the 2σ upper limit for $D_{\mathrm{res\text{-}atomic}}$, the positive value $1.4\times10^{-20}/\mathrm{s}$, is consistent with a shortening of the optical path length in the resonator. If this were caused by the deposition of molecules on the mirrors, the deposition rate would be one molecular layer on each mirror every 3×10^3 years or approximately 30 molecules/s within the laser beam cross section (1 mm diameter).

The cryogenic silicon resonator could potentially be used as a local oscillator with a performance beyond that of hydrogen masers and with autonomous operation. Future progress in cryostat technology may eventually allow suppressing the vibrations to a sufficiently low level so that a silicon resonator exhibits sub-10^{-17} fractional frequency instability, on all time scales, in addition to negligible drift. Until this potential is realized, another suggested implementation consists of a cryogenic silicon resonator combined with an improved version of the ULE-resonator-stabilized laser used here [18]. State-of-the-art ULE resonators are, in principle, capable of providing frequency instability at the 1×10^{-16} level for integration times of up to 1000 s (see, e.g., [25–27]), but this requires eliminating their drift, of typical magnitude $1\times10^{-16}/\mathrm{s}$. The drift would be determined by periodic comparison with the silicon resonator and would be compensated by a feedforward scheme. Our work suggests that the proposed solution will be robust and practical, since we showed uninterrupted operation of the resonator for 12 months without serious problems.

We thank I. Ernsting, Q.-F. Chen, U. Rosowski, D. Iwaschko, P. Dutkiewich, and R. Gusek for valuable contributions and M. Schioppo for comments. This work has been funded by European Space Agency Project No. 4000103508/11/D/JR and by Deutsche Forschungsgemeinschaft Project No. Schi 431/21-1.

E. W. and S. S. contributed equally to this work.

*Corresponding author.
step.schiller@hhu.de

[1] J.-P. Uzan, Varying constants, gravitation and cosmology, Living Rev. Relativ. **14**, 2 (2011).

[2] J. P. Turneaure, C. M. Will, B. F. Farrell, E. M. Mattison, and R. F. C. Vessot, Test of principle of equivalence by a null red-shift experiment, Phys. Rev. D **27**, 1705 (1983).

[3] C. Braxmaier, H. Müller, O. Pradl, J. Mlynek, A. Peters, and S. Schiller, Test of Relativity Using a Cryogenic Optical Resonator, Phys. Rev. Lett. **88**, 010401 (2001).

[4] H. Müller, S. Herrmann, C. Braxmaier, S. Schiller, and A. Peters, Modern Michelson-Morley Experiment Using Cryogenic Optical Resonators, Phys. Rev. Lett. **91**, 020401 (2003).

[5] P. Antonini, M. Okhapkin, E. Göklü, and S. Schiller, Test of constancy of speed of light with rotating cryogenic optical resonators, Phys. Rev. A **71**, 050101(R) (2005).

[6] S. Schiller, C. Lämmerzahl, H. Müller, C. Braxmaier, S. Herrmann, and A. Peters, Experimental limits for low-frequency space-time fluctuations from ultrastable optical resonators, Phys. Rev. D **69**, 027504 (2004).

[7] M. E. Tobar, P. Wolf, S. Bize, G. Santarelli, and V. Flambaum, Testing local Lorentz and position invariance and variation of fundamental constants by searching the derivative of the comparison frequency between a cryogenic sapphire oscillator and hydrogen maser, Phys. Rev. D **81**, 022003 (2010).

[8] J. Millo *et al.*, Ultralow noise microwave generation with fiber-based optical frequency comb and application to atomic fountain clock, Appl. Phys. Lett. **94**, 141105 (2009).

[9] T. Kessler, C. Hagemann, C. Grebing, T. Legero, U. Sterr, F. Riehle, M. J. Martin, L. Chen, and J. Ye, A sub-40-mHz-linewidth laser based on a silicon single-crystal optical cavity, Nat. Photonics **6**, 687 (2012).

[10] J. G. Hartnett, N. R. Nand, and C. Lu, Ultra-low-phase-noise cryocooled microwave dielectric-sapphire-resonator oscillators, Appl. Phys. Lett. **100**, 183501 (2012).

[11] J. G. Hartnett, C. R. Locke, E. N. Ivanov, M. E. Tobar, and P. L. Stanwix, Cryogenic sapphire oscillator with exceptionally high long-term frequency, Appl. Phys. Lett. **89**, 203513 (2006).

[12] S. Seel, R. Storz, G. Ruoso, J. Mlynek, and S. Schiller, Cryogenic Optical Resonators: A New Tool for Laser Frequency Stabilization at the 1 Hz Level, Phys. Rev. Lett. **78**, 4741 (1997).
[13] R. Storz, C. Braxmaier, K. Jäck, O. Pradl, and S. Schiller, Ultrahigh long-term dimensional stability of a sapphire cryogenic optical resonator, Opt. Lett. **23**, 1031 (1998).
[14] J.-P. Richard and J. J. Hamilton, Cryogenic monocrystalline silicon Fabry-Perot cavity for the stabilization of laser frequency, Rev. Sci. Instrum. **62**, 2375 (1991).
[15] E. Wiens, Q. Chen, I. Ernsting, H. Luckmann, A. Y. Nevsky, U. Rosowski, and S. Schiller, A silicon single-crystal cryogenic optical resonator, Opt. Lett. **39**, 3242 (2014).
[16] E. Wiens, Q. Chen, I. Ernsting, H. Luckmann, A. Y. Nevsky, U. Rosowski, and S. Schiller, Silicon single-crystal cryogenic optical resonator, Opt. Lett. **40**, 68(E) (2015).
[17] C. Hagemann, C. Grebing, C. Lisdat, S. Falke, T. Legero, U. Sterr, F. Riehle, M. J. Martin, and J. Ye, Ultra-stable laser with average fractional frequency drift rate below $5 \times 10^{-19}/\mathrm{s}$, Opt. Lett. **39**, 5102 (2014).
[18] See Supplemental Material at, http://link.aps.org/supplemental/10.1103/PhysRevLett.117.271102 which includes Refs. [9, 19], for details of the setup and experimental procedures.
[19] C. Braxmaier, O. Pradl, H. Müller, B. Eiermann, A. Peters, J. Mlynek, and S. Schiller, Fiber-coupled and monolithic cryogenic optical resonators, in *Conference on Precision Electromagnetic Measurements Digest* (IEEE, New York, 2000), pp. 192–193.
[20] D. Matsakis, P. Koppang, and R. M. Garvey, The Long-term stability of the U.S. Naval Observatory's masers, in *Proceedings of the 36th Annual Precise Time and Time Interval Systems and Applications Meeting, Washington, D.C.* (2004), pp. 411–422.
[21] A. Bauch and S. Weyers, New experimental limit on the validity of local position invariance, Phys. Rev. D **65**, 081101 (2002).
[22] S. M. Kopeikin, Optical cavity resonator in an expanding universe, Gen. Relativ. Gravit. **47**, 5 (2015).
[23] Y. J. Ng, Selected topics in Planck-scale physics, Mod. Phys. Lett. A **18**, 1073 (2003).
[24] Q. Chen, E. Magoulakis, and S. Schiller, High-sensitivity crossed-resonator laser apparatus for improved tests of Lorentz invariance and of space-time fluctuations, Phys. Rev. D **93**, 022003 (2016).
[25] Y. Y. Jiang, A. D. Ludlow, N. D. Lemke, R. W. Fox, J. A. Sherman, L.-S. Ma, and C. W. Oates, Making optical atomic clocks more stable with 10^{-16}-level laser stabilization, Nat. Photonics **5**, 158 (2011).
[26] T. L. Nicholson, M. J. Martin, J. R. Williams, B. J. Bloom, M. Bishof, M. D. Swallows, S. L. Campbell, and J. Ye, Comparison of Two Independent Sr Optical Clocks with 1×10^{-17} Stability at 10^3 s, Phys. Rev. Lett. **109**, 230801 (2012).
[27] S. Häfner, S. Falke, C. Grebing, S. Vogt, T. Legero, M. Merimaa, C. Lisdat, and U. Sterr, 8×10^{-17} fractional laser frequency instability with a long room-temperature cavity, Opt. Lett. **40**, 2112 (2015).

Resonator with Ultrahigh Length Stability as a Probe for Equivalence-Principle-Violating Physics: Supplemental Material

E. Wiens, A.Yu. Nevsky, and S. Schiller

*Institut für Experimentalphysik,
Heinrich-Heine-Universtität Düsseldorf, 40225
Düsseldorf, Germany*

Setup details.

Fig. 1 shows the setup of Fig. 1 in the main paper in detail and with an additional laser system. Laser 1 is used for the frequency-scan interrogation of the silicon resonator (the technique shown in Fig. 1 in the main paper), Laser 2 is used for frequency-locking to the silicon resonator using the Pound-Drever-Hall technique (PDH). Similar to the frequency-scan signal, the PDH error signal is also found to be strongly disturbed by the vibrations and also to be influenced by laboratory temperature. In addition, significant residual amplitude modulation is present, which drifts in time. Because the scatter of the $f_{\rm res}$ frequency values obtained by this method was larger than for the frequency-scan method, we base our analysis of the low-drift interval VII on the latter. During intervals I-VI, only PDH data was recorded.

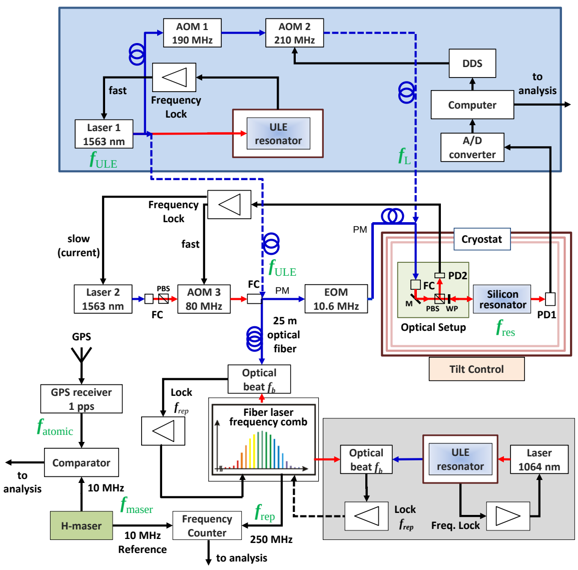

FIG. 1: (Color online). Schematic of the overall setup, containing the silicon resonator, three continuous-wave lasers and an optical frequency comb. To reduce the linewidth of the comb's modes, one of its modes was locked either to a 1.06 μm reference laser (modality A, gray background), to the Si-resonator-stabilized laser (modality B, no colored background), or to a 1.56 μm reference laser (modality C, blue background; dashed blue lines indicate connections when this modality is in use). FC: fiber coupler. AOM: acoustooptic frequency shifter. DDS: Synthesizer. EOM: electrooptic modulator. WP: quarter-wave plate; PBS: polarizing beam splitter. M: set of motorized mirrors. PD1, PD2: photodetectors. Red lines: free-space beams. Blue lines: optical fibers. All r.f. sources are referenced to the H-maser.

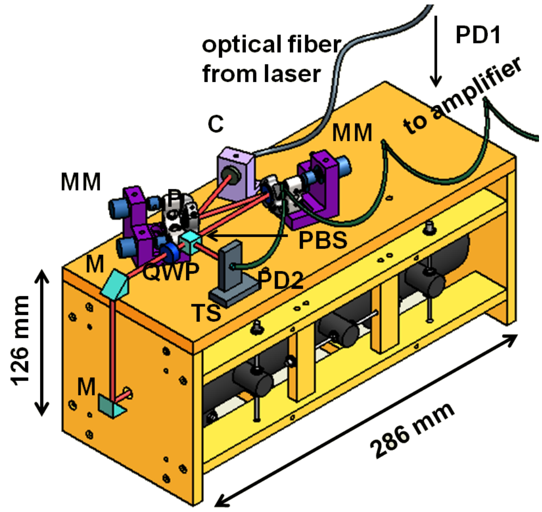

FIG. 2: (Color online). Schematic of the cryogenic resonator (in gray), its holder and the optics breadboard. All shown components are operated at 1.5 K. Laser light is coupled out of a single-mode optical fiber by a collimator C and is guided into the resonator with two motorized mirror mounts MM (for the position adjustment of the beam after cool-down), by a prism P, and a mirror M. Light reflected from the resonator is directed to the cryogenic photodetector PD2 mounted on a two-axis translation stage TS, by the quarter-wave plate QWP and the polarizing beam splitter PBS. The laser light transmitted through the resonator is monitored by photodetector PD1 (not shown). Relative dimensions are to scale.

Fig. 2 shows the cryogenic resonator and its associated optics. We note the difference in the mounting of the resonator in this work and in Ref. [9], where instead it is laying vertically on three columns.

For achieving a coupling of the laser wave into the resonator that is stable in time, it is advantageous to deliver the laser wave to the resonator via a fiber whose outcoupler is rigidly connected with the resonator [19]. In the present setup, wherein the resonator is mounted with wires, the relative alignment of the outcoupler and the resonator changes upon cool-down from room-temperature to cryogenic temperature. In order to be able to compensate for this, we implemented a cryogenic setup, see Fig. 2. It contains two mirrors MM, each actuated by two stepper motors, and a reflection photodetector mounted on a translation stage TS, actuated by two piezo motors.

Optical frequency measurement method and maser.

The measurements of $f_{\rm ULE}$ via the frequency comb are performed by measuring, firstly, the frequency $f_{\rm b}$ of the optical beat between laser and a single comb mode having a frequency near that of the laser and, secondly, the comb's repetition rate $f_{\rm rep} \simeq 250\,$MHz using for the latter a high-resolution counter (see Fig. 1). The carrier-envelope-offset frequency $f_{\rm ceo}$ was stabilized to a synthesizer. The reference frequency signal for the two frequency measurements and the synthesizer is an active hydrogen maser (Vremya-CH VCH-1005).

In order to reduce the linewidth of the comb's modes, with consequent reduction of the noise of the measurement of $f_{\rm rep}$, the comb was optically stabilized. In the course of the experiment, we used three modalities (A, B, C), in which one of the comb's modes was (A) phase-locked to a ULE-reference-cavity-stabilized 1.06 μm laser (days 1 - 132 after cool-down); (B) frequency-locked to the Si-resonator-stabilized laser (days 133 - 415), (C) phase-locked to a ULE-reference-cavity-stabilized 1.56 μm laser (days 257-420). For this purpose, part of the corresponding laser light was sent to the frequency comb, located in a neighboring laboratory, using a 25 m long optical fiber (no phase noise cancellation was implemented). The beat frequency $f_{\rm b}$ was detected with a photodiode and its signal was fed to a servo electronics so as to stabilize it to the value $f_{\rm b} = 50.4$ MHz by acting on the comb's cavity length via an intracavity electrooptic modulator. Under phase-lock conditions, the resulting beat linewidth was $\Delta f_{\rm b} < 1\,$Hz, with a signal-to-noise ratio > 30 dB.

Fig. 3 shows the drift of the maser frequency vs. GPS-delivered 1-pulse-per-second (pps) signals. The mean fractional frequency offset of the maser frequency $f_{\rm maser}$ from 10 MHz was $+1.02\times10^{-11}$, calculated from a linear fit of phase vs. time.

Operation details.

A pre-alignment of the laser beam exiting the out-coupler was performed while the cryostat was at room temperature. The resonator mode is identified by imaging the light exiting from the backside of the resonator through windows of the cryostat on a room-temperature CCD camera. After cool-down (Fig. 2 in the main paper), a realignment of the beam to the resonator and of the position of the reflection photodetector was necessary. This was done by operating the motors in two steps (for technical reasons), marked J_1 and J_2 in the figures, resulting in a sufficient coupling efficiency into the resonator, at 1.5 K. During both steps J_1 and J_2 (lasting approximately 30 min), the resonator temperature increased to 12 K and 14.5 K respectively, due to the power dissipation in the motor coils, and relaxed back to 1.4 K after several hours. We believe that the resonator frequency change accompanying each realignment was due to relaxation of the resonator after the thermal cycling. No further realignment or changes in the cryogenic setup were performed after day 21.

Most of the temperature peaks in Fig. 2 in the main paper occurred during brief (< 5 min) turn-offs of the cryostat compressor, introduced in order to temporarily eliminate cryostat vibrations and perform measurements of the stabilized laser's linewidth. Furthermore, during the presented measurement campaign three short power black-outs (few min) and one complete power shut-down of the building (30 min) occurred. In order to bridge the latter, we switched to an emergency power generator allowing to keep the compressor operating with only short interruption. However, lasers and electronics were kept off during this time. In anticipation of and during the power shut-down the compressor was off for durations ranging from a few to 10 min, in order to install and test the generator. Several instances of the temperature rise up to 4 K occurred at the end of the measurement period, due to temporary non-function of the Joule-Thomson stage, lasting a few days. We did not observe a residual frequency shift after re-cooling to 1.5 K, within our measurement uncertainty.

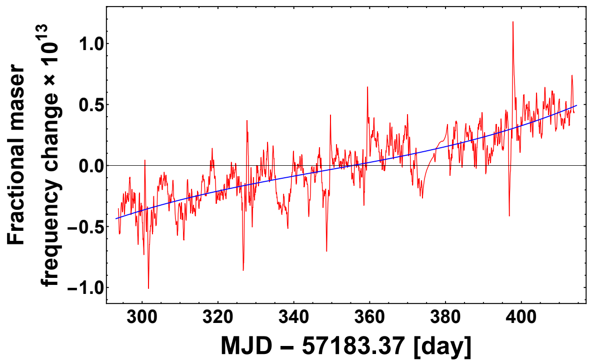

FIG. 3: (Color online) Long-term measurement of the hydrogen maser frequency with respect to atomic time. A GPS receiver provided the phase difference between the maser signal and the GPS signal. Red: maser frequency, computed as 1-day difference quotient of the phase averaged over 6 h. Blue line: maser frequency, computed from a *quartic* fit of the maser-GPS phase difference. The linear-in-time drift rate of the frequency, computed from a *quadratic* fit of the maser-GPS phase difference, is $D_{\rm maser-GPS} = 0.75 \times 10^{-20}$/s. It corresponds to the mean slope of the blue curve. The error is less than 1×10^{-22}/ s. The ordinate value zero corresponds to the mean fractional maser frequency offset, 1.02×10^{-11}.

In Fig. 2 in the main paper, J_3 and J_4 were caused by unintentional knocks of the cryostat, whereas at J_5 the cryostat was deliberately hit. J_6 was probably caused by a power shut-down and corresponding compensation activities. J_7 marks the reduction of the laser power incident on to the resonator.

Measurements of the frequency $f_{\rm res}$ by the frequency-scan technique and by the PDH technique were performed once per weekday over intervals not longer than 0.5 h. When no measurements were taken, laser 1 (used for the frequency scans) was always blocked. In contrast, until day 327, laser 2 was not blocked but its frequency

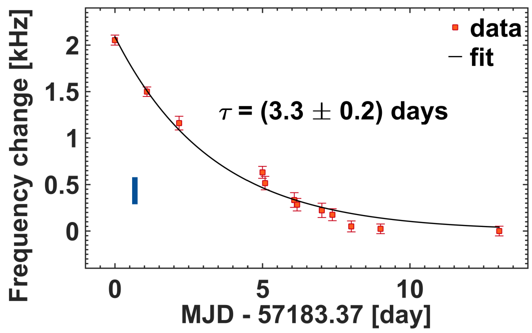

FIG. 4: (Color online) Resonator frequency change Δf_{res} during time interval I, starting after first reaching base temperature.

was detuned from resonance. Later, it was also blocked. The power of laser 2 in front of the fiber was approximately 150 μW during intervals I - VI, and was reduced to 60 μW from day 230 on.

Further characterizations.

The interval I of Fig. 2 in the main paper, displayed in more detail in Fig. 4, shows the frequency beginning 4 days after reaching the end of the cool-down, when the resonator temperature had first reached 1.5 K. We find an exponential relaxation of the frequency, with a time constant 3.3±0.2 days, indicating that the resonator and its holder reach equilibrium. In previous cool-down experiments we found values varying between 1.5 and 2.9 days.

F.3 Publication: Simulation of force-insensitive optical cavities in cubic spacers

Reproduced from

Eugen Wiens and Stephan Schiller

Simulation of force-insensitive optical cavities in cubic spacers

Applied Physics B **124**, 140 (2018)

DOI: https://doi.org/10.1007/s00340-018-7000-3

Author's contributions

All authors contributed to the work. My contributions to this work are:

- Performing of the FEM simulations and analyzing results.
- Co-writing the publication.

Applied Physics B (2018) 124:140
https://doi.org/10.1007/s00340-018-7000-3

Applied Physics B
Lasers and Optics

Simulation of force-insensitive optical cavities in cubic spacers

Eugen Wiens[1] · Stephan Schiller[1]

Received: 29 January 2018 / Accepted: 2 June 2018

Abstract

We analyze the properties of optical cavities contained in spacers with approximate octahedral symmetry and made of different materials, following the design of Webster and Gill (Opt Lett 36:3572, 2011). We show that, for isotropic materials with Young's modulus less than 200 GPa, the Poisson's ratio ν must lie in a "magic" range $0.13 < \nu < 0.23$ to null the influence of the forces supporting the spacer. This restriction can be overcome with the use of anisotropic materials such as silicon. A detailed study aiming at identification of all suitable crystal orientations of silicon with respect to the resonator body is performed, and the relation to the Poisson's ratio and the Young's modulus along these orientations is discussed. We also perform an analysis of the sensitivity of the cavity performance to errors in spacer manufacturing. We find that the orientation of the [110] or [100] crystallographic directions oriented along one of the three optical axes of the resonator provides low sensitivities to imprecise manufacturing and interesting options for fundamental physics experiments.

1 Introduction

Optical Fabry–Pérot resonators are widely used in different fields of optics and metrology. As passive optical resonators, they can provide the frequency reference for obtaining laser waves with ultra-stable frequencies for interrogation of transitions in atomic clocks [1–3], for gravitational wave detectors, or for fundamental tests of space–time structure [4–6]. Transfer of the frequency stability of laser waves into the microwave region potentially enables their application in radars and in navigation of deep space probes. High demands on frequency stability of laser light set forth by these applications require an optical resonator with a low sensitivity to vibrations.

Optical resonators are usually made of a spacer and two mirrors optically contacted to it. The frequency stability of such a resonator is determined, once evacuated, by the length stability of the resonator's spacer. Vibrations transferred from the surroundings to the resonator change the distance between the mirrors and tilt them, degrading the frequency stability. To fulfill the requirement of low vibration sensitivity, a careful design of the shape of the resonator and of the supporting frame is needed.

✉ Stephan Schiller
step.schiller@hhu.de

[1] Institut für Experimentalphysik, Heinrich-Heine-Universität Düsseldorf, Düsseldorf, Germany

The design with the lowest sensitivity to vibrations so far was presented by Webster and Gill [7]. The cavity structure (Fig. 1, top row) consists of a cube-shaped body made of ultra-low-expansion glass ULE material with a side length of 50 mm. It is held inside a frame (not shown in the figure) by four supports acting at four tetrahedrically oriented cube vertices. Three cavities are contained in the body. The cubic (more precisely: octahedral) symmetry of the cube-like spacer causes, upon action of a body force density (gravity or acceleration) oriented in arbitrary direction, an equal displacement of the centers of opposing faces, and, therefore, zero differential displacement. This makes the three cavities (completely) insensitive to accelerations along any axis. Experimentally, finite acceleration sensitivities are observed: of the three sensitivity coefficients, the smallest was $k_y = 1 \times 10^{-13}/g$, the largest $k_x = 2.5 \times 10^{-11}/g$. Values of this order can be explained by imperfections in fabrication or mounting.

Furthermore, the cube vertices are truncated to a depth of 6.7 mm. This value was determined by finite-element analysis (FEA) simulations and ensures that the external forces acting at the support points, if equal, do not shift the position of the centers of the faces of the cube. This means that the three cavity lengths are insensitive to the support forces.

The material ULE has the advantageous property of a zero Coefficient of Thermal Expansion (CTE) at or near room temperature and, therefore, makes the resonator insensitive to thermal fluctuations. The drawback of ULE

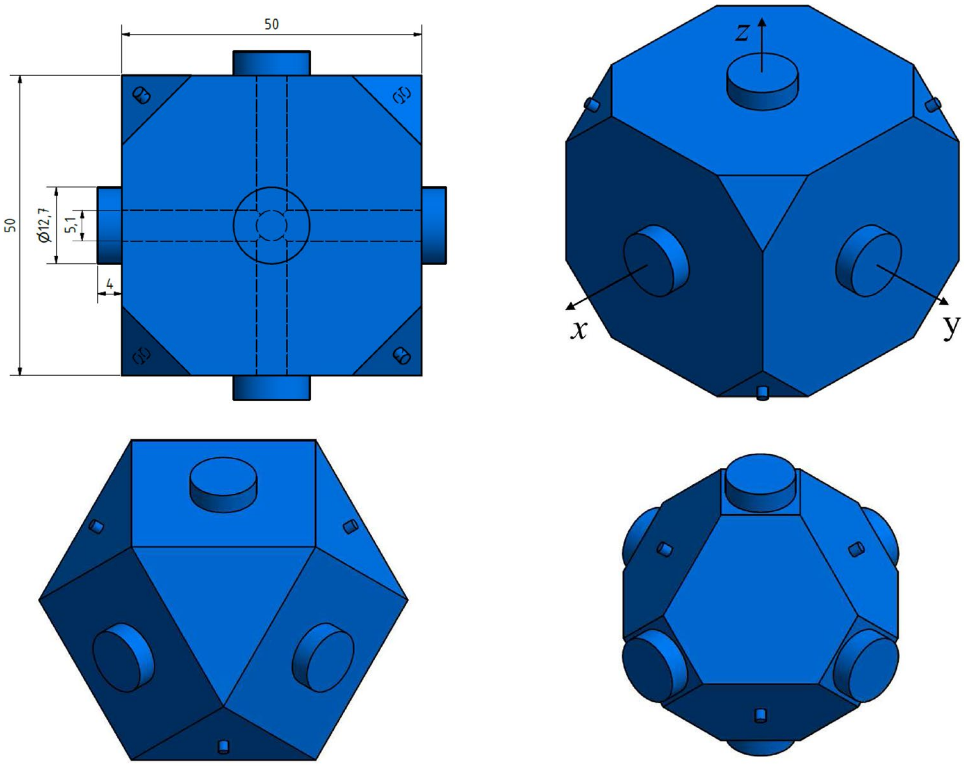

Fig. 1 Shapes and dimensions of cubic spacers. Top, left: cavity dimensions used in the FEA simulations. Top, right: orientation of the resonator with respect to the laboratory reference frame defined by (x, y, z). The shape is that derived by Webster and Gill. Bottom, left: transformation of the cube to its dual Platonic solid, the octahedron, when the cut depth of the vertices is equal to 14.47 mm. Bottom, right: cavity with a large cut depth, 23 mm

are a slow dimensional change due to its amorphous nature and the moderate Young's modulus $E = 67.6$ GPa, a value that is relevant if one considers deviations of the spacer from ideal symmetry (see Sect. 6). Another fundamental limitation is the thermal Brownian noise of the ULE spacer [8, 9]. The mirror substrates, usually made of the same or from a similar material (fused silica), also contribute to the thermal noise [10].

Reduction of the operating temperature of resonators down to cryogenic temperatures is an approach that can reduce thermal noise [8]. This has motivated the development of optical resonators cooled to cryogenic temperature [11]. Cryogenic resonators operated at particular temperatures or close to zero absolute temperature also exhibit an ultra-low CTE, which relaxes the requirements on temperature stability [11–15]. High-performance cryogenic optical resonators have so far been crystals, which also enjoy the advantage of a long-term drift orders of magnitude smaller than ULE [6, 16].

In this work, we present an analysis of the extension of the design of Webster and Gill [7] to other materials beside ULE, in particular, to materials that may be used advantageously at cryogenic temperatures. Because of the vibrational noise present in closed-cycle cryostats, it is particularly important to develop resonators with low acceleration sensitivity. In addition, the analysis seeks to answer the question whether it is possible to achieve an even lower acceleration sensitivity than possible with ULE when considering the influence of manufacturing errors.

2 Spacer geometry and modeling method

The main goal of the modeling is to find shapes and materials that lead to an insensitivity of the cavities contained in the cubic spacer to the strength of the forces acting on four vertices of the spacer. The insensitivity to acceleration arises automatically from the assumed octahedral symmetry of the spacer, and requires, at a first glance, no particular simulation. However, when there are deviations from symmetry, simulations allow to determine the acceleration sensitivity. We performed simulations using a commercial FEA software (Ansys). The FEA computation yields the fractional length change of each optical cavity upon application of a set of forces.

For concreteness, we chose the same dimensions for the spacer block as in Webster and Gill [7]: a cube with side length $L = 50$ mm. Its density and mass are denoted by ρ and m, respectively. The edges of the cube lie along the space-fixed coordinate system axes (x, y, z). Although only a single cavity, here, the x-cavity, is usually of interest, three mutually orthogonal cavities are formed by three through holes along the directions x, y, z, so as to preserve octahedral symmetry. For concreteness, they have radii $R_b = 2.55$ mm. A total of six mirror substrates of the same material as the block, each having a diameter of 12.7 mm and a thickness of 4 mm, are attached to the end faces of the spacer. The substrates and the block are assumed to form a single unit (see Fig. 1).

No pumping holes were included in the simulation. Since in the actual manufacturing, the hole diameter could be chosen small, we expect that its effect on the mechanical properties would be minor. The eight corners of the cavity are truncated to a depth d which is a free parameter.

The cavity is always simulated with four "holding" forces applied normal to four of the truncated corners. They each have an arbitrarily chosen but realistic magnitude of $F_c = 1\,\mathrm{N}$, and are applied via four cylindrically shaped supports (here, having $r = 2\mathrm{mm}$ diameter) rigidly attached to the resonator at the four corners with a tetrahedral symmetry. We consider two cases:

1. The application of only the four holding forces F_c, i.e., gravity is ignored. The sensitivity to support force strength, $\Delta L_i(F_c)/L = (L_i(F_c) - L)/L$, is calculated.
2. In the presence of F_c, an additional acceleration a_j acting along $j = x, y, z$ is applied. This simulates acceleration of the cavity support (and thus of the cavity body) or the gravitational acceleration. For this case, we define the acceleration sensitivity $k_{ij} = \Delta L_i(a_j)/(a_j L)$, where $\Delta L_i(a_j)$ is the additional cavity length change when a_j is added.

3 Spacer made of ULE

The computation was tested on a ULE cube with six mirror substrates made of ULE. The substrates considered in Webster and Gill [7] were from fused silica; this difference is minor. The cut depth was varied in the interval between 3 and 23 mm. The fractional length change $\Delta L_x(F_c)/L$ of the x-cavity occurring when the holding forces are applied, is depicted in Fig. 2, top left. Initially, for small cut depths, it is negative. This means that the distance between the mirrors is reduced upon application of the forces. At a cut depth of 6.6 mm, it crosses zero, for the first time, with a slope of 3.7×10^{-11}/mm. The cube deformation for this case is seen in Fig. 2 top right. Clearly, the central part of the mirror on the $+x$-face of the cube does not have any x-displacement. From symmetry, also the $-x$-face remains unaffected, and this results in $\Delta L_x(F_c)/L = 0$. After passing the cut depth of 14.5 mm, the shape of the spacer becomes octahedral. Soon after, at a cut depth of 15.7 mm, $\Delta L_x(F_c)/L$ is maximum and then starts to decrease with increasing cut depth. The second zero crossing is reached at a cut depth of 20.3 mm with a slope of -23×10^{-11}/mm. Among the two zero-sensitivity cut depths, the smaller one, 6.6 mm, is clearly more preferable, since the slope is six times smaller and so the shape is more forgiving in case of fabrication errors.

To justify our arbitrary choice of force magnitude $F_c = 1\,\mathrm{N}$ acting at each of the four supports, we analyzed the influence of force magnitude on optimum cut depth. We found no dependence of the position of zero-sensitivity cut depth on F_c when we varied the latter in the range 1 N$< F_c <$ 1 kN (see Fig. 2, middle left panel. Due to the large difference in scale, only simulation results for forces $F_c \leq 6$ N are presented there). This is expected, since the forces are small enough so that the material responds linearly.

We studied the influence of unequal forces at the four supports by holding the force F_c at a constant magnitude of $F_c = 1$ N at three support points and varying the force acting at the fourth support by a factor 2. Note that this is possible without causing an overall resonator displacement, since, in the simulations, each support surface is allowed to move only along the direction perpendicular to it. The overall effect of force variation at one support is equivalent to the application of additional longitudinal forces and generation of transversal forces at three remaining support surfaces. The results of this simulation are presented in Fig. 2, middle right panel. We found no dependence of optimal cut depth on variation of force at one support.

The optimum cut depth is found to increase with the size of the supports, as displayed in Fig. 2, bottom right. This could explain the small difference of 0.1 mm in optimum cut depth between the result presented here and in Webster and Gill [7]. Another crucial geometry parameter that has an influence on the position of the zero crossing is the size of the cavity bores. Figure 2, bottom left, shows that the zero-sensitivity cut depth near 6.6 mm only exists if the bore radius is below 3.5 mm. The second zero crossing at near 20.3 mm exists for all studied bore sizes, but has a slope that increases with increasing bore size.

3.1 Influence of shape on sensitivity

To study the influence of the resonator's shape on the sensitivity to the support forces, we considered other cavity block shapes with octahedral symmetry, such as the great rhomb–cube–octahedron [17], the rhomb–cube–octahedron [17], and the spherically shaped cube (see Fig. 3). All these bodies can be produced from the cube-shaped resonator by cutting out parts of the block in a symmetric way. The distance between the mirrors was kept at 50 mm for all shapes. Analogous to the truncated cube geometry already discussed, the supports were set in tetrahedral configuration and a force of 1 N applied on each. The cut depth was varied equally for all of them, within the limitations of the respective geometry. The results are presented in Fig. 4. The zero-sensitivity cut depths are the same for all geometries,

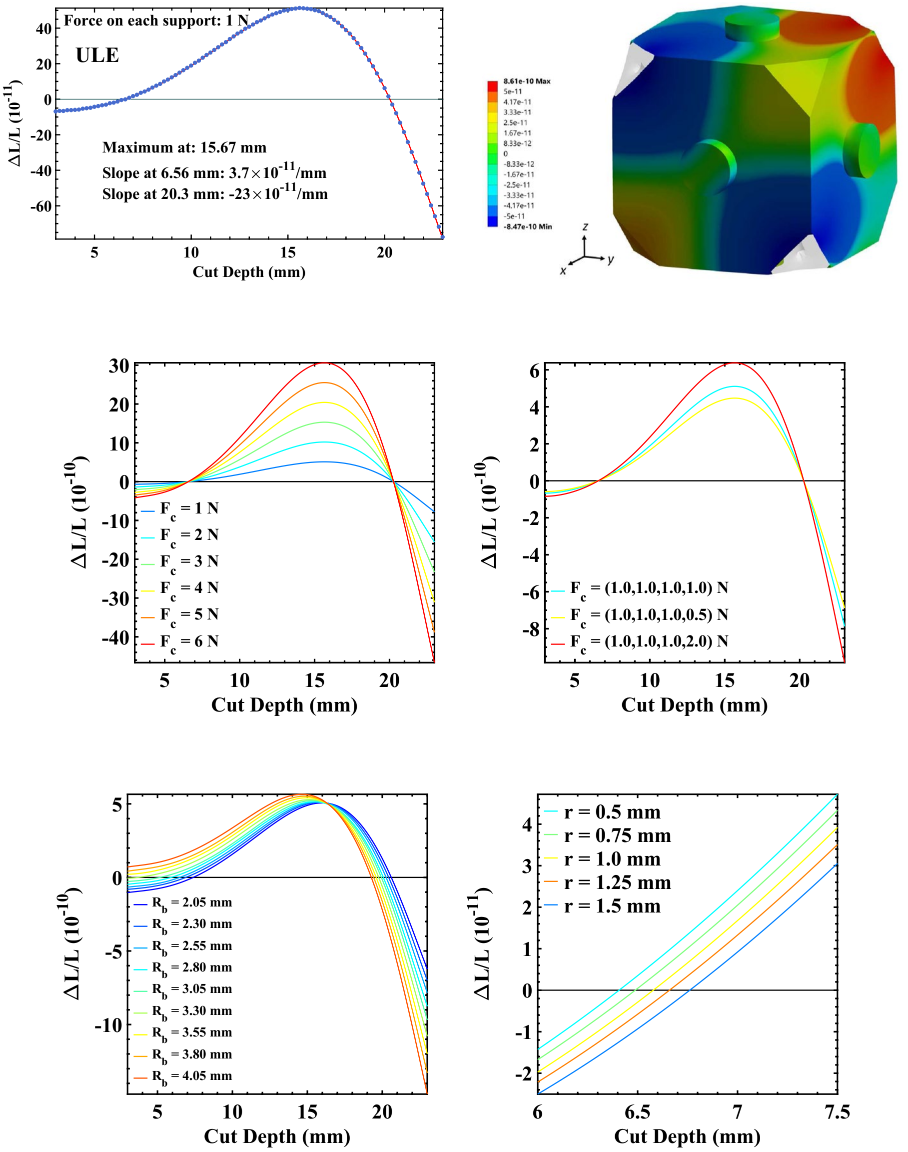

Fig. 2 Top left: fractional length change $\Delta L(F_c)/L$ of the cavity in an ULE block vs. the cut depths of the vertices. Top right: axial (x-axis) displacement at the optimum cut depth of 6.6 mm. The scale is in meter. Middle left: fractional length change $\Delta L(F_c)/L$ as function of force F_c applied at four support points. Middle right: fractional length change $\Delta L(F_c)/L$ as a function of force variation at one of the four supports. The magnitude of the force applied at each of the four supports is stated in the legend. Bottom left: fractional length change $\Delta L(F_c)/L$ as a function of cut depth, for various bore diameters R_b. Bottom right: fractional length change for different support radii

with the only difference being the corresponding limitations in cut depth. These results suggest that the dominant features depend only on the bulk properties of the material.

4 Cubic cavities made from the conventional optical materials

Nexcera, SiC, and Zerodur are well-known materials used for manufacturing optical components, in particular mirror substrates. Near room temperature, Nexcera and Zerodur exhibit a zero thermal expansion coefficient α. In contrast, for the material SiC, it is finite, but comparatively small [18]. Table 1 summarizes relevant physical properties of the materials. It is well known that a high specific stiffness E/ρ leads to low acceleration sensitivities of optical cavities. This is the reason for including SiC in the present analysis. Also listed in the table is the Poisson ratio ν, defined as the negative ratio of transverse strain to longitudinal strain. Thus, Poisson's ratio is responsible for the redistribution of strain in the directions normal to the direction of an applied force. Invar, an alloy with low thermal expansion coefficient at room temperature, is included for reference.

4.1 Support force sensitivity

Our simulations show that for Nexcera, Invar, and Zerodur, there does not exist an optimal cut depth (see Fig. 5). However, the sensitivity of Zerodur is low at high cut depth. Reduction of the diameter of the mirrors from half-inch to 10 mm results in a zero crossing of the fractional length change at a cut depth of 24.1 mm, with a slope of 30×10^{-11} /mm.

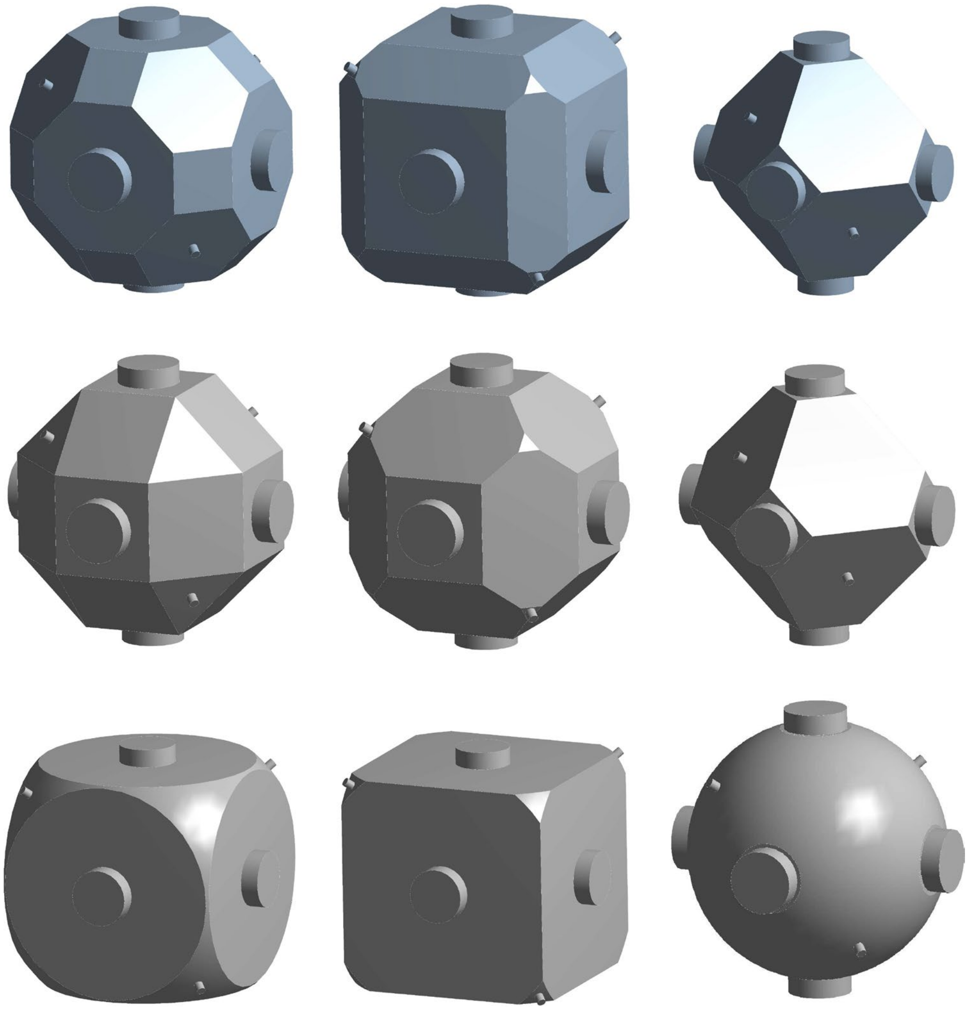

Fig. 3 Different simulated ULE resonator shapes, with the distance between the mirrors for all three cavities fixed at 50 mm. Top row: Left, great rhomb–cube–octahedron with the edge length of polygons being 13.1 mm and the two extremes with hexagons pulled out (middle) or in (right) by 7 mm. Middle row: Left, rhomb–cube–octahedron with the edge length of polygons being 20.7 mm and the two extremes with triangles pulled out (middle) by 3.3 mm or in (right) by 6.4 mm. Note that the geometries of the top row, right and middle row, right, are identical. Bottom row: Left, spherical cube resonator with circular faces of 49 mm diameter, and the two extremes with a cut depth of 3.3 mm (middle) and 17.3 mm (right)

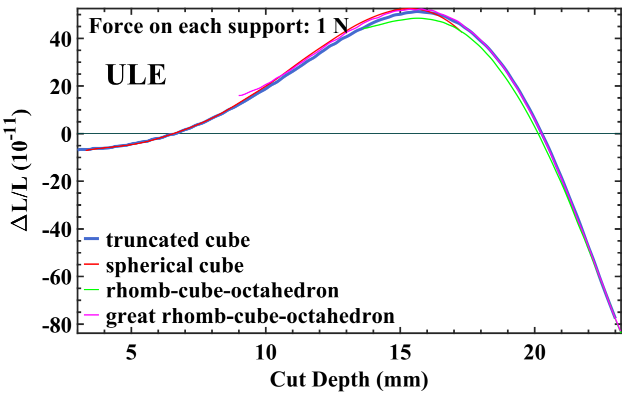

Fig. 4 Sensitivity $\Delta L_x(F_c)/L$ as function of cut depth for the truncated cube, for the great rhomb–cube–octohedron, for the rhomb–cube–octahedron, and for the spherically shaped cube

ULE is a modification of fused silica. Therefore, the fused silica resonator has zero sensitivity to F_c at essentially the same cut depth as the ULE resonator, but with a reduced slope because of its slightly higher Young's modulus.

Polycrystalline β-SiC has zero sensitivity at a cut depth of 22.2 mm and a slope which is comparable with ULE at 6.6 mm, due to the much larger Young's modulus. Figure 5, bottom right, shows the deformation of the β-SiC block having the zero-sensitivity geometry.

The overall ("peak–peak") variation of support force sensitivity over the complete range of cut depths is inversely proportional to the Young's modulus. It is largest for ULE (130×10^{-11}) and lowest for β-SiC (17×10^{-11}). The fractional length change at a 6.6 mm cut depth is the highest for Nexcera, followed in decreasing order by Zerodur, Invar, polycrystalline β-SiC, and the ULE (for which it is zero). With exception of Zerodur and Invar, that switch places, this sequence corresponds with the Poisson's ratio value.

To confirm this observation, we assumed a hypothetical material and varied either the Poisson ratio or the Young's modulus. The result is shown in Fig. 6. We find that both the Young's modulus and the Poisson's ratio are critical parameters. As expected, the deformation and the Young's modulus are inversely proportional to each other. Thus, a low Young's modulus leads to high deformation of the

Table 1 Comparison of some mechanical and thermomechanical properties of the considered isotropic materials

Material	ρ (g/cm^3)	E (GPa)	ν	E/ρ (MJ/kg)	α (10^{-6} K^{-1})
ULE [19]	2.21	67.6	0.17	30.59	0 ± 0.03
Nexcera [20]	2.58	140	0.31	54.26	< 0.05
Zerodur [21]	2.53	90.3	0.24	35.69	0 ± 0.1
β-SiC, polycrystalline [18]	3.21	466	0.21	145.2	2.2
Fused silica [21]	2.2	70.2	0.17	31.9	0.5
Invar [22]	8.05	141	0.259	17.52	1.0

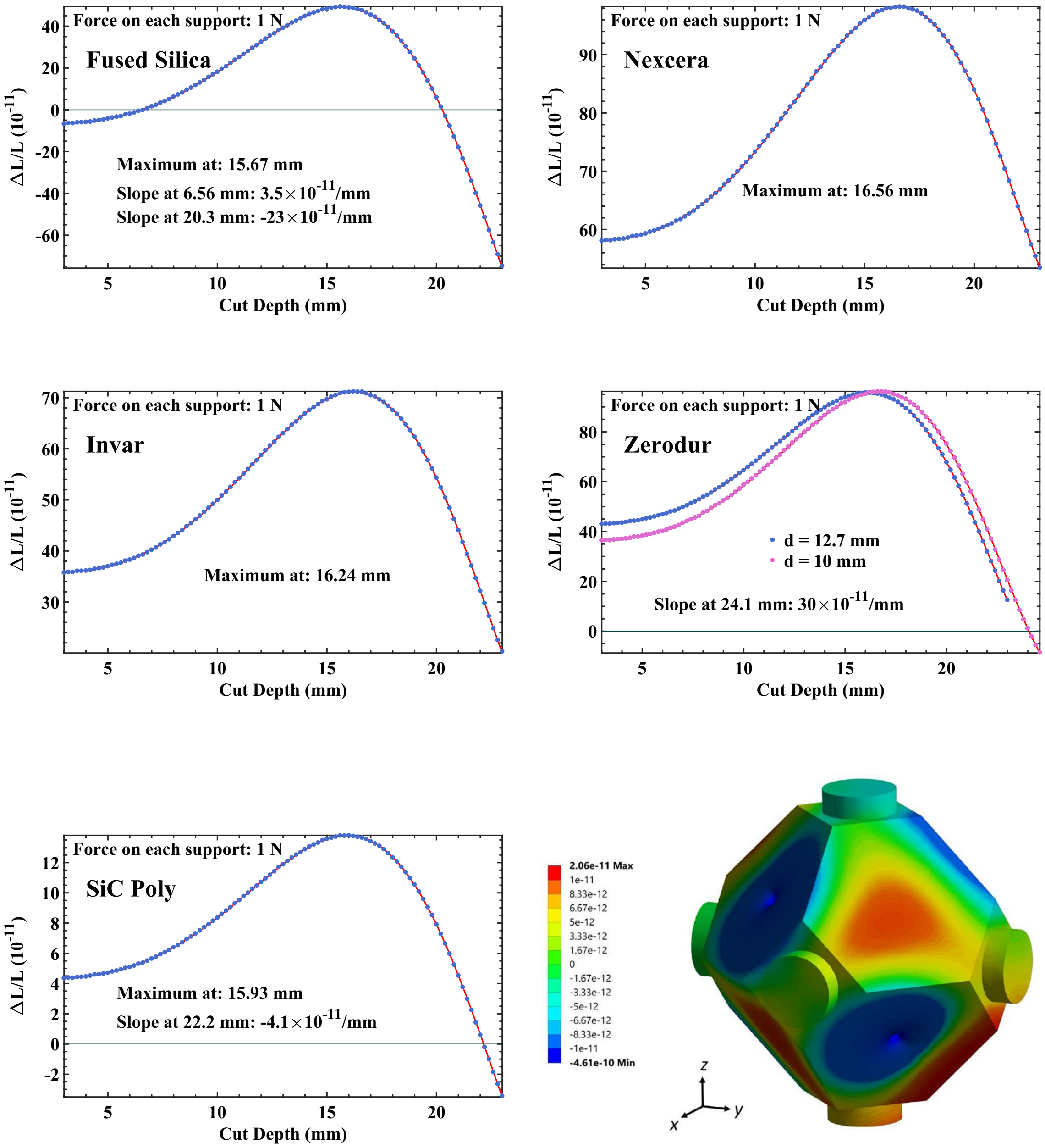

Fig. 5 Fractional length change of a resonator made of different materials and having different vertex cut depth. A force of 1 N acts at each support. Bottom right: axial x-deformation of the resonator made of β-SiC, for a cut depth of 22.2 mm. The scale is in m

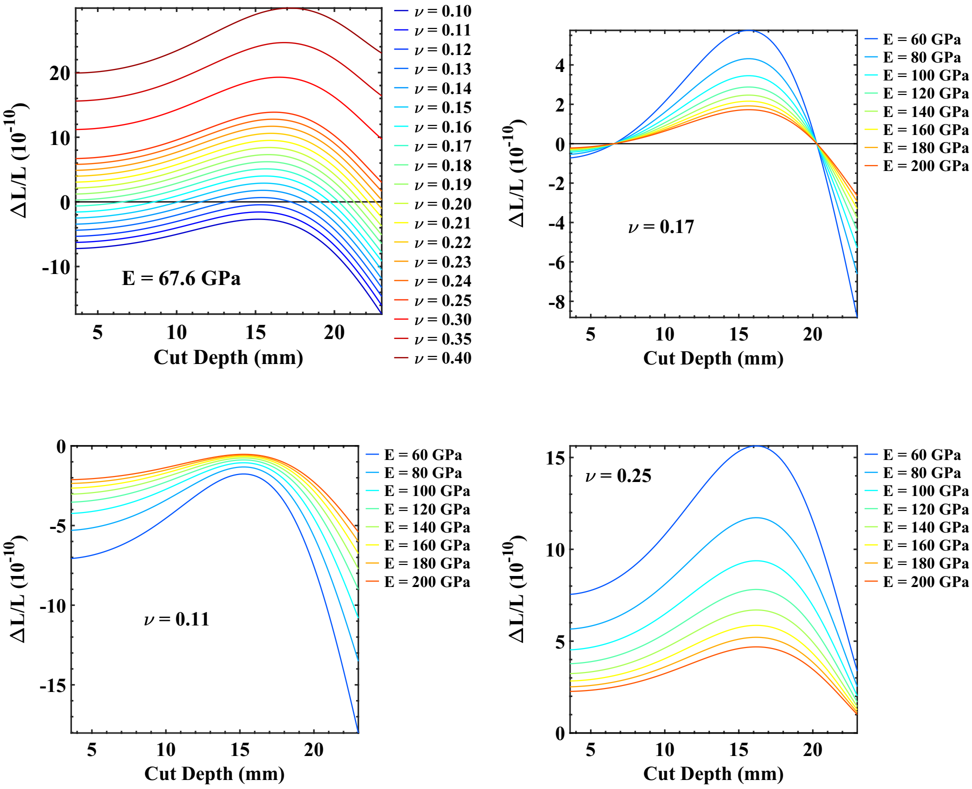

Fig. 6 Top: Left, dependence of the fractional length change of the resonator on vertex cut depth and on Poisson's ratio ν, with the Young's modulus held constant. Right: dependence on Young's modulus with a Poisson's ratio ν held constant at 0.17. Bottom: dependence on Young's modulus with a Poisson's ratio ν held constant at 0.11 (left) and 0.25 (right)

spacer and to high sensitivity to holding forces. On the other hand, a high Young's modulus reduces the deformation and, thus, the sensitivity. A small Poisson's ratio leads to an overall compression of a spacer, whereas a high Poisson's ratio effectively redistributes the strain and leads to an overall expansion of the spacer. Thus, comparing the sensitivities of two different materials, we can generally determine the material with higher sensitivity by comparing solely their Poisson's ratio values. If these materials have comparable values of Poisson's ratio, the Young's modulus must also be taken into account. Substantial difference in Young's modulus can change the sequence of the sensitivities based on the Poisson's ratio. This is the case for Invar and Zerodur, where Invar is the material with higher Poisson's ratio value (see Table 1) but lower sensitivity (see Fig. 5). To have a cut depth with zero sensitivity, the hypothetical material with the Young's modulus between 60 and 200 GPa must have the Poisson's ratio within a "magic" range $0.13 < \nu < 0.23$ (Fig. 7, left). This range is reduced to $0.13 < \nu < 0.18$ for the cut depths between 3 and 9 mm (Fig. 7, right).

Note that the density of the material does not play a role in this consideration. This leaves ULE, fused silica, and polycrystalline β-SiC as the only suitable materials among the considered isotropic ones.

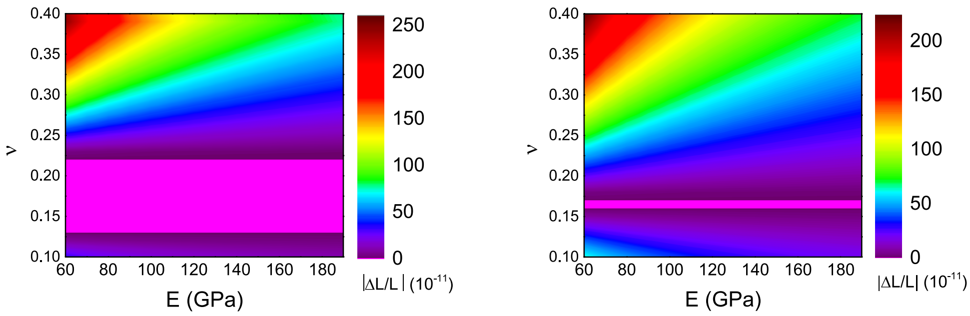

Fig. 7 Minimum absolute fractional length change $\mathrm{Min}|\Delta L(F_c)/L|$ among all cut depths between 3 and 23 mm (left) and 3 and 9 mm (right), as a function of the Young's modulus E and the Poisson's ratio ν. The region in magenta color indicates those values of E and ν for which cut depths exist that exhibit zero sensitivity to the support forces F_c

4.2 Acceleration sensitivity

The results presented in the previous sections were computed in the absence of gravity and of acceleration acting at the resonator. Equal forces F_c acting at each of the four tetrahedrically oriented supports on the block with octahedral symmetry, and pointing towards the center of the block, preserve the symmetry of arrangement.

When we include static gravity, which acts as a body force, i.e., on each volume element of the resonator, the resulting deformation lowers the resonator's symmetry. Depending on the magnitude of the deformation, this could make necessary an adjustment of the zero-sensitivity cut depths obtained in the previous sections.

We computed the effects of acceleration on the cubic ULE resonator having 6.6 mm cut depth. The resonator was fixed in space by the supports, a force $F_c = 1$N applied to each support, and was additionally subjected to a 1 g acceleration perpendicular or parallel to the x-axis (see Fig. 8). For the acceleration along the $-z$-axis, the displacements of the mirrors' center points along the x-axis are zero, see top left panel in the figure. In contrast, the 1 g-acceleration along the x-axis generates displacements of both mirrors on the nanometer scale ($\sim 5.1 \times 10^{-9}$ m), but equal ones, thus leaving the distance between the mirrors unchanged (see top right panel in the figure). The cancellation represents the numerical proof of the concept of Webster and Gill, which is based on the octahedral symmetry. Further simulations showed that the above displacements decrease with increasing Young's modulus, as expected.

We have performed similar simulations for various cut depths. The results are summarized in Fig. 8. It can be seen that, for the different sets of applied forces, the results are nearly equal. In particular, the optimal cut depth is not modified in the presence of gravity. We conclude that accelerations on the order of 1 g do not deform the resonator strongly enough to lower its symmetry so as to destroy the force insensitivity at the optimal cut depth determined assuming zero acceleration. We obtain the same results when the acceleration is increased by a factor 100.

5 Anisotropic materials

Additional candidate materials for a force-insensitive cubic cavity might be found among anisotropic materials, where E and ν depend on the crystallographic direction. Silicon and sapphire are two crystalline materials of this kind, and they

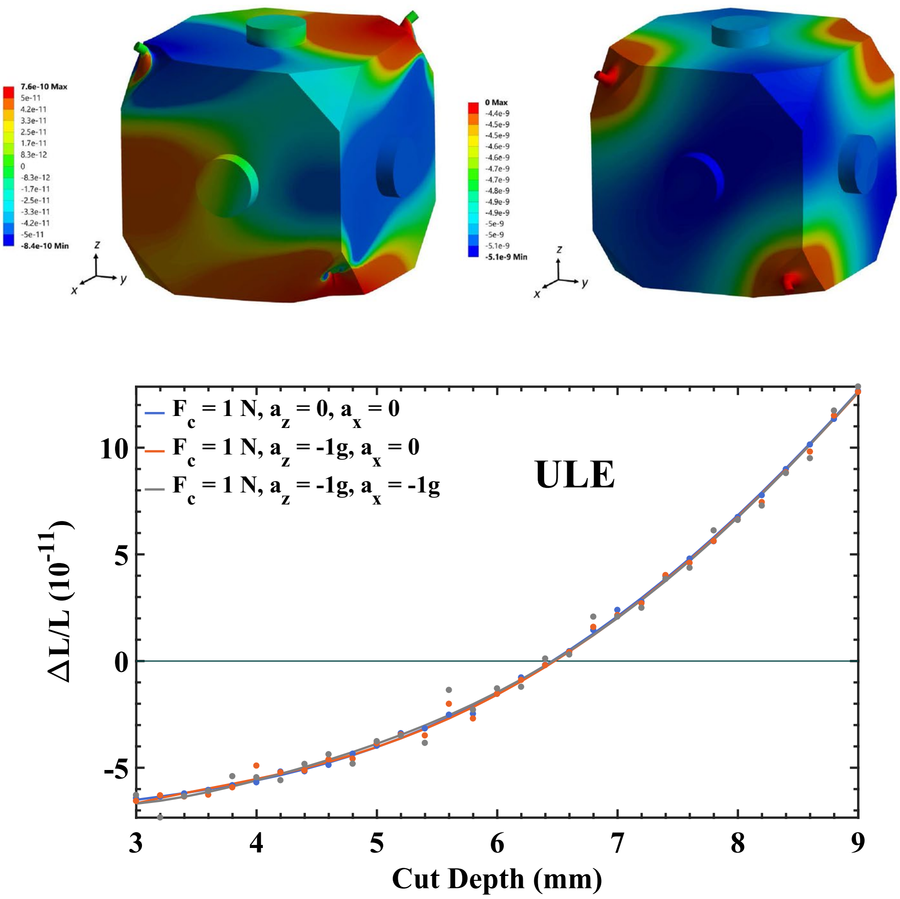

Fig. 8 ULE resonator subjected to an acceleration of magnitude $|a_j| = 1\,g$. Top left: acceleration applied along $-z$-axis. The deformation along the x-axis is displayed. Top right: acceleration applied along $-x$-axis. The deformation along the x-axis is displayed. Bottom: comparison of (1) sensitivity due to a force of 1 N on the supports, (2) with additional application of $-1\,g$ in the direction perpendicular to the x-axis, and (3) with additional 1 g accelerations acting both perpendicular and along the axis of the x-cavity. Results presented in this diagram were calculated with an acceleration of $|a_j| = 100\,g$ and scaled to $|a_j| = 1\,g$ afterwards

have already been used successfully for cryogenic optical resonators.

For an anisotropic material, the relation between the applied stress σ and the resulting strain ε is [23, 24]:

$$\sigma = C\varepsilon, \tag{1}$$

where σ and ε are second-rank tensors with 9 elements each and C is the fourth-rank stiffness tensor with 81 elements. For crystals with cubic symmetry (e.g., silicon), both σ and ε tensors contain only six independent elements. Using a simplified Voigt notation, the tensor C can be reduced to the 6×6 symmetric matrix with only three independent elements in the Cartesian coordinate system spanned by the $\mathbf{e}_1 = (1, 0, 0)$, $\mathbf{e}_2 = (0, 1, 0)$, and $\mathbf{e}_3 = (0, 0, 1)$ unit vectors pointing along [100], [010], and [001] crystallographic directions. The three independent elements are denoted by c_{11}, c_{12}, and c_{44} [25]:

$$C = \begin{bmatrix} c_{11} & c_{12} & c_{12} & 0 & 0 & 0 \\ c_{12} & c_{11} & c_{12} & 0 & 0 & 0 \\ c_{12} & c_{12} & c_{11} & 0 & 0 & 0 \\ 0 & 0 & 0 & c_{44} & 0 & 0 \\ 0 & 0 & 0 & 0 & c_{44} & 0 \\ 0 & 0 & 0 & 0 & 0 & c_{44} \end{bmatrix}. \tag{2}$$

To transform C to the stiffness matrix C' for any other Cartesian coordinate system, specified by the vectors $\mathbf{e'}_1$, $\mathbf{e'}_2$, and $\mathbf{e'}_3$, we first lay $\mathbf{e'}_1$ along a particular crystallographic direction defined by the Miller indices [hkl]. The two vectors $\mathbf{e'}_2$ and $\mathbf{e'}_3$ then necessarily lie in the crystallographic plane (hkl), at right angles to each other. The transformation of C is done using the algorithm described in [26]. The Young's modulus and the Poisson's ratio can be extracted from the compliance matrix S', the inverse of the stiffness matrix C', as follows: [26]:

$$E_{ii} = \frac{1}{S'_{ii}}, \tag{3}$$

$$\nu_{ij} = -\frac{S'_{ij}}{S'_{ii}}, \tag{4}$$

with $i, j = 1, 2, 3$ and $i \neq j$, where i and j denote the three orthogonal directions in the new coordinate system. Thus, E_{11} and (E_{22}, E_{33}) are the Young's moduli along the $\mathbf{e'}_1$ axis and perpendicular to it, respectively. (ν_{12}, ν_{13}) and ν_{23} are the Poisson's ratios for the directions along the $\mathbf{e'}_1$ axis and perpendicular to it, respectively.

5.1 Silicon

Silicon is an anisotropic material which enjoys increasing popularity as a material for cryogenic optical resonators [12, 13, 16, 28–30] due to the high thermal conductivity [31], the ultra-low expansion coefficient at cryogenic temperatures [14, 15, 32, 33], and the ultra-low-length drift [6, 16]. Three independent elements of the stiffness matrix C from Eq. (2) are $(c_{11}, c_{12}, c_{44}) = (165.7,\ 63.9,\ 79.6)$ GPa [34].

To set up the simulation for any desired crystallographic direction [hkl], we first orient the resonator with the optical axes of the three cavities laying parallel to the (x, y, z) coordinate axes of the fixed laboratory reference frame, as shown in Fig. 9, top left panel. Then, we define the new coordinate system by pointing $\mathbf{e'}_1$ along the [hkl] crystallographic direction and by defining the two vectors $\mathbf{e'}_2$ and $\mathbf{e'}_3$ in the crystallographic plane (hkl), at right angles to each other (see Fig. 9, top right panel). Because of the cubic symmetry of the silicon lattice, we only need to consider crystallographic directions that lie inside the unit stereographic triangle whose corners are defined by the [100], [110], and [111] directions. In the next step, we orient the crystal structure with the chosen crystallographic direction [hkl] along the x-axis of the cube. Two other unit vectors $\mathbf{e'}_2$ and $\mathbf{e'}_3$ are laid along the y- and z-axes, respectively (see Fig. 9, bottom left panel). To find all possible orientations of interest, we can introduce an additional degree of freedom by rotating the crystal counterclockwise around the [hkl] direction, as seen along the x-axis (see Fig. 9, bottom right panel). This is done first by rotating the vectors $\mathbf{e'}_2$ and $\mathbf{e'}_3$ in the crystallographic plane (hkl) by an angle α around the $\mathbf{e'}_1$ axis using Rodrigues' rotation formula [27] (see Fig. 9, bottom right panel). After rotation, the algorithm from [26] is applied again to obtain the stiffness matrix C', the Poisson's ratio ν_{12} and ν_{23}, and the Young's modulus E_{11} and E_{22}. This procedure is repeated for different values of α until one full circle of rotation is completed. We note that, due to rotation, we only need to consider E_{22} and ν_{12} as the Young's modulus and the Poisson's ratio for the direction perpendicular to the x-axis, respectively, as they contain all necessary information. The E_{33} and ν_{13} can be ignored.

The values of E, ν for rotation around the [100], [110], and [111] characteristic directions are visualized in Fig. 10, where the values of the Poisson's ratio that correspond to the "magic" range $0.13 < \nu < 0.23$ were colored green.

The maximum of the Young's modulus and the minimum of the Poisson's ratio for all angles of rotation for any given direction [hkl] inside the unit stereographic triangle are presented in Fig. 11. The Young's modulus varies from 130.1 to 187.9 GPa for the directions parallel to [hkl] (top, left) and from 169.1 to 187.9 GPa for the perpendicular direction (top, right). Directions which provide the highest stiffness are the [111] and [110] directions, respectively.

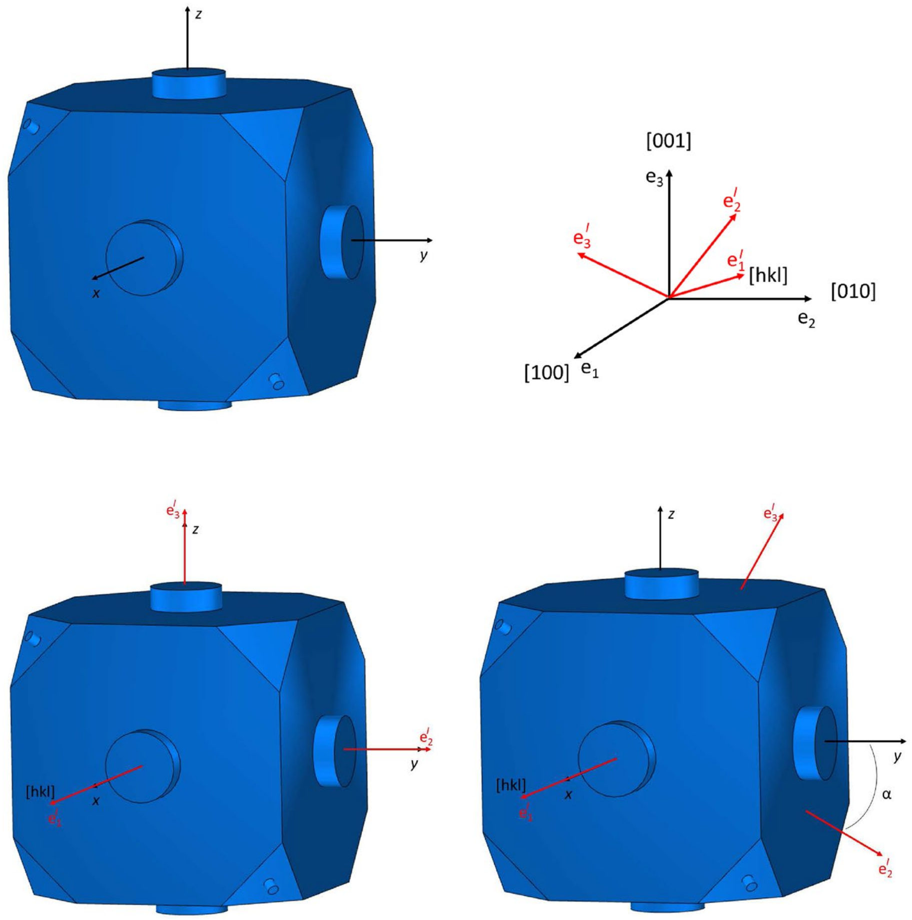

Fig. 9 Orientation of the crystal lattice with respect to the cavity body. Top left: the silicon resonator is always oriented with its cavities aligned with the (x, y, z) coordinate axes of the laboratory reference frame. Top right: orientation of the crystal-lattice-fixed coordinate system of the silicon crystal ($\mathbf{e}'_1$, $\mathbf{e}'_2$, and $\mathbf{e}'_3$) with vector $\mathbf{e}'_1$ coincident with a selected crystallographic direction [hkl], relative to the coordinate system defined by the ($\mathbf{e}_1$, $\mathbf{e}_2$, and $\mathbf{e}_3$) unit vectors oriented along the [100], [10], and [1] crystallographic directions, respectively. Bottom left: silicon crystal is oriented with the selected crystallographic direction [hkl] coincident with the x-axis of the laboratory frame and $\mathbf{e}'_3$ along z. Bottom right: rotation of the silicon crystal around the [hkl] direction by an angle α. For this orientation, the stiffness matrix C' is calculated

As we know from the foregoing discussion on isotropic materials, the Poisson's ratio plays the crucial role. To have zero sensitivity, it should lie within a "magic range" $0.13 < \nu < 0.23$. The Poisson's ratio varies from 0.062 to 0.26 for the parallel direction (bottom, left) with a minimum along [100] and a maximum along [111]. The variation in the perpendicular direction is from 0.062 to 0.28 with the minimum along [110] and the maximum along [100]. This large difference makes it impossible to predict which directions will have zero sensitivity and makes extensive simulations necessary.

Since the material is anisotropic, we now calculate the length changes of all three cavities within the cube, i.e., $\Delta L_i(F_c)/L$ for $i = x, y, z$, which may differ. We repeat the simulations for different crystallographic directions inside the unit stereographic triangle, which is oriented along the x-axis.

A first result of the FEA simulation is shown in Fig. 12, left column, where only the three characteristic directions [100], [110], and [111] are considered. The right column visualizes the corresponding crystal structure seen along these directions.

The [100] direction (top left panel) is the only one, for which all three cavities exhibit equal sensitivity to the holding force. For this direction, the FEA is performed directly with $C' = C$, Eq. (2). However, no zero sensitivity is possible with the half-inch mirror substrates (blue points). Reduction of the mirror diameter to $d = 10$ mm (magenta points) allows achieving a zero sensitivity for all three cavities simultaneously at a cut depth of 24.5 mm with a slope of 11×10^{-11}/mm. The corresponding simulation results are depicted in more detail in Fig. 13. We designate this geometry as Si-I.

The [110] direction (middle left panel) displays identical sensitivity for two cavities but without zero-sensitivity cut depth. The third cavity, the y-cavity, has zero sensitivity for two appropriate cut depths (see Fig. 12, middle left panel). The slopes at 13 mm and at 20 mm cut depth are 2.9×10^{-11}/mm and 6.5×10^{-11}/mm, respectively. They are smaller than for the ULE case.

The [111] direction (bottom left panel) has different sensitivities for all three cavities (see Fig. 12, bottom left panel). They all have zero sensitivity at large cut depths. The difference in optimum cut depth for the

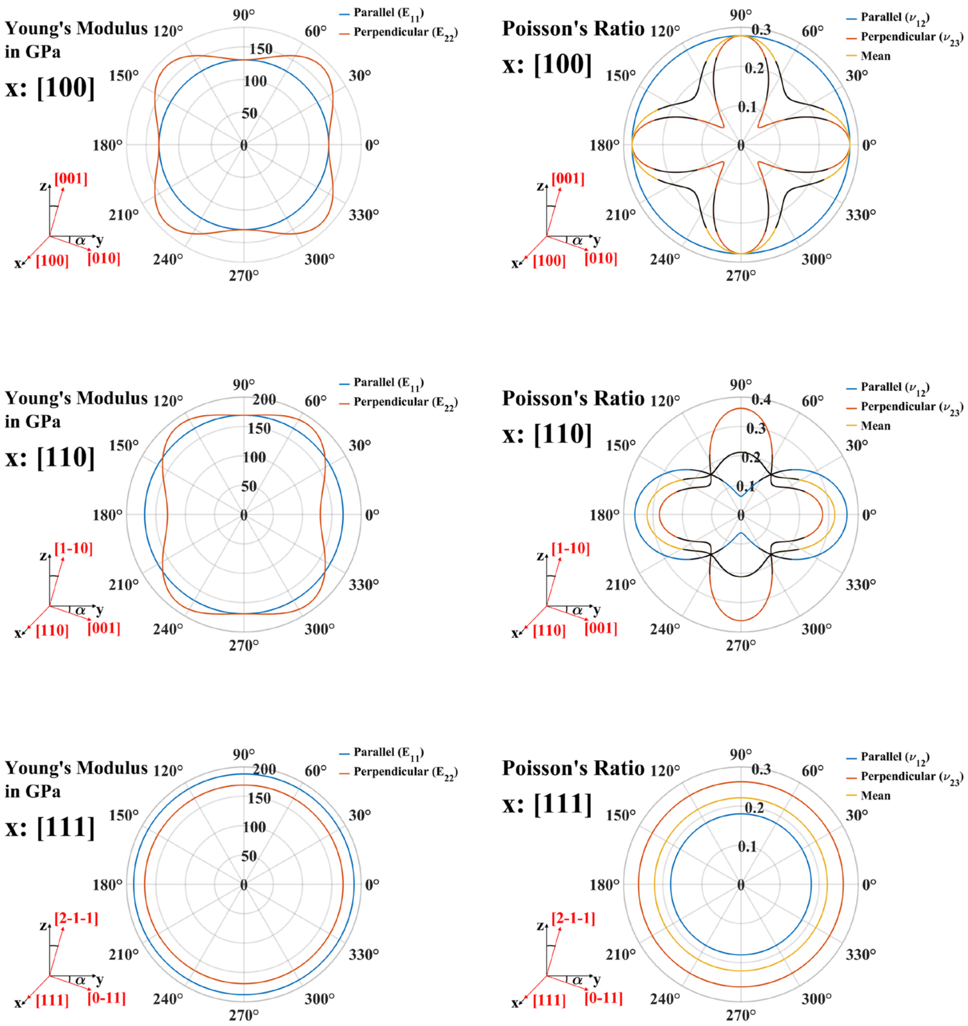

Fig. 10 Silicon's Young's modulus (left column) and Poisson's ratio (right column) calculated for the [100], [110], and [111] crystallographic directions (blue lines) and for directions perpendicular to them (red lines), for different values of angle α. Values of the Poisson's ratio that lie within a "magic" range $0.13 < \nu < 0.23$ are marked with black color. The definition of the angle α is shown in the small panels

y- and z-cavities is particularly low, 0.16 mm. This value is comparable with the typical manufacturing precision of 0.1 mm. Thus, the [111] orientation makes it possible to access two orthogonal cavities having small sensitivities. If the cut depth is chosen, such that the sensitivity of one cavity is zero, the sensitivity of the second cavity is then approximately 1.5×10^{-11}/mm.

The foregoing discussion makes it clear that there must be multiple orientations inside the unit triangle which yield zero sensitivity for at least one cavity. However, we are only interested in orientations which have the effective Young's modulus along the [hkl] direction and perpendicular to it as high as possible, to relax the requirement on the manufacturing precision of the vertices' cut depth. The effective Poisson's ratio for these directions must be in the range which allows the cavities to have zero sensitivity. To identify these directions, an extensive simulation was carried out, which is described in the next section.

5.2 Simulation procedure

We performed simulations for more than 100 different directions inside the unit triangle. The stiffness matrix C' for each direction was input into the simulation software. The chosen crystallographic direction was oriented along the x-axis of the laboratory reference frame. This orientation together with the stiffness matrix C' defines the orientation of the crystal along the y- and z-axes. Then, the crystal was turned in 10 degree steps around the x-axis of the laboratory reference frame (see Fig. 9). At each angle, the force F_c =1 N was applied at each of the supports and pointing to the center of the cube, and the deformations ΔL_j of the three cavities along their axes $j = x, y, z$ calculated.

The cut depth of the resonator was held constant at one particular value, since it would have been too time-consuming to vary this parameter, as well. Its value was chosen based on the foregoing discussion, which made clear that the slope of sensitivity is lower when the resonator has the shape

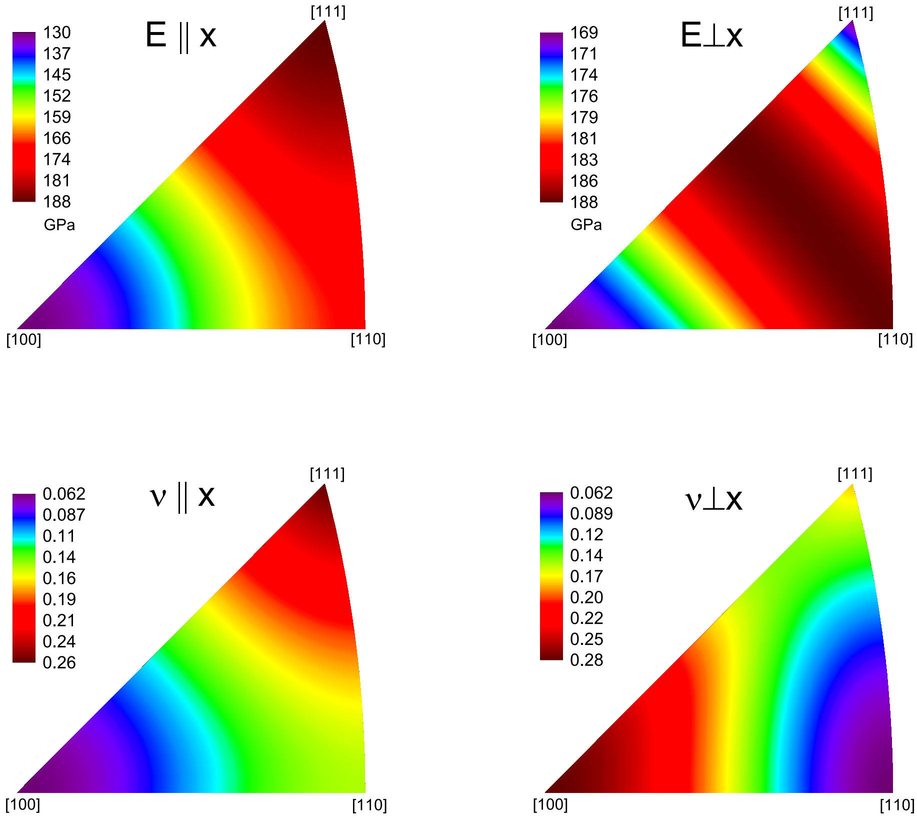

Fig. 11 Maximum of the Young's modulus and minimum of the Poisson's ratio for different crystallographic orientations of Si inside the unit stereographic triangle oriented along the x-axis of the resonator

of a truncated cube. At a cut depth of 14.47 mm, the shape of the resonator changes to a truncated octahedron, which always has a higher sensitivity slope. For that reason, the cut depth was fixed near the mean of the values corresponding to a truncated cube, 7.27 mm.

5.3 The support force sensitivity

The results for the three corner directions of the unity triangle, [100], [110], and [111], are presented in Fig. 14. As the top right panel shows, the fractional length changes of the three cavities are equal only for the x: [100] crystallographic direction and $\alpha = 0$ rotational angle. For all other orientations and angles (all panels), at least two of the three cavities display different fractional length changes. This is due to the differences in the lattice structure along the cavity axes. The x-cavity of the [100] orientation crosses zero fractional length change twice in the α angle interval between 0° and 90°. Two other cavities have an equal sensitivity at all angles with a minimum of 4×10^{-10}. The cube with the [110] material orientation (bottom left panel) has zero-sensitivity crossings for the y- and z-cavities and no crossing for the x-cavity. All cavities of the resonator with the [111] orientation (bottom right panel in the figure) have no zero sensitivity.

The minimum fractional length changes occurring over a full turn around all orientations (α varies between 0° and 360°) inside the unity triangle are displayed in Fig. 15. As we can see, there is only one favorable orientation for each cavity, shown in purple (top row). To have zero sensitivity for the x-cavity, the resonator must be oriented along the [100] direction, see top left panel. Zero sensitivity for the y- and z-cavities is only possible if resonator is oriented along the [110] direction, but not at the same angle. As Fig. 14, bottom left panel, suggests, there is an angle shift of 90 degrees between them. Our results rule out the possibility of having zero sensitivity for more then one cavity simultaneously, for the considered vertex cut depth. In Fig. 15, we display sensitivities along the two axes at an angle of minimum sensitivity for the one of the three axes. Similar to the case of isotropic materials, we compare our results with the Poisson's ratio (see Figs. 11 and 15). Both the x-cavity sensitivity and the Poisson's ratio have a minimum in the vicinity of the [100] direction. The minimum of the sensitivity for the y- and z-cavities and for [110] silicon orientation (see Fig. 15, top right panel) corresponds to the minimum of the Poisson's ratio calculated for the direction perpendicular to [110] (see Fig. 11, bottom right panel).

The evaluation of the Young's modulus for the direction parallel to the crystallographic orientation and perpendicular to it is presented in Fig. 15, top row panels. For example, we find that the direction [110], with the Young's modulus of 169.1 GPa along the x-axis and 187.9 GPa perpendicular to it, is more favorable than the [100] direction, for which the values are 130.1 and 169.1 GPa, respectively.

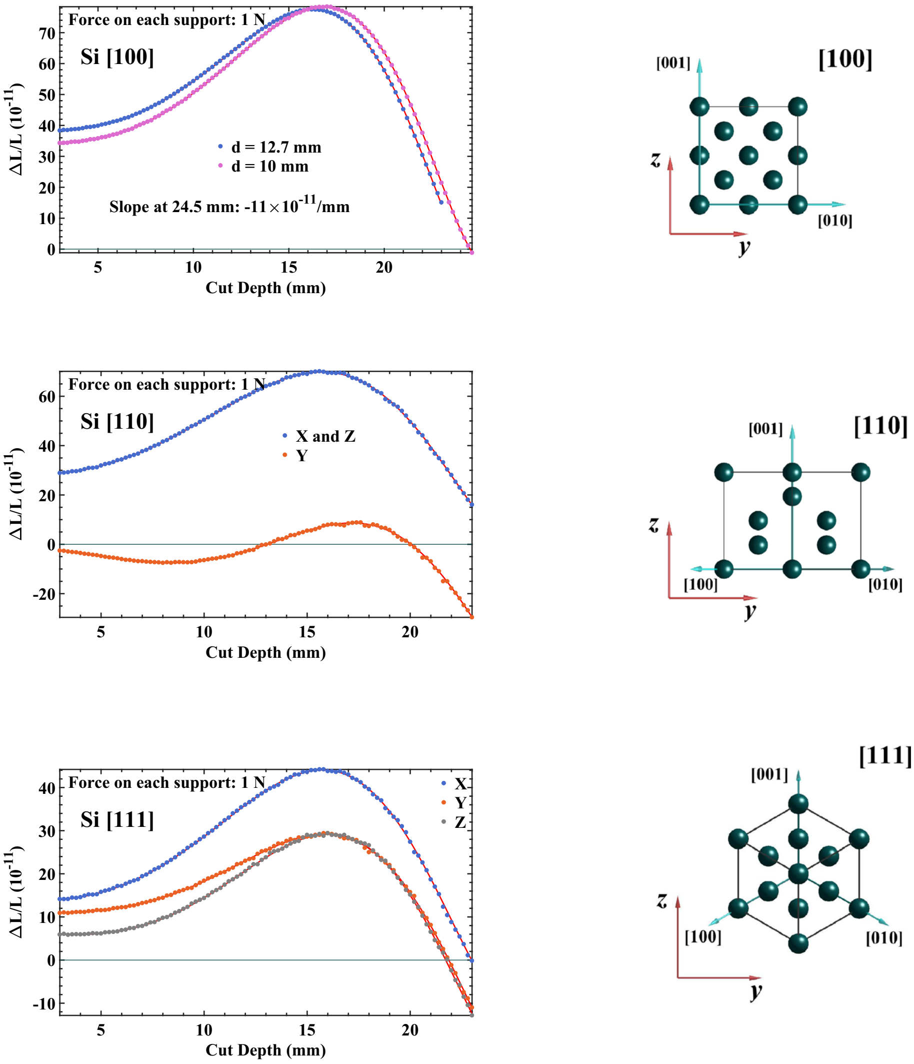

Fig. 12 Sensitivity to F_c for the three cavities when the Si crystal is oriented in particular crystallographic directions. The corresponding view on the crystal along the direction in question is shown on the right, each ball representing the top Si atom in the plane perpendicular to the observation direction

This difference should be reflected in the dependence of the fractional length change on the variation in cut depth and in angle of rotation around their optimal values. To obtain these numbers, we performed a series of simulations displayed in Fig. 16. We find that, for the x: [100] orientation (top row), both $\Delta L_x/L$ and its sensitivity to cut depth variation are zero at a cut depth of 7.54 mm and at angle $\alpha = 33.23°$. This case is denoted by Si-II in the following. The fractional length change varies by $12 \times 10^{-12}/°$ around the optimum angle and by 3.5×10^{-12}/mm around the optimum cut depth.

The bottom row of panels shows that the cube with x: [110] orientation has a zero sensitivity of the z-cavity at an angle of 18.49° and at a cut depth of 6.88 mm (geometry denoted by Si-III). The y-cavity displays a zero crossing at the same cut depth but at an angle which is shifted by 90° from that of the z-cavity (see Fig. 14, bottom left panel). The fractional sensitivity variations are 5.6×10^{-12}/deg and 2.8×10^{-12}/mm for the variations in angle and cut depth, respectively.

6 Effect of imperfections

We evaluated the effect of additional imperfections on the sensitivity to the supporting force and on the acceleration insensitivity, besides the already considered cut depth deviation and orientation deviation (for anisotropic materials). For silicon, we consider only the geometries Si-I, Si-II, and Si-III introduced above, and for ULE and β-SiC the shapes of Sect. 4. The results are presented in Table 2. Item 1 in the table reports results already discussed above.

The cut depth of the individual resonator vertices may vary due to the accuracy of manufacture. We analyze the case that only one vertex (also serving as support) deviates

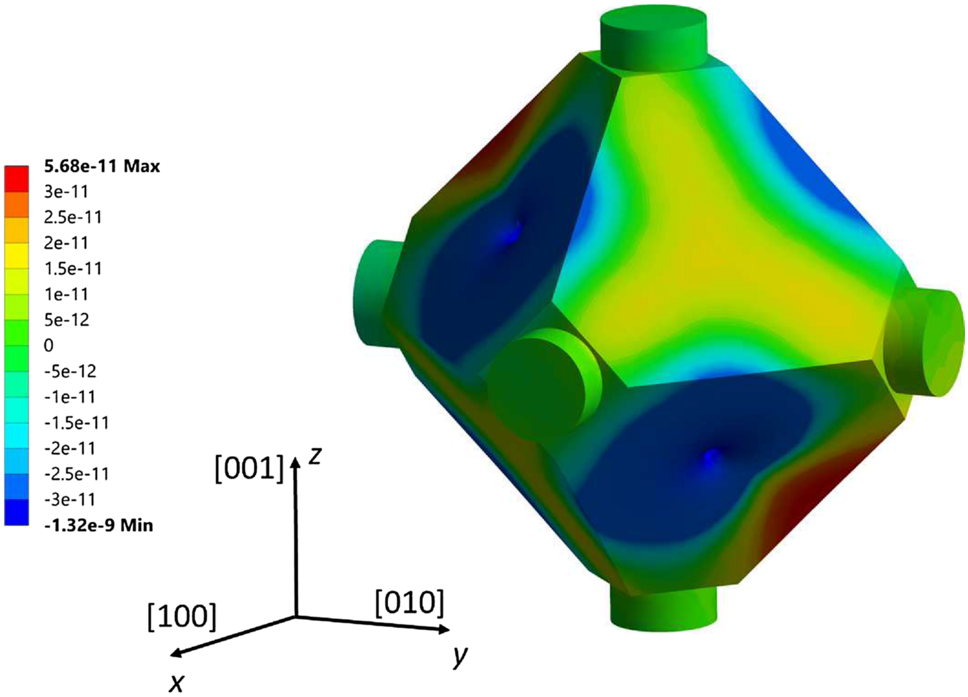

Fig. 13 Si [100] resonator structure having the special geometry Si-I: cut depth of 24.5 mm, with reduced mirror diameter of $d = 10$ mm. For an angle of material rotation $\alpha = 0$, all three cavities exhibit zero length change upon application of the four support forces $F_c = 1$ N. Shown are the displacements of the body along the x-axis. The scale is in meter

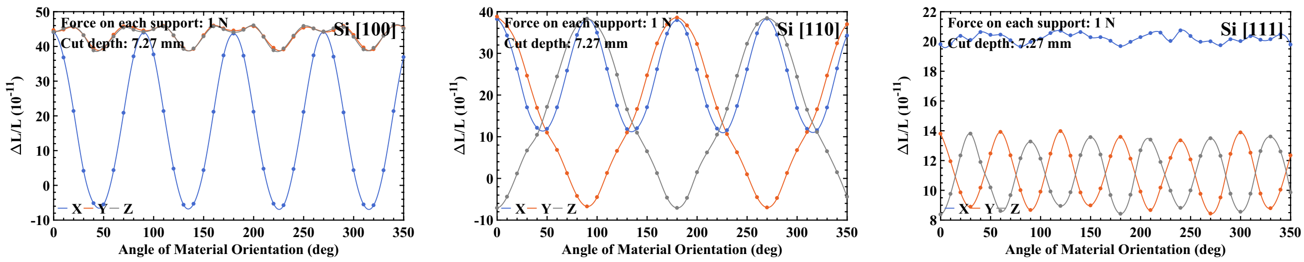

Fig. 14 Three plots show the cavity length changes upon rotation around the [100], [110], and [111] crystallographic directions of silicon, respectively

in cut depth from the other seven. Table 2, item 2, shows that for a cut depth imprecision of 0.1 mm, the cavity length deformation effects are at the level of 3×10^{-12} per N support force or smaller. In the gravity field, this imperfection introduces an acceleration sensitivity Max(k_{xx}, k_{xz}) on the order of $6 \times 10^{-12}/g$ or smaller.

Misplacement of the mirrors with respect to the symmetry axes of the cube can occur during assembly. As a result, the light propagation occurs along an axis shifted with respect to the symmetry axis. This breaks the symmetry assumed in the concept of the cubic block. Different deformation of the opposing mirrors at the intersection of the axis and the mirror surface introduces an additional length change and degrades the acceleration sensitivities k_{ij}. The calculation of the degradation was performed for a $\epsilon = 1$ mm shift of the optical axis in the direction having the largest deformation. The value 1 mm is larger than errors in fabrication and only serves as an example. Our result for ULE, given in the table (item 3), appears consistent with the FEA value reported by [7]. For silicon, we find acceleration sensitivities up to $3 \times 10^{-11}/g$.

The sensitivity to orientation of the Si crystal with respect to the resonator is reported under item 4; we find the acceleration sensitivities to be rather small if an error of 1° is assumed.

Asymmetrical mounting of the resonator in the frame with the supports displaced from their optimal position is another source of error (items 5 and 6 in the table). We see that the effects are not negligible. For an offset of $\epsilon = 0.1$ mm, in the case of ULE, the cavity length changes fractionally by $\simeq 1 \times 10^{-11}$ for a 1 N support force, and a sensitivity to acceleration perpendicular to the cavity $k_{xz} = 7 \times 10^{-12}/g$ arises. For silicon, the numbers are similar.

The above results make it clear that great care should be taken in mounting the resonator in the supporting frame. Together with the offsets of mirrors from the respective

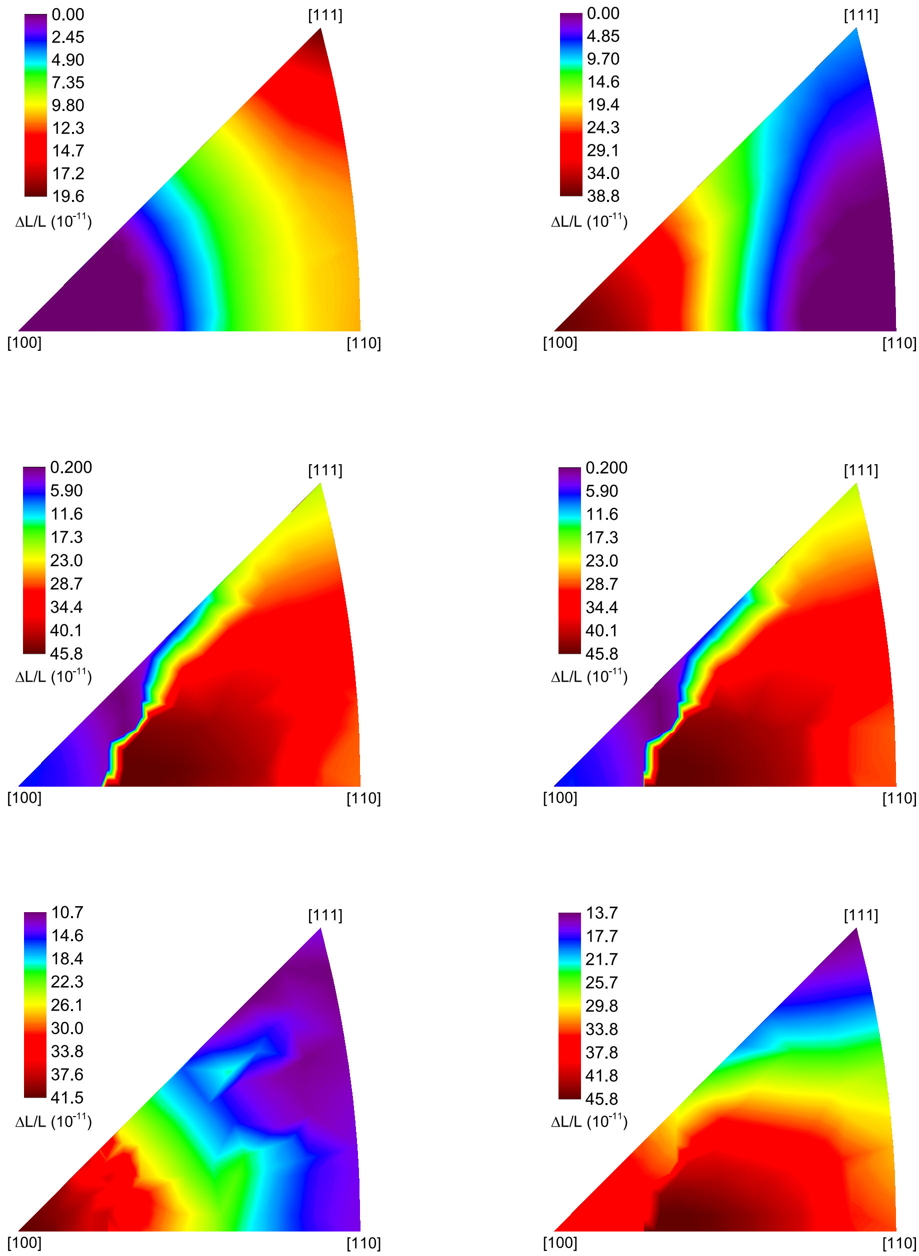

Fig. 15 Sensitivities of cavity lengths to the application of the four support forces $F_c = 1\,\mathrm{N}$, for all crystallographic orientations. Top row: maps of minimum fractional length change for the x-cavity (left) and for the y / z-cavities (right); Middle row: maps of the y-cavity sensitivity (left) and of the z-cavity sensitivity (right), both at the angle of smallest x-sensitivity; Bottom row, left: maps of the x / z-cavity sensitivity at the angle of smallest y-cavity sensitivity; bottom row, right: maps of the x / y-cavity sensitivity at the angle of smallest z-cavity sensitivity

symmetry axes, mounting errors appear to be a major potential cause of the degradation of sensitivity compared to the ideal. Comparing silicon with ULE we find that silicon is less sensitive to errors, but in several respects only by a factor approximately 2. Comparing the three silicon resonator geometries, Si-I, Si-II, and Si-III, we find Si-II to be more advantageous, in particular with respect to one critical error, the offset from the optical axis.

7 Error evaluation

To determine the influence of finite mesh size on the optimum cut depth, we performed simulations of a ULE block applying different mesh densities. Assuming that simulations with infinitely small mesh size adequately represent the reality, we extrapolated our results toward decreasing

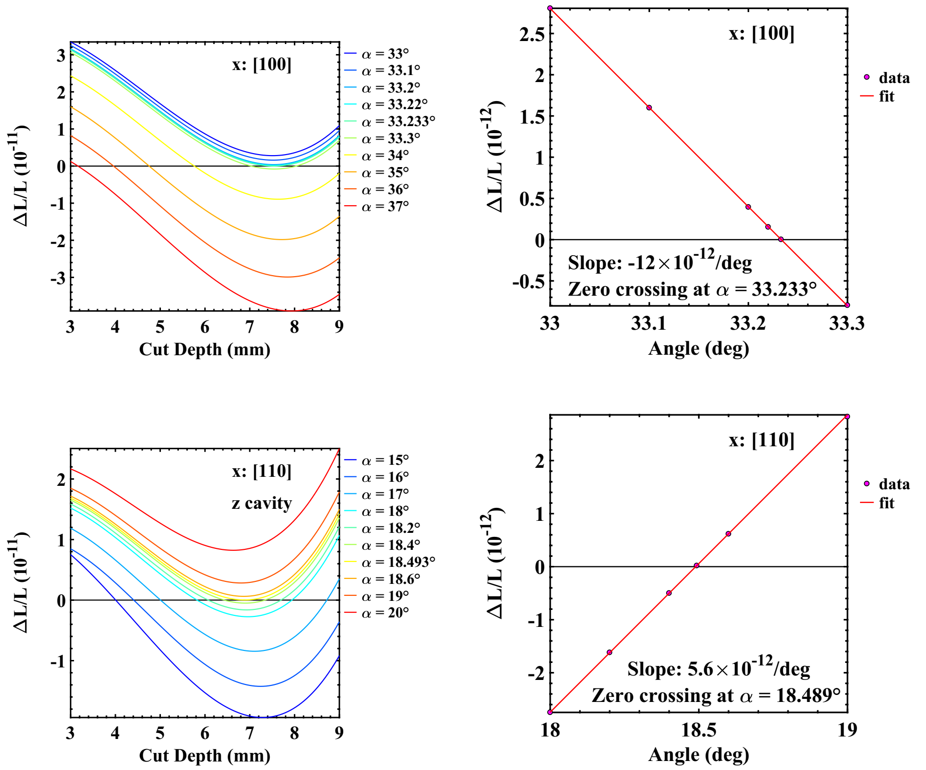

Fig. 16 Determination of an optimal angle and cut depth for the zero fractional length change of the x-cavity of the resonator and [100] silicon orientation (top) and z-cavity (or y-cavity with an angle α shifted by +90°) and [110] orientation (bottom). A force of 1 N is applied at each support

Table 2 For different geometries, acceleration sensitivities k_{ij} in the presence of a manufacturing error ϵ of 1 mm or 1 ° and sensitivity $S_\epsilon = \partial(\Delta L(F_c)/L)/\partial\epsilon$ of the length change caused by a $F_c = 1$ N force

Type of geometry change ϵ	Quantity (10^{-11})	Material and orientation				
		ULE	β-SiC	Si-I	Si-II	Si-III
1. Cut depth, all vertices	S_ϵ (mm^{-1})	3.7	4.1	11	0.35	0.28
	k (g^{-1})	0	0	0	0	0
2. Cut depth, one vertex	S_ϵ (mm^{-1})	0.8	1.1	3.3	0.01	0.41
	k_{xx}, k_{xz} (g^{-1})	6.4, 3.6	1.5, 0.13	1.01, 0.2	2.2, 0.61	4.2, 2.2
3. Offset of the optical axis	S_ϵ (mm^{-1})	2.7	0.07	0.6	0.7	3.5
	k_{xx}, k_{xz} (g^{-1})	0, 5	0, 0.4	0.23, 3.2	0, 1	0, 0.8
4. Orientation of material	S_ϵ (deg^{-1})	–	–	0.3	1.2	0.56
	k_{xx}, k_{xz} (g^{-1})	–	–	0, 0.002	0.05, 0.002	0, 0.15
5. Horizontal offset of one support	S_ϵ (mm^{-1})	13	2.9	14.4	7.7	5.7
	k_{xx}, k_{xz} (g^{-1})	5.4, 7.0	1.4, 0.12	4.7, 0.13	3.7, 3.8	5.0, 2.9
6. Vertical offset of one support	S_ϵ (mm^{-1})	7.5	2.0	8.41	3.6	3.8
	k_{xx}, k_{xz} (g^{-1})	3.2, 3.2	1.2, 0.84	3, 1.43	1.4, 1.8	1.9, 2.1

The geometries are specified in the text. Sensitivity to cut depth of one vertex as well as to the offset of one support were evaluated using the vertex and the support at the location defined by the vector $\mathbf{v} = (1, -1, 1)$. For the offset of the optical axis, we considered as symmetry axis the x-cavity axis in the case of ULE, polycrystalline β-SiC and Si [100], and the y-cavity axis in the case of Si [110]. The direction of the offset was assumed to be along the direction with the largest mirror deformation

mesh size and obtained an error of less than 0.08 mm for the optimum cut depth.

We also evaluated the scatter of data points in different simulation results by fitting them with a polynomial of high degree and plotting the distribution of the residuals. This evaluation indicates an error in sensitivity $\Delta L/L$ of $\pm 2 \times 10^{-12}$ for the simulations where no acceleration is involved and an error of $\pm 1 \times 10^{-11}$ whenever an acceleration is applied. This error was found to have approximately cubic dependence on mesh size.

Another way to validate our simulation procedures is to compare with the published results. In Matei et al. [35], a vertically oriented, biconical silicon resonator was simulated and the results experimentally validated. Our simulations are in good agreement.

8 Summary and conclusion

We analyzed the sensitivity to support forces of the three-cavity cubic block made of different materials. For isotropic materials, we identified a "magic" range for Poisson's ratio, $0.13 \leq \nu \leq 0.23$, for which the three cavity lengths become insensitive to the strength of the support force. Because of this particular range, apart from ULE, only fused silica and β-SiC are suitable materials among the common isotropic materials used in the optics industry. Silicon, as anisotropic material, offers multiple suitable orientations for providing zero sensitivity. Based on FEA simulations, we identified two orientations, [100] and [110], to be particularly suitable. Compared to ULE, they provide one cavity with more robustness to the errors in manufacturing: the acceleration sensitivity is reduced by a factor of approximately two or more compared to ULE, depending on the error.

We thus showed that silicon spacers with octahedral symmetry can provide a favorable option for cryogenic, support force-insensitive and vibration-insensitive cavities. Particularly attractive is the fact that there exists one geometry, with [100] orientation of the crystal, which provides simultaneously three nominally insensitive cavities in the same spacer. This geometry could be useful for certain applications, e.g., tests of Lorentz Invariance. Nevertheless, even with only 0.1 mm imprecision in manufacturing and mounting, a residual sensitivity to support force at the level of $14 \times 10^{-12}/\mathrm{N}$ level can occur. The corresponding residual vibrational sensitivity can be as high as $5 \times 10^{-12}/g$. Achieving a suitable design and production of the frame that provides stable support forces will be an important additional aspect of the overall system.

Acknowledgements We thank T. Legero (PTB) for providing us with the design of the biconical Si resonator allowing us to test our simulations, A. Nevsky for stimulating discussions, and D. Sutyrin for his help with the simulations. This work was performed in the framework of project SCHI 431/21-1 of the Deutsche Forschungsgemeinschaft.

References

1. N. Huntemann, C. Sanner, B. Lipphardt, C. Tamm, E. Peik, Phys. Rev. Lett. **116**, 063001 (2016)
2. A.D. Ludlow, M.M. Boyd, J. Ye, E. Peik, P.O. Schmidt, Rev. Mod. Phys. **87**, 637 (2015)
3. T. Nicholson, S. Campbell, R. Hutson, G. Marti, B. Bloom, R. McNally, W. Zhang, M. Barrett, M. Safronova, W. Strouse, G.F. Tew, J. Ye, Nat. Commun. **6**, 6896 (2015)
4. P. Antonini, M. Okhapkin, E. Göklü, S. Schiller, Phys. Rev. A **71**, 050101(R) (2005)
5. C. Eisele, A.Y. Nevsky, S. Schiller, Phys. Rev. Lett. **103**, 090401 (2009)
6. E. Wiens, A.Y. Nevsky, S. Schiller, Phys. Rev. Lett. **117**, 271102 (2016)
7. S. Webster, P. Gill, Opt. Lett. **36**, 3572 (2011)
8. K. Numata, A. Kemery, J. Camp, Phys. Rev. Lett. **93**, 250602 (2004)
9. M. Notcutt, L.S. Ma, A.D. Ludlow, S.M. Foreman, J. Ye, J.L. Hall, Phys. Rev. A **73**, 031804 (2006)
10. J. Davila-Rodriguez, F.N. Baynes, A.D. Ludlow, T.M. Fortier, H. Leopardi, S.A. Diddams, F. Quinlan, Opt. Lett. **42**, 1277 (2017)
11. S. Seel, R. Storz, G. Ruoso, J. Mlynek, S. Schiller, Phys. Rev. Lett. **78**, 4741 (1997)
12. D.G. Matei, T. Legero, S. Häfner, C. Grebing, R. Weyrich, W. Zhang, L. Sonderhouse, J.M. Robinson, J. Ye, F. Riehle, U. Sterr, Phys. Rev. Lett. **118**, 263202 (2017)
13. W. Zhang, J.M. Robinson, L. Sonderhouse, E. Oelker, C. Benko, J.L. Hall, T. Legero, D.G. Matei, F. Riehle, U. Sterr, J. Ye, Phys. Rev. Lett. **119**, 243601 (2017)
14. E. Wiens, Q. Chen, I. Ernsting, H. Luckmann, A.Y. Nevsky, U. Rosowski, S. Schiller, Opt. Lett. **39**, 3242 (2014)
15. E. Wiens, Q. Chen, I. Ernsting, H. Luckmann, A.Y. Nevsky, U. Rosowski, S. Schiller, Opt. Lett. **40**, 68 (2015)
16. C. Hagemann, C. Grebing, C. Lisdat, S. Falke, T. Legero, U. Sterr, F. Riehle, M.J. Martin, J. Ye, Opt. Lett. **39**, 5102 (2014)
17. P.R. Cromwell, *Polyhedra* (Cambridge University Press, Cambridge, 2008)
18. Product sheet from Rohm and Haas Co. http://www.dow.com/. Accessed 12 June 2018
19. Product sheet from Corning, Inc. https://www.corning.com. Accessed 12 June 2018
20. N118C Product sheet from Krosaki Harima. https://krosaki-fc.com/en/ceramics/nexcera.html. Accessed 12 June 2018
21. Product sheet from SCHOTT North America, Inc. http://www.us.schott.com/english/index.html. Accessed 12 June 2018
22. M. Bass, *Handbook of Optics*, 2nd edn. (McGraw-Hill, New York, 1995)
23. J.F. Nye, *Physical Properties of Crystals: Their Representation by Tensors and Matrices* (Clarendon Press, Oxford, 1964)
24. J.J. Wortman, R.A. Evans, J. Appl. Phys. **36**, 153 (1965)
25. M.A. Hopcroft, W.D. Nix, T.W. Kenny, J. Microelectromech. Syst. **19**, 229 (2010)
26. L. Zhang, R. Barrett, P. Cloetens, C. Detlefs, M. Sanchez del Rio, J. Synchrotron Radiat. **21**, 507 (2014)
27. R.H. Battin, *An introduction to the mathematics and methods of astrodynamics, rev. AIAA Education Series* (American Institute of Aeronautics and Astronautics Inc, Reston, 1999)
28. B. Parker, G. Marra, L.A.M. Johnson, H.S. Margolis, S.A. Webster, L. Wright, S.N. Lea, P. Gill, P. Bayvel, Appl. Opt. **53**, 8157 (2014)
29. J. Millo, C. Lacroute, A. Didier, E. Rubiola, Y. Kersal, J. Paris, in *Proc. of the 2014 European Frequency and Time Forum*, pp. 531–534 (IEEE, 2014). https://doi.org/10.1109/EFTF.2014.7331555
30. T. Kessler, C. Hagemann, C. Grebing, T. Legero, U. Sterr, F. Riehle, M.J. Martin, L. Chen, J. Ye, Nat. Photon. **6**, 687 (2012)
31. C.J. Glassbrenner, G.A. Slack, Phys. Rev. **134**, A1058 (1964)
32. K.G. Lyon, G.L. Salinger, C.A. Swenson, G.K. White, J. Appl. Phys. **48**, 865 (1977)
33. J.P. Richard, J.J. Hamilton, Rev. Sci. Instrum. **62**, 2375 (1991)
34. W.P. Mason, *Physical Acoustics and the Properties of Solids* (Van Nostrand, Princeton, 1958)
35. D.G. Matei, T. Legero, C. Grebing, S. Häfner, C. Lisdat, R. Weyrich, W. Zhang, L. Sonderhouse, J.M. Robinson, F. Riehle, J. Phys. Conf. Ser. **723**, 012031 (2016)

F.4 Publication: A simplified cryogenic optical resonator apparatus providing ultra-low frequency drift

Reproduced from

Eugen Wiens, Chang Jian Kwong, Timo Müller, and Stephan Schiller

A simplified cryogenic optical resonator apparatus providing ultra-low frequency drift

Rev. Sci. Instrum. **91**, 045112 (2020)

DOI: https://aip.scitation.org/doi/10.1063/1.5140321

Author's contributions

All authors contributed to the work. My contributions to this work are:

- Design of the resonator and the support structure.
- Installation of the resonator inside the cryostat and building an all-cryogenic optical setup for incoupling of laser light.
- Operation of the cryostat.
- Execution of the experiments.
- Analysis of the experimental data.
- Co-writing the publication.

Review of Scientific Instruments ARTICLE scitation.org/journal/rsi

A simplified cryogenic optical resonator apparatus providing ultra-low frequency drift

Cite as: Rev. Sci. Instrum. 91, 045112 (2020); doi: 10.1063/1.5140321
Submitted: 26 November 2019 • Accepted: 2 April 2020 •
Published Online: 17 April 2020

Eugen Wiens,[1] Chang Jian Kwong,[1] Timo Müller,[2] and Stephan Schiller[1,a)]

AFFILIATIONS

[1]Institut für Experimentalphysik, Heinrich-Heine-Universität Düsseldorf, 40225 Düsseldorf, Germany
[2]Siltronic AG, Johannes-Hess-Straße 24, 84489 Burghausen, Germany

[a)]Author to whom correspondence should be addressed: step.schiller@hhu.de

ABSTRACT

A system providing an optical frequency with instability comparable to that of a hydrogen maser is presented. It consists of a 5 cm long, vertically oriented silicon optical resonator operated at temperatures between 1.5 K and 3.6 K in a closed-cycle cryostat with a low-temperature Joule–Thomson stage. We show that with a standard cryostat, a simple cryogenic optomechanical setup, and no active or passive vibration isolation, a minimum frequency instability of 2.5×10^{-15} at $\tau = 1500$ s integration time can be reached. The influence of pulse-tube vibrations was minimized by using a resonator designed for low acceleration sensitivity. With reduced optical laser power and interrogation duty cycle, an ultra-low fractional frequency drift of -2.6×10^{-19}/s is reached. At 3.5 K, the resonator frequency exhibits a vanishing thermal sensitivity and an ultra-small temperature derivative $8.5 \times 10^{-12}/\mathrm{K}^2$. These are favorable properties that should lead to high performance also in simpler cryostats not equipped with a Joule–Thomson stage.

I. INTRODUCTION

Optical resonators play an important role in the generation of laser light with ultra-stable frequency. They are essential to the field of optical atomic clocks, where they are utilized for the pre-stabilization of the laser wave used for the interrogation of ultra-narrow atomic transitions.[1–3] Other applications are in gravitational wave detectors[4,5] and for tests of fundamental physics.[6–11]

The most common type of resonator consists of a hollow spacer of length L, which introduces a fixed separation between two mirrors that are optically contacted to its end surfaces. The design of the spacer geometry and support is usually optimized to reduce length variations produced by environmental vibrations. To counteract thermally induced variations in length, the resonators are usually made of materials that exhibit a particularly low thermal expansion coefficient at the desired operational temperature. Ultra-low-expansion (ULE) glass is today the most common material for use at or near room temperature. Another promising material is the ceramic Nexcera.[12–14] However, the Brownian motion imposes a fundamental limitation to their length stability.[15] This is on the order of 1×10^{-15} for room-temperature resonators with a typical length of ≤10 cm.[16–20] The instability was successfully lowered to 8×10^{-17} using a 48 cm long resonator.[21] Furthermore, room-temperature resonators made of the ULE material suffer from drift. The drift rates vary substantially between units, with one of the smallest values being 1.6×10^{-17}/s.[14] One approach for reducing both limitations is the operation of the resonators at cryogenic temperatures.[6,7,22–29]

Here, we present a cryogenic single-crystal silicon resonator developed for low vibration sensitivity and frequency stability comparable to that of a hydrogen maser, operated in a cryogenic system of moderate complexity. In order to reduce the resonator manufacturing cost, we simplified the design to a cylindrical shape. A fairly complete characterization of the resonator was possible using a system composed of a stable interrogation laser, a frequency comb, and a hydrogen maser.

II. DESIGN

A. Cryostat accelerations

The goal of our resonator design was to minimize its acceleration sensitivity in order to achieve good performance in closed-cycle cryostats that provide no advanced vibration isolation. In such units, the pulse-tube and seismic accelerations are transmitted to the optical setup. As an example, our closed-cycle cryostat (Leiden Cryogenics, CF-1K) exhibits the acceleration spectrum displayed in Fig. 1(a). The accelerations were measured on the optical setup, during operation at 1.5 K, for the three cartesian axes using a precise interferometric sensor. With an optical head of the sensor located outside the cryostat, we used optical windows to reflect a laser beam from the device under test. While it is best to measure the acceleration directly on the resonator, here, this was possible only for its vertical motion, because of the limited optical access. To measure this motion, the laser interferometer beam was reflected from one of its end faces. The motion along the two horizontal directions was instead measured by reflecting the sensing laser beams from two other silicon resonators (designated as "Si1" and "Si2") contained within the cryostat.

The spectrum consists of peaks at multiples of 1.4 Hz, the base frequency of the pulse-tube cooler. The total acceleration integrated over the frequency range from 1 Hz to 200 Hz is 4.9×10^{-3} g [see Fig. 1(b)]. The largest contribution arises from the vibrations introduced by the rotary valve stepper motor, which operates with a frequency close to 150 Hz. Contribution from the vibrations of the lab ground, measured with a high-sensitivity piezoelectric transducer, is shown in Figs. 1(c) and 1(d) and is on the order of 0.9×10^{-3} g. It is dominated by the vertical component.

Because of this high acceleration level (compared to a standard room-temperature setup placed on a standard active vibration isolation platform), a minimized acceleration sensitivity of the resonator frequency is clearly necessary.

B. FEM simulations

The resonator developed in this work is a vertically oriented, axially symmetric structure, supported at three points. It follows the concept presented in Refs. 22–24, 26, and 27 but was further simplified by avoiding the conical spacer shape and employing instead a simple cylindrical shape. The spacer diameter and length were chosen to be 37 mm and $L = 50$ mm, respectively; the mirror substrates are of standard one-inch diameter and 6.3 mm thick. All the other geometry parameters were optimized using a commercial finite-element-method (FEM) package (Ansys). The optical axis of the resonator was aligned with the [111] crystallographic direction of the silicon crystal, which is the direction with the highest Young's modulus. We used the silicon stiffness matrix from Ref. 30 in our simulation. The optimization was done by calculating the acceleration sensitivity of the resonator, defined as fractional length change per unit acceleration, $\Delta L/(a_i\, L)$, for different values of the geometrical parameters and for different directions i of the acceleration. After defining a set of values, we studied the influence of imprecise optical contacting, of an offset of the resonator's position relative to the

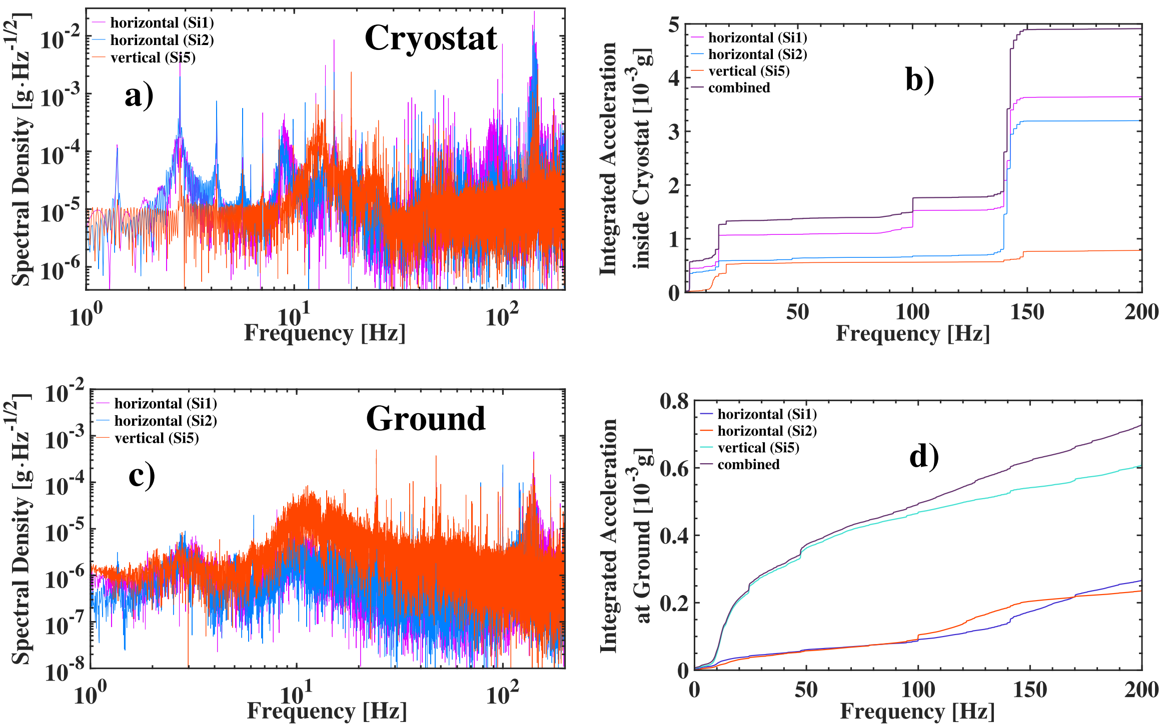

FIG. 1. Acceleration measured at three experimental plates inside the operating cryostat and ground acceleration. [(a) and (c)] Spectral density of acceleration $S_{a,i}(f)$, $i = x, y, z$, in the three spatial directions. The red curve in panel (a) indicates the level measured on the plate that supports the 5 cm resonator described in this work. [(b) and (d)] The total accelerations $\left[\int_0^f (S_{a,i}(f'))^2 df'\right]^{1/2}$. The combined total acceleration is the root sum-of-squares of the three individual total accelerations.

three support points (fixed in space), and of manufacturing tolerance (assumed to be 0.1 mm). Our optimization was aimed at minimization of these three sensitivities. This resulted in a support ring with diameter and thickness of 67 mm and 20 mm, respectively, an offset of the ring from the horizontal center plane toward the top of 0.51 mm, and a diameter of the central bore of 15 mm. The venting hole has 2 mm diameter, is located in the upper half of the resonator, is centered 5 mm below the top surface, and forms an angle of 63° with the [100] crystallographic direction of the silicon crystal. Partial results of the sensitivity calculations are displayed in Figs. 2(a)–2(c).

With three supports placed at a radial distance of 26 mm from the optical axis of the resonator, the acceleration sensitivity variation with a vertical offset of the support ring, under 1 g vertical acceleration, is $16 \times 10^{-11}/(g\ \mathrm{mm})$. The sensitivity to an imperfect radial positioning of the resonator relative to the supports is $5 \times 10^{-11}/(g\ \mathrm{mm})$, and the sensitivity to a parallel offset of the optical axis from the symmetry axis of the resonator is $4 \times 10^{-11}/(g\ \mathrm{mm})$.

We also simulated the effect of rotation of the resonator around the vertical symmetry axis, while the support points remained fixed in space. The result is presented in Fig. 2(d). It resembles closely

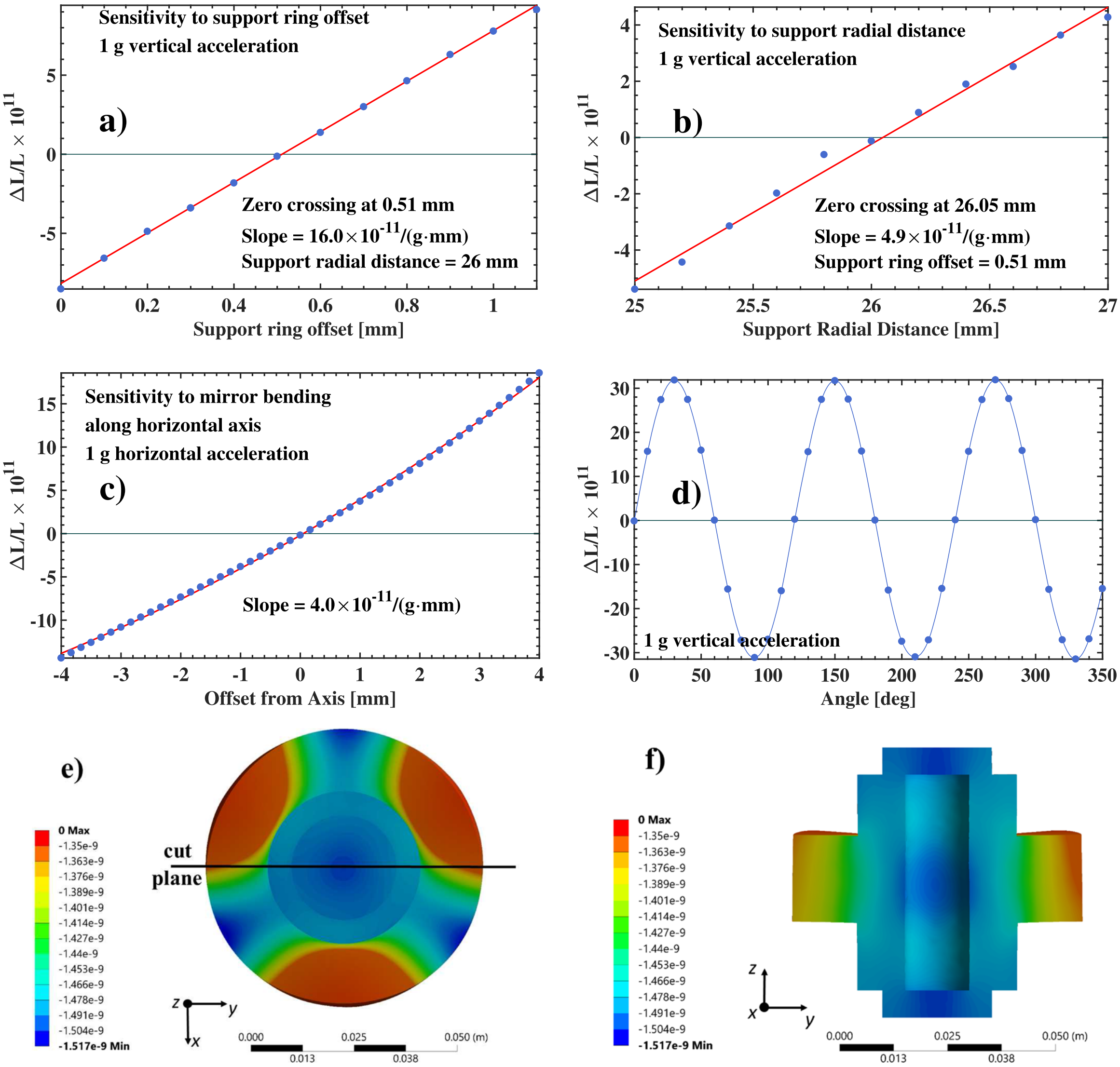

FIG. 2. Acceleration sensitivities of the resonator according to FEM simulations. (a) Influence of the imperfect manufacturing of the support ring on sensitivity during an application of 1 g vertical acceleration. (b) Sensitivity to changes in the radial position of the three supports and 1 g vertical acceleration. (c) Sensitivity to the offset of the optical axis from the symmetry axis of the resonator (1 g acceleration is applied in the transverse direction). (d) Sensitivity to rotation of the resonator around the symmetry axis and an application of 1 g vertical acceleration. [(e) and (f)] Examples of the simulation results for the resonator with optimized shape. Color indicates the displacement in meter along the vertical direction (z-axis) due to the application of 1 g vertical acceleration. In (e), the displacement of the surfaces is shown; in (f), the displacements of the volume elements in the midplane cut along the vertical YZ plane [see the definition of the cut plane in (e)] are shown.

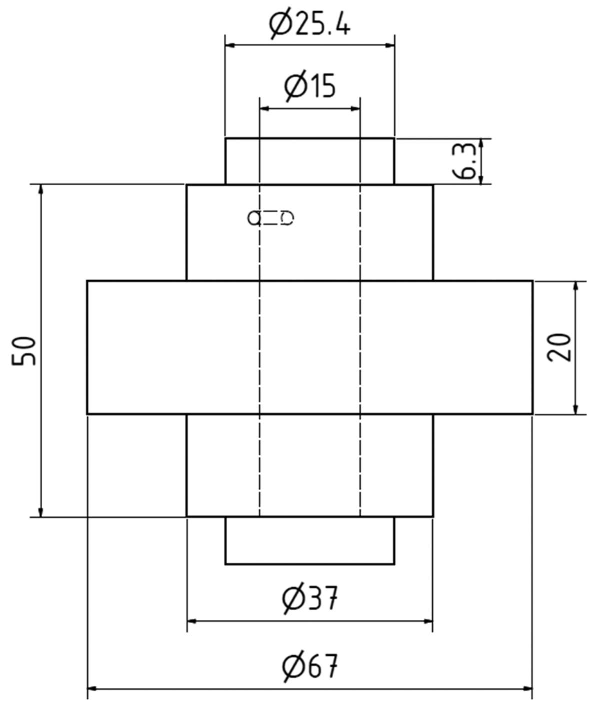

FIG. 3. Optimized design of the resonator, as determined using FEM simulations. The 2 mm diameter venting hole is located in the upper half at a distance of 5 mm from the top end. Dimensions are in mm.

the result obtained by Matei *et al.*[31] The sensitivity is periodic with a period of 120° due to silicon's anisotropic crystal structure and has an amplitude of $3 \times 10^{-10}/g$. This results in a slope of $5 \times 10^{-12}/(g$ deg) around the sensitivity's zero crossing.

Figures 2(e) and 2(f) display the deformation of the resonator of optimum shape (without manufacturing errors), which is placed on the three supports at the optimum position, with resultant zero sensitivities. In the simulation, vertically oriented 1 g acceleration is applied to all volume elements. The simulation reveals a displacement of the top and bottom mirrors by the same amount, approximately 1.5 nm, leaving the distance between them, and thus, the resonator frequency unchanged. The final geometry of the resonator after FEM optimization is presented in Fig. 3.

C. Modeling of thermal noise

Random Brownian movement of the atoms in the crystal lattice of the spacer and of the substrates as well as in the mirror coatings results in a random fluctuation of the distance between the mirror internal surfaces.[15] Thus, this motion directly influences the optical path length and sets fundamental limits to the frequency stability of a laser wave whose frequency is locked to the resonator. For future reference, we calculate the thermal-noise induced instability of the resonator length at 1.5 K, assuming the parameters listed in Table I. The results are presented in Table II. A 13-fold reduction in thermal noise from 300 K to 1.5 K is predicted to the level 2.8×10^{-17} at 1.5 K. The coating contributes over 96% to the total noise, because of its amorphous nature. The use of crystalline mirrors could here provide a significant further reduction. In the present work, the performance of the system is not limited by the thermal noise.

TABLE I. Parameters used for the calculation of thermal noise.

Symbol	Parameter	Value
λ	Laser light wavelength	1562 nm
L	Length of the spacer	50 mm
R_{sp}	Radius of the spacer	18.5 mm
r_b	Radius of the central bore	7.5 mm
$w_{R=1m}$	Beam waist at the curved mirror	338 μm
$w_{R=\infty}$	Beam waist at the flat mirror	329 μm
E	Young's modulus of Si along the [111] crystallographic direction[32]	187.9 GPa
ν	Poisson's ratio of Si along the [111] crystallographic direction[32]	0.18
$Q_{Si} = 1/\phi_{Si}$	Si quality factor[33]	10^8
ϕ_{ct}	Coating loss factor[34]	1 mrad
d_{ct}	Coating thickness	9.38 μm

TABLE II. Computed fractional frequency instability of the mirror distance due to Brownian noise for different operating temperatures. The contributions from the spacer, the substrates, and the coatings are given. The parameters of Table I were assumed. The fractional frequency instability is expressed as an Allan deviation σ_y, which is independent of integration time.

	σ_y (10^{-17})				
Temperature (K)	300	124	16.8	4	1.5
Spacer	0.21	0.13	0.05	0.02	0.01
Substrates	1.31	0.84	0.3	0.15	0.09
Coatings	39.0	25.1	9.2	4.5	2.8
Total	39.0	25.1	9.2	4.5	2.8

III. APPARATUS

A. Resonator and resonator support

The resonator (denoted by "Si5" in some figures) was manufactured from a cylindrical silicon crystal (resistivity 8 kΩ/cm and diameter 4 in.), grown along the [111] crystallographic direction using the float zone method. The optical axis of the resonator is aligned with this direction. The two end faces were polished to optical quality. High-reflectivity dielectric mirrors for 1.5 μm wavelength were optically contacted to them in-house. These silicon substrates originate from a different block of material, having a resistivity of 4 kΩ/cm and a diameter of 4 in. Their symmetry axes are oriented along the [100] crystallographic direction. This aspect was not included in the above simulations.

The resonator was installed in an optical setup inside a pulse-tube cryostat equipped with a Joule–Thomson stage (Leiden Cryogenics). A picture of the setup and the corresponding schematic are shown in Fig. 4. The resonator was supported from below at three

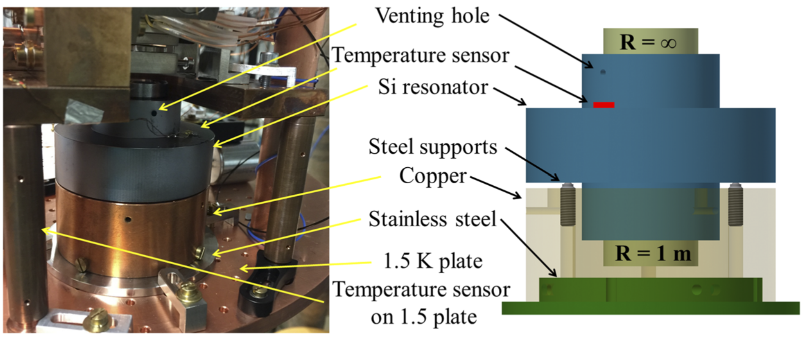

FIG. 4. Cryogenic resonator setup (left) and the corresponding schematic (right).

points. The supports were pressure screws with stainless steel balls at their ends. The balls were cut in half so as to produce a circular surface of 3 mm diameter. To increase the friction between the balls and the resonator, a layer of indium foil was placed between them. In order to reduce the fluctuations of the resonator's temperature caused by the fluctuations of cryostat temperature, we split the support into two parts: a copper cylinder as an intermediate part and a stainless steel base. The latter acts as a thermal low-pass filter, given its reduced thermal conductivity compared to copper. The resonator temperature was measured by using a sensor (cernox) attached to the top surface of the silicon support ring using a cryogenic grease.

B. Cryogenic optical setup

The coupling of the laser light into the resonator and the detection of the resonator response are performed on a cryogenic breadboard with a footprint of 116 × 140 mm^2, shown in Fig. 5. The compact design minimizes the optical path length in order to reduce the effect of unavoidable misalignments upon cooling to cryogenic temperature. Additionally, it incorporates two motorized mirror mounts allowing us to correct for the misalignments.

The light of the laser is carried to the breadboard setup using a single-mode polarization-maintaining fiber. The end of the fiber is fixed to the breadboard and coupled out using the fiber collimator (FC). The wave is guided to the resonator by reflecting off two motorized mirrors (MM). Upon reaching the polarizing beam splitter (PBS), a small part of the light is diverted to the quadrant photodetector, marked as QPD, for monitoring the beam position. The remainder is guided to the resonator, passing through a quarter-wave plate (not shown in the schematic). It is partially reflected from the front mirror. The reflected light is detected by using a high-bandwidth photodetector (PD). The signal can be used for a Pound–Drever–Hall-type lock (PDH), not implemented here. The light transmitted by the resonator is split by using a beam splitter. One part is detected by using a photodiode installed below the experimental plate (not shown). The other part exits the cryostat through a window and is used for the identification of the transverse mode excited by the laser. For this purpose, a high-sensitivity room-temperature InGaAs camera is installed outside the cryostat in the beam path.

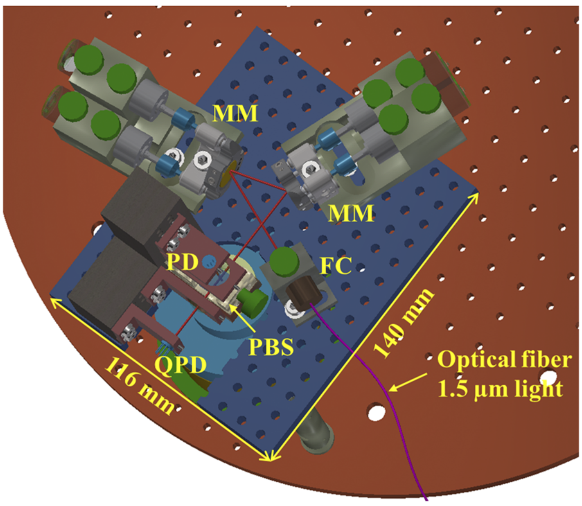

FIG. 5. CAD figure of the cryogenic optical setup. FC, fiber collimator; MM, motorized mirrors; PBS, polarizing beam splitter; QPD, quadrant photodetector; PD, photodetector; and CAM, high-sensitivity infrared InGaAs camera. Red lines indicate free-space paths.

C. Optical frequency stabilization system and procedures

The concept of the present system is to combine a laser with a good short-term ($\tau \leq 20$ s) frequency stability with a cryogenic resonator whose task is to provide a better frequency stability on medium (>20 s) and long (>1000 s) time scales than possible with a room-temperature reference resonator. Therefore, we use a room-temperature, 10 cm long ULE resonator for the pre-stabilization of the laser's frequency. The pre-stabilized laser then interrogates the TEM$_{00}$ mode of the cryogenic resonator. The overall layout of the optical setup is presented in Fig. 6. It includes components necessary for the characterization of the system performance.

The pre-stabilized laser (optical frequency f_{ULE}) has a linewidth of less than 1 Hz at its output. Part of this light is transferred to the cryogenics lab and into the cryostat via an approximately 50 m long optical fiber. Initially, no active fiber noise cancellation was installed for the path between the pre-stabilized laser and the cryogenic lab. The typical broadening of the linewidth due to fiber noise along this 40 m long path was measured to be 20 Hz. Additional noise is likely introduced by the vibrations inside the cryostat along the

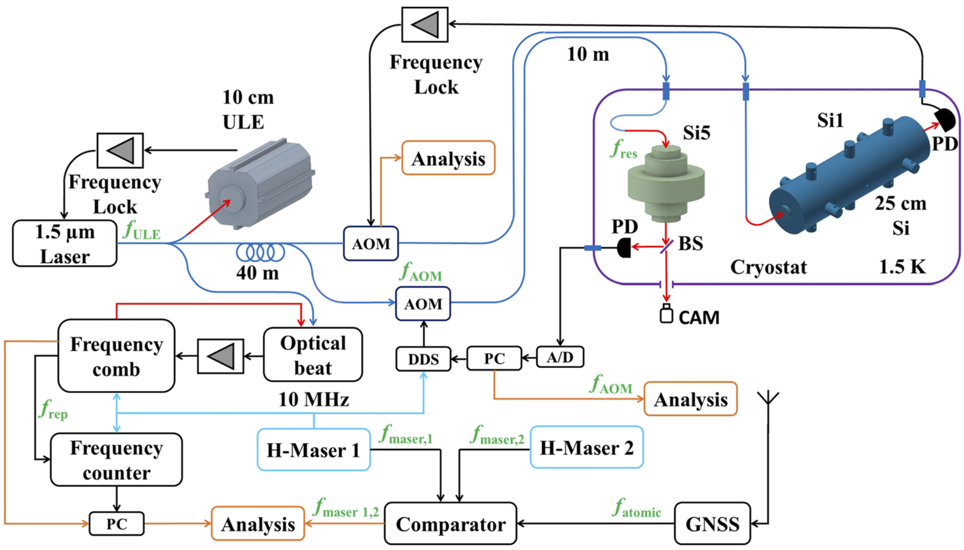

FIG. 6. Overall experimental setup. Red and blue lines indicate free-space and fiber-coupled optical paths, respectively. Black lines represent the electronic paths, and the light blue line is the 10 MHz reference signal from the hydrogen maser. f_{res}, frequency of the cryogenic silicon resonator; f_{ULE}, frequency of the room-temperature ULE resonator; f_{atomic}, frequency of the GNSS satellite signal; $f_{maser,i}$, frequencies of two hydrogen masers; f_{rep}, repetition rate of the frequency comb; f_{AOM}, frequency of the AOM; PC, personal computer; AOM, acousto-optical modulator; DDS, direct digital synthesizer; A/D, analog to digital signal converter; PD, photodiode; BS, beam splitter; and CAM, InGaAs infrared camera for mode detection.

remaining 10 m long fiber but could not be measured independently because no wave reflected back from the resonator or from the end of the fiber could be observed. One part of the pre-stabilized laser light is used for measuring the laser frequency f_{ULE} with a frequency comb referenced to an active hydrogen maser. The maser is continuously compared to a GNSS signal providing a reference frequency f_{atomic}. To improve the sensitivity of the frequency measurements, we reduce the spectral width of the comb lines by phase-locking the comb to the pre-stabilized laser. The repetition rate f_{rep} of the comb is measured with a low-noise frequency counter, and from the data, f_{ULE}/f_{maser} is computed.

Another part of laser light, fiber split in the cryogenic laboratory, is guided to the 25 cm cryogenic ultra-low drift silicon resonator[7] (denoted by "Si1" in some figures) installed on another optical breadboard inside the same cryostat. This resonator is also employed as a reference for determination of the frequency instability of the 5 cm resonator.

We use an acousto-optic modulator (AOM with frequency f_{AOM}) to bridge the gap between the laser frequency f_{ULE} and the frequency of the closest TEM_{00} mode of the silicon resonator, driven by a direct digital synthesizer (DDS) controlled by a personal computer (PC).

To determine the frequency of the resonator, we repeatedly measure the line center frequency. Two techniques have been employed: (1) scanning over the resonance line and (2) alternating interrogation of the half-transmission points of the resonance. Both techniques are compatible with the use of very low light power (≤1 μW). In addition, they do not require continuous coupling of laser light into the resonator but can be applied, if desired, with a low duty cycle. Together, these features help to reduce permanent or semi-permanent changes in the mirror coatings due to exposure to laser light. Another advantage is the absence of offsets introduced by active optical elements, e.g., residual amplitude modulation introduced by an electro-optical modulator (EOM) or laboratory-temperature-induced variations of the PDH electronics lock point. In the linescan technique, each center frequency determination is carried out by sweeping the frequency of the laser light over the resonance line with an AOM. The light transmitted through the resonator was detected by using the cryogenic detector and the signal sampled by using a 14-bit DAQ card with 40 kS/s. The frequency span was set to twice the linewidth, $2\Delta\nu = 40$ kHz, and the (one-way) scan time was set to 0.7 s. The data of two subsequent scans, upward and downward in frequency, were averaged. These data were subsequently fitted with a Lorentzian function to determine the AOM frequency f_{AOM} corresponding to the resonator's center frequency. This frequency value is thus obtained essentially immediately after each pair of scans. A digital control modifies the scan range settings so as to maintain the resonance frequency in the center of the range. In addition, the value f_{AOM} is stored and used to compute the resonator frequency as $f_{res}/f_{maser} = f_{ULE}/f_{maser} + f_{AOM}/f_{maser}$. In our measurements, the procedure is repeated continuously, but as mentioned, a wait time interval could be inserted if needed.

The detuning technique is realized by periodically shifting the laser light frequency by $\pm\Delta\nu/2$, relative to the resonance frequency f_{res}, to one of the two half-transmission detunings. The signal of the transmission photodiode for $-\Delta\nu/2$ detuning is measured at time step $i-1$ and averaged over a 500 ms time period, yielding the value A_{i-1}. Subsequently, the other half-transmission position is selected and the corresponding amplitude A_i recorded. Then, the frequency correction $\Delta f_{AOM,i} = (\Delta\nu/2)(A_i - A_{i-1})/(A_i + A_{i+1})$ is calculated and applied to the AOM. The absolute frequency of the resonator is computed as in the case of the linescan technique.

IV. CHARACTERIZATION

A. Temperature stability

The temperature stability of the resonator is important since it can affect its medium- and long-term frequency stability through the coefficient of thermal sensitivity of frequency (CTF). Figure 7 compares the temperature instability measured on the resonator and on

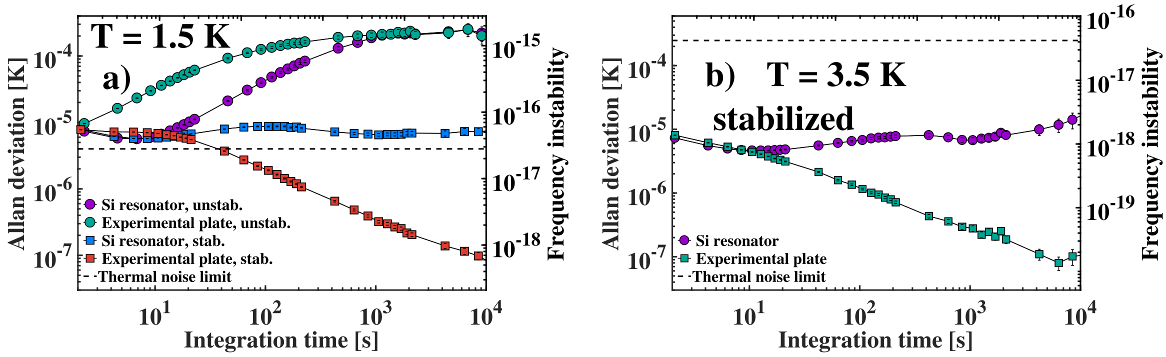

FIG. 7. Temperature instability of the experimental plate, measured with a sensor attached to it in close proximity to the resonator support structure, and of the resonator itself. (a) At 1.5 K, with and without active temperature stabilization, and (b) at 3.5 K, with active stabilization. The right axis in both diagrams shows the resulting fractional frequency instability, computed using the appropriate CTFs.

the base plate, at two operating temperatures, and under two different operating modes. The laser light was blocked during these measurements. The temperature instability is given as a modified Allan deviation and is computed from the temperature time series. At the temperature of 1.5 K, the instability of the free-running resonator temperature is lower than that of the base plate for integration times up to 1000 s. This shows that the baseplate temperature variations are substantially attenuated by the resonator support structure. The smallest temperature instability is 4.5 μK at 6 s integration time. The instability data combined with the thermal expansion coefficient of the resonator at 1.5 K, 7×10^{-12}/K, yield an estimate of the frequency instability of the resonator. This is shown on the right axis of Fig. 7. The instability is above the level of the calculated thermal noise for all integration times. Thus, for operation at 1.5 K, the current support structure would represent a limiting factor for the future resonator performance. An improvement could be realized by introducing a second stage of passive thermal isolation or, as done in this work, by actively stabilizing the temperature of the base plate [see Fig. 7(a)]. This improvement was not necessary for the experimental results presented here.

To operate the setup at 3.5 K, a temperature of particular interest (see below), an active temperature stabilization was implemented. The resulting temperature instability of the resonator is 10 μK or less for all integration times up to 10 000 s. The inferred frequency instability of the resonator, depicted on the right axis, was calculated assuming that the temperature set point has an undesired offset of 0.02 K from the optimum temperature. Such a small deviation is conservative, in view of the accuracy with which the optimum temperature is, in principle, measurable [see Fig. 10(d)]. The absolute value of the CTF is then less than 2×10^{-13}/K. This yields a frequency instability of less than 3×10^{-18}, significantly below the thermal noise limit.

The temperature instability presented in Fig. 7 must be viewed with caution. Variations of laboratory temperature affect the reference voltage in the control electronics of the active temperature stabilization circuit. The voltage variations are interpreted as variations of the cryogenic temperature. This explains the large difference between the instabilities measured by the loop base plate sensor and by the sensor attached to the resonator, as shown in Fig. 7(b). While the in-loop sensor suppresses the influence of the lab temperature variations, the monitor sensor at the resonator does not. Therefore, the temperature instability of the resonator is likely to be equal or below the instability presented in Fig. 7.

B. Resonator properties

After cooling down to 4 K, only a slight optimization of the in-coupling by actuating the mirrors was required. The cooling was then continued down to the operational temperature of 1.5 K. The TEM_{00} resonance was identified and could be routinely interrogated with the pre-stabilized laser. A typical scan is presented in Fig. 8(a). From fits of Lorentzian functions to a series of scans, we find a mean full width at half-maximum of 24.2 ± 0.2 kHz. This corresponds to a finesse of 120 000. The measured in-coupling $(1 - P_{r,on}/P_{r,off})$, where $P_{r,on}$ is the on-resonance reflected power and $P_{r,off}$ is the off-resonance reflected power, was 10%. The mode matching efficiency, determined by characterizing the in-coupling of other transverse modes, was 60%. The fit residuals in this figure deviate clearly from near zero when the laser frequency is tuned to the vicinity of the half-maximum resonator transmission frequency [bottom panel in Fig. 8(a)]. This indicates the presence of frequency fluctuations of the resonator. They are due to the vibrations generated by the cryostat, as can be seen from the fact that the residuals are weaker when the cooler is off [see Fig. 8(b)].

C. Acceleration sensitivity

One of the goals of this work was minimization of the resonator's acceleration sensitivity. The characterization of this property is, therefore, of importance. It is usually done by shaking the resonator along one of the three orthogonal spatial directions and observing the frequency shift of the resonator. However, in our case, the structure of the cryostat prevented us from producing controlled vibrations in desired directions and, thus, made it impossible to measure the vibration sensitivity for the three spatial directions individually. However, we were able to estimate the overall sensitivity of the resonator submitted to the accelerations produced by the cryostat by measuring the variations of the transmission signal caused by the deformations of the resonator.

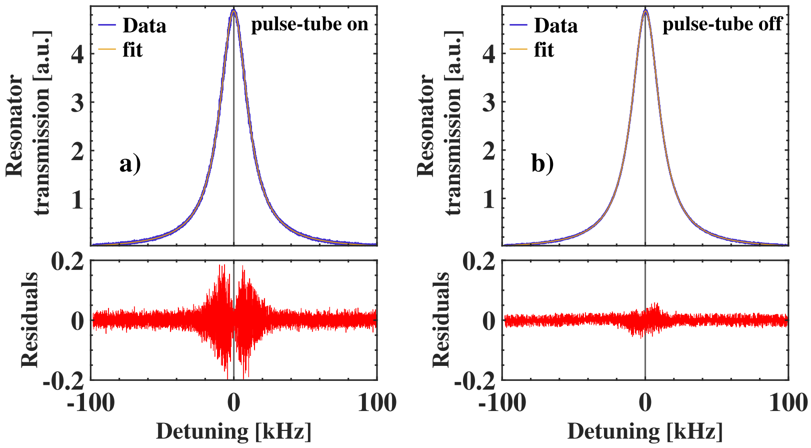

FIG. 8. One-way frequency scans of the pre-stabilized laser frequency over the resonator TEM_{00} mode. Scan duration is 80 s. The signal is the light power transmitted through the resonator. The pulse-tube cooler is on [panel (a)] and off [panel (b)]. The orange lines are Lorentzian fits. Operating temperature: 1.5 K.

An estimate of the sensitivity can be obtained using a side-of-fringe discriminator technique. For this, the laser light is frequency-tuned so that the (time-averaged) transmission signal is half the maximum. Then, the fluctuations of the transmission signal are recorded. Figure 9(a) shows a time trace (orange). For comparison, we also determined the contribution arising from power variations of the laser wave. They were measured with the laser frequency tuned to the maximum transmission of the resonator. Finally, we measured the background noise in the coaxial cable by blocking the laser light. We calculated the rms amplitude deviations corresponding to these

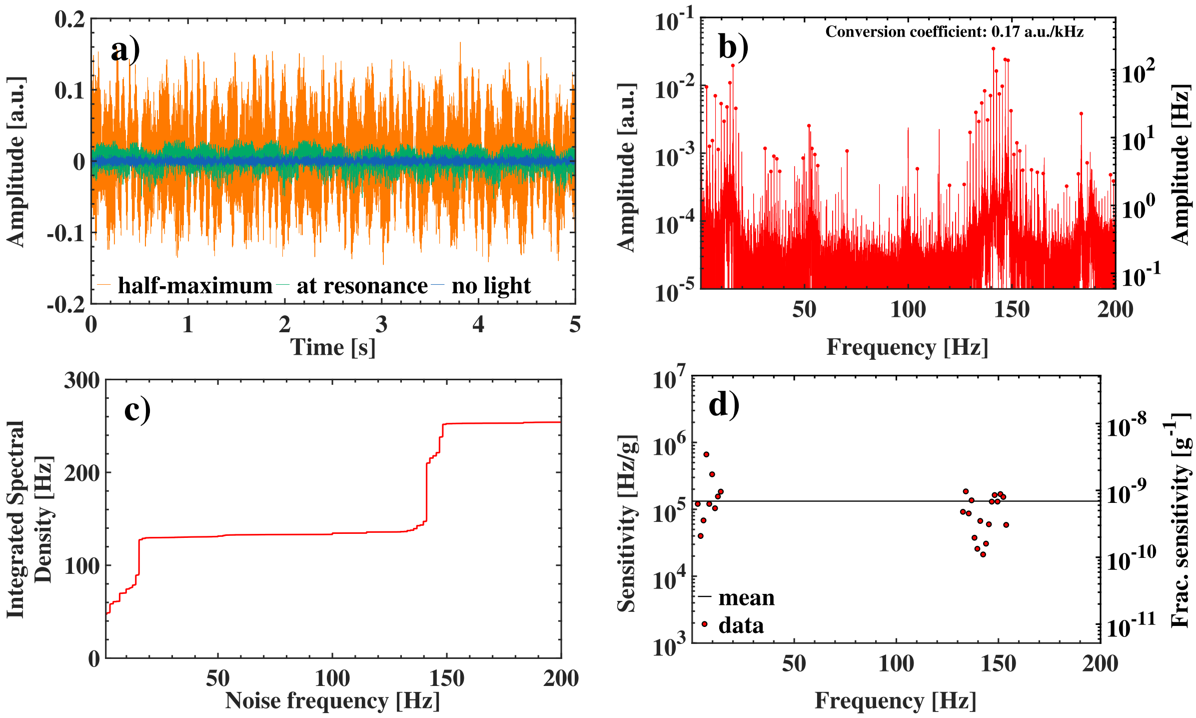

FIG. 9. Determination of the resonator sensitivity to vibrations. (a) Time traces of the cavity transmission signal, with subtracted offset, measured with the laser frequency tuned to the half-transmission of the resonance (orange) and on-resonance (green). The green time trace includes a factor of 1/2 to account for the larger transmitted power. Blue: background signal taken with laser off. (b) Spectrum calculated from the time trace at half-maximum and after subtraction of the spectrum taken with the laser tuned to the resonance and of the noise spectrum. Right y-axis gives the frequency fluctuation level after applying the conversion factor $S = 0.17$ a.u./kHz (slope of the transmission signal at the half-maximum value). (c) Contribution to the linewidth from vibrations in the frequency region up to 200 Hz. (d) Sensitivity of the resonator to vibrations at different frequencies obtained by division of the spectrum from panel (b) by the spectrum of cryostat accelerations defined as root sum-of-squares of the three individual accelerations. The black line indicates the mean of the shown data points.

three situations, ΔA_S, ΔA_T, and ΔA_N. The rms signal deviation at the half-transmission detuning due to relative frequency fluctuations between laser and resonator, ΔA_{eff}, is obtained after subtraction of $\Delta A_T/2 + \Delta A_N$ from ΔA_S. The correction compared to using only ΔA_S is at the 1% level.

Using ΔA_{eff} together with the slope of resonator transmission at half-maximum, $S = 0.17$ a.u./kHz, and the total acceleration a_{total}, we obtain the acceleration sensitivity $\sigma_{total} = 61.5$ kHz/g ($3.2 \times 10^{-10}/g$).

We obtained the spectrum of frequency fluctuations from the power spectra corresponding to the time traces in Fig. 9(a). It is presented in Fig. 9(b). Conversion into frequency units was done using the transmission signal sensitivity S. Integration of the power spectral density provides an estimate of the linewidth that a laser locked to the resonator would exhibit, assuming that the measured frequency fluctuations are solely due to the resonator length fluctuations. Figure 9(c) shows the integrated frequency noise. The total contribution within the detected bandwidth is 250 Hz. This value is in agreement with the first estimate above. The frequency fluctuations and thus the acceleration noise in the frequency bands [1, 20] Hz and [140, 150] Hz contribute most to the linewidth.

The data in Fig. 9(b) together with the acceleration data in Fig. 1 allow a direct determination of the resonator acceleration sensitivity as a function of frequency by computing their ratio. We show this for the frequency bands mentioned above in Fig. 9(d). The mean

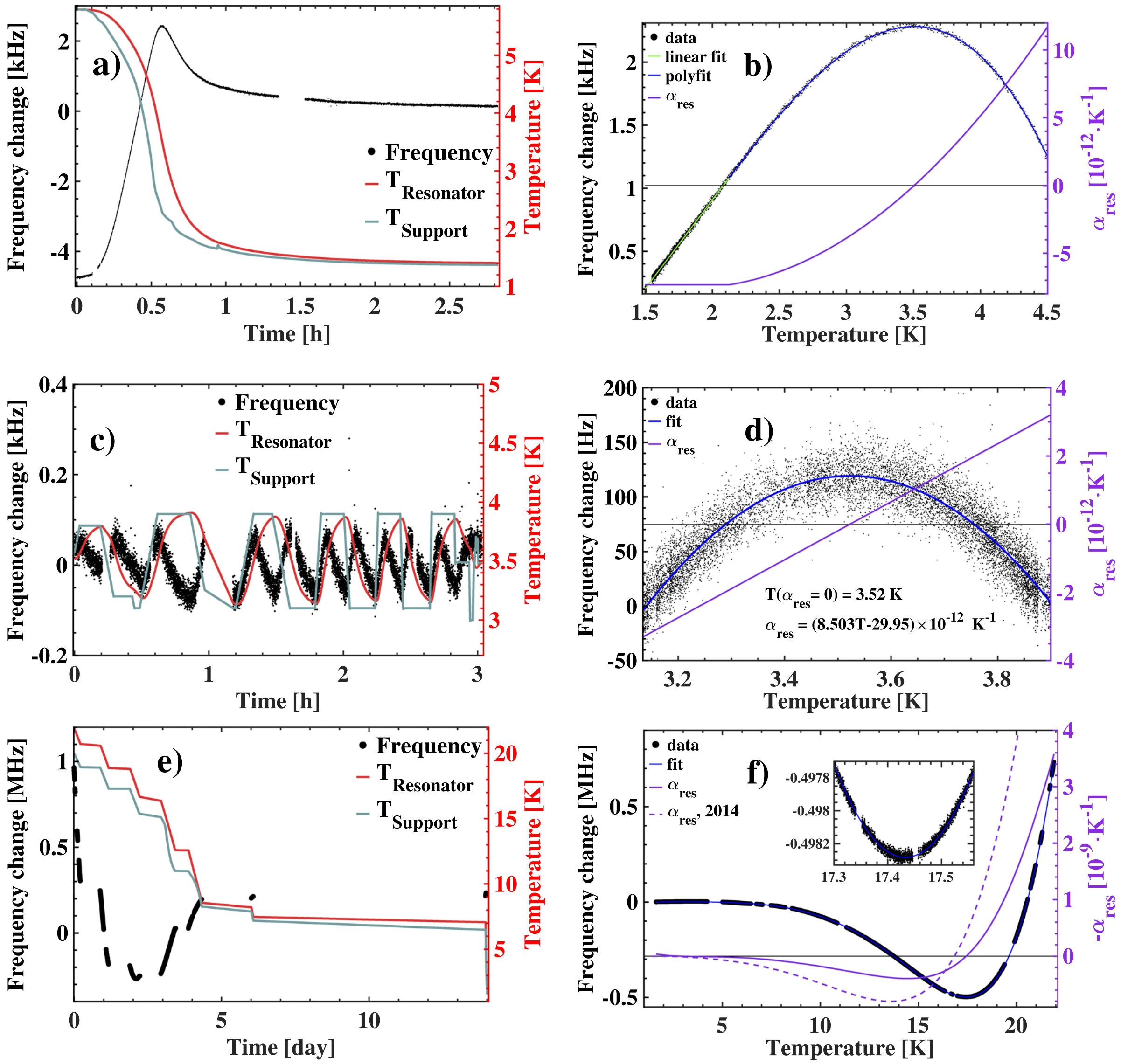

FIG. 10. Measurements of the thermally induced frequency change of the resonator in three temperature ranges: [(a) and (b)] between 1.5 K and 4.5 K, [(c) and (d)] around T_0 = 3.52 K (zero CTF), and [(e) and (f)] from 22 K to 1.5 K. The red dashed line in (f) is the result of Ref. 28.

sensitivity is 133 kHz/g ($6.9 \times 10^{-10}/g$). Note that the individual values in the spectrum vary by one order of magnitude around the mean. The largest value is 7×10^2 kHz/g ($5 \times 10^{-9}/g$) at a frequency of 7 Hz. In view of the fact that we cannot separate the contributions of the three spatial components of the acceleration in the transmission signal, our analysis cannot be more precise.

D. Coefficient of thermal sensitivity

The coefficient of thermal sensitivity of frequency (CTF) of our resonator, α_{res}, was determined in the temperature range between 5.5 K and 1.5 K by cooling down or heating up the cryostat over several hours and simultaneously measuring the resonator frequency using the half-transmission detuning technique described above. The raw data of the experiments are presented in Figs. 10(a), 10(c), and 10(e). The total change in resonator frequency from 5.5 K to 1.5 K is 7 kHz. Clearly, the resonator frequency exhibits an extremum at 3.52 K; its CTF vanishes there.

The CTF in the temperature region below 2.12 K was determined by a linear-in-T fit to the data [see Fig. 10(b)]. The resulting CTF is constant; $\alpha_{res}(T < 2.1\text{ K}) = -7.33 \times 10^{-12}\text{ K}^{-1}$ with a fit error smaller than 0.3%. The remaining data were fitted with a cubic polynomial [see Fig. 10(b)]. We find $\alpha_{res}(2.1\text{ K} < T < 4.5\text{ K}) = (2.72(T/\text{K})^2 - 10.0\ (T/\text{K}) + 1.65) \times 10^{-12}\text{ K}^{-1}$. While the uncertainty of the T^2 coefficient is 2%, it is smaller than 1% for the two remaining coefficients.

In order to determine precisely the temperature of zero CTF, a sinusoidal modulation of the temperature was applied around the mean temperature of $T = 3.5$ K using a heater attached to the experimental plate. The corresponding change in frequency of the resonator is depicted in Fig. 10(c). A quadratic fit was performed [see Fig. 10(d)], yielding a zero CTF temperature $T_0 = 3.52 \pm 0.02$ K with derivative $d\alpha_{res}/dT = 8.5 \times 10^{-12}/\text{K}^2$. This value is a factor of 40 smaller than at the zero-CTF-temperature 17.4 K, where it is $-3.4 \times 10^{-10}/\text{K}^2$ (see below), and a factor of 2000 lower than at 124.2 K, $1.7 \times 10^{-8}/\text{K}^2$.[26] Assuming that the operating temperature has an undesired offset of 0.02 K from the zero-CTF temperature, the CTF is a factor of 35 smaller than the CTF at 1.5 K.

We also determined the CTF in the extended temperature range between 22 K and T_0 from data obtained during a 15-day-long slow cool-down of the cryostat. The results are presented in Figs. 10(e) and 10(f).

Our results on the CTF for the temperature range below 6 K were confirmed on different occasions: upon heating and cooling of the setup, after prolonged operation (>0.5 year) at 1.5 K and twice immediately after heating of the whole setup to over 100 K. During these measurements, we found a minor variation of the zero CTF temperatures and of the slope at this temperature: ±20 mK and $\pm 1 \times 10^{-12}/\text{K}^2$, respectively.

The CTF results differ significantly from the data published in Ref. 28, which was obtained for a silicon resonator with a different support. While, in that work, the supporting frame was also made of copper, the resonator was held by 10 flexible steel wires that reduced strongly the influence of the thermal expansion of the copper frame. In the present work, the resonator and the copper frame are connected by friction. Thus, a temperature change of the whole setup may conceivably cause a strain $\epsilon = \Delta R/R$ along the radial direction of the resonator due to the much higher expansion coefficient of the copper support, $\alpha_{Cu}(T = 3.52\text{ K}) = 2.3 \times 10^{-9}$/K (Ref. 35) compared to $\alpha_{Si}(T = 3.52\text{ K}) = 2.1 \times 10^{-11}$/K.[28] This strain is converted into a change in distance between the mirrors $\Delta L/L$ via the material's Poisson's ratio $(\Delta L/L) = -\epsilon\nu$. This hypothesis can be tested by considering the CTF at higher temperatures, where the difference between the CTF of silicon and of copper is larger. For example, at 20 K, $\alpha_{Si}(T = 20\text{ K}) = 4 \times 10^{-9}$/K (Ref. 28) and $\alpha_{Cu}(T = 20\text{ K}) = 0.27 \times 10^{-6}$/K (Ref. 36). However, we find a CTF similar to our previous work [see Fig. 10(f)]. The second zero-CTF temperature is $T_0' = 17.4$ K, compared to our earlier $T_0' = 16.8$ K.

Thus, more detailed studies are necessary to determine the precise reason for the zero crossing, including FEM simulations and measurements with different implementations of the contact surfaces between frame and resonator.

V. FREQUENCY STABILITY

We measured the stability of the laser frequency when referenced to the silicon resonator using both techniques outlined above.

A. Medium-term frequency instability

The result of a frequency measurement, allowing us to determine the medium-term frequency instability, and obtained with the linescan technique, is presented in Fig. 11(a). Here, the temperature of the resonator was at 1.47 K and was not actively stabilized. As shown in Fig. 11(a), the frequency stability of the resonator is compromised by the periodic variations of the laboratory temperature. This can be more clearly seen in the FFT spectrum of frequency and temperature time traces, presented in Fig. 11(b). We observe a modulation of frequency with an amplitude of 4 Hz at a time period of 23 min, which is identical to the duration of the laboratory temperature variations. Therefore, we only consider the most stable part of the data, exhibiting the lowest drift, and computed the modified Allan deviation [see Fig. 11(c)]. We find that for integration times up to 1000 s, the laser frequency instability is slightly higher than the beat instability of our two active hydrogen masers and approaches the minimum value of 0.5 Hz (2.5×10^{-15}) at $\tau = 1500$ s. It is possible that this level has a contribution from the temperature variations of the resonator [see Fig. 7(a)].

To verify our results presented in Fig. 11(c), we apply the half-amplitude technique to stabilize the ULE laser light to both the 5 cm resonator and the 25 cm silicon resonator using two independent AOMs (see schematic in Fig. 6). We use the frequency difference between these two resonators for the estimation of frequency instability. This procedure allows us to eliminate fluctuations of the ULE frequency and to avoid an introduction of potentially present additional noise coming from the frequency comb. The result of the measurement is presented in Fig. 12. To determine the frequency instability of the 5 cm resonator, we use the most stable part with a duration of 2 h. The calculated modified Allan deviation of this part is presented in Fig. 12(b).

For integration times $\tau \leqslant 10$ s, the resulting instability is below the instability of the maser. The beat with the ULE resonator shows an instability of 2 Hz (1×10^{-14}) at 1 s integration time.

For integration times from 10 s to 1000 s, the instability of the Si5–Si1 beat follows closely the instability of the maser–maser beat

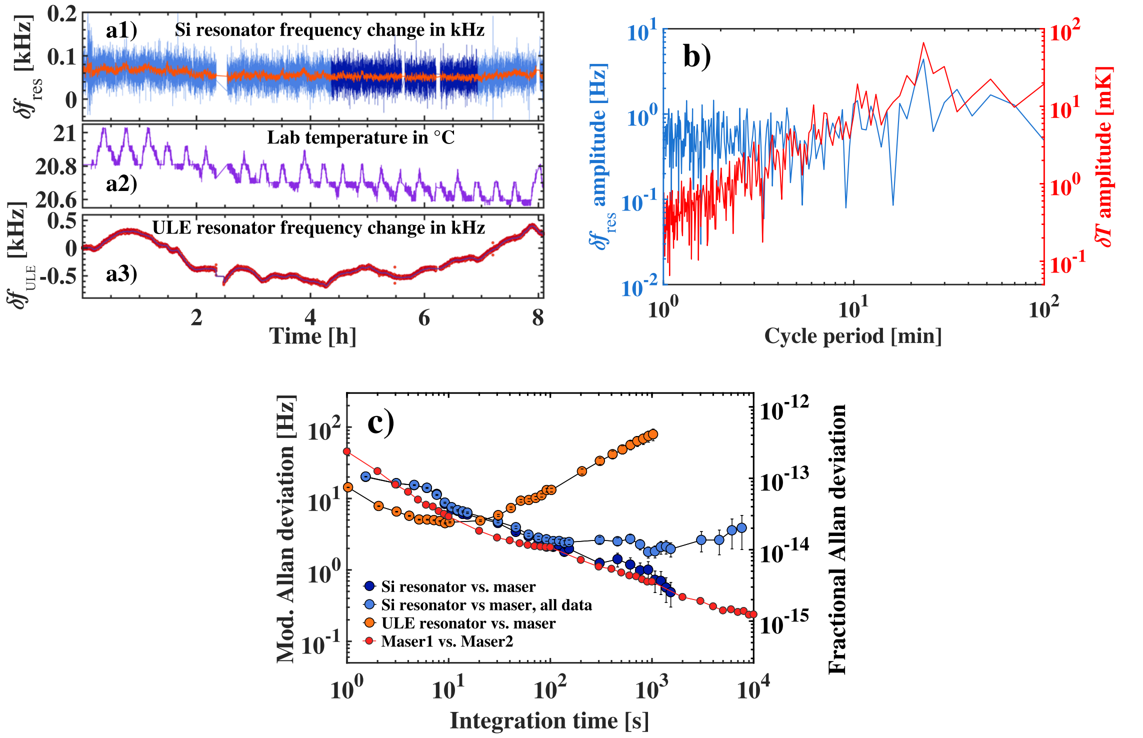

FIG. 11. (a) An 8-h-long laser frequency measurement, with respect to the maser, when the frequency-shifted laser wave tracks the silicon resonator [plot (a1)]. The dark colored interval is used for the calculation of Allan deviation in panel (c). Plots (a2) and (a3) show the temperature of the lab housing the cryostat and the frequency change of the pre-stabilized laser used for interrogation of the silicon resonator, respectively. (b) FFT of the lab temperature and resonator frequency time traces presented in panel (a). (c) Modified Allan deviation of the silicon resonator frequency [whole dataset (light blue markers) and selected part (dark colored blue markers)] and of the pre-stabilized laser (orange markers). No drift was removed. The red points in (c) show the maser instability, determined from a measurement of the frequency difference of two nominally identical masers on a different occasion.

and approaches the minimum instability of 0.8 Hz or 4×10^{-15} at $\tau = 1000$ s integration time. With the assumption that both resonators contribute equally to the instability, we can divide the above result by a factor of $\sqrt{2}$ and obtain 0.6 Hz (3×10^{-15}) at $\tau = 1000$ s integration time.

VI. LONG-TERM FREQUENCY DRIFT

The long-term ($\tau > 10\,000$ s) frequency drift of the resonator is mainly determined by the length changes of the spacer due to the relaxation processes in the crystal lattice and photochemical changes

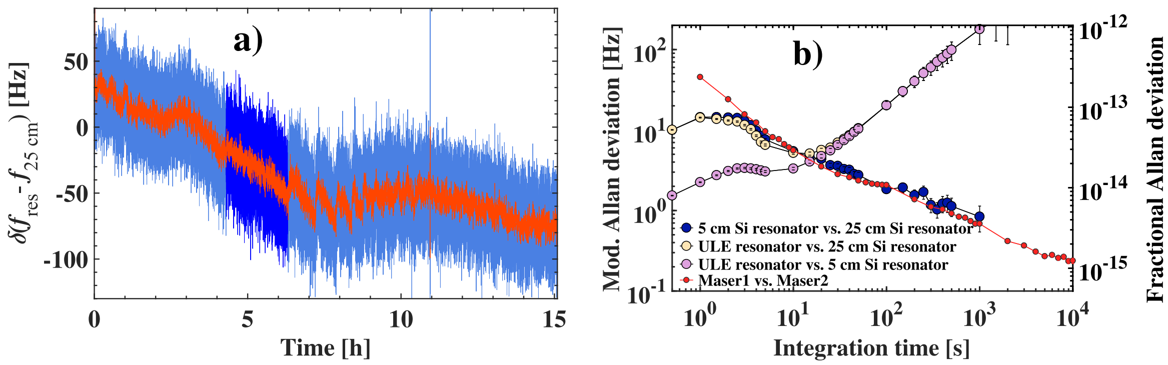

FIG. 12. (a) A 15-h-long measurement of the frequency of the 5 cm silicon resonator relative to the frequency of the 25 cm silicon resonator. The 2-h-long dark colored interval is used for the calculation of Allan deviation. (b) Modified Allan deviation of the frequency difference [selected part in panel (a)] between the silicon resonator and the 25 cm silicon resonator (dark blue markers). A drift of 5 mHz/s was removed. Purple and yellow markers represent the frequency instability of the silicon resonator and the 25 cm silicon resonator relative to the ULE resonator, respectively, measured simultaneously. Red points show the maser instability, determined from a measurement of the frequency difference of two nominally identical masers 1 and 2 on a different occasion.

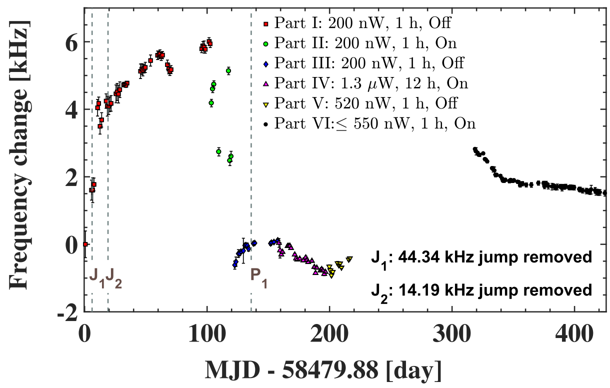

FIG. 13. Frequency change of the resonator measured over a time span of 425 days. Between day 217 and 318, no data were recorded because the temperature of the resonator was changed to measure the coefficient of thermal sensitivity. J_1 and J_2 mark two frequency jumps that occurred during the measurement; P_1 marks the time when we changed from the line scan technique to the half-amplitude detuning technique. The legend sates for each part: the incident optical power of the laser during the measurements, the measurement duration per working day, and whether the laser light was on or off in-between measurements on subsequent days.

in the mirror coatings. The latter are found to depend on the cumulative irradiation duration by the laser and the applied laser power. In our previous work with horizontally oriented silicon resonators supported as described above, we observed an exponential relaxation of the frequency and a positive drift rate after a long time.[7] In those measurements, we interrogated the resonator with a pre-stabilized laser wave of 1 μW power for a duration of 1 h each day and blocked the laser light for the remaining 23 h.

The long-term frequency drift rate of the 5 cm resonator was determined by repeatedly scanning over its resonance line with the pre-stabilized laser light over a time period of 425 days, starting at a day zero (MJD 58479.88), when the system reached the temperature of 1.5 K. The results are presented in Fig. 13. We subtracted two frequency jumps, marked as J_1 and J_2. They were probably caused by spontaneous relaxation processes in the crystalline spacer and/or in the substrates.

In order to gain insight into the drift behavior, we varied the incident laser power. It was kept at 200 nW for all measurements up to day 154. From the following day and up to day 197, the optical power was increased to the level of 1.3 μW. It was reduced again to 520 nW for the days up to day 216. From day 320 to day 425, the power was subsequently reduced from 550 nW to 100 nW. On five days between day 102 and day 122, we optimized the in-coupling of the laser light to the lower mirror of the resonator for the installation of the Pound–Drever–Hall setup attached to the vacuum enclosure of the cryostat. The incident light power on these occasions was on the order of 1 mW.

To determine the frequency of the resonator, we used the linescan technique from day 1 to day 137. After this day, marked as P_1 in the diagram, we changed to the half-transmission technique. The daily interrogation duration was ~1 h on all working days except for two time periods from day 159 to day 197 and from day 320 to day

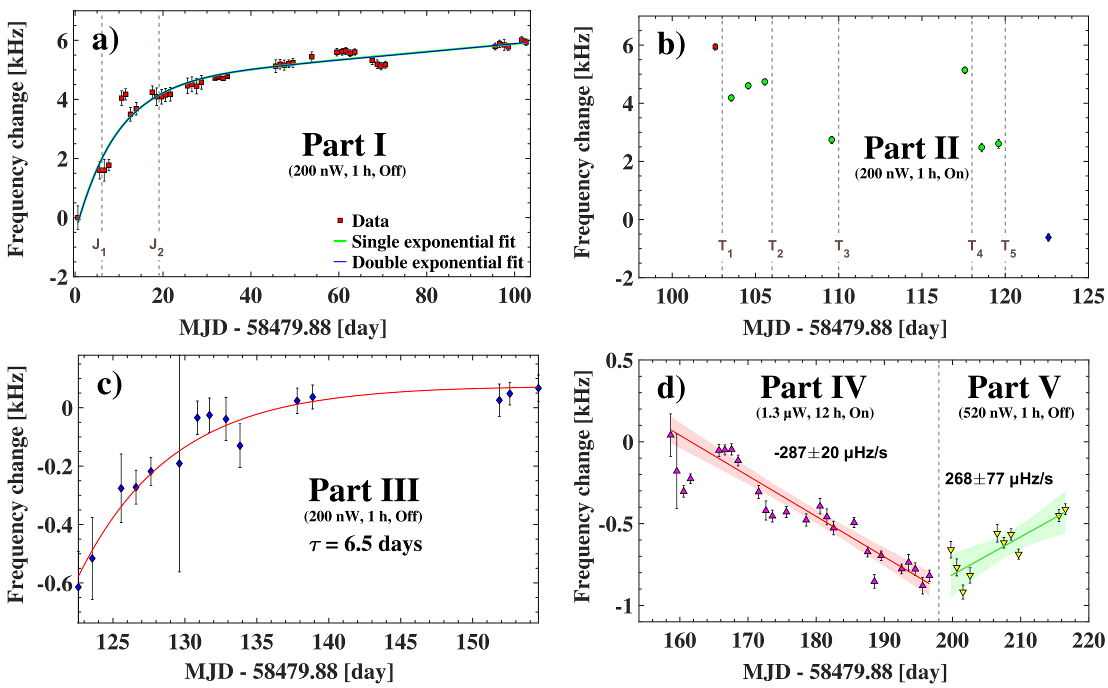

FIG. 14. Zoomed-in views of different intervals of the long-term frequency measurement campaign: (a) part I; (b) part II: T_1–T_5 mark the times when a separate 1 mW free-space laser beam was coupled to the resonator on the bottom side and in addition, regular 1 h-long daily frequency measurements were performed with an incident optical power of 200 nW; (c) part III: subsequent relaxation (interrogation at low power); and (d) parts IV and V. Linear fits and corresponding drift rates are shown.

425 when it was increased to 12 h and 8 h on average, respectively. The laser light was blocked between the measurements from day 1 to day 158. For the two mentioned time periods from day 159 to day 197 and from day 320 to day 425, the laser light was not at resonance when no measurements were performed (i.e., for 12 h per working day and 24 h on the weekend days), but it was still incident on the front mirror of the resonator.

Starting immediately after cool-down, we observed a relaxation of the resonator frequency with a measured total frequency change of 6 kHz over the first 100 days. We denote this measurement period as part I in Fig. 14. The frequency change is positive, meaning that the distance between the two mirrors is decreasing with time. The rate of frequency change is not constant over time.

At the end of part I, the drift rate was 9.7×10^{-19}/s. This value is a factor of 3 higher than the drift measured on a resonator with comparable dimensions by Ref. 24 and a factor of 70 higher compared to our previous result obtained with a 25 cm long silicon resonator.[7] However, this latter drift was measured after almost a year-long continuous operation at 1.5 K. The drift after the first 100 days was almost identical to the current result, 1×10^{-18}/s.

During part II [Fig. 13(b)], on five occasions with a duration of ~4 h each (marked as T_i in this figure), a laser beam with 1 mW optical power was coupled to the resonator mode for most of that time through a cryostat window and to the bottom end of the resonator. Frequency measurements during this time interval (performed as usual) display negative frequency changes. After each optimization of the PDH setup, there is a frequency jump on the order of −2 kHz to −3 kHz. These jumps have a different sign, compared to two jumps J_1 and J_2 [see Fig. 13(a)], suggesting that the two underlying processes are different in nature.

After completion of the optimization, we observe an exponential relaxation process with $\tau = 6.6$ days over the next month [part III, see Fig. 14(c)]. As shown in Fig. 13, the resonator frequency did not return to the original value, implying that the changes induced by high-power irradiation were permanent.

Figure 14(d) displays the next two parts of the measurement campaign, parts IV and V. The frequency drift rate changes from negative to positive after the reduction in power from 1.3 μW to 520 nW and interrogation time from 12 h to 1 h.

During part VI, we performed a systematic study of the frequency drift dependence on the optical laser power, where we continuously decreased the level of optical power from 550 nW to 100 nW [see Fig. 15(a)]. To simulate the realistic conditions of a day-to-day operation of the resonator, we increased the duty cycle to an average duration of 8 h per day [see Fig. 15(b)]. To exclude possible thermal influences, we actively stabilized the temperature at 1.4 K during this time period. In line with the measurements in parts VI and V, we observe a decrease in the frequency drift with the reduction in optical power. The lowest drift of -48.7 ± 3.5 μHz/s (-2.6×10^{-19}/s) is measured at an optical power of 100 nW.

Our observation of negative and positive drift is in contrast to the results presented by Robinson *et al.*,[24] where the drift was always negative, regardless of the optical power. This discrepancy may be due to the differences in the mirror coatings, as well as differences in purity and internal stress of the mirror substrate material. Another factor could be the length of time that the resonator was operated at cryogenic temperature.

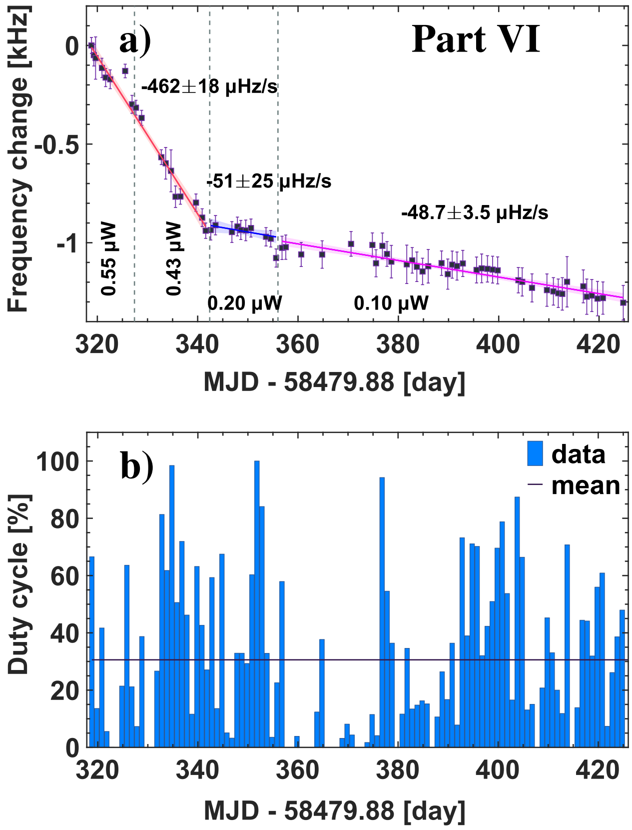

FIG. 15. (a) Frequency change of the resonator measured over a time span of 105 days as a function of optical power. (b) The duty cycle of the resonator interrogation in percent per day.

VII. CONCLUSION

We have developed a relatively simple system for the stabilization of the frequency of a laser on short- and medium-time intervals with the goal of reaching a performance and a reliability comparable to a hydrogen maser. The system is based on a 5 cm long, vertically oriented, silicon resonator operated at cryogenic temperature. The system was characterized in detail. First, it is capable of continuous operation. Except for realignment after initial cool-down, no significant intervention is necessary when the resonator is operated either at 1.5 K or at 3.5 K. Here, we reported on over one year of data and the characterization of the resonator's properties.

Second, the resonator vibration sensitivity was measured to be $3 \times 10^{-10}/g$ in fractional terms. Together with vibrations produced by the cryostat, we expect this to be the limiting factor for the short-term frequency instability of the resonator, which is equal to 1×10^{-14} at 1 s.

At long integration times (1500 s), the instability is not more than 2.5×10^{-15}, similar to the instability of the reference hydrogen maser.

The long-term frequency drift rate was found to depend on the power of the interrogating laser wave and on the duty cycle of the interrogation. Our results, together with previous studies,[7,24,27] indicate that in the limit of very low interrogation laser power and very low duty cycle, the drift rate becomes extremely small.

By varying these parameters, we could change the amplitude and sign of the drift rate. The drift rate can be rather precisely modified, and this feature might, in the future, be used to produce a nearly drift-free frequency reference.

We also characterized the temperature dependence of the resonator frequency. We found two temperature values at which the frequency has zero sensitivity with respect to temperature: 3.5 K and 17.4 K. While the latter value is well known, the former is new. The much smaller temperature derivative of the thermal frequency sensitivity at 3.5 K is highly advantageous, allowing us to suppress temperature-induced frequency instability below the Brownian noise for all integration times. Moreover, the temperature value 3.5 K is sufficiently high that it may be reached in cryostats not equipped with a Joule–Thomson stage. This implies reduced complexity and purchase and maintenance costs. Detailed studies are necessary to determine the origin of this promising property.

To improve the performance of our system, a cryostat that decouples vibrations of the cooler from the resonator is required. Such cryostats are commercially available. We also note that the linewidth of the resonator (24.2 kHz) could be lowered by replacing the current mirrors with mirrors having lower loss; this could also improve the performance of the system. In the future, a more precise characterization of the instability could be done using as reference a high-performance atomic standard (Cs clock or optical atomic clock).

ACKNOWLEDGMENTS

We are thankful to M. G. Hansen for his help with the operation of the frequency comb and A. Yu. Nevsky for stimulating discussions.

E.W. acknowledges a fellowship from the Professor W. Behmenburg-Schenkung. This work was performed in the framework of project SCHI 431/21-1 of the Deutsche Forschungsgemeinschaft.

REFERENCES

[1] A. D. Ludlow, M. M. Boyd, J. Ye, E. Peik, and P. O. Schmidt, "Optical atomic clocks," Rev. Mod. Phys. **87**, 637 (2015).
[2] A. Derevianko and H. Katori, "Colloquium: Physics of optical lattice clocks," Rev. Mod. Phys. **83**, 331 (2011).
[3] N. Poli, C. W. Oates, P. Gill, and G. M. Tino, "Optical atomic clocks," Riv. Nuovo Cimento **36**, 555 (2013).
[4] C. M. Will, "The Confrontation between General Relativity and Experiment," Living Rev. Relativ. **17**, 4 (2014).
[5] R. X. Adhikari, "Gravitational radiation detection with laser interferometry," Rev. Mod. Phys. **86**, 121 (2014).
[6] C. Braxmaier, H. Müller, O. Pradl, J. Mlynek, A. Peters, and S. Schiller, "Test of relativity using a cryogenic optical resonator," Phys. Rev. Lett. **88**, 010401 (2002).
[7] E. Wiens, A. Y. Nevsky, and S. Schiller, "Resonator with ultrahigh length stability as a probe for equivalence-principle-violating physics," Phys. Rev. Lett. **117**, 271102 (2016).
[8] Q. Chen, E. Magoulakis, and S. Schiller, "High-sensitivity crossed-resonator laser apparatus for improved tests of Lorentz invariance and of space-time fluctuations," Phys. Rev. D **93**, 022003 (2016).
[9] M. E. Tobar, P. Wolf, S. Bize, G. Santarelli, and V. Flambaum, "Testing local Lorentz and position invariance and variation of fundamental constants by searching the derivative of the comparison frequency between a cryogenic sapphire oscillator and hydrogen maser," Phys. Rev. D **81**, 022003 (2010).
[10] C. Eisele, A. Nevsky, and S. Schiller, "A laboratory test of the isotropy of light propagation at the 10^{-17} level," Phys. Rev. Lett. **103**, 090401 (2009).
[11] M. Nagel, S. R. Parker, E. V. Kovalchuk, P. L. Stanwix, J. G. Hartnett, E. N. Ivanov, A. Peters, and M. E. Tobar, "Direct terrestrial test of Lorentz symmetry in electrodynamics to 10^{-18}," Nat. Commun. **6**, 8174 (2015).
[12] A. Takahashi, "Long-term dimensional stability of a line scale made of low thermal expansion ceramic nexcera," Meas. Sci. Technol. **23**, 035001 (2012).
[13] K. Hosaka, H. Inaba, D. Akamatsu, M. Yasuda, J. Sugawara, A. Onae, and F.-L. Hong, "A Fabry-Perot etalon with an ultralow expansion ceramic," Jpn. J. Appl. Phys., Part 1 **52**, 032402 (2013).
[14] I. Ito, A. Silva, T. Nakamura, and Y. Kobayashi, "Stable cw laser based on low thermal expansion ceramic cavity with 4.9 mHz/s frequency drift," Opt. Express **25**, 26020 (2017).
[15] K. Numata, A. Kemery, and J. Camp, "Thermal-noise limit in the frequency stabilization of lasers with rigid cavities," Phys. Rev. Lett. **93**, 250602 (2004).
[16] A. D. Ludlow, X. Huang, M. Notcutt, T. Zanon-Willette, S. M. Foreman, M. M. Boyd, S. Blatt, and J. Ye, "Compact, thermal-noise-limited optical cavity for diode laser stabilization at 1×10^{-15}," Opt. Lett. **32**, 641 (2007).
[17] S. A. Webster, M. Oxborrow, S. Pugla, J. Millo, and P. Gill, "Thermal-noise-limited optical cavity," Phys. Rev. A **77**, 033847 (2008).
[18] Q.-F. Chen, A. Nevsky, M. Cardace, S. Schiller, T. Legero, S. Häfner, A. Uhde, and U. Sterr, "A compact, robust, and transportable ultra-stable laser with a fractional frequency instability of 1×10^{-15}," Rev. Sci. Instrum. **85**, 113107 (2014).
[19] D. Świerad, S. Häfner, S. Vogt, B. Venon, D. Holleville, S. Bize, A. Kulosa, S. Bode, Y. Singh, K. Bongs, E. M. Rasel, J. Lodewyck, R. Le Targat, C. Lisdat, and U. Sterr, "Ultra-stable clock laser system development towards space applications," Sci. Rep. **6**, 33973 (2016).
[20] J. Davila-Rodriguez, F. N. Baynes, A. D. Ludlow, T. M. Fortier, H. Leopardi, S. A. Diddams, and F. Quinlan, "Compact, thermal-noise-limited reference cavity for ultra-low-noise microwave generation," Opt. Lett. **42**, 1277 (2017).
[21] S. Häfner, S. Falke, C. Grebing, S. Vogt, T. Legero, M. Merimaa, C. Lisdat, and U. Sterr, "8×10^{17} fractional laser frequency instability with a long room-temperature cavity," Opt. Lett. **40**, 2112–2115 (2015).
[22] D. G. Matei, T. Legero, S. Häfner, C. Grebing, R. Weyrich, W. Zhang, L. Sonderhouse, J. M. Robinson, J. Ye, F. Riehle, and U. Sterr, "1.5 μm lasers with sub-10 mHz linewidth," Phys. Rev. Lett. **118**, 263202 (2017).
[23] W. Zhang, J. M. Robinson, L. Sonderhouse, E. Oelker, C. Benko, J. L. Hall, T. Legero, D. G. Matei, F. Riehle, U. Sterr, and J. Ye, "Ultrastable silicon cavity in a continuously operating closed-cycle cryostat at 4 K," Phys. Rev. Lett. **119**, 243601 (2017).
[24] J. M. Robinson, E. Oelker, W. R. Milner, W. Zhang, T. Legero, D. G. Matei, F. Riehle, U. Sterr, and J. Ye, "Crystalline optical cavity at 4 K with thermal-noise-limited instability and ultralow drift," Optica **6**, 240–243 (2019).
[25] S. Seel, R. Storz, G. Ruoso, J. Mlynek, and S. Schiller, "Cryogenic optical resonators: A new tool for laser frequency stabilization at the 1 Hz level," Phys. Rev. Lett. **78**, 4741 (1997).
[26] T. Kessler, C. Hagemann, C. Grebing, T. Legero, U. Sterr, F. Riehle, M. J. Martin, L. Chen, and J. Ye, "A sub-40-mHz-linewidth laser based on a silicon single-crystal optical cavity," Nat. Photonics **6**, 687 (2012).
[27] C. Hagemann, C. Grebing, C. Lisdat, S. Falke, T. Legero, U. Sterr, F. Riehle, M. Martin, and J. Ye, "Ultra-stable laser with average fractional frequency drift rate below 5×10^{-19}/s," Opt. Lett. **39**, 5102 (2014).
[28] E. Wiens, Q. Chen, I. Ernsting, H. Luckmann, A. Y. Nevsky, U. Rosowski, and S. Schiller, "A silicon single-crystal cryogenic optical resonator," Opt. Lett. **39**, 3242 (2014).
[29] H. Müller, C. Braxmaier, S. Herrmann, O. Pradl, C. Lämmerzahl, J. Mlynek, S. Schiller, and A. Peters, "Testing the foundation of relativity using cryogenic optical resonators," Int. J. Mod. Phys. D **11**, 1101 (2002).

[30] J. J. Hall, "Electronic effects in the elastic constants of n-type silicon," Phys. Rev. **161**, 756 (1967).
[31] D. G. Matei, T. Legero, C. Grebing, S. Häfner, C. Lisdat, R. Weyrich, W. Zhang, L. Sonderhouse, J. M. Robinson, F. Riehle, J. Ye, and U. Sterr, "A second generation of low thermal noise cryogenic silicon resonators," J. Phys.: Conf. Ser. **723**, 012031 (2016).
[32] L. Zhang, R. Barrett, P. Cloetens, C. Detlefs, and M. Sanchez del Rio, "Anisotropic elasticity of silicon and its application to the modelling of x-ray optics," J. Synchrotron Radiat. **21**, 507 (2014).
[33] R. Nawrodt, A. Zimmer, T. Koettig, C. Schwarz, D. Heinert, M. Hudl, R. Neubert, M. Thürk, S. Nietzsche, W. Vodel, P. Seidel, and A. Tünnermann, "High mechanical Q-factor measurements on silicon bulk samples," J. Phys.: Conf. Ser. **122**, 012008 (2008).
[34] M. Granata, K. Craig, G. Cagnoli, C. Carcy, W. Cunningham, J. Degallaix, R. Flaminio, D. Forest, M. Hart, J.-S. Hennig, J. Hough, I. MacLaren, I. W. Martin, C. Michel, N. Morgado, S. Otmani, L. Pinard, and S. Rowan, "Cryogenic measurements of mechanical loss of high-reflectivity coating and estimation of thermal noise," Opt. Lett. **38**, 5268 (2013).
[35] K. O. McLean, "Low temperature thermal expansion of copper, silver, gold and aluminum," Ph.D. thesis, Iowa State University, 1969.
[36] *Materials at Low Temperatures*, edited by R. P. Reed and A. F. Clark (American Society for Metals, 1983).

References

[1] T. Maiman. Stimulated Optical Radiation in Ruby. *Nature*, 187:493, 1960. URL https://doi.org/10.1038/187493a0.

[2] Alexius J. Herba. *The Physics of Metrology*. Springer-Verlag, 2010. URL https://www.springer.com/gp/book/9783211783801.

[3] Feng-Lei Hong. Optical frequency standards for time and length applications. *Meas. Sci. Technol.*, 28:012002, 2016. URL https://doi.org/10.1088/1361-6501/28/1/012002.

[4] W. R. Milner, J. M. Robinson, C. J. Kennedy, T. Bothwell, D. Kedar, D. G. Matei, Th. Legero, U. Sterr, F. Riehle, H. Leopardi, T. M. Fortier, J. A. Sherman, J. Levine, J. Yao, J. Ye, and E. Oelker. Demonstration of a Timescale Based on a Stable Optical Carrier. *Phys. Rev. Lett.*, 123:173201, 2020. URL https://link.aps.org/doi/10.1103/PhysRevLett.123.173201.

[5] E. J. Salumbides, A. N. Schellekens, B. Gato-Rivera, and W. Ubachs. Constraints on extra dimensions from precision molecular spectroscopy. *New J. Phys.*, 17:033015, 2015. URL https://doi.org/10.1088%2F1367-2630%2F17%2F3%2F033015.

[6] S. Alighanbari, M. G. Hansen, V. I. Korobov, and S. Schiller. Rotational spectroscopy of cold and trapped molecular ions in the Lamb-Dicke regime. *Nat. Phys.*, 14:555, 2018. URL https://doi.org/10.1038/s41567-018-0074-3.

[7] R. Oswald, M. G. Hansen, E. Wiens, A. Yu. Nevsky, and S. Schiller. Characteristics of long-lived persistent spectral holes in Eu^{3+}:Y_2SiO_5 at 1.2 k. *Phys. Rev. A*, 98:062516, 2018. URL https://link.aps.org/doi/10.1103/PhysRevA.98.062516.

[8] Sayan Patra, M. Germann, J.-Ph. Karr, M. Haidar, L. Hilico, V. I. Korobov, F. M. J. Cozijn, K. S. E. Eikema, W. Ubachs, and J. C. J. Koelemeij. Proton-electron mass ratio from laser spectroscopy of HD^+ at the part-per-trillion level. *Science*, 369(6508):1238, 2020. URL https://doi.org/10.1126/science.aba0453.

[9] M. Hori, H. Aghai-Khozani, A. S, A. Dax, and D. Barna. Laser spectroscopy of pionic helium atoms. *Nature*, 581:37, 2020. URL https://doi.org/10.1038/s41586-020-2240-x.

[10] L. Ju, D. G. Blair, and C. Zhao. Detection of gravitational waves. *Rep. Prog. Phys.*, 63:1317, 2000. URL https://doi.org/10.1088/0034-4885/63/9/201.

[11] Clifford M. Will. The confrontation between general relativity and experiment. *Living Rev. Relativity*, 17(4), 2014. URL https://doi.org/10.12942/lrr-2014-4.

[12] Rana X. Adhikari. Gravitational radiation detection with laser interferometry. *Rev. Mod. Phys.*, 86(1):121, 2014. URL https://link.aps.org/doi/10.1103/RevModPhys.86.121.

[13] A. Derevianko and H. Katori. Colloquium: Physics of optical lattice clocks. *Rev. Mod. Phys.*, 83:331, May 2011. URL https://link.aps.org/doi/10.1103/RevModPhys.83.331.

[14] N. Poli, C. W. Oates, P. Gill, and G. M. Tino. Optical atomic clocks. *Rivista del Nuovo Cimento*, 36:555, 2013. URL https://www.sif.it/riviste/sif/ncr/econtents/2013/036/12/article/0.

[15] B. J. Bloom, T. L. Nicholson, J. R. Williams, S. L. Campbell, M. Bishof, X. Zhang, W. Zhang, S. L. Bromley, and J. Ye. An optical lattice clock with accuracy and stability at the 10^{-18} level. *Nature*, 506(7486):71, 2014. URL http://dx.doi.org/10.1038/nature12941.

[16] A. D. Ludlow, M. M. Boyd, J. Ye, E. Peik, and P. O. Schmidt. Optical atomic clocks. *Rev. Mod. Phys.*, 87:637, 2015. URL https://link.aps.org/doi/10.1103/RevModPhys.87.637.

[17] T.L. Nicholson, S.L. Campbell, R.B. Hutson, G.E. Marti, B.J. Bloom, R.L. McNally, W. Zhang, M.D. Barrett, M.S. Safronova, W.L. Strouse, G.F. Tew, and J. Ye. Systematic evaluation of an atomic clock at 2×10^{-18} total uncertainty. *Nat. Comm.*, 6:6896, 2015. URL https://doi.org/10.1038/ncomms7896.

[18] S. B. Koller, J. Grotti, St. Vogt, A. Al-Masoudi, S. Dörscher, S. Häfner, U. Sterr, and Ch. Lisdat. Transportable optical lattice clock with 7×10^{-17} uncertainty. *Phys. Rev. Lett.*, 118:073601, 2017. URL https://link.aps.org/doi/10.1103/PhysRevLett.118.073601.

[19] S. Origlia, M. S. Pramod, S. Schiller, Y. Singh, K. Bongs, R. Schwarz, A. Al-Masoudi, S. Dörscher, S. Herbers, S. Häfner, U. Sterr, and Ch. Lisdat. Towards an optical clock for space: Compact, high-performance optical lattice clock based on bosonic atoms. *Phys. Rev. A*, 98: 053443, 2018. URL https://link.aps.org/doi/10.1103/PhysRevA.98.053443.

[20] Y. V. Stadnik and V. V. Flambaum. Enhanced effects of variation of the fundamental constants in laser interferometers and application to dark-matter detection. *Phys. Rev. A*, 93:063630, 2016. URL https://link.aps.org/doi/10.1103/PhysRevA.93.063630.

[21] A. A. Geraci, C. Bradley, D. Gao, J. Weinstein, and A. Derevianko. Searching for Ultralight Dark Matter with Optical Cavities. *Phys. Rev. Lett.*, 123:031304, 2019. URL https://link.aps.org/doi/10.1103/PhysRevLett.123.031304.

[22] C. J. Kennedy, E. Oelker, J. M. Robinson, T. Bothwell, D. Kedar, W. R. Milner, G. E. Marti, A. Derevianko, and J. Ye. Precision Metrology Meets Cosmology: Improved Constraints on Ultralight Dark Matter from Atom-Cavity Frequency Comparisons. *Phys. Rev. Lett.*, 125:201302, 2020. URL https://link.aps.org/doi/10.1103/PhysRevLett.125.201302.

[23] Sh. Doeleman, T. Mai, A. E. E. Rogers, J. G. Hartnett, M. E. Tobar, and N. Nand. Adapting a Cryogenic Sapphire Oscillator for Very Long Baseline Interferometry. *Publ. Astron. Soc. Pac.*, 123:582, 2011. URL https://doi.org/10.1086/660156.

[24] Ch.-H. Li, A. J. Benedick, P. Fendel, A. G. Glenday, F. X. Kner, D. F. Phillips, D. Sasselov, A. Szentgyorgyi, and R. L. Walsworth. A laser frequency comb that enables radial velocity measurements with a precision of 1 cm s^{-1}. *Nature*, 452:610, 2008. URL https://doi.org/10.1038/nature06854.

[25] T. Herr and R. A. McCracken. Astrocombs: Recent Advances. *IPTL*, 31:1890, 2019. URL https://ieeexplore.ieee.org/document/8887498.

[26] R. Bondarescu, A. Schärer, A. Lundgren, G. Hetényi, N. Houlié, Ph. Jetzer, and M. Bondarescu. Ground-based optical atomic clocks as a tool to monitor vertical surface motion. *Geophys. J. Int.*, 202:1770, 2015. URL https://academic.oup.com/gji/article/202/3/1770/610100.

[27] J. Grotti, S. Koller, S. Vogt, S. Häfner, U. Sterr, Ch. Lisdat, H. Denker, C. Voigt, L. Timmen, A. Rolland, F. N. Baynes, H. S. Margolis, M. Zampaolo, P. Thoumany, M. Pizzocaro, B. Rauf, F. Bregolin, A. Tampellini, P. Barbieri, M. Zucco, G. A. Costanzo, C. Clivati, F. Levi, and D. Calonico. Geodesy and metrology with a transportable optical clock. *Nature Physics*, 14: 437, 2018. URL https://doi.org/10.1038/s41567-017-0042-3.

[28] Ch. Lisdat, G. Grosche, N. Quintin, C. Shi, S.M.F. Raupach, C. Grebing, D. Nicolodi, F. Stefani, A. Al-Masoudi, S. Dörscher, S. Häfner, J.-L. Robyr, N. Chiodo, S. Bilicki, E. Bookjans, A. Koczwara, S. Koke, A. Kuhl, F. Wiotte, F. Meynadier, E. Camisard, M. Abgrall, M. Lours,

T. Legero, H. Schnatz, U. Sterr, H. Denker, C. Chardonnet, Y. Le Coq, G. Santarelli, A. Amy-Klein, R. Le Targat, J. Lodewyck, O. Lopez, and P.-E. Pottie. A clock network for geodesy and fundamental science. *Nat. Comm.*, 7:12443, 2016. URL https://doi.org/10.1038/ncomms12443.

[29] T. Takano, M. Takamoto, I. Ushijima, N. Ohmae, T. Akatsuka, A. Yamaguchi, Y. Kuroishi, H. Munekane, B. Miyahara, and H. Katori. Geopotential measurements with synchronously linked optical lattice clocks. *Nat. Photonics*, 10:662, 2016. URL https://doi.org/10.1038/nphoton.2016.159.

[30] C. Braxmaier, H. Müller, O. Pradl, J. Mlynek, A. Peters, and S. Schiller. Test of relativity using a cryogenic optical resonator. *Phys. Rev. Lett.*, 88:010401, 2001. URL https://link.aps.org/doi/10.1103/PhysRevLett.88.010401.

[31] C. Eisele, A. Nevsky, and S. Schiller. A laboratory test of the isotropy of light propagation at the 10^{-17} level. *Phys. Rev. Lett.*, 103:090401, 2009. URL https://journals.aps.org/prl/abstract/10.1103/PhysRevLett.103.090401.

[32] M. E. Tobar, P. Wolf, S. Bize, G. Santarelli, and V. Flambaum. Testing local lorentz and position invariance and variation of fundamental constants by searching the derivative of the comparison frequency between a cryogenic sapphire oscillator and hydrogen maser. *Phys. Rev. D*, 81:022003, 2010. URL https://link.aps.org/doi/10.1103/PhysRevD.81.022003.

[33] M. Nagel, S. R. Parker, E. V. Kovalchuk, P. L. Stanwix, J. G. Hartnett, E. N. Ivanov, A. Peters, and M. E. Tobar. Direct terrestrial test of lorentz symmetry in electrodynamics to 10^{-18}. *Nat. Commun*, 6:1, 2015. URL https://www.nature.com/articles/ncomms9174.

[34] Q.F. Chen, E. Magoulakis, and S. Schiller. High-sensitivity crossed-resonator laser apparatus for improved tests of lorentz invariance and of space-time fluctuations. *Phys. Rev. D*, 93:022003, 2016. URL https://link.aps.org/doi/10.1103/PhysRevD.93.022003.

[35] E. Wiens, A. Yu. Nevsky, and S. Schiller. Resonator with ultrahigh length stability as a probe for equivalence-principle-violating physics. *Phys. Rev. Lett.*, 117:271102, 2016. URL https://link.aps.org/doi/10.1103/PhysRevLett.117.271102.

[36] P. Delva, J. Lodewyck, S. Bilicki, E. Bookjans, G. Vallet, R. Le Targat, P.-E. Pottie, C. Guerlin, F. Meynadier, C. Le Poncin-Lafitte, O. Lopez, A. Amy-Klein, W.-K. Lee, N. Quintin, Ch. Lisdat, A. Al-Masoudi, S. Dörscher, C. Grebing, G. Grosche, A. Kuhl, S. Raupach, U. Sterr, I. R. Hill, R. Hobson, W. Bowden, J. Kronjäger, G. Marra, A. Rolland, F. N. Baynes, H. S. Margolis, and P. Gill. Test of special relativity using a fiber network of optical clocks. *Phys. Rev. Lett.*, 118:221102, Jun 2017. URL https://link.aps.org/doi/10.1103/PhysRevLett.118.221102.

[37] P. Delva, A. Hees, and P. Wolf. Clocks in Space for Tests of Fundamental Physics. *Space Sci Rev*, 212:1385, 2017. URL https://doi.org/10.1007/s11214-017-0361-9.

[38] R. W. P. Drever, J. L. Hall, F. V. Kowalski, J. Hough, G. M. Ford, A. J. Munley, and H. Ward. Laser phase and frequency stabilization using an optical resonator. *Appl. Phys. B*, 31:97, 1983. URL https://doi.org/10.1007/BF00702605.

[39] E. Black. Notes on the Pound-Drever-Hall technique. Technical Report LIGO-T980045-00-D, LIGO, 1998. URL http://jila1.nickersonm.com/papers/Notes%20on%20the%20Pound-Drever-Hall%20technique.pdf.

[40] E. D. Black. An introduction to pound–drever–hall laser frequency stabilization. *Am. J. Phys.*, 69(1):79, 2001. URL https://doi.org/10.1119/1.1286663.

[41] Ch. Eisele, M. Okhapkin, A. Yu. Nevsky, and S. Schiller. A crossed optical cavities apparatus for a precision test of the isotropy of light propagation. *Opt. Commun.*, 281:1189, 2008. URL https://doi.org/10.1016/j.optcom.2007.10.071.

[42] Ch. J. Kwong, M. G. Hansen, J. Sugawara, and S. Schiller. Characterization of the long-term dimensional stability of a NEXCERA block using the optical resonator technique. *Meas. Sci. Technol.*, 29(7):075011, 2018. URL http://stacks.iop.org/0957-0233/29/i=7/a=075011.

[43] U. Sterr. Ultrastabile Laser. *PTB Mitteilungen*, 128(3):7–15, 2018. URL https://www.ptb.de/cms/fileadmin/internet/publikationen/ptb_mitteilungen/mitt2018/Heft3/PTB-Mitteilungen_2018_Heft_3.pdf.

[44] T. Legero, T. Kessler, and U. Sterr. Tuning the thermal expansion properties of optical reference cavities with fused silica mirrors. *J. Opt. Soc. Am. B*, 27(5):914, 2010. URL http://josab.osa.org/abstract.cfm?URI=josab-27-5-914.

[45] A. D. Ludlow, X. Huang, M. Notcutt, T. Zanon-Willette, S. M. Foreman, M. M. Boyd, S. Blatt, and J. Ye. Compact, thermal-noise-limited optical cavity for diode laser stabilization at 1×10^{-15}. *Opt.Lett.*, 32:641, 2007. URL https://doi.org/10.1364/OL.32.000641.

[46] S. A. Webster, M. Oxborrow, S. Pugla, J. Millo, and P. Gill. Thermal-noise-limited optical cavity. *Phys. Rev. A*, 77(3):033847, 2008. URL https://link.aps.org/doi/10.1103/PhysRevA.77.033847.

[47] Q.-F. Chen, A. Yu. Nevsky, M. Cardace, S. Schiller, T. Legero, S. Häfner, A. Uhde, and U. Sterr. A compact, robust, and transportable ultra-stable laser with a fractional frequency instability of 1×10^{-15}. *Rev. Sci. Instrum.*, 85:113107, 2014. URL https://doi.org/10.1063/1.4898334.

[48] D. Świerad, S. Häfner, S. Vogt, B. Venon, D. Holleville, S. Bize, A. Kulosa, S. Bode, Y. Singh, K. Bongs, E. M. Rasel, J. Lodewyck, R. Le Targat, Ch. Lisdat, and U. Sterr. Ultra-stable clock laser system development towards space applications. *Sci. Rep.*, 6:33973, 09 2016. URL http://dx.doi.org/10.1038/srep33973.

[49] J. Davila-Rodriguez, F. N. Baynes, A. D. Ludlow, T. M. Fortier, H. Leopardi, S. A. Diddams, and F. Quinlan. Compact, thermal-noise-limited reference cavity for ultra-low-noise microwave generation. *Opt. Lett.*, 42(7):1277, 2017. URL https://www.osapublishing.org/abstract.cfm?uri=ol-42-7-1277.

[50] K. Numata, A. Kemery, and J. Camp. Thermal-noise limit in the frequency stabilization of lasers with rigid cavities. *Phys. Rev. Lett.*, 93(25):250602, 2004. URL https://link.aps.org/doi/10.1103/PhysRevLett.93.250602.

[51] T. Kessler, T. Legero, and U. Sterr. Thermal noise in optical cavities revisited. *J. Opt. Soc. Am. B*, 29(1):178, 2012. URL http://josab.osa.org/abstract.cfm?URI=josab-29-1-178.

[52] Y. Y. Jiang, A. D. Ludlow, N. D. Lemke, R. W. Fox, J. A. Sherman, L.-S. Ma, and C. W. Oates. Making optical atomic clocks more stable with 10^{-16}-level laser stabilization. *Nat. Photon.*, 5:158, 2011. URL https://doi.org/10.1038/nphoton.2010.313.

[53] T. L. Nicholson, M. J. Martin, J. R. Williams, B. J. Bloom, M. Bishof, M. D. Swallows, S. L. Campbell, and J. Ye. Comparison of two independent Sr optical clocks with 1×10^{-17} stability at 10^3 s. *Phys. Rev. Lett.*, 109:230801, 2012. URL https://link.aps.org/doi/10.1103/PhysRevLett.109.230801.

[54] S. Häfner, S. Falke, C. Grebing, S. Vogt, T. Legero, M. Merimaa, Ch. Lisdat, and U. Sterr. 8×10^{-17} fractional laser frequency instability with a long room-temperature cavity. *Opt. Lett.*, 40(9):2112, 2015. URL https://doi.org/10.1364/OL.40.002112.

[55] L. Jin, Y. Jiang, Y. Yao, H. Yu, Z. Bi, and L. Ma. Laser frequency instability of 2×10^{-16} by stabilizing to 30-cm-long Fabry-Pt cavities at 578 nm. *Opt. Express*, 26(14):18699, 2018. URL https://doi.org/10.1364/OE.26.018699.

[56] S. Häfner, S. Herbers, S. Vogt, Ch Lisdat, and U. Sterr. Transportable interrogation laser system with an instability of mod $\sigma_y = 3 \times 10^{16}$. *Opt. Express*, 28(11):16407, 2020. URL https://doi.org/10.1364/OE.390105.

[57] E. D'Ambrosio. Nonspherical mirrors to reduce thermoelastic noise in advanced gravitational wave interferometers. *Phys. Rev. D*, 67(10):102004, 2003. URL https://link.aps.org/doi/10.1103/PhysRevD.67.102004.

[58] B. Mours, E. Tournefier, and J.-Y. Vinet. Thermal noise reduction in interferometric gravitational wave antennas: using high order TEM modes. *Class. Quantum Gravity*, 23(20):5777, 2006. URL https://doi.org/10.1088%2F0264-9381%2F23%2F20%2F001.

[59] S. Amairi, T. Legero, T. Kessler, U. Sterr, J. B. Wübbena, O. Mandel, and P. O. Schmidt. Reducing the effect of thermal noise in optical cavities. *Appl. Phys. B*, 113(2):233, 2013. URL https://doi.org/10.1007/s00340-013-5464-8.

[60] A. Noack, Ch. Bogan, and B. Willke. Higher-order Laguerre-Gauss modes in (non-) planar four-mirror cavities for future gravitational wave detectors. *Opt. Lett.*, 42(4):751, 2017. URL https://doi.org/10.1364/OL.42.000751.

[61] X. Y. Zeng, Y. X. Ye, X. H. Shi, Z. Y. Wang, K. Deng, J. Zhang, and Z. H. Lu. Thermal-noise-limited higher-order mode locking of a reference cavity. *Opt. Lett.*, 43(8):1690, 2018. URL https://doi.org/10.1364/OL.43.001690.

[62] G. D. Cole, W. Zhang, M. J. Martin, J. Ye, and M. Aspelmeyer. Tenfold reduction of brownian noise in high-reflectivity optical coatings. *Nat. Photon.*, 7:644, 2013. URL https://doi.org/10.1038/nphoton.2013.174.

[63] G. D. Cole, W. Zhang, B. J. Bjork, D. Follman, P. Heu, C. Deutsch, L. Sonderhouse, J. Robinson, C. Franz, A. Alexandrovski, M. Notcutt, O. H. Heckl, J. Ye, and M. Aspelmeyer. High-performance near- and mid-infrared crystalline coatings. *Optica*, 3(6):647, 2016. URL https://doi.org/10.1364/OPTICA.3.000647.

[64] S. Seel, R. Storz, G. Ruoso, J. Mlynek, and S. Schiller. Cryogenic Optical Resonators: A new tool for laser frequency stabilization at the 1 Hz level. *Phys. Rev. Lett.*, 78:4741, 1997. URL https://link.aps.org/doi/10.1103/PhysRevLett.78.4741.

[65] H. Müller, C. Braxmaier, S. Hermann, O. Pradl, C. Lämmerzahl, J. Mlynek, S. Schiller, and A. Peters. Testing the foundation of relativity using cryogenic optical resonators. *IJMPD*, 11: 1101, 2002. URL https://doi.org/10.1142/S0218271802002608.

[66] T. Kessler, C. Hagemann, C. Grebing, T. Legero, U. Sterr, F. Riehle, M. J. Martin, L. Chen, and J. Ye. A sub-40-mHz-linewidth laser based on a silicon single-crystal optical cavity. *Nat. Photon.*, 6:687, 2012. URL https://doi.org/10.1038/nphoton.2012.217.

[67] C. Hagemann, C. Grebing, C. Lisdat, S. Falke, T. Legero, U. Sterr, F. Riehle, M.J. Martin, and J. Ye. Ultra-stable laser with average fractional frequency drift rate below 5×10^{-19}/s. *Opt. Lett.*, 39:5102, 2014. URL https://doi.org/10.1364/OL.39.005102.

[68] E. Wiens, Q. Chen, I. Ernsting, H. Luckmann, A. Y. Nevsky, U. Rosowski, and S. Schiller. A silicon single-crystal cryogenic optical resonator. *Opt. Lett.*, 39:3242, 2014. URL https://doi.org/10.1364/OL.39.003242.

[69] D. G. Matei, T. Legero, S. Häfner, C. Grebing, R. Weyrich, W. Zhang, L. Sonderhouse, J. M. Robinson, J. Ye, F. Riehle, and U. Sterr. 1.5 μm lasers with sub-10 mHz linewidth. *Phys. Rev. Lett.*, 118:263202, 2017. URL https://link.aps.org/doi/10.1103/PhysRevLett.118.263202.

[70] W. Zhang, J. M. Robinson, L. Sonderhouse, E. Oelker, C. Benko, J. L. Hall, T. Legero, D. G. Matei, F. Riehle, U. Sterr, and J. Ye. Ultrastable silicon cavity in a continuously operating closed-cycle cryostat at 4 K. *Phys. Rev. Lett.*, 119(24):243601, 2017. URL https://link.aps.org/doi/10.1103/PhysRevLett.119.243601.

[71] J. M. Robinson, E. Oelker, W. R. Milner, W. Zhang, T. Legero, D. G. Matei, F. Riehle, U. Sterr, and J. Ye. Crystalline optical cavity at 4 K with thermal-noise-limited instability and ultralow drift. *Optica*, 6(2):240, 2019. URL https://doi.org/10.1364/OPTICA.6.000240.

[72] A. Takahashi. Long-term dimensional stability of a line scale made of low thermal expansion ceramic nexcera. *Meas. Sci. Technol.*, 23:035001, 2012. URL https://iopscience.iop.org/article/10.1088/0957-0233/23/3/035001.

[73] K. Hosaka, H. Inaba, D. Akamatsu, M. Yasuda, J. Sugawara, A. Onae, and F.-L. Hong. A Fabry-Perot etalon with an ultralow expansion ceramic. *Jpn. J. Appl. Phys.*, 52:03242, 2013. URL https://iopscience.iop.org/article/10.7567/JJAP.52.032402.

[74] I. Ito, A. Silva, T. Nakamura, and Y. Kobayashi. Stable CW laser based on low thermal expansion ceramic cavity with 4.9 mHz/s frequency drift. *Opt. Exp.*, 25:26020, 2017. URL https://doi.org/10.1364/OE.25.026020.

[75] C. Y. Ho, R. W. Powell, and P. E. Liley. Thermal conductivity of the elements. *J. Phys. Chem. Ref. Data*, 1(2):279, 1972. URL https://aip.scitation.org/doi/10.1063/1.3253100.

[76] Y. S. Touloukian, R. W. Powell, C. Y. Ho, and P. C. Klemens. *Thermophysical properties of matter*, volume 2. CINDAS/Purdue University, 1971.

[77] R. Storz, C. Braxmaier, K. Jäck, O. Pradl, and S. Schiller. Ultrahigh long-term dimensional stability of a sapphire cryogenic optical resonator. *Opt. Lett.*, 23:1031, 1998. URL https://doi.org/10.1364/OL.23.001031.

[78] R. Storz. *Frequenzstabilisierung von Festkörper-Lasern auf makroskopische und mikroskopische Referenzen*. PhD thesis, Universität Konstanz, Germany, 1998.

[79] S. Schiller, C. Lämmerzahl, H. Müller, C. Braxmaier, S. Herrmann, and A. Peters. Experimental limits for low-frequency space-time fluctuations from ultrastable optical resonators. *Phys. Rev. D*, 69:027504, 2004. URL https://link.aps.org/doi/10.1103/PhysRevD.69.027504.

[80] P. Antonini, M. Okhapkin, E. Göklü, and S. Schiller. Test of constancy of speed of light with rotating cryogenic optical resonators. *Phys. Rev. A*, 71:050101(R), 2005. URL https://link.aps.org/doi/10.1103/PhysRevA.71.050101.

[81] M. E. Tobar, P. L. Stanwix, J. J. McFerran, J. Guéna, M. Abgrall, S. Bize, A. Clairon, Ph. Laurent, P. Rosenbusch, D. Rovera, and G. Santarelli. Testing local position and fundamental constant invariance due to periodic gravitational and boost using long-term comparison of the SYRTE atomic fountains and H-masers. *Phys. Rev. D*, 87:122004, 2013. URL https://link.aps.org/doi/10.1103/PhysRevD.87.122004.

[82] J.-P. Richard and J. J. Hamilton. Cryogenic monocrystalline silicon Fabry-Perot cavity for the stabilization of laser frequency. *Rev. Sci. Instrum.*, 62:2375, 1991. URL https://doi.org/10.1063/1.1142249.

[83] Uwe Sterr. Frequenzstabilisierungsvorrichtung, August 2012. Patent number DE102011015489 B3.

[84] L. Zhang, R. Barrett, P. Cloetens, C. Detlefs, and M. Sanchez del Rio. Anisotropic elasticity of silicon and its application to the modelling of X-ray optics. *J. Synchrotron Rad.*, 21:507, 2014. URL `https://doi.org/10.1107/S1600577514004962`.

[85] R. Nawrodt, A. Zimmer, T. Koettig, C. Schwarz, D. Heinert, M. Hudl, R. Neubert, M. Thürk, S. Nietzsche, W. Vodel, P Seidel, and A. Tünnermann. High mechanical Q-factor measurements on silicon bulk samples. *J. Phys. Conf. Ser.*, 122(1):012008, 2008. URL `https://iopscience.iop.org/article/10.1088/1742-6596/122/1/012008`.

[86] M. Granata, K. Craig, G. Cagnoli, C. Carcy, W. Cunningham, J. Degallaix, R. Flaminio, D. Forest, M. Hart, J-S. Hennig, J. Hough, I. MacLaren, I. W. Martin, Chr. Michel, N. Morgado, S. Otmani, L. Pinard, and Sh. Rowan. Cryogenic measurements of mechanical loss of high-reflectivity coating and estimation of thermal noise. *Opt. Lett.*, 38(24):5268, 2013. URL `https://doi.org/10.1364/OL.38.005268`.

[87] L.-S. Ma, P. Jungner, J. Ye, and J. L. Hall. Delivering the same optical frequency at two places: accurate cancellation of phase noise introduced by an optical fiber or other time-varying path. *Opt. Lett.*, 19(21):1777, November 1994. URL `https://doi.org/10.1364/OL.19.001777`.

[88] E. Wiens and S. Schiller. Simulation of force-insensitive optical cavities in cubic spacers. *Appl. Phys. B*, 124:140, 2018. URL `https://doi.org/10.1007/s00340-018-7000-3`.

[89] M. Pelliccione, A. Sciambi, J. Bartel, A. J. Keller, and D. Goldhaber-Gordon. Design of a scanning gate microscope for mesoscopic electron systems in a cryogen-free dilution refrigerator. *Rev. Sci. Instrum.*, 84(3):033703, 2013. URL `https://aip.scitation.org/doi/10.1063/1.4794767`.

[90] A. M. J. den Haan, G. H. C. J. Wijts, F. Galli, O. Usenko, G. J. C. van Baarle, D. J. van der Zalm, and T. H. Oosterkamp. Atomic resolution scanning tunneling microscopy in a cryogen free dilution refrigerator at 15 mK. *Rev. Sci. Instrum.*, 85(3):035112, 2014. URL `https://aip.scitation.org/doi/10.1063/1.4868684`.

[91] C. Lee, H. S. Jo, C. S. Kang, G. B. Kim, I. Kim, S. R. Kim, Y. H. Kim, H. J. Lee, J. H. So, and Y. S. Yoon. Vibration isolation system for cryogenic phonon-scintillation calorimeters. *J. Instrum.*, 12(02):C02057, 2017. URL `https://iopscience.iop.org/article/10.1088/1748-0221/12/02/C02057`.

[92] M. de Wit, G. Welker, K. Heeck, F. M. Buters, H. J. Eerkens, G. Koning, H. van der Meer, D. Bouwmeester, and T. H. Oosterkamp. Vibration isolation with high thermal conductance for a cryogen-free dilution refrigerator. *Rev. Sci. Instrum.*, 90(1):015112, 2019. URL `https://aip.scitation.org/doi/10.1063/1.5066618`.

[93] E. Wiens, C. J. Kwong, T. Müller, and S. Schiller. A simplified cryogenic optical resonator apparatus providing ultra-low frequency drift. *Rev. Sci. Instrum.*, 91:045112, 2020. URL `https://doi.org/10.1063/1.5140321`.

[94] M. R. Blom, M. G. Beker, A. Bertolini, J. F. J. van den Brand, H. J. Bulten, E. Hennes, F. A. Mul, D. S. Rabeling, and A. Schimmel. Seismic attenuation system for the external injection bench of the Advanced Virgo gravitational wave detector. *Nucl. Instrum. Method A*, 718:466, 2013. URL `http://www.sciencedirect.com/science/article/pii/S0168900212014556`.

[95] M. Blom. *Seismic attenuation for Advanced Virgo. Vibration isolation for the external injection bench.* PhD thesis, Vrije Universiteit Amsterdam, Amsterdam, 2015.

[96] G. Cella, V. Sannibale, R. DeSalvo, S. Marka, and A. Takamori. Monolithic geometric anti-spring blades. *Nucl. Instrum. Method A*, 540(2):502, March 2005. URL https://doi.org/10.1016/j.nima.2004.10.042.

[97] M. Assig, A. Koch, W. Stiepany, C. Straßer, A. Ast, K. Kern, and C. R. Ast. Miniature active damping stage for scanning probe applications in ultra high vacuum. *Rev. Sci. Instrum.*, 83(3):033701, 2012. URL https://doi.org/10.1063/1.3689769.

[98] S. Webster and P. Gill. Force-insensitive optical cavity. *Opt. Lett.*, 36(18):3572, 2011. URL https://doi.org/10.1364/OL.36.003572.

[99] J. Sanjuan, K. Abich, M. Gohlke, A. Resch, Th. Schuldt, T. Wegehaupt, G. P. Barwood, P. Gill, and C. Braxmaier. Long-term stable optical cavity for special relativity tests in space. *Opt. Express*, 27(25):36206, 2019. URL https://doi.org/10.1364/OE.27.036206.

[100] S. Wang, J. Cao, J. Yuan, D. Liu, H. Shu, and X. Huang. Integrated multiple wavelength stabilization on a multi-channel cavity for a transportable optical clock. *Opt. Express*, 28(8):11852, 2020. URL https://doi.org/10.1364/OE.383115.

[101] W. Riley. *Handbook of Frequency Stability Analysis*. Nat. Inst. Standards Technol., Gaithersburg, MD, USA, 2008. URL https://tf.nist.gov/general/pdf/2220.pdf.

[102] H. P. Robertson. Postulate *versus* observation in the special theory of relativity. *Rev. Mod. Phys.*, 21:378, 1949. URL https://link.aps.org/doi/10.1103/RevModPhys.21.378.

[103] R. Mansouri and R. U. Sexl. A test theory of special relativity: I. Simultaneity and clock synchronization. *Gen. Rel. Grav.*, 8:497, 1977. URL https://doi.org/10.1007/BF00762634.

[104] G. F. Smoot, M. V. Gorenstein, and R. A. Muller. Detection of anisotropy in the cosmic blackbody radiation. *Phys. Rev. Lett.*, 39:898, 1977. URL https://link.aps.org/doi/10.1103/PhysRevLett.39.898.

[105] D. Hils and J. L. Hall. Improved Kennedy-Thorndike experiment to test Special Relativity. *Phys. Rev. Lett.*, 64:1697, 1990. URL https://link.aps.org/doi/10.1103/PhysRevLett.64.1697.

[106] P. Wolf, M. E. Tobar, S. Bize, A. Clairon, A. N. Luiten, and G. Santarelli. Whispering gallery resonators and tests of Lorentz invariance. *Gen. Rel. Grav.*, 36:2351, 2004. URL https://doi.org/10.1023/B:GERG.0000046188.87741.51.

[107] P. Bretagnon and G. Francou. Planetary theories in rectangular and spherical variables - VSOP 87 solutions. *Astron. Astrophys.*, 202:309, August 1988. URL http://adsabs.harvard.edu/abs/1988A%26A...202..309B.

[108] J. P. Turneaure, C. M. Will, B. F. Farrell, E. M. Mattison, and R. F. C. Vessot. Test of principle of equivalence by a null red-shift experiment. *Phys. Rev. D*, 27:1705, 1983. URL https://link.aps.org/doi/10.1103/PhysRevD.27.1705.

[109] A. Godone, C. Novero, and P. Tavella. Null gravitational redshift experiment with nonidentical atomic clocks. *Phys. Rev. D*, 51:319, 1995. URL https://journals.aps.org/prd/abstract/10.1103/PhysRevD.51.319.

[110] N. Ashby, T. E. Parker, and B. R. Patla. A null test of general relativity based on a long-term comparison of atomic transition frequencies. *Nat. Phys.*, 14:822, June 2018. URL https://doi.org/10.1038/s41567-018-0156-2.

[111] J. Degallaix, R. Flaminio, D. Forest, M. Granata, Ch. Michel, L. Pinard, T. Bertrand, and G. Cagnoli. Bulk optical absorption of high resistivity silicon at 1550 nm. *Opt. Lett.*, 38:2047, 2013. URL https://doi.org/10.1364/OL.38.002047.

[112] R.A. Ibrahim. Recent advances in nonlinear passive vibration isolators. *J. Sound Vib.*, 314:371, 2008. URL https://doi.org/10.1016/j.jsv.2008.01.014.

[113] J. M. Gere and B. G. Goodno. *Mechanics of materials*. Cengage Learning, 1120 Birchmount Road Toronto ON M1K 5G4 Canada, 7th edition, 2009. ISBN 978-0-534-55397-5.

[114] J. L. Hutter. Comment on Tilt of Atomic Force Microscope Cantilevers: Effect on Spring Constant and Adhesion Measurements. *Langmuir*, 21(6):2630, March 2005. URL https://doi.org/10.1021/la047670t.

[115] M.V. Plissi. Cantilever blade analysis for Advanced LIGO, 2003. URL https://dcc.ligo.org/public/0027/T030107/000/T030107-00.pdf.

[116] Alessandro Bertolini. Personal Communication, 2018.

[117] Calum Iain Eachan Torrie. *Development of Suspensions for the GEO 600 Gravitational Wave Detector*. PhD thesis, University of Glasgow, Glasgow, 2000.

[118] Online Materials Information Resource - MatWeb. URL http://www.matweb.com/.

[119] NGK BERYLCO. URL http://www.ngk-alloys.com/.